



Cardiff  
Catalysis Institute  

---

Sefydliad Catalysis  
Caerdydd



# PASSIVE CATALYTIC SOOT OXIDATION

Thesis submitted in accordance with the requirements  
of Cardiff University for the degree of  
Doctor of Philosophy

Owain Meredith

September 2017

## DECLARATION

This work has not been submitted in substance for any other degree or award at this or any other university or place of learning, nor is being submitted concurrently in candidature for any degree or other award.

Signed ..... (candidate) Date .....

## STATEMENT 1

This thesis is being submitted in partial fulfillment of the requirements for the degree of .....(insert MCh, MD, MPhil, PhD etc, as appropriate)

Signed ..... (candidate) Date .....

## STATEMENT 2

This thesis is the result of my own independent work/investigation, except where otherwise stated.

Other sources are acknowledged by explicit references. The views expressed are my own.

Signed ..... (candidate) Date .....

## STATEMENT 3

I hereby give consent for my thesis, if accepted, to be available for photocopying and for inter-library loan, and for the title and summary to be made available to outside organisations.

Signed ..... (candidate) Date .....

## STATEMENT 4: PREVIOUSLY APPROVED BAR ON ACCESS

I hereby give consent for my thesis, if accepted, to be available for photocopying and for inter-library loans **after expiry of a bar on access previously approved by the Academic Standards & Quality Committee.**

Signed ..... (candidate) Date .....

## Acknowledgements

Firstly, I would like to express my sincerest gratitude to my supervisors; Professor Stanislaw Golunski and Professor Stuart Taylor for giving me the opportunity to undertake this research project. I also wish to thank them for their guidance, encouragement and reassurance throughout the course of this project, it has been invaluable and is greatly appreciated. I would like to thank Jaguar Land Rover for organising and funding this project, as well as providing numerous opportunities for me to present my work to those with a wide range of experience and expertise in this field. I always found the feedback and suggestions provided to me during such events to be most helpful and constructive towards my research, and I am grateful to all who contributed. In particular, I would like to thank Dr. Jamil Khan and Dr. David Sellick for the interest they have shown in my work, and the support and encouragement they have provided throughout this project.

I would like to extend my best wishes to Dr. Catherine Davies, and express my gratitude for all the advice and technical assistance given to me during this project. I also thank Dr. David Morgan for interpretation of XPS data. In addition, I would like to thank all colleagues and staff at the Cardiff Catalysis Institute and Cardiff University with whom I have had dealings or have received help from over the last few years.

Finally, none of my achievements would be possible without the unconditional support and constant encouragement of my close family and friends, and for that I am deeply grateful.

## Abstract

Increasingly stringent legislation limiting the emissions of particulate matter (commonly referred to as soot particulates) has led to the adoption of particulate filters in the exhausts of both diesel and gasoline passenger vehicles. While filters are highly effective at reducing these emissions, it is necessary to periodically remove trapped particulates in order to avoid their accumulation and the resulting loss of vehicle performance associated with back-pressure build-up. An effective method of removing soot particulates is through combustion (oxidation) with the oxygen-containing species present in the atmosphere of the exhaust, however this is unattainable at the temperatures experienced under normal driving conditions. A catalyst able to lower the temperature of soot oxidation is therefore desirable in order to achieve passive regeneration of the filter.

Previous studies have identified ceria,  $\text{CeO}_2$  as a promising soot oxidation catalyst due to its outstanding redox properties, and have shown that it can be enhanced by doping with various other metals. In this work, ceria-based catalysts have been prepared by the co-precipitation method. Ceria was doped with zirconium, lanthanum, praseodymium and neodymium in various ratios in order to enhance its catalytic properties. Each of these materials also contained alumina in order to improve their thermal stability. Of these materials, the most active for soot oxidation was found to be a  $\text{CeO}_2\text{-Nd}_2\text{O}_3\text{-Al}_2\text{O}_3$  catalyst prepared in a 7:3:10 molar ratio of Ce:Nd:Al and calcined at  $750^\circ\text{C}$  under flowing air. This catalyst lowered the temperature at which soot oxidation reached its peak rate by over  $100^\circ\text{C}$ . It was also demonstrated that the catalytic activity of these materials benefited considerably from the presence of alkali metals within their structure. The use of the ceria-based materials as supports by impregnating them with other species previously identified as active soot oxidation catalysts was also investigated, which resulted in a further lowering of the soot oxidation temperature.

Structural characterisation of the materials was carried out by X-ray powder diffraction (XRD), Raman spectroscopy, X-ray photoelectron spectroscopy (XPS) and surface area analysis (BET), while their redox properties were analysed by temperature-programmed reduction (TPR). The catalytic activity of the materials towards soot oxidation was investigated using thermogravimetric analysis (TGA).

## Glossary

BET	(Brunauer, Emmett, Teller) Surface area analysis
CI	Compression Ignition
CLA	CeO <sub>2</sub> -La <sub>2</sub> O <sub>3</sub> -Al <sub>2</sub> O <sub>3</sub>
CLZA	CeO <sub>2</sub> -La <sub>2</sub> O <sub>3</sub> -ZrO <sub>2</sub> -Al <sub>2</sub> O <sub>3</sub>
CPA	CeO <sub>2</sub> -Pr <sub>6</sub> O <sub>11</sub> -Al <sub>2</sub> O <sub>3</sub>
CNA	CeO <sub>2</sub> -Nd <sub>2</sub> O <sub>3</sub> -Al <sub>2</sub> O <sub>3</sub>
CZA	CeO <sub>2</sub> -ZrO <sub>2</sub> -Al <sub>2</sub> O <sub>3</sub>
DPF	Diesel particulate filter
fcc	face-centred cubic
GDI	Gasoline Direct Injection
GPF	Gasoline particulate filter
OSC	Oxygen storage capacity
PFI	Port fuel injection
PM	Particulate matter
RE	Rare-Earth
TGA	Thermogravimetric analysis
TPR	Temperature-programmed reduction
TM	Transition metal
XPS	X-ray photoelectron spectroscopy
XRD	X-ray powder diffraction

# Table of contents

Declaration .....	i
Acknowledgements .....	ii
Abstract .....	iii
Glossary .....	iv
<b>1 Introduction .....</b>	<b>1</b>
<b>1.1 Introduction to catalysis .....</b>	<b>1</b>
<b>1.2 Project Background .....</b>	<b>4</b>
<b>1.2.1 Particulate matter .....</b>	<b>4</b>
1.2.1.1 Formation, structure and toxicological effects .....	5
<b>1.2.2 Emission limiting legislation and technologies .....</b>	<b>10</b>
1.2.2.1 Historic and existing legislations .....	10
1.2.2.2 Exhaust aftertreatment technologies .....	13
<b>1.3 Literature Review .....</b>	<b>16</b>
<b>1.3.1 Uncatalysed soot oxidation .....</b>	<b>16</b>
<b>1.3.2 Catalysed soot oxidation .....</b>	<b>17</b>
<b>1.3.3 Ceria redox catalysts for soot oxidation .....</b>	<b>21</b>
1.3.3.1 Introduction .....	21
1.3.3.2 CeO <sub>2</sub> -containing mixed metal oxides .....	24
1.3.3.3 Transition metal promoters .....	26
1.3.3.4 Alkali metal promoters .....	30
<b>1.4 Project Aims .....</b>	<b>34</b>
<b>1.5 References .....</b>	<b>34</b>
<b>2 Experimental Techniques.....</b>	<b>41</b>
<b>2.1 Introduction.....</b>	<b>41</b>
<b>2.2 Catalyst Preparation.....</b>	<b>41</b>
<b>2.2.1 Catalyst support preparation – co-precipitation (manual             method).....</b>	<b>43</b>
<b>2.2.2 Catalyst support preparation – co-precipitation (automated             method).....</b>	<b>43</b>

2.2.2.1	Preparation of Ce-Zr-Al-O <sub>x</sub> catalyst supports, varying precipitating agent and washing.....	44
2.2.2.2	Preparation of Ce-M-Al-O <sub>x</sub> catalyst supports.....	44
<b>2.2.3</b>	<b>Metal Supported Oxide Preparation – Wet impregnation method.....</b>	<b>46</b>
2.2.3.1	Silver supported catalysts.....	46
2.2.3.2	Potassium supported catalysts.....	46
2.2.3.3	Combined silver and potassium supported catalysts.....	46
2.2.3.4	Comparison of transition metals on CZA support.....	46
2.2.3.5	Copper supported catalysts.....	46
<b>2.3</b>	<b>Catalyst characterisation.....</b>	<b>47</b>
<b>2.3.1</b>	<b>X-ray diffraction (XRD).....</b>	<b>47</b>
2.3.1.1	Principle.....	47
2.3.1.2	Experimental.....	48
<b>2.3.2</b>	<b>Raman spectroscopy.....</b>	<b>48</b>
2.3.2.1	Principle.....	48
2.3.2.2	Experimental.....	49
<b>2.3.3</b>	<b>X-ray photoelectron spectroscopy (XPS).....</b>	<b>50</b>
2.3.3.1	Principle.....	50
2.3.3.2	Experimental.....	50
<b>2.3.4</b>	<b>Brunauer Emmet Teller surface area analysis (BET).....</b>	<b>51</b>
2.3.4.1	Principle.....	51
2.3.4.2	Experimental.....	52
<b>2.3.5</b>	<b>Temperature-programmed reduction (TPR).....</b>	<b>52</b>
2.3.5.1	Principle.....	52
2.3.5.2	Experimental.....	53
<b>2.4</b>	<b>Catalyst Testing – Thermogravimetric analysis (TGA).....</b>	<b>54</b>
<b>2.5</b>	<b>References.....</b>	<b>55</b>
<b>3</b>	<b>Study into the reproducibility of CZA supports and effects of altering the co-precipitation method.....</b>	<b>56</b>
<b>3.1</b>	<b>Manual co-precipitation of Ce<sub>0.35</sub>Zr<sub>0.15</sub>Al<sub>0.5</sub>O<sub>1.75</sub> supports.....</b>	<b>57</b>
<b>3.1.1</b>	<b>Characterisation.....</b>	<b>57</b>

3.1.2	Soot oxidation testing.....	61
3.2	Automated co-precipitation of $\text{Ce}_{0.35}\text{Zr}_{0.15}\text{Al}_{0.5}\text{O}_{1.75}$ supports – comparison with manually prepared supports.....	65
3.2.1	Characterisation.....	66
3.2.2	Soot oxidation testing.....	72
3.3	Varying the automated preparation method of $\text{Ce}_{0.35}\text{Zr}_{0.15}\text{Al}_{0.5}\text{O}_{1.75}$ supports.....	73
3.3.1	Investigation into varying washing of Na-CZA catalysts.....	74
3.3.1.1	Characterisation.....	74
3.3.1.2	Soot oxidation testing.....	77
3.3.2	Alternative alkali metal carbonates as precipitating agent (potassium and caesium).....	80
3.3.3	Investigation into varying washing of K-CZA catalysts.....	81
3.3.3.1	Characterisation.....	82
3.3.3.2	Soot oxidation testing.....	87
3.4	Conclusions.....	89
3.5	References.....	91
4	Rare-Earth metal dopants in ceria-alumina catalyst supports.....	91
4.1	Rare-Earth metal alternatives to zirconium in ceria-alumina catalyst supports.....	95
4.1.1	Characterisation.....	95
4.1.2	Soot oxidation testing.....	102
4.2	Varying Ce:Zr ratio of CZA.....	106
4.2.1	Characterisation.....	106
4.2.2	Soot oxidation testing.....	111
4.3	Varying Ce:(La,Zr) ratio of CLZA.....	113
4.3.1	Characterisation.....	113
4.3.2	Soot oxidation testing.....	119
4.4	Varying Ce:La ratio of CLA.....	121
4.4.1	Characterisation.....	121
4.4.2	Soot oxidation testing.....	126
4.5	Varying Ce:Pr ratio of CPA.....	128



	4.5.1	Characterisation.....	128
	4.5.2	Soot oxidation testing.....	132
4.6		Varying Ce:Nd ratio of CNA.....	134
	4.6.1	Characterisation.....	135
	4.6.2	Soot oxidation testing.....	143
4.7		Varying calcination conditions of CNA catalysts.....	142
	4.7.1	Characterisation.....	143
	4.7.2	Soot oxidation testing.....	151
4.8		Summary and conclusions.....	154
4.9		References.....	158
5		Alkali and transition metal catalysts on ceria-based supports.....	160
	5.1	Silver and potassium on CZA catalyst supports.....	160
	5.1.1	Characterisation.....	162
	5.1.2	Soot oxidation testing.....	166
	5.2	Silver and potassium on alternative ceria-based catalyst supports.....	171
	5.2.1	Characterisation.....	172
	5.2.2	Soot oxidation testing.....	176
	5.3	Screening of alternative transition metals for impregnation on CZA.....	179
	5.3.1	Characterisation.....	180
	5.3.2	Soot oxidation testing.....	188
	5.4	Impregnating copper on catalyst supports.....	192
	5.4.1	Characterisation.....	192
	5.4.2	Soot oxidation testing.....	198
	5.5	Conclusions.....	201
	5.6	References.....	203
6		Conclusions.....	205
	6.1	Final conclusions.....	205
	6.2	Future work.....	210
	6.3	References.....	212
7		Appendix.....	213
	7.1	Characterisation.....	213
	7.1.1	Raman.....	213

<b>7.1.2</b>	<b>XPS</b> .....	213
	7.1.2.1 Chapter 3.....	213
	7.1.2.2 Chapter 4.....	215
	7.1.2.3 Chapter 5.....	219
<b>7.1.3</b>	<b>Thermogravimetric analysis</b> .....	222
	7.1.3.1 Chapter 4.....	222
	7.1.3.2 Chapter 5.....	225
<b>7.2</b>	<b>Soot oxidation testing – TGA</b> .....	225
<b>7.2.1</b>	<b>Chapter 3</b> .....	225
<b>7.2.2</b>	<b>Chapter 4</b> .....	227
<b>7.2.3</b>	<b>Chapter 5</b> .....	231

## 1. Introduction

### 1.1 Introduction to catalysis

A catalyst can be defined as “a substance that increases the rate at which a chemical system approaches equilibrium, without being consumed in the process”<sup>1</sup>.

The term catalysis, from the Greek *cata-*, meaning down, and *lysein*, meaning to split or break, was coined in 1835 by J.J. Berzelius, who hypothesised that certain substances had a “catalytic power”<sup>2</sup> that could “break down the normal forces which inhibit the reactions of molecules”<sup>1</sup>. The phenomenon now understood to be the process of catalysis had been observed many times prior to this. In the late 18<sup>th</sup> century, Elizabeth Fulhame demonstrated that the oxidation of certain metals occurred only in the presence of water, that water was decomposed during the reaction and subsequently regenerated at the end of the reaction<sup>3</sup>. Early 19<sup>th</sup> century discoveries included the hydrolysis of starch by traces of acid, and the presence of low concentrations of metal ions effecting the decomposition of hydrogen peroxide<sup>1,4</sup>. The availability of platinum and palladium brought about several more interesting discoveries, including oxidation of ethanol vapour (M. Faraday), and oxidation of hydrogen (J.W. Döbereiner), the latter of which led to the development of a lamp-lighter, the first practical use of the effect. In 1831 Peregrine Phillips patented the process of sulphur dioxide oxidation using platinum, later forming the basis of sulphuric acid manufacture. These phenomena could not be reconciled with the understanding of chemical reactivity at that time, and so Berzelius’s explanation offered the first attempt at rationalising them<sup>1</sup>.

During his study into acid-catalysed oxidation of hydrogen iodide by bromic acid in 1887, Ostwald observed a system in which the reaction took place at a measurable rate without the presence of the catalyst, leading him to surmise that catalysts do not *induce* a chemical reaction, but rather *accelerate* them<sup>5</sup>. Sabatier’s work into catalytic hydrogenation complemented this by viewing a catalytic reaction not as a single reaction, but as a series of reactions between catalyst and reagents to form intermediate species, eventually resulting in the formation of the final products and the reformation of the catalyst. This formulated the molecular basis of catalysis<sup>6</sup>.

Catalytic reactions could therefore be rationalised in terms of the thermodynamics and kinetics of chemical reactions. In thermodynamics, a reaction is said to be spontaneous, or favourable, if there is a negative change in the Gibbs free energy between reactants and products<sup>7</sup>. The change in Gibbs free energy  $G$ , is related to changes in enthalpy  $H$ , and entropy  $S$ , shown in equation 1.1 below, where  $T$  is absolute temperature<sup>8</sup>.

**Equation 1.1**

A fundamental principle of thermodynamics is that  $\Delta G$ ,  $\Delta H$  and  $\Delta S$  depend only on the initial and final states of the system<sup>1</sup>. Since a catalyst is not consumed during a reaction, its net contribution between initial and final states is zero. Consequently it cannot influence the position of thermodynamic equilibrium and therefore cannot induce a reaction that is thermodynamically unfavourable<sup>1</sup>. The time taken for a reaction to occur is not related to thermodynamics, but is a matter of kinetics. In practice, a thermodynamically favourable reaction may not proceed at a useful rate (or even at all) if it is not kinetically favourable. This is due to the activation energy, which must be overcome in order for the transition from reactants to products to occur. A catalyst is able to lower this energy by introducing an alternative pathway from reactants to products via a series of intermediate species. Sabatier's principle stated that the reaction intermediates formed on the surface of a catalyst must have an optimum stability; stable enough to allow their formation, but not too stable that they do not decompose<sup>6,9</sup>.

The absolute rate theory links the rate coefficient,  $k$  to the activation energy (equation 1.2).

---

**Equation 1.2**

Where  $k_B$  is the Boltzmann constant,  $\Delta G^\ddagger$  is the Gibbs free energy of activation, and  $h$  is the Planck constant.

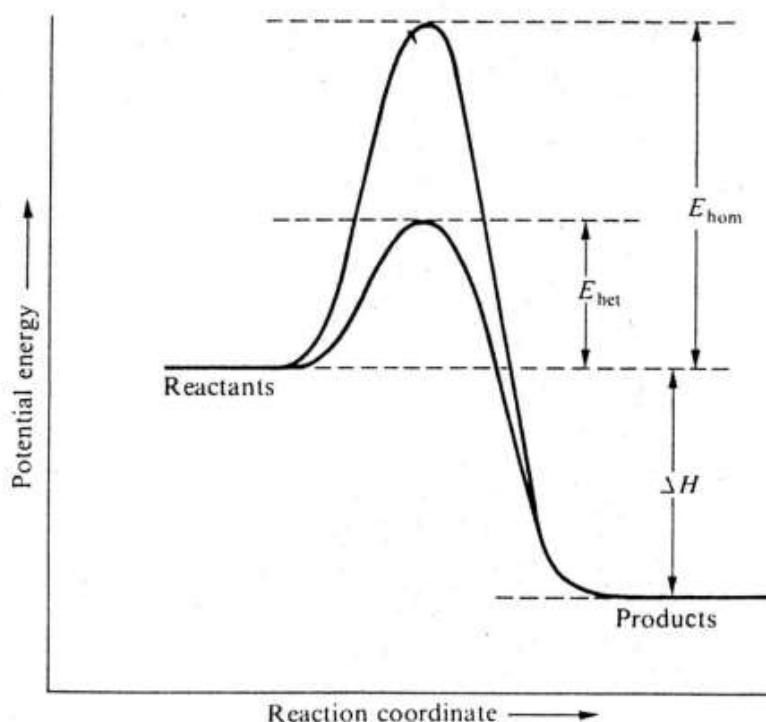


**Figure 1.1** Potential energy profile for an exothermic reaction, showing the effect of a catalyst on the activation energy of the reaction<sup>1</sup>

Catalysts are able to influence the kinetics of a reaction by lowering the Gibbs free energy of activation, which is composed of an entropy and enthalpy of activation. For a catalysed reaction, the transition state is immobilised on the catalyst surface, resulting in a loss of translational freedom, meaning a lower entropy. To compensate for this there must also be a corresponding decrease in enthalpy<sup>1</sup>. Figure 1.1 shows the potential energy profiles of a reaction. The position of the reactants and products are unchanged in both scenarios, however the catalysed reaction has a lower activation energy. Providing Sabatier's conditions are satisfied, a catalytic reaction may involve numerous intermediates, with each one more stable than its precursor.

Catalytic systems can be split into two distinct categories. A system whereby there is no phase boundary between catalyst and reactants is called *Homogenous catalysis*, and may take place in the gas or liquid phase. *Heterogeneous catalysis* is the term used to describe a system where a phase boundary separates the catalyst from the reactants, typically the catalyst/reactant in this category are liquid/gas, solid/liquid, solid/gas, solid/liquid+gas<sup>1</sup>.

## 1.2 Project background

The discovery and widespread use of fossil fuels as combustible materials in the late-18<sup>th</sup> and 19<sup>th</sup> centuries, known as the industrial revolution, has resulted in an unprecedented period of sustained technological and social advancement. Fossil fuels form over millions of years from the decomposition of buried dead organisms. They are comprised mainly of organic compounds which, when combusted with oxygen react to form the greenhouse gas carbon dioxide (CO<sub>2</sub>) and water. A partial or incomplete combustion process as well as the presence of impurities in the fuel also result in the formation of harmful compounds such as carbon monoxide (CO), nitrogen oxides (NO<sub>x</sub>), ammonia (NH<sub>3</sub>), sulphur oxides (SO<sub>x</sub>), unburnt hydrocarbons and particulates<sup>10,11</sup>. This period has therefore also coincided with increasing global temperatures and air pollution, and the consensus of the scientific community is that it “is extremely likely that human influence has been the dominant cause”<sup>12</sup>. With the ever-increasing energy demands of the global population, in particular with the emergence of the newly industrialised countries, this has led to a vast body of scientific research in numerous fields aimed at reducing harmful emissions.

The automotive industry relies heavily on the combustion of fossil fuels to power the internal combustion engines which propel the vast majority of motor vehicles. This is one such area which has therefore dedicated considerable resources towards research into limiting harmful emissions. Advances in engine design and aftertreatment technologies have resulted in huge reductions in emissions through improved fuel economy and removal of toxic by-products from the exhaust stream. However with increasing worldwide demand for passenger vehicles and as emission standards become increasingly stringent<sup>13-15</sup>, there is pressure on manufacturers to continually develop new technologies to improve their systems.

### 1.2.1 Particulate matter

The focus of this project is on particulate emissions from passenger vehicles. The term particulate matter (PM) can be used to refer to a complex mixture of organic and inorganic solids, liquids, powders and droplets suspended in the air which includes fine dust, soot, mist, fog and smog<sup>16,17</sup>. In the narrower context of vehicle emissions, this can be considered all substances, other than unbound water, that are present in exhaust gas in the solid or liquid phases<sup>18</sup>.

### 1.2.1.1 Formation, structure and toxicological effects

Soot particulates form as a consequence of incomplete or partial combustion of fuel in both diesel and gasoline engines. This can occur due to high temperatures and local sub-stoichiometric oxygen conditions which prevent full combustion to CO<sub>2</sub><sup>19</sup>. This has historically been an issue for diesel vehicles as their compression ignition (CI) engines inject fuel directly into the combustion chamber, preventing sufficient air/fuel mixing on a molecular level and resulting in localised fuel-rich regions which do not undergo full combustion<sup>20</sup>. More recently, the increasing market share of the more fuel-efficient gasoline direct injection (GDI) over port fuel injection (PFI) engines has resulted in a similar problem emerging in gasoline-fuelled vehicles<sup>18,21</sup>. Much of the understanding of soot particulates, their formation, structure and composition has therefore been based on studies with diesel emissions. However there is a growing literature on gasoline particulates and how these compare with their diesel counterparts<sup>21–23</sup>.

The particulates are commonly referred to as “soot” as they are mainly composed of a carbonaceous fraction consisting of elemental and organic carbon<sup>18,24</sup>. The initial process summarised in figure 1.2 leads to the formation of the “soot core”, which can go on to adsorb the various other organic and inorganic substances present.

Rather than combustion to CO<sub>2</sub>, the lack of oxygen results in the pyrolysis of the fuel molecules to form small unsaturated molecules, usually ethyne. These molecules undergo polymerisation and eventually ring closure to form polycyclic structures known as “platelets”. The next phase is nucleation, in which these graphitelike structures stack to form “crystallites”, which in turn stack in a random orientation around the centre of the particle to form “turbostratic particles”. Coagulation and surface growth then takes place which is instigated by the addition of gaseous carbonaceous species. As the temperature decreases, surface growth stops and “primary soot particles” are formed. These continue to coagulate to form chainlike aggregates that can themselves accumulate to form large agglomerates<sup>19,20</sup>.

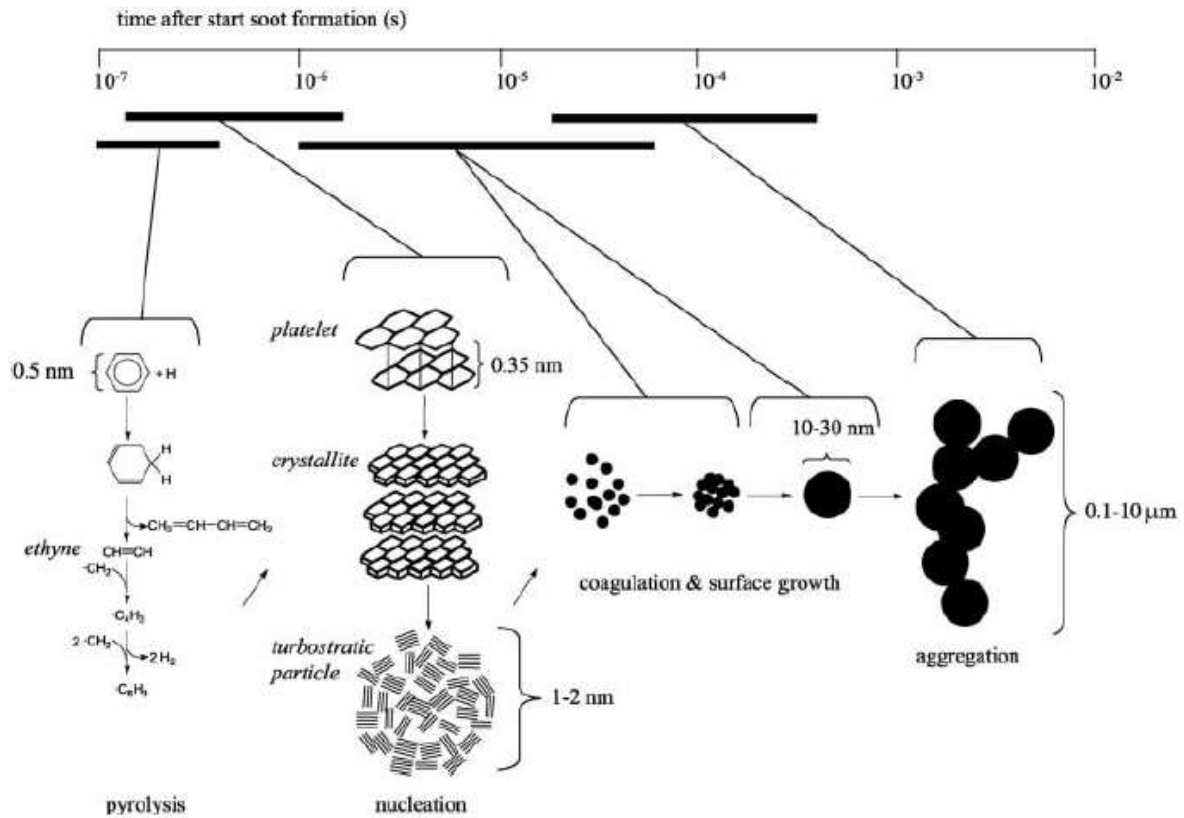


Figure 1.2 Schematic mechanism of the formation of soot particles<sup>20</sup>

As the temperature continues to decrease, various volatile or soluble organic compounds (known as the soluble organic fraction, SOF) are condensed and can form into small particulates or can be adsorbed onto the surface of the existing soot particles. The SOF consists of polycyclic aromatic compounds containing oxygen, nitrogen and sulphur also produced during the combustion of the fuel. Some of the sulphur in the fuel is oxidised to  $\text{SO}_3$  which in turn can lead to sulphuric acid and sulphates forming on the particles. Other inorganic materials such as metals (from engine wear, impurities and catalyst leaching) and ashes (from lubricant oils) may also be present<sup>25</sup>. A schematic representation of the particulate structures is shown in figure 1.3<sup>18</sup>.



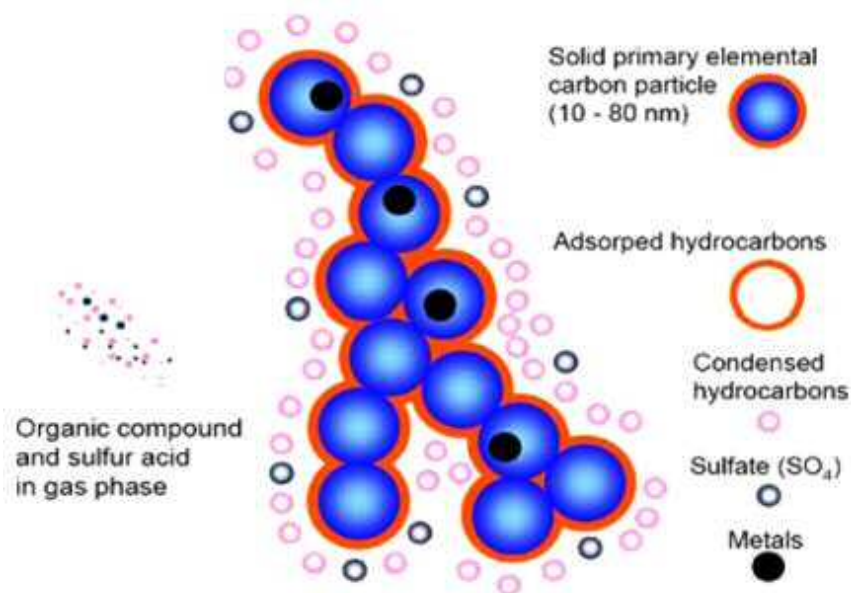


Figure 1.3 Agglomerated diesel particle<sup>18</sup>

The quantity and composition of particulates is dependent on numerous factors including the engine type, fuel composition, engine load, and atmospheric temperature<sup>23,26</sup>. A study by Uy *et al.* into particulate matter extracted from both diesel compression ignition and gasoline

**Table 1.1** XRF elemental composition of diesel and gasoline soot samples<sup>22</sup>

Element	Diesel A	GTDI D
P	0.029	2.06
S	0.024	0.49
Ca	0.038	4.19
Zn	0.024	1.89
Mg	0.002	
Mo		0.025
Na		
Fe	0.061	4.70
Cr	0.003	0.82
Ni	0.004	0.52
Al	0.015	0.13
Cu	0.004	0.17
Cl		0.059
Si	0.004	0.086
K	0.003	0.013
O	0.14	8.41
C/CH <sub>2</sub>	99.64	76.3

direct injection spark ignition vehicles noted significant differences in composition<sup>22</sup>. Table 1.1 shows the elemental composition (in atomic wt%) of diesel and gasoline (GTDI) particulate matter analysed by X-ray fluorescence spectroscopy (XRF) (other diesel and gasoline samples were also analysed in the study, the results shown have been chosen as both samples were collected in the same manner, upstream from their respective aftertreatment systems). The gasoline PM contained a much greater quantity of non-carbon elements. This was attributed to the greater contact between fuel and oil additives (containing P, S, Ca, Zn and Mo) in gasoline DI engines compared to diesel CI, and greater engine wear contributing to the increase in Fe, Cr, Al and Cu<sup>22</sup>. It has also been reported that the sulphuric acid/sulphates and metal fractions present in PM from comparable sources are proportional to the sulphur and metal content of the fuel, respectively<sup>20,25-27</sup>. Increasing the engine load has been reported to decrease diesel PM emissions (per kilometre) due to greater efficiency of combustion, as well as reducing the metal content<sup>26</sup>. Ambient temperature is also a factor in the quantity of particulate emissions,

as low temperatures during ignition (known as “cold start”) decreases the air-fuel ratio, lowering oxidation and increasing carbon formation<sup>25</sup>. As mentioned, the formation of particulates from the volatile materials in the exhaust is reliant on condensation. Their number, size and growth rates are therefore dependent on factors which affect this, including temperature, dilution rate, residency time, humidity and the surface area of the existing soot particles<sup>18</sup>. The position of the particulates within the exhaust is therefore an important factor in determining the extent to which these species are present, and differences in composition have been observed depending on where the particulates were collected<sup>20,25</sup>.

These factors also have consequences for the size distribution of the particulates. Particulate emissions are classified into ‘modes’ based on their size. Particles in the “nucleation” mode primarily consist of the condensed volatile materials described above, and have a particle size typically below 30 nm. While the “accumulation” mode consists of the larger carbonaceous particles typically greater than 100-300 nm in size<sup>11,18,25</sup>. The typical size distribution of particulates in a diesel exhaust are shown in figure 1.4<sup>25</sup>. This shows that particles in the “accumulation” mode account for the bulk of the particulate mass, whereas particles in the “nucleation” mode account for only 1-20 % of the total mass of particulates. This is in stark contrast to the distribution by particle number, where the smaller “nucleation” particles account for over 90 % of particulates.

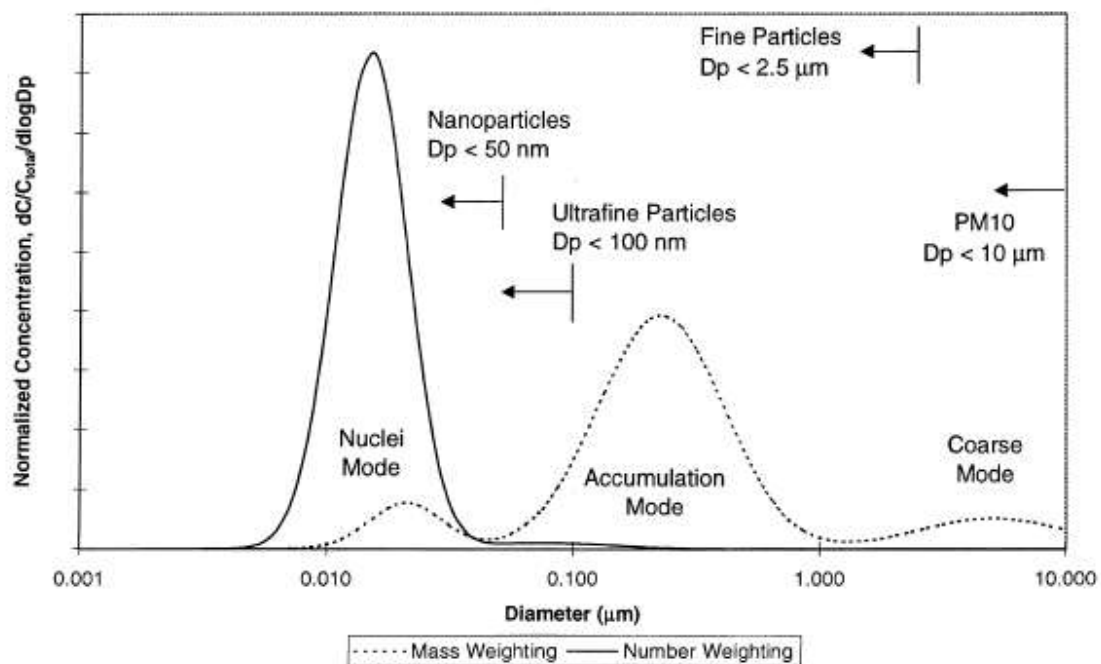


Figure 1.4 Typical size distribution of particulate matter from diesel exhaust by mass and number<sup>25</sup>

These size distributions have significant implications for the methods by which particulate emissions are measured, which will be discussed in greater detail later, but also their adverse health effects. This is due to the extent to which particles are able to penetrate the respiratory system depending on their size. Figure 1.4 also shows some of the definitions of size for atmospheric particles. Particles with a diameter of less than 10  $\mu\text{m}$  are known as  $\text{PM}_{10}$ , when inhaled these are able to pass beyond mucus and cilia in the nose and throat, and can be deposited deep into the alveoli and bronchioles<sup>28</sup>. Fine particles (diameter  $<2.5 \mu\text{m}$ ) can penetrate the gaseous exchange system and enter the bloodstream and are deposited on artery walls, causing plaques which can lead to atherosclerosis and various cardiovascular diseases<sup>29</sup>. Penetration of cell membranes is possible with a diameter below 100 nm, known as ultrafine particles, allowing for entry into tissue and vital organs, including the brain<sup>30</sup>. As seen in figure 1.4, the vast majority of particles fall below this threshold. While the accumulation of foreign matter at various levels of penetration is itself a health concern, this is compounded further by the nature of the particulates themselves. Polycyclic aromatic hydrocarbons (PAHs) present in exhaust particulates are widely reported as having carcinogenic and mutagenic properties<sup>31,32</sup>, most notably benzo[*a*]pyrene which has been classified as carcinogenic by the International Agency for Research on Cancer (IARC)<sup>33</sup>. Prenatal exposure to PAHs has also been reported as having a negative impact on cognitive development leading to learning and behavioural difficulties<sup>34</sup>.

An assessment by the United States Environmental Protection Agency (US EPA) in 2002 on the health impact of particulate inhalation concluded that short-term (acute) exposure to particulate emissions can cause irritation and inflammatory symptoms in the respiratory tract of a transient nature, while long-term (chronic) exposure likely posed an increased risk of lung cancer as well as other chronic lung damage<sup>24</sup>. The World Health Organisation (WHO) considers that fine particles ( $\text{PM}_{2.5}$ ) are “strongly associated with mortality and other endpoints such as hospitalization for cardio-pulmonary disease”, but that no specific size threshold could be identified below which no adverse health effects occurred. It also considers the extractable organic compounds of particulate matter (especially PAHs) to “exert pro-inflammatory as well as adjuvant effects”<sup>17</sup>. Both reports acknowledge the carcinogenic and mutagenic properties of many of the PAHs and their nitro- and oxy-derivatives.

As well as their effects on human health, particulate emissions in the atmosphere also have negative effects on the environment. They reduce visibility, settle on plants and interfere with photosynthesis by blocking stomata, and contribute towards climate change<sup>20</sup>.

## **1.2.2 Emission limiting legislation and technologies**

### *1.2.2.1 Historic and existing legislations*

The negative health and environmental impact of decreasing air quality due to pollutants necessitated the introduction of legislation to limit harmful vehicle emissions. The geography, weather patterns and high vehicle density of Los Angeles made it particularly susceptible to the accumulation of smog throughout the 20<sup>th</sup> century. The correlation between air pollution and cars was first made by researchers in California in the 1950s<sup>35</sup>. This led to the creation of the California Air Resources Board (CARB) in 1967 and was followed in 1970 by the establishment of the US Environmental Protection Agency (EPA) in order to tackle air pollution. A European convention on transboundary air pollution was also proposed by the Nordic countries in the 1970s, resulting in the Convention on Long-range Transboundary Air Pollution (CLRTAP), which to date has been signed by 51 nations committing them to gradually reduce and prevent air pollution<sup>36</sup>.

However no single governing body exists to regulate global vehicle emissions, and so various standards exist worldwide. The most widely recognised and progressive legislation on vehicle emissions standards are considered to be those of the European Parliament, which sets the standards for all European Union (EU) & European Economic Area (EEA) member states, and CARB. Under the United States Clean Air Act, CARB is permitted to set its own emissions standards for California independently of the US EPA, which sets minimum standards for the rest of the United States. All other states may choose between either standard, but may not set their own<sup>35,37</sup>. As of 2017, 13 other states and the District of Columbia currently adopt the standards set out by CARB<sup>38</sup>. Due to the share of the vehicle sales market in these areas and the strictness of the legislation, manufacturers strive to comply with the standards set by these organisations.

CARB introduced the Low-Emission Vehicle (LEV) Program in 1990 which limited emissions of non-methane organic gases (NMOG), CO, NO<sub>x</sub>, PM and formaldehyde (HCHO) in passenger

vehicles and over time these standards have become more stringent, through to LEV III, introduced in 2012<sup>13,35</sup>. The first European legislation for passenger vehicles was introduced in 1992 with the Euro 1 emissions standards, which set limits on CO, NO<sub>x</sub> and hydrocarbon emissions for all passenger vehicles, and PM emissions for diesel passenger vehicles. As shown in table 1.2, over time these standards have evolved to take into account the differing emissions challenges presented by diesel and gasoline vehicles, and have become increasingly stringent, resulting in the most recent standard Euro 6, introduced in 2014<sup>14</sup>.

**Table 1.2** EU emission standards for diesel (**bold**) and gasoline fuelled passenger cars (g/km unless stated)<sup>15</sup>

Tier	Timeframe	CO	THC	NMHC	NO <sub>x</sub>	HC + NO <sub>x</sub>	PM	PN (#/km)
<b>Euro 1</b>	1992	<b>2.72</b>	-	-	-	<b>0.97</b>	<b>0.14</b>	-
		2.72	-	-	-	0.97	-	-
<b>Euro 2</b>	1996	<b>1.0</b>	-	-	-	<b>0.7</b>	<b>0.08</b>	-
		2.2	-	-	-	0.5	-	-
<b>Euro 3</b>	2000	<b>0.64</b>	-	-	<b>0.50</b>	<b>0.56</b>	<b>0.05</b>	-
		2.3	0.20	-	0.15	-	-	-
<b>Euro 4</b>	2005	<b>0.50</b>	-	-	<b>0.25</b>	<b>0.30</b>	<b>0.025</b>	-
		1.0	0.10	-	0.08	-	-	-
<b>Euro 5a</b>	2009	<b>0.50</b>	-	-	<b>0.180</b>	<b>0.230</b>	<b>0.005</b>	-
		1.0	0.1	0.068	0.060	-	0.005*	-
<b>Euro 5b</b>	2011	<b>0.50</b>	-	-	<b>0.180</b>	<b>0.230</b>	<b>0.005</b>	<b>6x10<sup>11</sup></b>
		1.0	0.1	0.068	0.060	-	0.005*	-
<b>Euro 6</b>	2014	<b>0.50</b>	-	-	<b>0.080</b>	<b>0.170</b>	<b>0.005</b>	<b>6x10<sup>11</sup></b>
		1.0	0.1	0.068	0.060	-	0.005*	6x10 <sup>11</sup> **

CO = carbon monoxide

THC = total hydrocarbons

NMHC = non-methane hydrocarbons

PM = Particle mass

PN = Particle number

\*Applies to vehicles with GDI engines

\*\*6x10<sup>12</sup> #/km within first three years Euro 6 effective dates

The limit on PM emissions can be seen to have gradually decreased from 0.14 g/km in Euro 1 to the current level of 0.005 g/km in Euro 6. Until Euro 5, no PM limit was enforced on gasoline passenger vehicles. A limit for gasoline port-injection (PFI) vehicles was unnecessary as they easily complied with the limits set for diesel vehicles<sup>39</sup>. However gasoline direct injection (GDI) vehicles have been found to emit significantly higher levels of PM, which could potentially exceed the limits imposed on diesel vehicles. Their expected increase in market share due to

their superior fuel efficiency over PFI vehicles has necessitated their inclusion in particulate limiting legislation, hence their inclusion in Euro 5<sup>39</sup>.

In 2011 the Euro 5b standards introduced a particle number (PN)-based limit on PM emissions in addition to the longstanding mass limit. As mentioned in the previous section, ultrafine- and nano-particles account for a large proportion of exhaust PM by particle number, but a much lower proportion by mass. Since these smaller particles have been established as the most hazardous, limitations by this method of measurement are arguably more relevant to improving air quality. This was also found to have implications for GDI vehicles, which have been reported as producing a greater proportion of smaller particles than diesel vehicles<sup>18,40,41</sup>. Despite Euro 5 model GDI vehicles complying with the PM mass limit, it has been reported that they would not comply with the PN limit of  $6 \times 10^{11}$  #/km, with some exceeding it by up to 1½ orders of magnitude<sup>39,42</sup>. As of 2014 this limit has been extended to GDI vehicles in Euro 6, however a relaxed limit of  $6 \times 10^{12}$  #/km during a three year transitional period was granted in order to allow for improvements to GDI exhaust aftertreatment systems<sup>21</sup>. Particles below a size of ~23 nm are not measured as these are considered to be mainly low-volatile hydrocarbons, which may vary considerably and could undermine the PN measurement<sup>43</sup>.

All vehicle models must demonstrate that they comply with current standards by undergoing a regulatory test procedure. Emissions are collected and later analysed as the vehicle is driven at varying speeds designed to represent typical driving conditions. Until September 2017, Euro emissions tests on all new passenger vehicle models were conducted under standard conditions known as the New European Driving Cycle (NEDC). The initial stage of the test is comprised of four repetitions of the Urban Driving Cycle (UDC), which is designed to represent typical urban driving conditions in busy European cities and is characterised by low engine load, low exhaust temperature and a maximum speed of 50 km/h. This is then followed by the Extra Urban Driving Cycle (EUDC), which accounts for more aggressive, high speed driving, reaching a maximum speed of 120 km/h<sup>44</sup>. This has subsequently been replaced by the Worldwide harmonized Light vehicles Test Procedure (WLTP), which features a more dynamic speed profile than the NEDC and consists of four speed phases (low, medium, high and extra high) designed to more accurately resemble real-world variations in driving conditions<sup>45</sup>.

Figure 1.5 shows how the driving speed varies over time in both the NEDC and WLTP conditions.

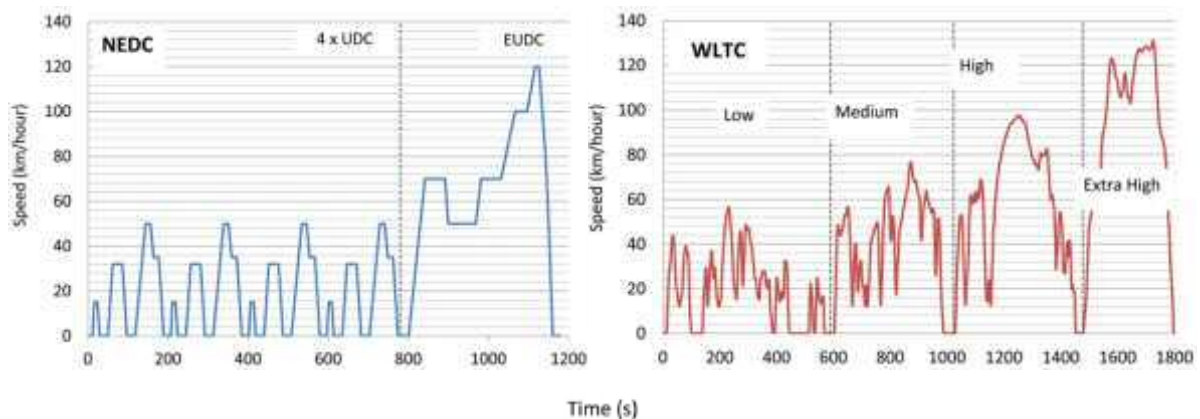


**Figure 1.5** New European Driving Cycle (left) and Worldwide harmonized Light vehicles Test Procedure (right)<sup>45</sup>

Increasingly stringent legislation has resulted in the development of various strategies aimed at reducing harmful emissions. These have included modifications to engines, alternative fuels/fuel additives, and a considerable effort towards exhaust aftertreatment technologies<sup>10</sup>.

#### 1.2.2.2 Exhaust aftertreatment technologies

Modern passenger vehicles are equipped with a range of catalytic exhaust aftertreatment technologies which are able to effectively reduce harmful emissions. In gasoline vehicles, the three-way catalytic converter (TWC) is able to oxidise CO and hydrocarbons (HCs), and reduce NO<sub>x</sub> emissions to harmless CO<sub>2</sub>, H<sub>2</sub>O and N<sub>2</sub> using a combination of platinum/palladium and rhodium catalysts<sup>46</sup>. Diesel vehicles are unable to utilise TWC due to their lean burn combustion conditions<sup>47</sup>. Diesel oxidation catalysts (DOCs) use Pt/Pd to oxidise CO, HCs and the SOF fraction of particulate matter<sup>42</sup>. Diesel NO<sub>x</sub> emissions are dealt with by a separate system, either by using selective catalytic reduction (SCR), which catalyses the reaction of NO<sub>x</sub> with NH<sub>3</sub> (generated by the upstream injection of urea) to N<sub>2</sub> and H<sub>2</sub>O<sup>48</sup>, or by using the lean NO<sub>x</sub> trap (LNT) which catalyses the reaction of NO<sub>x</sub> with CO and HCs to form N<sub>2</sub>, CO<sub>2</sub> and H<sub>2</sub>O<sup>49</sup>.

The most straightforward method of reducing PM emissions is by using a filter to trap particulates<sup>10</sup>. Due to the longstanding limitations on diesel PM emissions, there is widespread use of diesel particulate filters (DPFs) in diesel passenger vehicles. Several types of filters have been developed, including foam and flow-through filters. However the most effective and widely used are the ceramic wall-flow filters, being the only filter capable of

complying with the most recent PN emission limits<sup>50</sup>. These are comprised of a large honeycomb-structured monolith usually made from cordierite or silicon carbide (SiC)<sup>28,42</sup>. As shown in figure 1.6, alternate passages are plugged in order to force the exhaust gases through the porous channel walls, however the PM is unable to do so and is thus trapped<sup>11</sup>. Cordierite and SiC are the preferred materials as they provide high filtration efficiencies, low pressure drops, high maximum operating temperatures, low thermal expansion, resistance to thermal stress, and chemical resistance to the metal ashes present in PM<sup>42</sup>.

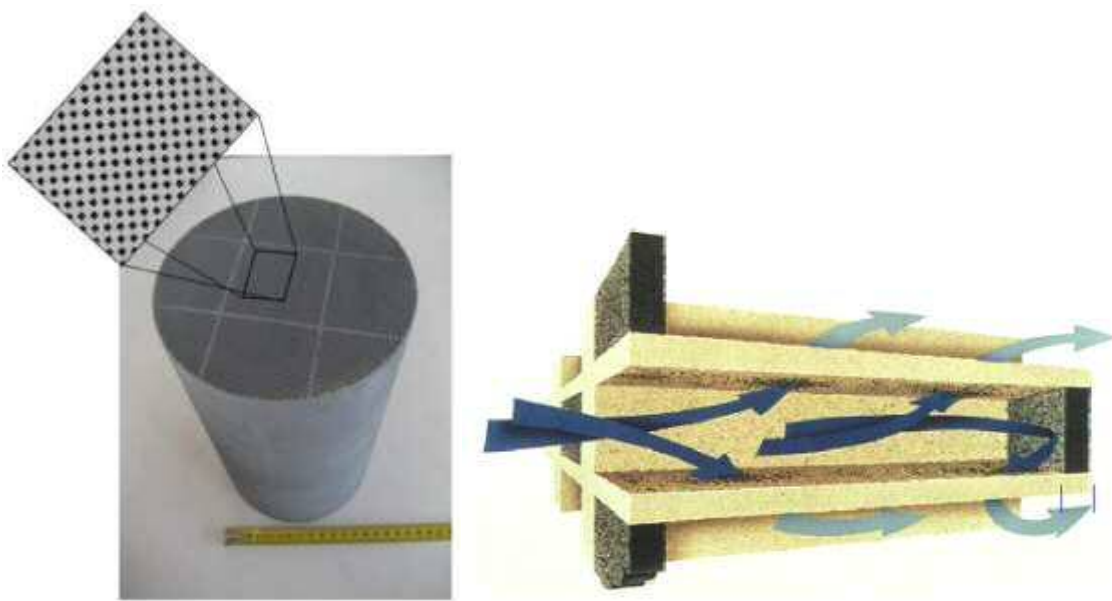


**Figure 1.6** (left) A commercial SiC DPF with alternate channels blocked<sup>28</sup> and (right) internal schematic of channels with porous walls<sup>11</sup>

DPFs are considered highly effective at reducing PM emissions, with a reported reduction in excess of 95 % in terms of mass and >99 % in particle number over a wide range of engine conditions<sup>42</sup>. For this reason similar systems, referred to as gasoline particulate filters (GPF) have been proposed to tackle the issue of particulate emissions from GDI vehicles in order to comply with Euro 6. Several studies have reported that the introduction of GPFs to GDI vehicle exhausts are cost-effective and do not result in additional fuel penalties<sup>21,51</sup>.

The main drawback of particulate filters is the increase in backpressure associated with the accumulation of PM on the filter walls, as shown in figure 1.7. Excessive backpressure leads to degradation of engine performance due to the expulsion of exhaust gases being restricted and if allowed to continue to rise, can ultimately lead to engine failure<sup>11,50,51</sup>.



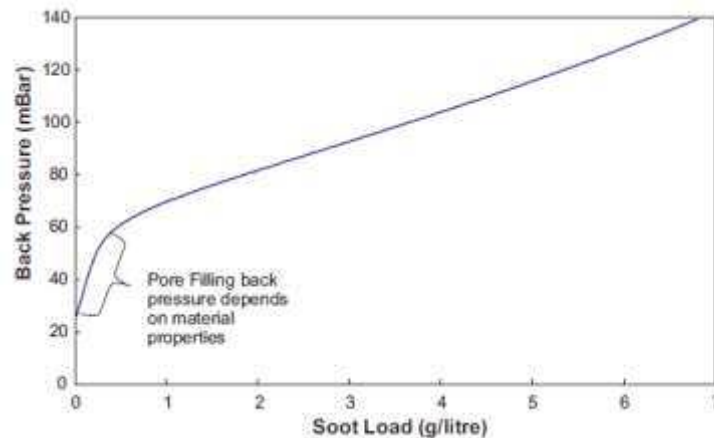


Figure 1.7 Typical backpressure across DPF as a function of trapped PM<sup>11</sup>

To avoid this outcome it is therefore necessary to remove PM from the filter before the backpressure reaches a predetermined limit. This can be achieved by regeneration of the filter by oxidising PM to CO<sub>2</sub>. Filter regeneration falls into two categories; “passive” and “active” regeneration. Passive regeneration occurs when the temperature of the exhaust is sufficient for the oxidation of PM to take place during normal driving without intervention. In heavy-duty diesel vehicles, this has been achieved using the continuously regenerating trap (CRT) invented by Johnson Matthey, which utilises a close-coupled DOC catalyst upstream from the filter to oxidise NO to NO<sub>2</sub>, which has a high oxidising potential, allowing oxidation of PM to take place continuously under normal driving conditions<sup>52</sup>. However, to reach the required temperature for this method to function for a DPF in a diesel passenger vehicle, this would require driving speeds of around 100 km/h which are not achieved under urban driving conditions<sup>11</sup>. Therefore for these vehicles it is necessary to employ an active regeneration strategy. This involves periodically injecting additional fuel into the engine in order to raise the exhaust gas temperature sufficiently to allow PM oxidation to take place<sup>50</sup>. This is controlled by a sensor which monitors the backpressure caused by the filter, and typically takes place every 400-2000 km<sup>11</sup>. The disadvantages to this method are the decrease in fuel economy, and the reduced lifespan of the filter due to the damage that can be caused by the uncontrolled exotherm produced by the ignition of the soot<sup>20</sup>. Passive regeneration by means of decreasing the soot oxidation temperature using a catalyst is therefore seen as a more desirable approach.

### 1.3 Literature Review

The desire to achieve passive regeneration of particulate filters has resulted in wide-ranging investigations into materials capable of catalysing soot oxidation at lower temperatures, which will be discussed later. It is necessary to briefly discuss the mechanism by which the soot oxidation reaction takes place in order to identify effective catalytic materials.

#### 1.3.1 Uncatalysed soot oxidation

The reactivity of carbon materials is dependent on several factors including crystallite size/orientation, the concentration of structural defects, and the location, type and concentration of impurities. These properties control the “active surface area” which is the fraction of a carbon material susceptible to oxygen-carbon reactions<sup>20</sup>.

Several studies into the carbon-oxygen reaction were conducted by Moulijn *et al.* and proposed a stepwise mechanism containing simplified oxygen complexes and graphitic carbon structures as shown in figure 1.8<sup>53–55</sup>, described below<sup>20</sup>.

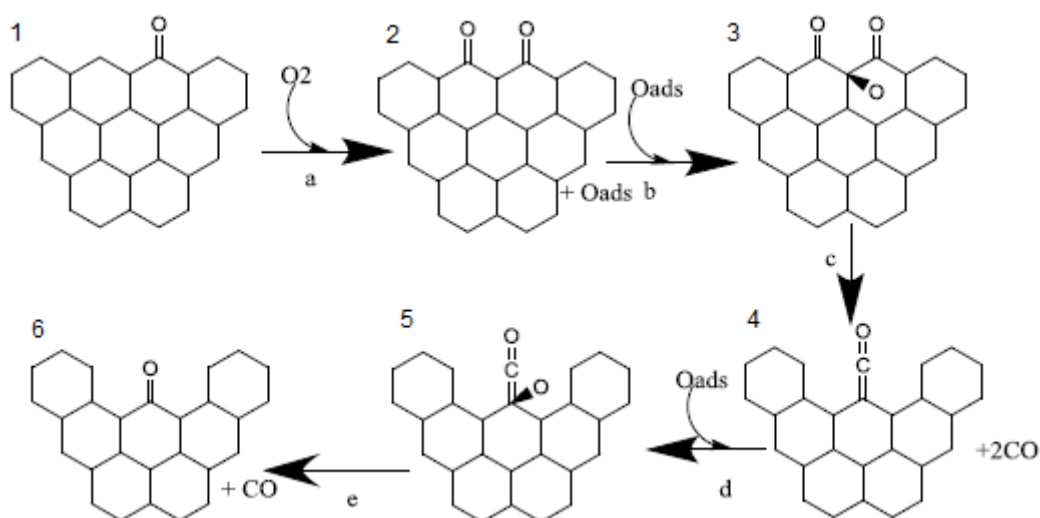


Figure 1.8 Reaction mechanism of noncatalysed oxidation of carbon<sup>20</sup>

Step a) Graphite with a ketone “surface-oxygen complex” (SOC) (structure 1) reacts with gas-phase  $O_2$  to form a surface semiquinone group and physically adsorbed oxygen (2). The C-C bond strength of the semiquinone complex is only slightly weaker than that of graphite, it is therefore unlikely to decompose and is a “stable surface-oxygen complex”.

b) The carbon atom between the C=O groups becomes a target for bonding with oxygen due to the electronegativity of the oxygen atoms in the semiquinone complex. This forms a semiquinone complex with off-plane oxygen (3).

c) This results in a weakening of the C-C bonds of the neighbouring carbon atoms which leads to the complex decomposing to CO, leaving a graphite structure with a carbonyl group (4).

d) The carbon atom next to the carbonyl group becomes a target for bonding with oxygen due to the electronegativity of the oxygen in the carbonyl group. A carbonyl group with off-plane oxygen is formed (5).

e) This results in a lowering of the C-C bond strength in the neighbouring carbon atom, which decomposes to release CO, leaving another structure with a SOC (6), and the reaction cycle can then restart with step a).

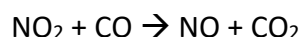
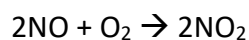
The reaction rate is determined by the number of carbon complexes on the active surface area rather than the rate-constants of the individual steps.

A similar proposal involves the adsorption of gas phase oxygen (from numerous sources available in a vehicle exhaust, including CO, CO<sub>2</sub>, NO, N<sub>2</sub>O, H<sub>2</sub>O, and most effectively O<sub>2</sub> and NO<sub>2</sub>) to form SOCs which subsequently decompose to CO/CO<sub>2</sub>. This leaves highly reactive surface carbon atoms with unsaturated valences (called free carbon sites) which can then be readily oxidised to SOCs by other oxygen-containing molecules, repeating the cycle<sup>19,28</sup>. This mechanism will be discussed further as part of the catalysed reaction.

### 1.3.2 Catalysed soot oxidation

Soot oxidation can be achieved either by direct contact or indirect contact with a catalyst. Catalysis by indirect contact does not require intimate physical contact between soot and catalyst. Instead, they act by catalysing the formation of a mobile compound that is more reactive than O<sub>2</sub> (e.g. NO<sub>2</sub>, O<sub>ads</sub> etc.)<sup>20</sup>. The known reaction mechanisms for this type of soot oxidation are;

The “NO<sub>x</sub>-aided gas-phase mechanism”, which catalyses the oxidation of NO to NO<sub>2</sub> in order to accelerate soot combustion<sup>56</sup>:



The “spillover mechanism”, whereby the catalyst is able to dissociate  $\text{O}_2$  to adsorbed oxygen and transfer it to the soot particle (as shown in figure 1.9). While this is more effective with direct contact, there have been several studies reporting this mechanism having occurred without the need for contact between catalyst and soot<sup>57–59</sup>.

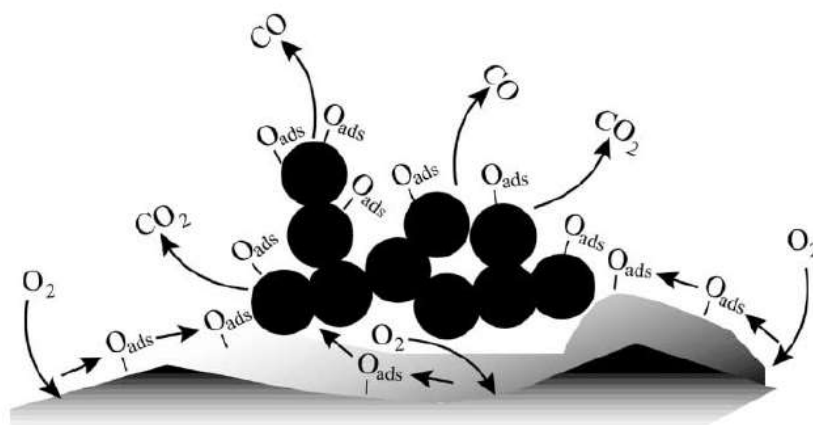


**Figure 1.9** Spillover mechanism of catalysed soot oxidation<sup>20</sup>

As stated above, the spillover mechanism also occurs during direct contact soot oxidation. The other process that can occur with direct contact is the redox mechanism. As shown in figure 1.10, this process follows a Mars-van Krevelen mechanism whereby lattice oxygen ( $\text{O}_L$ ) from a reducible metal oxide can migrate to the surface ( $\text{O}_S$ ) and is utilised to oxidise soot particles in contact with the surface of the catalyst to  $\text{CO}_2$  (the reduction step). The metal oxide is subsequently re-oxidised by the surrounding gas-phase oxygen (oxidation step)<sup>60</sup>.

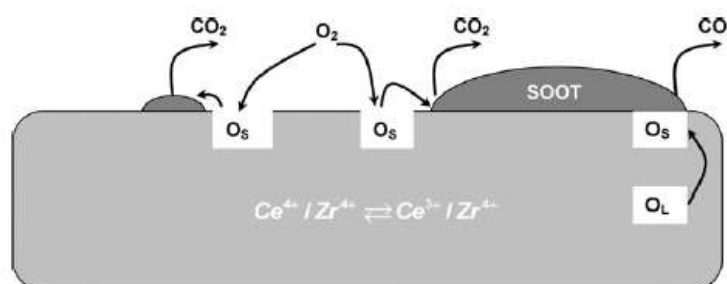


**Figure 1.10** Redox mechanism of catalysed soot oxidation<sup>60</sup>

Achieving direct contact soot oxidation under real-world scenarios is challenging due to the difficulty in establishing intimate contact between catalyst and soot on a particulate filter<sup>20</sup>. Several studies have shown the importance the degree of contact with soot has on the activity achieved by a catalyst<sup>19,61–64</sup>. The investigations by Neeft *et al.* into catalyst/soot contact established the definition of two types of contact; “loose” – which involves mixing of the catalyst and soot with a spatula, and “tight” – whereby intimate contact between catalyst and soot is achieved by mechanical grinding<sup>65</sup>. They found that the soot oxidation temperatures under tight contact were significantly lower than loose contact with each of the various metal-oxide catalysts that were tested, with differences up to almost 200 °C. It was also observed that the results obtained from the loose contact tests were comparable to tests carried out on soot that had been flowed onto a catalyst bed through an exhaust stream, indicating that loose contact was more representative of real-world soot/catalyst contact<sup>64</sup>. Test results using tight contact conditions are therefore regarded as meaningless from a practical application perspective<sup>28</sup>, and comparisons between the soot oxidation temperatures achieved by catalysts from different studies should be approached with caution due to the difficulties in establishing comparable testing conditions.

The materials studied for soot oxidation catalysis can be placed into two categories; platinum-group metal (PGM) catalysts and PGM-free catalysts.

PGM catalysts are used in a wide variety of oxidation reactions due to their remarkable activity and resistance to corrosion<sup>66</sup>. As mentioned previously, they have applications in several automotive aftertreatment technologies including DOCs, TWC and CRT. Many studies have demonstrated the activity of PGM catalysts for soot oxidation, and have proposed direct and indirect roles depending on the atmospheric composition. In the presence of O<sub>2</sub>, soot oxidation can be achieved by the spillover of activated oxygen onto the surface of the soot<sup>67</sup>, while a mix of NO<sub>x</sub>/O<sub>2</sub> allows the catalytic oxidation of NO upstream from the soot to form NO<sub>2</sub>, a much stronger oxidiser<sup>68</sup>. PGMs in direct contact with soot have also shown to catalyse the cooperative carbon-NO<sub>2</sub>-O<sub>2</sub> reaction, by simultaneously increasing the concentration of SOCs on the surface of soot via the aforementioned spillover mechanism and promoting the formation of NO<sub>2</sub> which subsequently reacts at those sites<sup>68–70</sup>.

The advantage of PGM catalysts therefore is that they do not require good contact with soot – which is difficult to provide – in order to act effectively, and in the case of diesel vehicles can be positioned upstream from the particulate filter to catalyse NO to NO<sub>2</sub> (e.g. DOC, CRT). However the disadvantages of PGM materials is their high cost and the formation of sulphates associated with them. Their viability as soot oxidation catalysts for use in conjunction with a GPF in gasoline vehicles is limited due to the upstream conversion of NO<sub>x</sub> to N<sub>2</sub> by the TWC<sup>71</sup>. Likewise, future strategies to reduce NO<sub>x</sub> concentrations upstream from a particulate filter in all vehicles may result in PGM catalysts becoming less effective.

Interest in PGM-free soot oxidation catalysts have increased due to their low cost of production and increasingly evident activity. Several classes of compounds have been reported as showing good soot oxidation activity. Various metal oxide/mixed metal oxide-based catalysts have been investigated. Pure oxides identified as showing catalytic activity towards soot oxidation include Co<sub>3</sub>O<sub>4</sub>, V<sub>2</sub>O<sub>5</sub>, Fe<sub>2</sub>O<sub>3</sub>, La<sub>2</sub>O<sub>3</sub>, Mn<sub>2</sub>O<sub>3</sub> and NiO under tight contact conditions only, while PbO, Cr<sub>2</sub>O<sub>3</sub>, MoO<sub>3</sub>, CuO and Ag<sub>2</sub>O also displayed activity under loose contact with soot<sup>65</sup>. The oxides of metals that are readily able to change valency have shown superior activity due to their use of the redox mechanism described above, as an example, Fe, Co, Cu have been found to be more active than Ni and Zn<sup>19,72</sup>. Many mixed metal oxide combinations have been investigated, including transition metals; Co-Ni<sup>73</sup>, Li,Na,K,V/Cu-Fe<sup>74</sup>, K-Cu, K-Co<sup>75</sup>, Co,Ba,K-Ce<sup>76</sup>, Cu-V-K, Cs-V<sup>77</sup>, Cs-Fe-V<sup>78</sup>, Cu-Mo, K-Mo, K-Cu-Mo<sup>79</sup>, Cu-Nb<sup>80</sup> and rare-Earth metals; Ce-La<sup>81</sup>, La-Cr<sup>82</sup>, Pr-Cr<sup>83</sup>, La-K<sup>84</sup>, La-K-Cr<sup>85</sup>, La-K-Mn<sup>86</sup>, La-K-Cu-V<sup>87</sup>, Co-Ce<sup>88</sup>, Ce-Co-K<sup>89</sup>, Sm-K<sup>90</sup>, due to their redox properties<sup>91</sup>. Many of these studies investigated the use of alkali/alkaline earth metals as promoters. Their ability to enhance the activity of soot oxidation catalysts has been attributed to their high mobility, which improves the catalyst/soot contact, and their ability to form carbonate intermediates, rather than affecting the redox ability of the materials<sup>71</sup>. Perovskite/spinel/hydroxalcite/delafossite catalysts have also received attention due to their stability<sup>92,93</sup>, and their oxidising as well as NO<sub>x</sub> removal abilities<sup>52,69,94,95</sup>. Of particular note are perovskites containing potassium- and strontium-substituted LaMO<sub>3</sub> (where M = Mn, Fe, Co and various combinations thereof), which have shown similar or superior soot oxidation and NO<sub>x</sub> decomposition to some PGM catalysts<sup>96,97</sup>. Several MCr<sub>2</sub>O<sub>4</sub> (M = Co, Mn) spinel oxide catalysts were reported to be active for soot oxidation due to their high concentration of suprafacial, weakly-chemisorbed oxygen

contributing towards the spillover effect<sup>98</sup>. The low melting point of eutectic salt mixtures containing  $\text{Cs}_2\text{O}$ ,  $\text{V}_2\text{O}_5$ , and  $\text{MoO}_3$  has been reported as favourable for soot oxidation above  $350\text{ }^\circ\text{C}$  as the liquid catalysts are able to wet the soot and achieve superior contact<sup>69,99</sup>. Cerium oxide ( $\text{CeO}_2$ , ceria) has been identified as an exceptionally effective material for several catalytic applications, and has been used for pollution control in TWCs for gasoline vehicles since the 1980s<sup>28</sup>. The ability of cerium to fluctuate between +4 and +3 oxidation states depending on the surrounding conditions effectively allows it to store and release oxygen, a desirable property in the dynamic atmosphere of vehicle exhausts<sup>71</sup>. Much work has been done on doping ceria with various foreign cations in order to improve its catalytic properties, most notably including transition and rare-Earth metals. This is discussed further in the following section.

Bueno-López and colleagues have conducted soot oxidation experiments on a wide range of the materials mentioned in this section, under identical experimental conditions. They conclude that ceria-based catalysts are consistently among the most effective for soot combustion<sup>28</sup>.

### **1.3.3 Ceria redox catalysts for soot oxidation**

In this project, the preparation of active soot oxidation catalysts containing ceria was investigated. As mentioned above, many investigations have identified the catalytic properties of ceria and methods by which it can be improved for use as a soot oxidation catalyst. This is discussed in greater detail in this section.

#### *1.3.3.1 Introduction*

Ceria is renowned as having exceptional oxygen storage capacity (OSC). This property allows for the release or storage of oxygen depending on various external parameters including gas composition, temperature and pressure. Ceria demonstrates this property due to the ability of cerium to switch between +4 ( $\text{CeO}_2$ ) and +3 ( $\text{Ce}_2\text{O}_3$ ) oxidation states. The redox capabilities of the  $\text{Ce}^{3+/4+}$  couple, as well as its ability to exchange oxygen with the gas phase provide ceria with exceptional catalytic performance which has found many applications including TWCs in gasoline vehicles<sup>100</sup> and as water gas shift catalysts for fuel cells<sup>28,71</sup>. The crystal structure of  $\text{CeO}_2$  is that of the fluorite structure (space group  $\text{Fm}\bar{3}\text{m}$ ) as shown in figure 1.11, in which

every cerium atom is surrounded by 8 oxygen anions which occupy tetrahedral positions. When switching from  $\text{Ce}^{4+}$  to  $\text{Ce}^{3+}$  the resulting loss of  $\text{O}^{2-}$  ions results in the formation of mobile oxygen vacancies,  $\text{V}_\text{O}$ . Even with a large concentration of vacancies the fluorite structure is maintained, allowing rapid re-oxidation upon exposure to oxygen<sup>101</sup>.

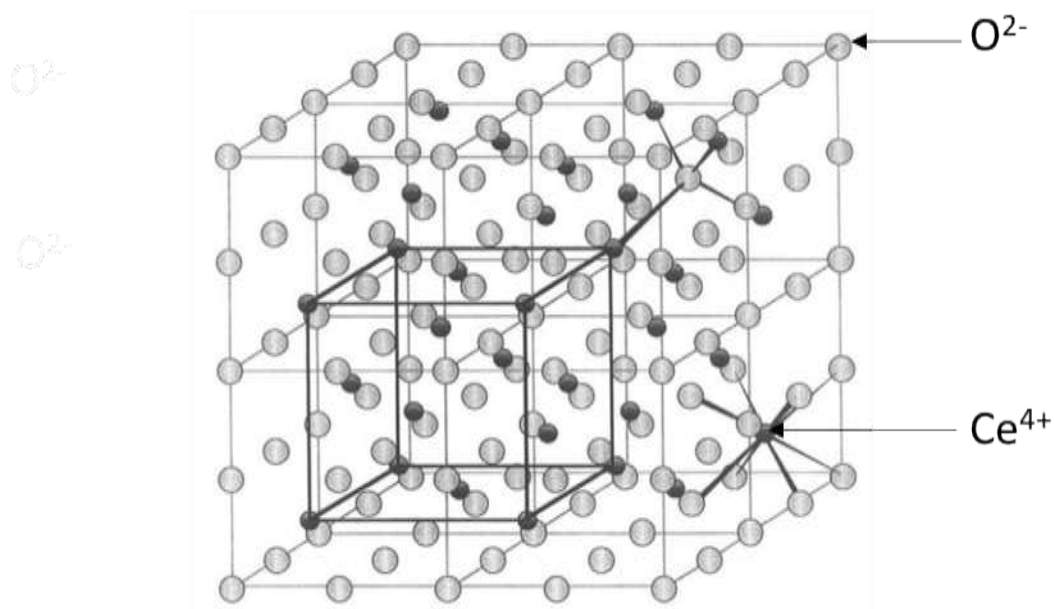


**Figure 1.11** The fcc cell of  $\text{CeO}_2$  with fluorite structure, showing octahedral cerium coordination and tetrahedral oxygen coordination<sup>101</sup>

As a catalyst for soot oxidation, the ability to store and release oxygen is advantageous due to the fluctuating composition of the exhaust atmosphere. This allows a material such as ceria to compensate during periods of rich exhaust stoichiometry ( $\text{O}_2$  deficient) by releasing oxygen from its lattice for soot oxidation, which can subsequently be replenished by oxygen from the gas-phase during periods of lean stoichiometry (excess of  $\text{O}_2$ )<sup>101</sup>. Also, its high redox capability and labile lattice oxygen make ceria an effective catalyst for total oxidation reactions such as soot oxidation ( $\text{C} + \text{O}_2 \rightarrow \text{CO}_2$ )<sup>71,102</sup>.

Two mechanisms have been proposed for the catalysed oxidation of soot by ceria. These are referred to as the “active oxygen” and “ $\text{NO}_2$ -assisted” mechanisms, which are shown in figure 1.12<sup>28</sup>.



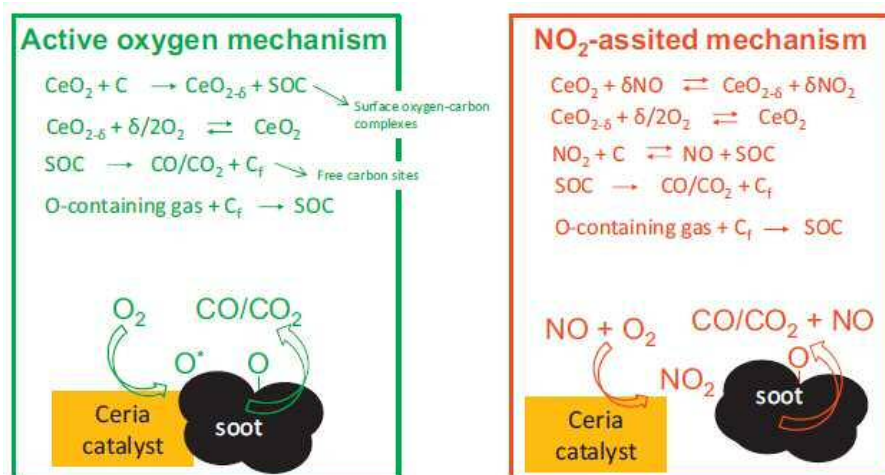


Figure 1.12 Active oxygen and NO<sub>2</sub>-assisted mechanisms of ceria-catalysed soot oxidation<sup>28</sup>

During the “active oxygen” mechanism, oxidation occurs by the transfer of lattice oxygen from the surface of the ceria catalyst to the soot through a Mars-van Krevelen mechanism<sup>71</sup>. As mentioned, in an O<sub>2</sub>-rich gas stream (such as a diesel exhaust), ceria is able to exchange oxygen with gas-phase O<sub>2</sub>. During this exchange, highly reactive oxygen species are created (the “active oxygen”) which can be involved in the soot oxidation reaction by transferring to the surface of the soot to form SOC, which decompose to CO/CO<sub>2</sub> and leave a free carbon site as described in the previous section. This mechanism has been reported by several studies using labelled O<sub>2</sub> experiments to confirm the oxidation of soot by lattice oxygen rather than gas-phase O<sub>2</sub><sup>81,103,104</sup>. The effectiveness of the mechanism depends strongly on the level of contact achieved between ceria and soot, and TAP (temporal analysis of products) experiments have suggested that where soot is not available to be oxidised, the active oxygen recombines to form O<sub>2</sub><sup>28,81</sup>.

The “NO<sub>2</sub>-assisted” mechanism relies on the oxidation of NO to NO<sub>2</sub>. Above 300 °C, ceria is able to catalyse this reaction using its lattice oxygen as shown in figure 1.12<sup>28</sup>. As mentioned previously, NO<sub>2</sub> is a much stronger oxidiser than O<sub>2</sub> due to its greater ease of dissociation, and is therefore better able to react with soot to form SOC<sup>105</sup>. The reaction mechanism subsequent to the formation of the SOC closely resembles that of the “active oxygen” mechanism; ceria is re-oxidised by gas-phase O<sub>2</sub>, and the SOC decomposes to CO/CO<sub>2</sub> leaving a reactive free carbon site. Further oxidising species are then able to attack these sites and contribute to soot oxidation. Thus it can be said that NO<sub>2</sub> acts as an initiator of the reaction<sup>103,106,107</sup>.

Above around 450 °C it has been reported that the oxidation of NO to NO<sub>2</sub> by ceria is as effective as a Pt catalyst as both achieve the maximum level of NO<sub>2</sub> allowed by the thermodynamic equilibrium<sup>28,107</sup>. This means that under conditions where the “NO<sub>2</sub>-assisted” mechanism is prevalent, ceria is capable of being as effective as a Pt-containing catalyst for soot oxidation. Under conditions where the “active oxygen” mechanism is favoured, ceria can outperform it, as a Pt catalyst is not able to utilise this method<sup>28</sup>.

Despite this, pure ceria is unsuitable as a soot oxidation catalyst operating under the conditions of a passenger vehicle exhaust. The major drawbacks of ceria are related to its poor thermal resistance and low-temperature activity<sup>101</sup>. After subjection to high temperature (1000 °C) aging, the OSC capabilities of ceria are irreversibly compromised due to the sintering of its particles, inhibiting the cycle of Ce between oxidation states<sup>108</sup>. This, coupled with its poor low-temperature activity for soot oxidation means that ceria is unable to comply with the demands of a catalyst for a particulate filter under the increasingly stringent emissions standards. This has led to researchers investigating new compositions of ceria catalysts in order to improve its properties as a soot oxidation catalyst<sup>28,71,101</sup>.

Introducing dopant metals into the ceria structure can promote soot oxidation in two ways: “Ceria amplifier”; the dopant metals act by improving the catalytic properties of ceria by enhancing its abilities to oxidise NO, to generate active oxygen, or by improving the contact between ceria and soot. “Ceria synergy”; the dopants themselves contain active sites for soot oxidation and can function alongside ceria to lower the soot oxidation temperature<sup>71</sup>.

### 1.3.3.2 CeO<sub>2</sub>-containing mixed metal oxides

There have been many studies investigating the incorporation of “ceria amplifier” dopants into the ceria lattice to improve its redox abilities. As mentioned above, the reduction of ceria results in the formation of mobile oxygen vacancies, V<sub>O</sub> which are essential to the material’s ability to release oxygen and subsequently re-oxidise. According to the mechanism and dynamics of oxygen storage, an increase in the concentration of V<sub>O</sub> should correspond to an increase in the OSC of the material providing the active redox elements are not significantly decreased and the V<sub>O</sub> do not cluster<sup>101</sup>. Mixed metal oxides containing ceria with a range of dopants including transition metals such as Zr, Hf<sup>109</sup> and rare-Earth metals such as La, Pr, Nd<sup>110</sup>, Sm<sup>111</sup>, Gd, Yb<sup>112</sup>, Tb, Lu<sup>113</sup> have been investigated. Other than Pr, which is stable in both

+3 and +4 oxidation states, these dopants themselves have little redox ability. Their role is to form Ce-based solid solutions which distort the ceria lattice due to their ionic radii differing from those of  $\text{Ce}^{3+/4+}$ , increasing the concentration of defects and thus enhancing the redox properties of ceria<sup>71,114</sup>.

Ceria-zirconia ( $\text{CeO}_2\text{-ZrO}_2$ ) is perhaps the most widely reported such combination. Despite  $\text{Zr}^{4+}$  having a smaller ionic radius (0.84 Å) than  $\text{Ce}^{4+}$  (0.97 Å), they are able to form solid solutions in a range of compositions, and have shown to enhance the redox properties of ceria at lower temperatures, as well as improving thermal stability<sup>28,46,60,109,114</sup>. The superior redox has been attributed to the shrinkage of the  $\text{CeO}_2$  cell parameter by the substitution of  $\text{Ce}^{4+}$  for  $\text{Zr}^{4+}$ . Stress to the structure induced by variations in the cell parameter favours the formation of structural defects, in turn enhancing oxygen mobility<sup>101</sup>.

In contrast, the rare-Earth metals listed above exhibit larger ionic radii than  $\text{Ce}^{4+}$ <sup>111</sup>. It has been reported that when incorporated into the  $\text{CeO}_2$  structure they induce structural stress by increasing the cell parameter compared to pure ceria. Moreover, the incorporation of trivalent (+3 oxidation state) rare-Earth cations into the  $\text{CeO}_2$  lattice induces stress by forcing the formation of oxygen vacancies in order to fulfil charge neutrality<sup>81,110,111,115</sup>. As with zirconia, the introduction of rare-Earth metal oxides has shown to improve the redox properties, as well as demonstrating greater thermal stability than pure ceria<sup>28</sup>. As mentioned above, unlike the other rare-Earth cations which remain in the +3 oxidation state, praseodymium ions are able exchange between +3/+4 states like cerium. It has been reported that incorporation of Pr cations into the ceria lattice increases the concentration of oxygen vacancies and hence oxygen mobility in the structure due to the redox cycle of  $\text{Pr}^{3+/4+}$ <sup>116</sup>.

The incorporation of alumina ( $\text{Al}_2\text{O}_3$ ) with ceria has been reported to significantly improve the thermal stability of the material through a concept known as the “diffusion barrier”. It is thought that contact between the primary ceria nano-particles enables particle growth at higher temperatures, which leads to sintering and a loss of activity. The concept of the diffusion barrier, as shown in figure 1.13, is the introduction of another oxide which does not react with the primary particles – in this case alumina – which restricts the contact between them and thus inhibits particle growth and sintering. A study by Morikawa *et al.* introduced alumina among ceria-zirconia particles on the nanometre-scale, and was found to inhibit particle growth during durability testing up to 1000 °C<sup>117</sup>.

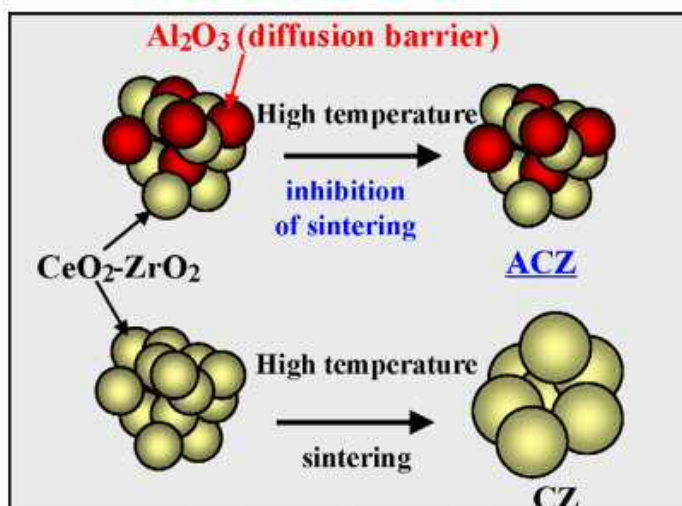


Figure 1.13 Illustration of diffusion barrier concept<sup>117</sup>

### 1.3.3.3 Transition metal promoters

Several transition metals were investigated in this project for use as promoters on ceria-based supports. This initially focussed on silver, however a brief investigation into other transition metals was also undertaken.

Silver has been found to be an efficient partial oxidation catalyst, with applications ranging from the epoxidation of ethylene to ethylene epoxide, the oxy-dehydration of methane to formaldehyde, and the oxidation of CO, hydrocarbons and ammonia<sup>118</sup>. The ability of silver to promote the formation of highly reactive superoxide,  $\text{O}_2^-$  species has encouraged investigations into its use for soot oxidation catalysis. Using electron spin resonance (ESR), Machida *et al.* showed that  $\text{O}_2^-$  formation increased when metallic silver was present on  $\text{CeO}_2$  compared to the bare support, and resulted in enhanced soot oxidation activity<sup>119</sup>. Studies by Aneggi and Corro impregnated silver on different supports including  $\text{CeO}_2$ ,  $\text{ZrO}_2$ ,  $\text{Al}_2\text{O}_3$  and  $\text{SiO}_2$ <sup>118,120</sup>. They also reported that the formation of superoxide by metallic silver ( $\text{Ag}^0$ ) was responsible for the improvements observed in soot oxidation activity. It was observed that  $\text{Ag}/\text{ZrO}_2$  and  $\text{Ag}/\text{Al}_2\text{O}_3$  were improved to a greater extent than  $\text{Ag}/\text{CeO}_2$  compared to their bare supports. This was attributed to the different interactions between silver and the various supports. In the case of  $\text{ZrO}_2$  and  $\text{Al}_2\text{O}_3$  it was observed that  $\text{Ag}^0$  was preferentially formed on the surface of the support during calcination. With  $\text{CeO}_2$  it was found that much of the silver was stabilised as  $\text{Ag}_2\text{O}$  on the surface of the support, and that  $\text{Ag}^0$  existed as a smooth layer on top of the oxide. This resulted in a lower proportion of silver in the active metallic phase,

and also decreased dispersion compared to the other two supports<sup>118</sup>. However other studies have achieved more favourable results from silver-promoted ceria catalysts. As well as the formation of superoxide species, silver has been found to act as a “ceria amplifier” by interacting with the ceria support, considerably weakening Ce-O bonds and favouring the formation of  $\text{Ce}^{3+}$  and oxygen vacancies which aid the Mars-van Krevelen mechanism of soot oxidation<sup>121,122</sup>. In a study by Shimizu *et al.*, the impregnation of Ag nanoparticles on  $\text{CeO}_2$  was found to decrease the activation energy of  $\text{Ce}^{4+}$  reduction to  $\text{Ce}^{3+}$ , increasing oxygen vacancies on the ceria surface. They proposed a mechanism, shown in figure 1.14 whereby gas-phase  $\text{O}_2$  is chemisorbed on the  $\text{V}_\text{O}$  site adjacent to the  $\text{Ce}^{3+}$  ion and silver nanoparticle to form a reactive  $\text{O}_n^{\text{x-}}$  species (likely superoxide  $\text{O}_2^-$ ) which then migrates to the surface of the soot particle and oxidises it to  $\text{CO}_2$ <sup>123</sup>.

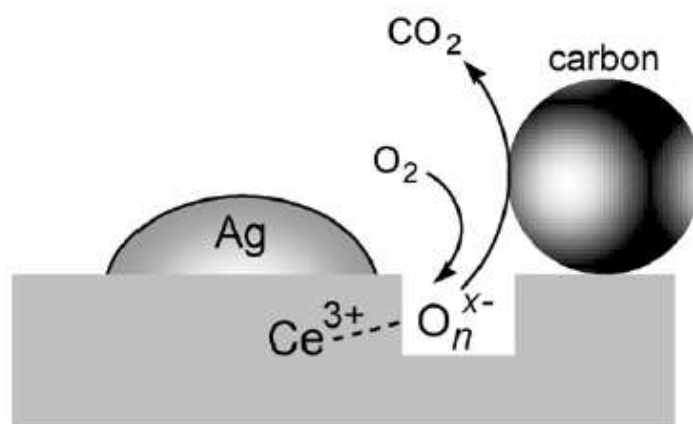


**Figure 1.14** Schematic mechanism of soot oxidation over Ag/ $\text{CeO}_2$  catalyst<sup>123</sup>

Yamazaki *et al.* prepared a  $\text{CeO}_2$ -Ag catalyst by co-precipitation which formed a “rice-ball” morphology, a unique agglomeration nanostructure consisting of an Ag particle surrounded by fine  $\text{CeO}_2$  particles (figure 1.15). This structure enabled a large Ag/ $\text{CeO}_2$  interface and was able to prevent sintering of Ag particles<sup>124</sup>.

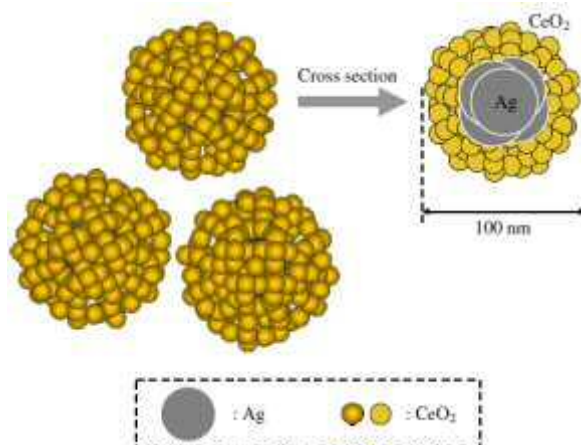


**Figure 1.15** Structural schematic of CeO<sub>2</sub>-Ag "rice-ball" morphology proposed by Yamazaki<sup>124</sup>

The proposed mechanism by which this material was able to catalyse soot oxidation is shown in figure 1.16. It suggests that oxygen is adsorbed on the surface of the Ag particle either from gas-phase O<sub>2</sub> or by ceria lattice oxygen at the CeO<sub>2</sub>-Ag interface to form atomic oxygen. This oxygen then migrates to the surface of the CeO<sub>2</sub> particles (spillover) via the interface and becomes O<sub>x</sub><sup>n-</sup> (some of which is O<sub>2</sub><sup>-</sup>) by interaction with V<sub>O</sub> on the ceria surface. This mobile active oxygen species is able to migrate along the ceria surface and react with soot to form CO<sub>2</sub> at the CeO<sub>2</sub>/soot interface. The large CeO<sub>2</sub>/Ag interface allows for fast migration of the oxygen species. Wang *et al.* found that the promotion of V<sub>O</sub> on the surface of ceria by Ag particles helped to generate more active oxygen species. However, they also found that when migrating O<sub>2</sub><sup>-</sup> species interacted with successive V<sub>O</sub> they were reduced to less active O<sup>-</sup> and O<sup>2-</sup>. This suggested that an excessive concentration of V<sub>O</sub> on the ceria surface was detrimental to the soot oxidation activity of the catalyst and therefore a high silver-loading was disadvantageous to the catalyst<sup>125</sup>.

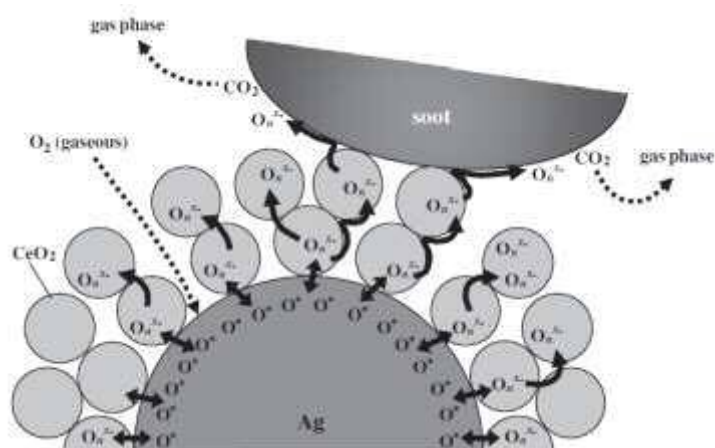


**Figure 1.16** Schematic mechanism for soot oxidation over the CeO<sub>2</sub>-Ag catalyst<sup>124</sup>

Several other transition metals have shown catalytic activity for soot oxidation, drawing interest due to their low-cost and availability. Neef *et al.* conducted soot oxidation tests with numerous metal oxide catalysts including Co, Mo, V, Fe, Mn, Cu and Ni. These were described as very to moderately active catalysts for soot oxidation under tight contact conditions<sup>65</sup>. Their activity is derived from their ability to release oxygen at the catalyst/soot interface, hence the need for good contact. Several studies into the soot oxidation activity of iron oxide catalysts have been conducted<sup>57,126,127</sup>. These concluded that soot oxidation took place via a modified Mars-van Krevelen mechanism, as shown in figure 1.17. The role of  $\text{Fe}_2\text{O}_3$  was the transfer of surface and sub-surface oxygen to the soot at the point of contact to form SOC intermediates. The reduced Fe is then re-oxidised by neighbouring oxygen, which leads to a cascade of formation and refilling of surface oxygen vacancies which are finally filled by gas-phase oxygen a distance from the catalyst/soot contact point. Mul *et al.* also concluded that the same mechanism was applicable in the case of  $\text{Co}_3\text{O}_4$ <sup>57</sup>.

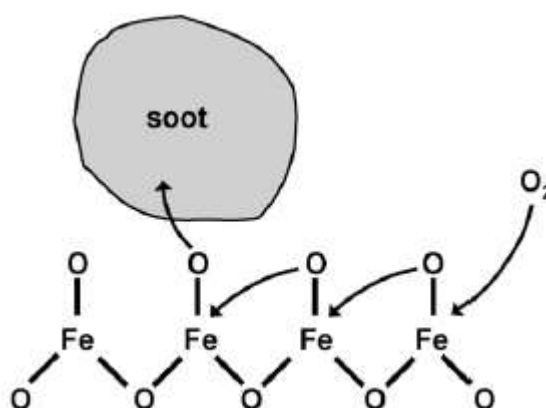
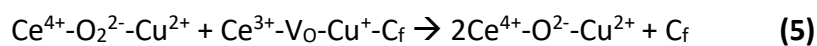
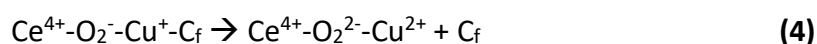
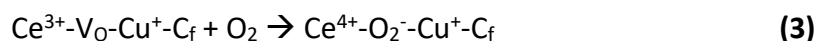
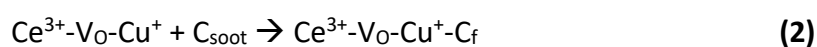
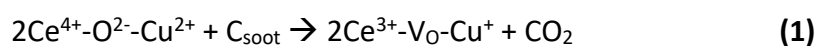


**Figure 1.17** Mechanistic scheme of the oxygen transfer from the  $\text{Fe}_2\text{O}_3$  catalyst to soot<sup>126</sup>

These metal oxides have also been studied as dopants for ceria/ceria-based catalysts, with varying levels of success. Aneggi *et al.* showed that a co-precipitated Ce-Fe mixed metal oxide catalyst showed an improvement in soot oxidation activity due to the formation of a solid solution and the interaction between the two metals which improved the redox abilities of ceria. However, this activity was lost after thermal aging up to 700 °C due to crystallisation of the  $\text{Fe}_2\text{O}_3$  phase, which gradually segregated from  $\text{CeO}_2$ <sup>128</sup>. An Fe-Ce-Zr catalyst prepared via a gel-combustion synthesis method by Alinezhadchamazketi and colleagues concluded that the Fe-Ce interactions did not influence the redox behaviour of cerium, and had no positive effect on the soot oxidation activity of the catalyst<sup>129</sup>. Harrison *et al.* demonstrated that the

activity of CeO<sub>2</sub> could be improved by the presence of Co<sub>3</sub>O<sub>4</sub>, either through co-precipitation or impregnation. Testing of these catalysts showed that soot oxidation took place at the same temperature as H<sub>2</sub>-reduction of the cobalt oxide phase, suggesting a redox mechanism which may have been assisted by oxygen spillover on the CeO<sub>2</sub> support<sup>88</sup>. This was also observed by Dhakad *et al.* with a co-precipitated Co<sub>3</sub>O<sub>4</sub>-CeO<sub>2</sub> catalyst<sup>92</sup>.

Copper has also attracted attention as an active soot oxidation catalyst due to its redox properties. CuO has been reported as particularly active phase due to the ease with which it is able to release oxygen due to the reduction of Cu<sup>2+</sup>. This has been reported to enable the oxidation of NO to NO<sub>2</sub> and also to complete the oxidation of soot by catalysing the reaction of CO to CO<sub>2</sub><sup>130</sup>. CuO has also demonstrated an ability to improve the catalytic properties of ceria. Reddy & Rao noted that the incorporation of CuO into the CeO<sub>2</sub> lattice increased the formation of oxygen vacancies in the structure and led to the increased reactivity of lattice oxygen for soot oxidation<sup>131</sup>. Liang *et al.* also observed well-dispersed CuO strongly interacting with the surface of CeO<sub>2</sub> and CeO<sub>2</sub>-ZrO<sub>2</sub> supports which improved the reducibility of ceria<sup>132</sup>. They made use of a Mars-van Krevelen-type mechanism previously reported by Martínez-Arias *et al.* for the oxidation of CO by Cu-CeO<sub>2</sub> to show how the Cu-Ce interaction aids soot oxidation, as shown below. Both Cu<sup>2+</sup> and Ce<sup>4+</sup> at the Cu/Ce interface are rapidly reduced by soot to form CO<sub>2</sub>, in equation (1). Equations (2)-(4) then take place to partially re-oxidise the catalyst with gas-phase O<sub>2</sub>, and convert it to peroxide which can migrate and fill the remaining oxygen vacancies in equation (5)<sup>133</sup>.



(Where C<sub>f</sub> is the adjacent carbon species adsorbed on the Cu-Ce surface)

#### 1.3.3.4 Alkali metal promoters

As mentioned in section 1.3.2, there have been many studies into the use of alkali metals, usually as promoters for soot oxidation catalysts such as ceria<sup>71,134,135</sup>, spinels<sup>74</sup>,



perovskites<sup>86,87</sup> and various other metal/mixed metal-oxides<sup>69,136</sup>. Their high activity is attributed to their high surface mobility due to their low melting points. This increases the contact between catalyst and soot and allows for a more facile reaction. They lower the activation energy of soot oxidation by favouring the formation of intermediate carbonate species<sup>71,129,134–139</sup>. They are also able to act as electron donors, enabling the dissociative chemisorption of electron accepting gas-phase oxygen<sup>139</sup>.

Aneggi *et al.* put forward an extensive work on alkali metal-catalysed soot oxidation<sup>134</sup>. They prepared various alkali metal (Na, K, Rb, Cs) catalysts on both redox active ( $\text{CeO}_2$ ) and inactive ( $\text{ZrO}_2$  and  $\text{TiO}_2$ ) supports. The results of their soot oxidation tests are shown in figure 1.18.

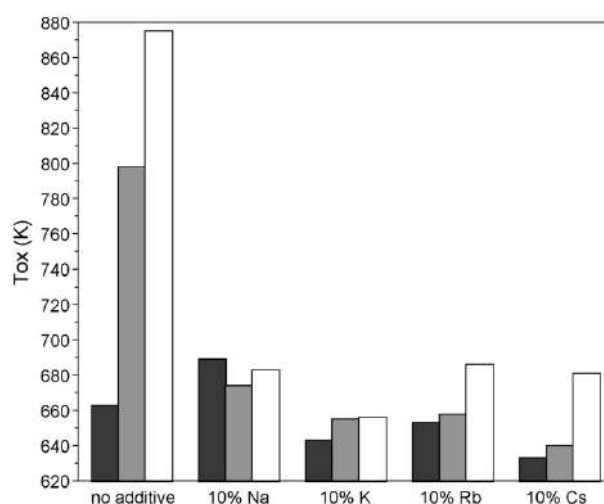
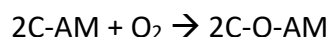
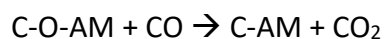
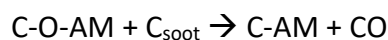


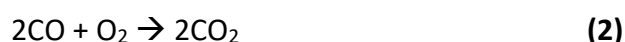
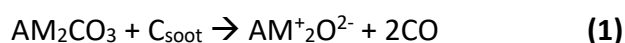
**Figure 1.18** Soot oxidation temperatures of  $\text{CeO}_2$  (black),  $\text{ZrO}_2$  (grey),  $\text{TiO}_2$  (white) with 10%Na/K/Rb/Cs<sup>134</sup>

It has been suggested that alkali metals are able to act with a redox mechanism correlated to the redox cycle of  $\text{CeO}_2$ . In a study by Zhu *et al.*, it was suggested that the catalytic role of potassium can be attributed to an oxidation-reduction cycle in which  $\text{K}_x\text{O}_y$  is oxidised by  $\text{O}_2$  to  $\text{K}_x\text{O}_{y+1}$ , which then transfers oxygen to reduced ceria to restore it to  $\text{CeO}_2$ <sup>140</sup>. However, the high activity achieved on each of the supports in figure 1.18 suggested the alkali metal was able to catalyse soot oxidation without the need for a redox cycle with an active support. The mechanism proposed for this reaction relies on the alkali metal promoting the formation of carbon-oxygen complexes, which are the active sites. The alkali metal favours the chemisorption of molecular oxygen with the carbon surface complex, which subsequently reacts with soot:



Where AM is the alkali metal, C-O-AM and C-AM are oxidised and reduced forms of the carbon-oxygen complexes. The alkali metal therefore acts as an oxygen carrier which transfers gas-phase oxygen to the carbon surface<sup>134</sup>.

This same study, as well as others, investigated the activity of various different types of alkali metal compounds, most notably those containing potassium. There is general agreement that the trend in activity is;  $\text{K}_2\text{CO}_3 \approx \text{KOH} > \text{KHCO}_3 > \text{KNO}_3 > \text{K}_2\text{SO}_4 > \text{KCl}$ <sup>134,136,139</sup>. A study by Peralta *et al.* found that  $\text{KNO}_3$  was more active than  $\text{K}_2\text{CO}_3$ , however  $\text{KNO}_3$  was much less stable at higher temperatures<sup>141</sup>. This trend has been explained by the stability of the salts. In the presence of a strong anion, such as  $\text{Cl}^-$ , the interaction between potassium and the carbon on the surface of the soot is not favoured, as such the formation of the active sites described above is hindered<sup>134</sup>. It has also been suggested that alkali metal-carbonates can utilise their carbonate species as the active catalytic species. This was first proposed by Kimura *et al.* using  $\text{Na}_2\text{CO}_3$  on the surface of a  $\text{K}_2\text{CO}_3/\text{Na}$  based nepheline<sup>142</sup>, and has been investigated further at Cardiff University, with the mechanism below proposed<sup>143</sup>;



In equation (1) the AM-carbonate is reduced by the surface carbon of the soot to form an AM-oxide and two equivalents of CO. The CO is then subsequently oxidised to  $\text{CO}_2$  in equation (2). The AM-oxide is re-carbonated by gas-phase  $\text{CO}_2$  in equation (3). Thus the overall

reaction, shown in equation (4) results in the reformation of the AM-carbonate and the oxidation of soot to CO<sub>2</sub>.

In general it is reported that descending through the alkali metal group follows a trend of increasing soot oxidation activity; Cs > Rb ≈ K > Na > Li. This can be explained by the trend of decreasing melting points down the group, which allow for greater mobility and hence contact with soot, and also to the increasing electropositivity, which favours electron donation and the dissociative chemisorption of oxygen<sup>144–146</sup>. However, this has been reported as varying depending on a number of factors, including; the alkali metal species used, the intimacy of catalyst/soot contact, and soot the type of support (as shown in figure 1.18<sup>134</sup>). Neft *et al.* found that in loose contact, the trend in activity for AM-carbonates was Cs > Na > K > Li, while in tight contact it was Cs > K > Na > Li. In AM-hydroxides the trend was K > Cs > Na in loose contact, and Cs > K > Na in tight contact<sup>65</sup>. In a study into AM on ceria-zirconia by Liang *et al.* the trend in activity was found to be K > Na > bare CZ support > Li. This was linked to the relative sizes of the AM ionic radii compared to cerium; K<sup>+</sup> > Na<sup>+</sup> > Ce<sup>4+</sup> > Li<sup>+</sup>. The larger ions were attributed with causing lattice distortion and increasing oxygen vacancies leading to an increase in superoxide species through gas-phase O<sub>2</sub>/lattice oxygen exchange<sup>135</sup>.

However the main drawback of alkali metal catalysts is their poor thermal stability. Several of the above studies have noted the significant loss of metal content from the catalysts after thermal aging<sup>71,147</sup>. After aging at 800 °C for 50 h in air, it was observed by Aneghi that the loss of alkali-metal increased down the group, ranging from ~15 % in Na/CeO<sub>2</sub> to ~95 % in Cs/CeO<sub>2</sub>. The same experiment conducted in the presence of water resulted in a loss of ~55 % of Rb and at least 85 % of Na, K, Cs from their respective catalysts. This was attributed to the formation of volatile compounds, which is exacerbated in the presence of water. This also resulted in severe deactivation of the catalysts observed during subsequent soot oxidation testing<sup>134</sup>.

## 1.4 Project Aim

The project, titled 'Passive Catalytic Soot Oxidation' was conducted at the Catalysis Institute at Cardiff University, funded by Jaguar Land Rover and EPSRC.

The aim of the project was to design materials capable of catalysing the combustion of trapped soot particulate, without the need for the addition of heat or reactants to the exhaust. The ultimate aim is the continuous regeneration of particulate filters for two aftertreatment processes; diesel compression-ignition, and gasoline direct-injection spark-ignition. The brief therefore demanded that the materials be suitable for use as a washcoat for both diesel and gasoline particulate filters (DPF and GPF). The lean-burn conditions of diesel CI engines results in a high concentration of O<sub>2</sub> in the exhaust stream, however temperatures rarely exceed 250 °C and are too low for uncatalysed soot oxidation<sup>11</sup>. While the temperature is considerably higher in a gasoline exhaust, between 350-500 °C in urban driving conditions and reaching 700 °C during motorway speeds, the stoichiometric fuel/air mix in the engine results in a shortage of oxygen in the exhaust stream<sup>39</sup>.

As explained in the above sections, the previous studies into cerium oxide, CeO<sub>2</sub> suggest that it is capable of addressing the issues for both these applications. In diesel exhausts primarily by activating the high concentration of gas-phase oxygen to lower the soot oxidation temperature, and in gasoline exhausts by utilising its OSC properties to provide greater availability of oxygen. This project therefore investigated the capability of various ceria-containing materials to catalyse soot oxidation, using an iterative experimental approach. The preparation, characterisation and testing of the catalysts was carried out using various techniques, with an emphasis on the robustness of the materials to ensure suitability for the above applications.

## 1.5 References

1. G. C. Bond, *Heterogeneous Catalysis: Principles and Applications*, Oxford University Press, Oxford Oxfordshire ; New York, 2nd Revised edition edition., 1987.
2. J. J. Berzelius, *Årsberättelse om framstegen i fysik och kemi*, Norstedt, 1835.
3. M. Fulhame, J. Humphreys and R. Van Dyke, *An essay on combustion, with a view to a new art of dying and painting : wherein the phlogistic and antiphlogistic*

- hypotheses are proved erroneous*, Philadelphia : Printed and sold by James Humphreys, corner of Second and Walnut-street, 1810.
4. M. W. Roberts, *Catal. Lett.*, 2000, **67**, 1–4.
  5. D. Steinborn, *Fundamentals of Organometallic Catalysis*, John Wiley & Sons, 2011.
  6. M. Beller, A. Renken and R. A. van Santen, Eds., *Catalysis: From Principles to Applications*, Wiley VCH, Weinheim, Germany, 2012.
  7. A. Burrows, J. Holman, A. Parsons, G. Pilling and G. Price, *Chemistry<sup>3</sup>: Introducing inorganic, organic and physical chemistry*, OUP Oxford, Oxford, 2 edition., 2013.
  8. M. Kaufman, *Principles of Thermodynamics*, CRC Press, 2002.
  9. O. Deutschmann, H. Knözinger, K. Kochloefl and T. Turek, in *Ullmann's Encyclopedia of Industrial Chemistry*, Wiley-VCH Verlag GmbH & Co. KGaA, 2000.
  10. J. P. A. Neeft, M. Makkee and J. A. Moulijn, *Fuel Process. Technol.*, 1996, **47**, 1–69.
  11. M. V. Twigg, *Catal. Today*, 2011, **163**, 33–41.
  12. Intergovernmental Panel on Climate, *Climate Change 2013: The Physical Science Basis: Working Group I Contribution to the Fifth Assessment Report of the Intergovernmental Panel on Climate Change*, Cambridge University Press, 2014.
  13. CARB, Low Emission Vehicle (LEV) Program, <https://www.arb.ca.gov/msprog/levprog/levprog.htm>.
  14. European Commission, Road Vehicles - Transport - Air - Environment - European Commission, <http://ec.europa.eu/environment/air/transport/road.htm>.
  15. Emission Standards: Europe: Cars and Light Trucks, <https://www.dieselnet.com/standards/eu/ld.php>.
  16. G. A. Stratakis, Thesis, University of Thessaly, 2004.
  17. WHO, *Health Aspects of Air Pollution with Particulate Matter, Ozone and Nitrogen Dioxide*, Bonn, Germany, 2003.
  18. C. L. Myung and S. Park, *Int. J. Automot. Technol. Dordr.*, 2012, **13**, 9–22.
  19. B. R. Stanmore, J. F. Brilhac and P. Gilot, *Carbon*, 2001, **39**, 2247–2268.
  20. B. A. A. L. van Setten, M. Makkee and J. A. Moulijn, *Catal. Rev.*, 2001, **43**, 489–564.
  21. S. Spiess, K.-F. Wong, J.-M. Richter and R. Klingmann, *Top. Catal.*, 2013, **56**, 434–439.
  22. D. Uy, M. A. Ford, D. T. Jayne, A. E. O'Neill, L. P. Haack, J. Hargas, M. J. Jagner, A. Sammut and A. K. Gangopadhyay, *Tribol. Int.*, 2014, **80**, 198–209.
  23. U. Mathis, M. Mohr and A.-M. Forss, *Atmos. Environ.*, 2005, **39**, 107–117.
  24. US EPA, *Health Assessment Document for Diesel Engine Exhaust (Final 2002)*, .
  25. D. B. Kittelson, *J. Aerosol Sci.*, 1998, **29**, 575–588.
  26. M. Sharma, A. K. Agarwal and K. V. L. Bharathi, *Atmos. Environ.*, 2005, **39**, 3023–3028.
  27. Y.-F. Wang, K.-L. Huang, C.-T. Li, H.-H. Mi, J.-H. Luo and P.-J. Tsai, *Atmos. Environ.*, 2003, **37**, 4637–4643.
  28. A. Bueno-López, *Appl. Catal. B Environ.*, 2014, **146**, 1–11.
  29. C. A. Pope, R. T. Burnett, M. J. Thun, E. E. Calle, D. Krewski, K. Ito and G. D. Thurston, *JAMA*, 2002, **287**, 1132–1141.
  30. G. Oberdörster, Z. Sharp, V. Atudorei, A. Elder, R. Gelein, W. Kreyling and C. Cox, *Inhal. Toxicol.*, 2004, **16**, 437–445.
  31. A. Luch, *The Carcinogenic Effects of Polycyclic Aromatic Hydrocarbons*, World Scientific, 2005.
  32. F. Liang, M. Lu, T. C. Keener, Z. Liu and S.-J. Khang, *J. Environ. Monit.*, 2005, **7**, 983–988.

33. K. Straif, R. Baan, Y. Grosse, B. Secretan, F. El Ghissassi and V. Cogliano, *Lancet Oncol.*, 2005, **6**, 931–932.
34. F. P. Perera, D. Tang, S. Wang, J. Vishnevetsky, B. Zhang, D. Diaz, D. Camann and V. Rauh, *Environ. Health Perspect.*, 2012, **120**, 921–926.
35. P. Bera and M. S. Hegde, *J. Indian Inst. Sci.*, 2010, **90**, 299–325.
36. UNECE, Environmental Policy - Conventions and Protocols - Air - Air Pollution, <http://www.unece.org/env/lrtap/welcome.html>.
37. US EPA, Vehicle Emissions California Waivers and Authorizations, <https://www.epa.gov/state-and-local-transportation/vehicle-emissions-california-waivers-and-authorizations>.
38. S. Edelstein, Which states follow California's emission and zero-emission vehicle rules?, [http://www.greencarreports.com/news/1109217\\_which-states-follow-californias-emission-and-zero-emission-vehicle-rules](http://www.greencarreports.com/news/1109217_which-states-follow-californias-emission-and-zero-emission-vehicle-rules).
39. A. Mamakos, *Feasibility of Introducing Particulate Filters on Gasoline Direct Injection Vehicles. A Cost Benefit Analysis*, Publications Office of the European Union, 2012.
40. H. Burtscher, *J. Aerosol Sci.*, 2005, **36**, 896–932.
41. H. Ström and S. Sasic, *Catal. Today*, 2012, **188**, 14–23.
42. B. Guan, R. Zhan, H. Lin and Z. Huang, *J. Environ. Manage.*, 2015, **154**, 225–258.
43. B. Giechaskiel, P. Dilara, E. Sandbach and J. Andersson, *Meas. Sci. Technol.*, 2008, **19**, 095401.
44. Emission Test Cycles: ECE 15 + EUDC / NEDC, [https://www.dieselnet.com/standards/cycles/ece\\_eudc.php](https://www.dieselnet.com/standards/cycles/ece_eudc.php).
45. A. Marotta, J. Pavlovic, B. Ciuffo, S. Serra and G. Fontaras, *Environ. Sci. Technol.*, 2015, **49**, 8315–8322.
46. J. Kašpar, P. Fornasiero and M. Graziani, *Catal. Today*, 1999, **50**, 285–298.
47. Diesel Catalysts, [https://www.dieselnet.com/tech/cat\\_diesel.php](https://www.dieselnet.com/tech/cat_diesel.php).
48. X. Song, J. H. Johnson and J. D. Naber, *Int. J. Engine Res.*, 2015, **16**, 738–749.
49. Lean NOx Catalyst, [https://www.dieselnet.com/tech/cat\\_lean-nox.php](https://www.dieselnet.com/tech/cat_lean-nox.php).
50. A. Mamakos, *Feasibility of Introducing Particulate Filters on Gasoline Direct Injection Vehicles. A Cost Benefit Analysis*, Publications Office of the European Union, 2012.
51. A. Mamakos, N. Steininger, G. Martini, P. Dilara and Y. Drossinos, *Atmos. Environ.*, 2013, **77**, 16–23.
52. D. Fino, S. Bensaid, M. Piumetti and N. Russo, *Appl. Catal. Gen.*, 2016, **509**, 75–96.
53. J. A. Moulijn and F. Kapteijn, *Carbon*, 1995, **33**, 1155–1165.
54. S. G. Chen, R. T. Yang, F. Kapteijn and J. A. Moulijn, *Ind. Eng. Chem. Res.*, 1993, **32**, 2835–2840.
55. J. P. A. Neeft, T. X. Nijhuis, E. Smakman, M. Makkee and J. A. Moulijn, *Fuel*, 1997, **76**, 1129–1136.
56. B. J. Cooper and J. E. Thoss, *Role of NO in Diesel Particulate Emission Control*, SAE Technical Paper, Warrendale, PA, 1989.
57. G. Mul, F. Kapteijn, C. Doornkamp and J. A. Moulijn, *J. Catal.*, 1998, **179**, 258–266.
58. E. Baumgarten and A. Schuck, *Appl. Catal.*, 1988, **37**, 247–257.
59. R. T. K. Baker and J. J. Chludzinski, *Carbon*, 1981, **19**, 75–82.
60. E. Aneggi, C. de Leitenburg and A. Trovarelli, *Catal. Today*, 2012, **181**, 108–115.
61. B. A. A. L. van Setten, J. M. Schouten, M. Makkee and J. A. Moulijn, *Appl. Catal. B Environ.*, 2000, **28**, 253–257.

62. M. A. Peralta, M. S. Gross, B. S. Sánchez and C. A. Querini, *Chem. Eng. J.*, 2009, **152**, 234–241.
63. J. P. A. Neeft, M. Makkee and J. A. Moulijn, *Fuel*, 1998, **77**, 111–119.
64. J. P. A. Neeft, O. P. van Pruissen, M. Makkee and J. A. Moulijn, *Appl. Catal. B Environ.*, 1997, **12**, 21–31.
65. J. P. A. Neeft, M. Makkee and J. A. Moulijn, *Appl. Catal. B Environ.*, 1996, **8**, 57–78.
66. T. Andana, M. Piumetti, S. Bensaid, L. Veyre, C. Thieuleux, N. Russo, D. Fino, E. A. Quadrelli and R. Pirone, *Appl. Catal. B Environ.*, 2017, **209**, 295–310.
67. G. Neri, L. Bonaccorsi, A. Donato, C. Milone, M. G. Musolino and A. M. Visco, *Appl. Catal. B Environ.*, 1997, **11**, 217–231.
68. A. Setiabudi, M. Makkee and J. A. Moulijn, *Appl. Catal. B Environ.*, 2004, **50**, 185–194.
69. A. M. Hernández-Giménez, D. Castelló, and A. Bueno López, *Chem. Pap.*, 2014, **68**, 1154–1168.
70. M. Jeguirim, V. Tschamber and P. Ehrburger, *Appl. Catal. B Environ.*, 2007, **76**, 235–240.
71. S. Liu, X. Wu, D. Weng and R. Ran, *J. Rare Earths*, 2015, **33**, 567–590.
72. C. Setzer, W. Schütz and F. Schüth, *Stud. Surf. Sci. Catal.*, 1993, **75**, 2629–2632.
73. B. P. Tarasov, V. E. Muradyan, Y. M. Shul’ga, E. P. Krinichnaya, N. S. Kuyunko, O. N. Efimov, E. D. Obratsova, D. V. Schur, J. P. Maehlen, V. A. Yartys and H.-J. Lai, *Carbon*, 2003, **41**, 1357–1364.
74. W. F. Shangguan, Y. Teraoka and S. Kagawa, *Appl. Catal. B Environ.*, 1998, **16**, 149–154.
75. N. Nejar, J. M. García-Cortés, C. Salinas-Martínez de Lecea and M. J. Illán-Gómez, *Catal. Commun.*, 2005, **6**, 263–267.
76. V. G. Milt, C. A. Querini, E. E. Miró and M. A. Ulla, *J. Catal.*, 2003, **220**, 424–432.
77. P. Ciambelli, V. Palma, P. Russo and S. Vaccaro, *J. Mol. Catal. Chem.*, 2003, **204**, 673–681.
78. G. Neri, G. Rizzo, L. Bonaccorsi, C. Milone and S. Galvagno, *Catal. Today*, 2005, **100**, 309–313.
79. G. Mul, J. P. A. Neeft, F. Kapteijn, M. Makkee and J. A. Moulijn, *Appl. Catal. B Environ.*, 1995, **6**, 339–352.
80. A. Bellaloui, J. Varloud, P. Mériaudeau, V. Perrichon, E. Lox, M. Chevrier, C. Gauthier and F. Mathis, *Catal. Today*, 1996, **29**, 421–425.
81. A. Bueno-López, K. Krishna, M. Makkee and J. A. Moulijn, *J. Catal.*, 2005, **230**, 237–248.
82. N. Russo, D. Fino, G. Saracco and V. Specchia, *J. Catal.*, 2005, **229**, 459–469.
83. D. Fino and V. Specchia, *Chem. Eng. Sci.*, 2004, **59**, 4825–4831.
84. V. G. Milt, C. A. Querini and E. E. Miró, *Thermochim. Acta*, 2003, **404**, 177–186.
85. D. Fino, N. Russo, G. Saracco and V. Specchia, *J. Catal.*, 2003, **217**, 367–375.
86. Y. Teraoka, K. Kanada and S. Kagawa, *Appl. Catal. B Environ.*, 2001, **34**, 73–78.
87. D. Fino, P. Fino, G. Saracco and V. Specchia, *Appl. Catal. B Environ.*, 2003, **43**, 243–259.
88. P. G. Harrison, I. K. Ball, W. Daniell, P. Lukinskas, M. Céspedes, E. E. Miró and M. A. Ulla, *Chem. Eng. J.*, 2003, **95**, 47–55.
89. E. E. Miró, F. Ravelli, M. A. Ulla, L. M. Cornaglia and C. A. Querini, *Catal. Today*, 1999, **53**, 631–638.
90. L. Sui, L. Yu and Y. Zhang, *Energy Fuels*, 2006, **20**, 1392–1397.

91. Y. Zhang and X. Zou, *Catal. Commun.*, 2007, **8**, 760–764.
92. M. Dhakad, S. S. Rayalu, R. Kumar, P. Doggali, S. Bakardjieva, J. Subrt, T. Mitsuhashi, H. Haneda and N. Labhsetwar, *Catal. Lett.*, 2008, **121**, 137–143.
93. P. Doggali, H. Kusaba, S. Rayalu, Y. Teraoka and N. Labhsetwar, *Top. Catal.*, 2013, **56**, 457–461.
94. Y. Teraoka, K. Nakano, S. Kagawa and W. F. Shangguan, *Appl. Catal. B Environ.*, 1995, **5**, L181–L185.
95. J. Zhu and A. Thomas, *Appl. Catal. B Environ.*, 2009, **92**, 225–233.
96. T. Hirano, T. Tosho, T. Watanabe and T. Akiyama, *J. Alloys Compd.*, 2009, **470**, 245–249.
97. G. Zhang, Z. Zhao, J. Liu, J. Xu, Y. Jing, A. Duan and G. Jiang, *J. Rare Earths*, 2009, **27**, 955–960.
98. D. Fino, N. Russo, G. Saracco and V. Specchia, *J. Catal.*, 2006, **242**, 38–47.
99. S. J. Jelles, B. A. A. L. van Setten, M. Makkee and J. A. Moulijn, *Appl. Catal. B Environ.*, 1999, **21**, 35–49.
100. R. M. Heck and R. J. Farrauto, *Appl. Catal. Gen.*, 2001, **221**, 443–457.
101. A. Trovarelli, *Comments Inorg. Chem.*, 1999, **20**, 263–284.
102. A. Trovarelli, *Catal. Rev.*, 1996, **38**, 439–520.
103. N. Guillén-Hurtado, A. García-García and A. Bueno-López, *Appl. Catal. B Environ.*, 2015, **174–175**, 60–66.
104. K. Harada, T. Oishi, S. Hamamoto and T. Ishihara, *J. Phys. Chem. C*, 2014, **118**, 559–568.
105. J.-O. Müller, B. Frank, R. E. Jentoft, R. Schlögl and D. S. Su, *Catal. Today*, 2012, **191**, 106–111.
106. I. Atribak, B. Azambre, A. Bueno López and A. García-García, *Appl. Catal. B Environ.*, 2009, **92**, 126–137.
107. I. Atribak, B. Azambre, A. Bueno-Lopez and A. Garcia-Garcia, *Top. Catal.*, 2009, **52**, 2092.
108. S. J. Schmieg and D. N. Belton, *Appl. Catal. B Environ.*, 1995, **6**, 127–144.
109. B. M. Reddy, P. Bharali, G. Thrimurthulu, P. Saikia, L. Katta and S.-E. Park, *Catal. Lett.*, 2008, **123**, 327–333.
110. P. Dulgheru and J. A. Sullivan, *Top. Catal.*, 2013, **56**, 504–510.
111. A. Rangaswamy, P. Sudarsanam and B. M. Reddy, *J. Rare Earths*, 2015, **33**, 1162–1169.
112. S. Babu, R. Thanneeru, T. Inerbaev, R. Day, A. E. Masunov, A. Schulte and Sudipta Seal, *Nanotechnology*, 2009, **20**, 085713.
113. M. A. Matecka, L. Kępiński and W. Miśta, *Appl. Catal. B Environ.*, 2007, **74**, 290–298.
114. A. Trovarelli, M. Boaro, E. Rocchini, C. de Leitenburg and G. Dolcetti, *J. Alloys Compd.*, 2001, **323**, 584–591.
115. L. Katta, P. Sudarsanam, G. Thrimurthulu and B. M. Reddy, *Appl. Catal. B Environ.*, 2010, **101**, 101–108.
116. Z. Song, W. Liu, H. Nishiguchi, A. Takami, K. Nagaoka and Y. Takita, *Appl. Catal. Gen.*, 2007, **329**, 86–92.
117. A. Morikawa, T. Suzuki, T. Kanazawa, K. Kikuta, A. Suda and H. Shinjo, *Appl. Catal. B Environ.*, 2008, **78**, 210–221.
118. E. Aneggi, J. Llorca, C. de Leitenburg, G. Dolcetti and A. Trovarelli, *Appl. Catal. B Environ.*, 2009, **91**, 489–498.



119. M. Machida, Y. Murata, K. Kishikawa, D. Zhang and K. Ikeue, *Chem. Mater.*, 2008, **20**, 4489–4494.
120. G. Corro, U. Pal, E. Ayala and E. Vidal, *Catal. Today*, 2013, **212**, 63–69.
121. V. Shapovalov and H. Metiu, *J. Catal.*, 2007, **245**, 205–214.
122. G. Preda and G. Pacchioni, *Catal. Today*, 2011, **177**, 31–38.
123. K. Shimizu, H. Kawachi and A. Satsuma, *Appl. Catal. B Environ.*, 2010, **96**, 169–175.
124. K. Yamazaki, T. Kayama, F. Dong and H. Shinjoh, *J. Catal.*, 2011, **282**, 289–298.
125. H. Wang, S. Liu, Z. Zhao, X. Zou, M. Liu, W. Liu, X. Wu and D. Weng, *Catal. Sci. Technol.*, 2017, **7**, 2129–2139.
126. D. Reichert, H. Bockhorn and S. Kureti, *Appl. Catal. B Environ.*, 2008, **80**, 248–259.
127. S. Wagloehner and S. Kureti, *Appl. Catal. B Environ.*, 2012, **125**, 158–165.
128. E. Aneggi, C. de Leitenburg, G. Dolcetti and A. Trovarelli, *Catal. Today*, 2006, **114**, 40–47.
129. A. Alinezhadchamazketi, A. A. Khodadadi, Y. Mortazavi and A. Nemati, *J. Environ. Sci.*, 2013, **25**, 2498–2506.
130. F. E. López-Suárez, A. Bueno-López and M. J. Illán-Gómez., *Appl. Catal. B Environ.*, 2008, **84**, 651–658.
131. B. M. Reddy and K. N. Rao, *Catal. Commun.*, 2009, **10**, 1350–1353.
132. Q. Liang, X. Wu, D. Weng and Z. Lu, *Catal. Commun.*, 2008, **9**, 202–206.
133. A. Martínez-Arias, M. Fernández-García, O. Gálvez, J. M. Coronado, J. A. Anderson, J. C. Conesa, J. Soria and G. Munuera, *J. Catal.*, 2000, **195**, 207–216.
134. E. Aneggi, C. de Leitenburg, G. Dolcetti and A. Trovarelli, *Catal. Today*, 2008, **136**, 3–10.
135. H. Liang, S. Wu, Y. Hong, S. Li, Y. Chen, X. Yu and D. Ye, *Catal. Lett.*, 2014, **144**, 685–690.
136. R. Jiménez, X. García, C. Cellier, P. Ruiz and A. L. Gordon, *Appl. Catal. Gen.*, 2006, **297**, 125–134.
137. L. Sui, L. Yu and Y. Zhang, *J. Dispers. Sci. Technol.*, 2007, **28**, 607–612.
138. H. Shimokawa, Y. Kurihara, H. Kusaba, H. Einaga and Y. Teraoka, *Catal. Today*, 2012, **185**, 99–103.
139. A. Rinkenburger, T. Toriyama, K. Yasuda and R. Niessner, *ChemCatChem*, n/a-n/a.
140. Z. H. Zhu, G. Q. Lu and R. T. Yang, *J. Catal.*, 2000, **192**, 77–87.
141. M. A. Peralta, M. S. Zanuttini and C. A. Querini, *Appl. Catal. B Environ.*, 2011, **110**, 90–98.
142. R. Kimura, J. Wakabayashi, S. P. Elangovan, M. Ogura and T. Okubo, *J. Am. Chem. Soc.*, 2008, **130**, 12844–12845.
143. J. Gabb, Cardiff University, 2015.
144. M. Ogura, R. Kimura, H. Ushiyama, F. Nikaido, K. Yamashita and T. Okubo, *ChemCatChem*, 2014, **6**, 479–484.
145. P. Legutko, W. Kaspera, P. Stelmachowski, Z. Sojka and A. Kotarba, *Catal. Commun.*, 2014, **56**, 139–142.
146. L. Castoldi, R. Matarrese, L. Lietti and P. Forzatti, *Appl. Catal. B Environ.*, 2009, **90**, 278–285.
147. G. Pecchi, B. Cabrera, A. Buljan, E. J. Delgado, A. L. Gordon and R. Jimenez, *J. Alloys Compd.*, 2013, **551**, 255–261.

## **2. Experimental Techniques**

### **2.1 Introduction**

This chapter describes the experimental techniques used in this project. This includes the preparation methods and equipment used to prepare the various catalysts presented in this work, as well as the equipment and conditions used for the characterisation and testing of these catalysts.

The mixed metal oxide catalyst supports were prepared by a co-precipitation method.

The preparation of metal-supported oxides was achieved by the wet impregnation method.

Catalysts were characterised by X-ray Diffraction (XRD), Raman Spectroscopy, X-ray Photoelectron Spectroscopy (XPS), Surface Area Analysis (BET), and Temperature-programmed Reduction (TPR).

Catalysts were tested for soot oxidation activity using Thermogravimetric Analysis (TGA).

### **2.2 Catalyst Preparation**

A series of mixed metal oxide catalyst supports and metal-supported oxides were prepared in the methods described below. All chemical precursors used in the preparations of catalysts in this project are listed in table 2.1.

**Table 2.1** Precursor chemicals used in preparation of mixed metal oxide and metal-supported oxide catalysts

<b>Precursor</b>	<b>Source and purity</b>
<b>ammonium cerium nitrate, (NH<sub>4</sub>)<sub>2</sub>Ce(NO<sub>3</sub>)<sub>6</sub></b>	Sigma Aldrich, ≥98.5%
<b>aluminium nitrate nonahydrate, Al(NO<sub>3</sub>)<sub>3</sub>·9H<sub>2</sub>O</b>	Sigma Aldrich, ≥98%
<b>zirconyl oxynitrate hydrate, ZrO(NO<sub>3</sub>)<sub>2</sub>·xH<sub>2</sub>O</b>	Sigma Aldrich, 99%
<b>lanthanum nitrate hexahydrate, La(NO<sub>3</sub>)<sub>3</sub>·6H<sub>2</sub>O</b>	Sigma Aldrich, 99.9%
<b>praseodymium nitrate hexahydrate, Pr(NO<sub>3</sub>)<sub>3</sub>·6H<sub>2</sub>O</b>	Sigma Aldrich, 99.9%
<b>neodymium nitrate hexahydrate, Nd(NO<sub>3</sub>)<sub>3</sub>·6H<sub>2</sub>O</b>	Sigma Aldrich, 99.9%
<b>silver nitrate, AgNO<sub>3</sub></b>	Sigma Aldrich, 99.99%
<b>potassium carbonate, K<sub>2</sub>CO<sub>3</sub></b>	Fisher Scientific ≥99%
<b>copper nitrate hemi(pentahydrate), Cu(NO<sub>3</sub>)<sub>2</sub>·2.5H<sub>2</sub>O</b>	Sigma Aldrich, 99.99%
<b>manganese nitrate hydrate, Mn(NO<sub>3</sub>)<sub>2</sub>·xH<sub>2</sub>O</b>	Sigma Aldrich, 99.99%
<b>iron nitrate nonahydrate, Fe(NO<sub>3</sub>)<sub>3</sub>·9H<sub>2</sub>O</b>	Sigma Aldrich, 99.95%
<b>cobalt nitrate hexahydrate, Co(NO<sub>3</sub>)<sub>2</sub>·6H<sub>2</sub>O</b>	Sigma Aldrich, 99.99%
<b>nickel nitrate hexahydrate, Ni(NO<sub>3</sub>)<sub>2</sub>·6H<sub>2</sub>O</b>	Sigma Aldrich, 99.99%
<b>sodium carbonate, Na<sub>2</sub>CO<sub>3</sub></b>	Fisher Scientific ≥98.5%
<b>caesium carbonate, Cs<sub>2</sub>CO<sub>3</sub></b>	Fisher Scientific ≥99%

### 2.2.1 Catalyst Support Preparation – Co-precipitation (manual method)

Ceria-zirconia-alumina (CZA) catalyst supports were prepared by a co-precipitation method. 0.25M solutions of ammonium cerium nitrate, zirconyl oxynitrate hydrate, and aluminium nitrate nonahydrate were prepared. These solutions were then combined into a single 50 ml solution so that a Ce:Zr:Al molar ratio of 7:3:10 was achieved. 5 ml of the solution was placed in a 100 ml round bottomed flask and heated to 80 °C under constant magnetic stirring, at which point the precipitating agent, a 1 M solution of sodium carbonate, was added dropwise until a pH of 9 was reached. At this point the remaining nitrate precursor solution was added dropwise via pipette while the sodium carbonate solution was added via a dropping funnel, both at a rate that ensured that the pH was maintained at 9 and the temperature at 80 °C. Once the addition of the nitrate solution was completed, the suspension was allowed to age at 80 °C for 1 hour. The resulting precipitate was filtered and washed with 500 ml warm deionised water. This was then dried in at 110 °C for 16 hours. Finally, the dried solid was calcined under an atmosphere of static air by heating to 500 °C at 10 °Cmin<sup>-1</sup> and dwelling at the final temperature for 5 hours. For the purposes of testing the reproducibility of the method, 3 batches were prepared in an identical manner as described above.

### 2.2.2 Catalyst Support Preparation – Co-precipitation (automated method)

Several mixed metal oxide catalyst supports were prepared by co-precipitation similar to the method described above. However, a Metrohm 902 Titrando system was used for the addition of the nitrate precursor solution and carbonate precipitating agent. 0.25 M solutions of ammonium cerium nitrate, zirconyl oxynitrate hydrate, lanthanum nitrate hexahydrate, praseodymium nitrate hexahydrate, neodymium nitrate hexahydrate and aluminium nitrate nonahydrate were used as the nitrate precursor solutions. For each catalyst preparation, these solutions were mixed into a single 200 ml solution, according to the desired composition of metal oxides and their molar ratios, e.g. a catalyst support consisting of Ce:Zr:Al in a molar ratio of 7:3:10 would require a precursor solution containing 70 ml, 30 ml and 100 ml of 0.25 M solutions of ammonium cerium nitrate, zirconyl oxynitrate hydrate and aluminium nitrate nonahydrate respectively. 1 M solutions of sodium/potassium/caesium carbonate were used as the precipitating agents.

20 ml of the nitrate solution was added to a precipitation vessel and heated to 80 °C under constant mechanical stirring, the precipitating agent was then added until pH 9 was reached. The nitrate solution was then added at a rate of 3 ml min<sup>-1</sup> for 50 minutes, while the precipitating agent was added at an appropriate rate to maintain a pH of 9. Once the addition of the nitrate solution was completed, the suspension was allowed to age at 80 °C for 1 hour. The resulting precipitate was filtered and washed with various volumes of warm deionised water (specified below). This was then dried at 110 °C for 16 hours. Finally, the dried solid was calcined under various conditions described in further detail below.

### 2.2.2.1 Preparation of Ce-Zr-Al-O<sub>x</sub> catalyst supports, varying precipitating agent and washing

Ceria-zirconia-alumina catalyst supports were prepared in a Ce:Zr:Al molar ratio of 7:3:10 by the method described in 2.2.2. Each catalyst was calcined under static air at 500 °C at a heating rate of 10 °Cmin<sup>-1</sup>, dwelling at the final temperature for 5 hours. Table 2.2 summarises the catalyst supports prepared and indicates which conditions were altered between each preparation.

**Table 2.2** Summary of CZA 7:3:10 catalyst supports prepared by automated co-precipitation method

Catalyst Support	Precipitating agent	Washing (vol/litres)	Reference (section)
<b>Ce<sub>0.35</sub>Zr<sub>0.15</sub>Al<sub>0.5</sub>O<sub>1.75</sub></b>	Na <sub>2</sub> CO <sub>3</sub> (1M)	0.5	Auto-CZA (3.2)
			Na-CZA0.5L (3.3)
<b>Ce<sub>0.35</sub>Zr<sub>0.15</sub>Al<sub>0.5</sub>O<sub>1.75</sub></b>	Na <sub>2</sub> CO <sub>3</sub> (1M)	1.0	Na-CZA1.0L
<b>Ce<sub>0.35</sub>Zr<sub>0.15</sub>Al<sub>0.5</sub>O<sub>1.75</sub></b>	Na <sub>2</sub> CO <sub>3</sub> (1M)	1.5	Na-CZA1.5L
<b>Ce<sub>0.35</sub>Zr<sub>0.15</sub>Al<sub>0.5</sub>O<sub>1.75</sub></b>	Na <sub>2</sub> CO <sub>3</sub> (1M)	2.0	Na-CZA2.0L
<b>Ce<sub>0.35</sub>Zr<sub>0.15</sub>Al<sub>0.5</sub>O<sub>1.75</sub></b>	K <sub>2</sub> CO <sub>3</sub> (1M)	0.5	K-CZA0.5L
<b>Ce<sub>0.35</sub>Zr<sub>0.15</sub>Al<sub>0.5</sub>O<sub>1.75</sub></b>	K <sub>2</sub> CO <sub>3</sub> (1M)	2.0	K-CZA2.0L
<b>Ce<sub>0.35</sub>Zr<sub>0.15</sub>Al<sub>0.5</sub>O<sub>1.75</sub></b>	Cs <sub>2</sub> CO <sub>3</sub> (1M)	0.5	Cs-CZA0.5L*

\*The Cs-CZA0.5L catalyst was prepared by Takudzwa Bere using the above method<sup>1</sup>

### 2.2.2.2 Preparation of Ce-M-Al-O<sub>x</sub> catalyst supports

Ceria-zirconia-alumina, ceria-lanthana-zirconia-alumina, ceria-lanthana-alumina, ceria-praseodymium oxide-alumina and ceria-neodymium oxide-alumina catalyst supports were

prepared by the method described in 2.2.2. The precipitating agent used in each case was 1 M sodium carbonate, and washing also remained constant at 2.0 L warm deionised water during filtration. Table 2.3 summarises the catalyst supports prepared by the above method, and indicates which conditions were altered between each preparation.

**Table 2.3** Summary of Ce-M-Al catalyst supports prepared by automated co-precipitation method

<b>Catalyst Support</b>	<b>M</b>	<b>Molar ratio Ce:M:Al</b>	<b>Calcination conditions</b>	<b>Reference (section)</b>
<b>Ce<sub>0.35</sub>Zr<sub>0.15</sub>Al<sub>0.5</sub>O<sub>1.75</sub></b>	Zr	7:3:10	500°C, Static air	CZA 7:3:10
<b>Ce<sub>0.25</sub>Zr<sub>0.25</sub>Al<sub>0.5</sub>O<sub>1.75</sub></b>	Zr	5:5:10	500°C, Static air	CZA 5:5:10
<b>Ce<sub>0.15</sub>Zr<sub>0.35</sub>Al<sub>0.5</sub>O<sub>1.75</sub></b>	Zr	3:7:10	500°C, Static air	CZA 3:7:10
<b>Ce<sub>0.35</sub>La<sub>0.075</sub>Zr<sub>0.075</sub>Al<sub>0.5</sub>O<sub>1.71</sub></b>	La,Zr	7:1.5:1.5:10	500°C, Static air	CLZA 7:3:10
<b>Ce<sub>0.25</sub>La<sub>0.125</sub>Zr<sub>0.125</sub>Al<sub>0.5</sub>O<sub>1.69</sub></b>	La,Zr	5:2.5:2.5:10	500°C, Static air	CLZA 5:5:10
<b>Ce<sub>0.15</sub>La<sub>0.175</sub>Zr<sub>0.175</sub>Al<sub>0.5</sub>O<sub>1.66</sub></b>	La,Zr	3:3.5:3.5:10	500°C, Static air	CLZA 3:7:10
<b>Ce<sub>0.35</sub>La<sub>0.15</sub>Al<sub>0.5</sub>O<sub>1.68</sub></b>	La	7:3:10	500°C, Static air	CLA 7:3:10
<b>Ce<sub>0.25</sub>La<sub>0.25</sub>Al<sub>0.5</sub>O<sub>1.63</sub></b>	La	5:5:10	500°C, Static air	CLA 5:5:10
<b>Ce<sub>0.15</sub>La<sub>0.35</sub>Al<sub>0.5</sub>O<sub>1.58</sub></b>	La	3:7:10	500°C, Static air	CLA 3:7:10
<b>Ce<sub>0.35</sub>Pr<sub>0.15</sub>Al<sub>0.5</sub>O<sub>1.72</sub></b>	Pr	7:3:10	500°C, Static air	CPA 7:3:10
<b>Ce<sub>0.25</sub>Pr<sub>0.25</sub>Al<sub>0.5</sub>O<sub>1.71</sub></b>	Pr	5:5:10	500°C, Static air	CPA 5:5:10
<b>Ce<sub>0.15</sub>Pr<sub>0.35</sub>Al<sub>0.5</sub>O<sub>1.69</sub></b>	Pr	3:7:10	500°C, Static air	CPA 3:7:10
<b>Ce<sub>0.35</sub>Nd<sub>0.15</sub>Al<sub>0.5</sub>O<sub>1.68</sub></b>	Nd	7:3:10	500°C, Static air	CNA 7:3:10 (4.1, 4.6) CNA 500°C Static air (4.7)
<b>Ce<sub>0.25</sub>Nd<sub>0.25</sub>Al<sub>0.5</sub>O<sub>1.63</sub></b>	Nd	5:5:10	500°C, Static air	CNA 5:5:10
<b>Ce<sub>0.15</sub>Nd<sub>0.35</sub>Al<sub>0.5</sub>O<sub>1.58</sub></b>	Nd	3:7:10	500°C, Static air	CNA 3:7:10
<b>Ce<sub>0.35</sub>Nd<sub>0.15</sub>Al<sub>0.5</sub>O<sub>1.68</sub></b>	Nd	7:3:10	750°C, Static air	CNA 750°C Static air
<b>Ce<sub>0.35</sub>Nd<sub>0.15</sub>Al<sub>0.5</sub>O<sub>1.68</sub></b>	Nd	7:3:10	750°C, Flowing air	CNA 750°C Flowing air
<b>Ce<sub>0.35</sub>Nd<sub>0.15</sub>Al<sub>0.5</sub>O<sub>1.68</sub></b>	Nd	7:3:10	750°C, Flowing H <sub>2</sub>	CNA 750°C H <sub>2</sub> /Ar

## 2.2.3 Metal Supported Oxide Preparation – Wet Impregnation Method

### 2.2.3.1 Silver supported catalysts

A silver nitrate solution (2% - 0.047 g, 5% - 0.118 g for a 1.5 g catalyst) was impregnated onto the support (CZA 7:3:10) by heating to 80 °C under constant magnetic stirring, until a viscous suspension remained. This was then dried at 110 °C for 16 hours, and calcined by heating to 500 °C at a rate of 10 °Cmin<sup>-1</sup>, dwelling at the final temperature for 5 hours.

### 2.2.3.2 Potassium supported catalysts

A potassium carbonate solution (10% - 0.265 g for a 1.5 g catalyst) was impregnated onto the support (CZA 7:3:10) by the method described above, then dried and calcined also by the method described above.

### 2.2.3.3 Combined silver and potassium supported catalysts

A silver nitrate solution and potassium carbonate solution (2% - 0.047 g and 10% - 0.265 g respectively for 1.5 g catalyst) were impregnated onto the support (CZA/CLZA/CLA/CPA/CNA 7:3:10) by the method described above, then dried and calcined also by the method described above.

### 2.2.3.4 Comparison of transition metals on CZA support

Various transition metals Fe (0.543 g), Co (0.370 g), Ni (0.372 g), Cu (0.274 g), Ag (0.118 g) as nitrate solutions (5% for 1.5 g catalysts) were each impregnated onto a Ce-Zr-Al-O<sub>x</sub> support (CZA 7:3:10) by the method described above, then dried and calcined also by the method described above.

### 2.2.3.5 Copper supported catalysts

A copper nitrate solution (5% - 0.274 g copper for a 1.5 g catalyst) was impregnated onto the support (CZA/CLZA/CLA/CPA/CNA 7:3:10) by the method described above, then dried and calcined also by the method described above.

## 2.3 Catalyst Characterisation

### 2.3.1 X-Ray Diffraction (XRD)

X-ray diffraction (XRD) is a non-destructive technique which analyses the bulk crystal structure of a material. It can identify the crystalline phases of a material, as well as provide information on crystallite sizes.

#### 2.3.1.1 Principle

XRD is based on the detection of monochromatic X-ray radiation diffracted by the atoms or ions of a periodic lattice. In 1913, W.H. & W.L. Bragg explained that a crystal could be modelled as a set of discrete parallel planes separated by a constant spacing<sup>2</sup>. When X-ray radiation is directed at the surface plane, a portion will strike an atom/ion and be diffracted, and the rest will pass beyond, and subsequently be diffracted at a lower plane. When conditions satisfy Bragg's Law (equation 2.1), constructive interference can occur between the X-rays diffracted at different planes.

#### Equation 2.1

Where  $n$  is an integer,  $\lambda$  is the wavelength of the X-ray,  $d$  is the periodic spacing between planes,  $\theta$  is the angle of incident radiation.

Constructive interference occurs when X-rays are in phase with each other, i.e. the difference in path lengths between reflected X-rays is an integer of the wavelength. For a certain  $d$ -spacing, a corresponding angle of incident radiation,  $\theta$  will result in constructive interference. Figure 2.1 illustrates this.

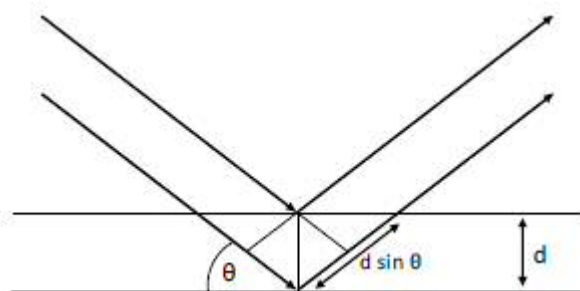


**Figure 2.1** X-ray diffraction pattern according to Bragg's Law. When  $2d\sin\theta$  (the difference in path lengths between both rays) is equal to an integer of the wavelength, constructive interference occurs



The greater the number of regularly spaced planes in the lattice of a structure, the greater the constructive interference between reflected X-rays at a certain angle. This results in a greater intensity of detection by the instrument. At angles where radiation is out of phase, destructive interference is said to occur, and thus is not detected<sup>3</sup>. A diffractogram plots the response of the detector against the angle of incident radiation. Crystalline phases can be identified by their distinctive diffractogram pattern<sup>4</sup>.

Crystallite sizes can also be determined by XRD diffractograms. The Scherrer equation (equation 2.2) relates particle size with the broadening of peak width in a diffraction pattern<sup>5</sup>.

---

**Equation 2.2**

Where  $L$  is a measure of particle size,  $\lambda$  is the wavelength of the X-ray,  $\beta$  is the line width at half the maximum intensity (FWHM),  $\theta$  is the peak position,  $K$  is a constant called the shape factor, usually taken to be 1.

#### *2.3.1.2 Experimental*

XRD analysis was performed on a PANalytical X'PERT Pro diffractometer using a CuK $\alpha$  radiation source operating at 40 KeV and 40 mA. Each sample was run for 1 hour,  $2\theta$  ranged from 10-80°. PANalytical HighScore Plus was used for the analysis of the data and spectra. The JCPDS database was used as a reference for identification of crystalline phases. Crystallite sizes were calculated by the Scherrer equation.

### **2.3.2 Raman Spectroscopy**

Raman is a spectroscopic technique which probes the vibrational, rotational and other low frequency modes of chemical bonds within a material. It is used as a bulk characterisation technique and can be used to complement the findings of XRD.

#### *2.3.2.1 Principle*

When a substance is illuminated, the molecular vibrations absorb photons and are excited to a higher energy state, photons are subsequently emitted and the vibrations return to a lower

energy state. This is referred to as scattering, and is the principle on which Raman spectroscopy is based. There are three possible outcomes to this scattering, illustrated in figure 2.2.

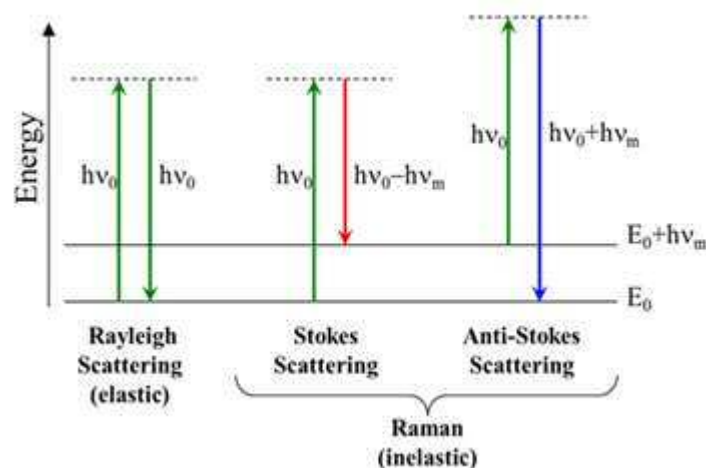


**Figure 2.2** Diagram of vibrational energy states, illustrating possible scattering outcomes

When the energy of the emitted photon is the same as the incident photon, the vibration returns to its initial energy state and this is referred to as elastic scattering (Rayleigh scattering). When the energy of the emitted photon is different from the incident photon, the energy level of the vibrational state is different to its initial state and an inelastic scattering is said to occur, referred to as Stokes and Anti-Stokes scattering. Stokes scattering is when the emitted photon is of higher energy to the incident photon, and Anti-Stokes scattering is when the emitted photon is of lower energy. The Rayleigh scattering does not provide information regarding the sample, since its energy is unchanged from the incident radiation. However the Stokes and Anti-Stokes scatterings are distinctive to particular vibrational and rotational modes, which themselves are distinctive to certain compounds, and so can be used to identify the structure of a sample<sup>5</sup>.

### 2.3.2.2 Experimental

Raman spectroscopy analysis was performed on a Renishaw inVia Microscope, using a Spectra physics green argon laser of wavelength 514 nm and power of 20 mW.

### 2.3.3 X-ray Photoelectron Spectroscopy (XPS)

X-ray photoelectron spectroscopy is another non-destructive analysis technique. It is a surface-sensitive characterisation method, which provides information on the elemental composition of a material surface, as well as the oxidation states of those elements. It is therefore a useful tool for analysing heterogeneous catalysts, since surface species play a significant role in catalyst/reactant interactions.

#### 2.3.3.1 Principle

XPS works on the principle that when a sample is irradiated by monochromatic X-rays under ultra-high vacuum, it emits photoelectrons from core energy levels of atoms. XPS is a surface-sensitive technique, as emitted photoelectrons from below the surface of the sample will interact with atoms and ions from the material before they can escape into the vacuum<sup>5</sup>. The binding energy ( $E_{binding}$ ) of an atom can be calculated based on the known energy of the irradiating X-rays, using equation 2.3.

$$E_{binding} = E_{photon} - (E_{kinetic} + \phi)$$

Equation 2.3

Where  $E_{photon}$  is the energy of the incident X-rays,  $E_{kinetic}$  is the kinetic energy of the emitted photoelectron,  $\phi$  is the work function of the spectrometer, which is the minimum energy required to remove an electron from the highest (Fermi) energy level to a state at rest in the vacuum.

Atoms of a particular element in a particular oxidation state have a distinctive binding energy, which can be used to identify them<sup>5</sup>.

An XPS spectra plots the intensity (the number of electron counts) against binding energy, providing identification and quantification of elements in their oxidation states.

#### 2.3.3.2 Experimental

XPS was performed on a Kratos Axis Ultra-DLD photoelectron spectrometer, with an aluminium monochromatic source and a dual Al/Mg achromatic source. Spectra were calibrated to the C(1s) line of adventitious carbon at a binding energy of 284.7 eV. Spectra were analysed using CasaXPS.

### 2.3.4 Brunauer Emmet Teller Surface Area Analysis (BET)

BET surface area analysis is a technique used to determine the specific surface area (surface area per unit mass) of a material. As with XPS, this is a useful technique for analysing heterogeneous catalysts, as there is often a correlation between surface area and catalyst activity.

#### 2.3.4.1 Principle

The Brunauer-Emmet-Teller theory describes the adsorption of inert gas molecules on the surface of a solid material<sup>6</sup>. It can be considered an extension of the Langmuir theory, which describes the surface of a material as a series of individual adsorption sites, each able to bind to an adsorbate<sup>7</sup>. In the BET model, at a certain partial pressure the gas molecules are adsorbed onto these sites, forming layers on top of each other. At a constant temperature, a material surrounded by a gas will adsorb a certain amount of gas molecules, depending on the vapour pressure of the gas, and proportional to its surface area. The BET equation (2.4) can be used to calculate the volume of the surface monolayer<sup>8</sup>.

$$\frac{v}{v_m} = \frac{cP}{(P_0 - P) \left( 1 + \frac{c-1}{c} \frac{P}{P_0} \right)}$$

Equation 2.4 BET equation

Where  $v$  is the volume of gas adsorbed,  $v_m$  is the volume of the surface monolayer,  $P$  is the applied pressure,  $P_0$  is the saturation vapour pressure,  $c$  is the BET constant, a measure of enthalpy.

If the molar volume of adsorbate gas is known then the specific surface area of the sample can be calculated through equation 2.5 and 2.6

Equation 2.5

Where  $S_{total}$  is the surface area of the sample,  $v_m$  is the volume of the surface monolayer,  $N$  is Avogadro's number,  $s$  is the adsorption cross-section of the adsorbing species,  $V$  is the molar volume of the adsorbate gas.

---

**Equation 2.6**

Where  $S_{BET}$  is the specific surface area and  $\alpha$  is the mass of the sample.

Specific surface area is measured in units of  $m^2g^{-1}$

#### *2.3.4.2 Experimental*

Surface area analysis was carried out using a Micromeritics Gemini 2360 instrument, using a 5 point BET measurement. Analysis on the samples (100 mg) was performed at 77 K, using liquid nitrogen to cool the sample, after an initial degassing at 120 °C for 1 hour using  $N_2$ . Evacuation time was 1 minute and equilibrium time 10 seconds. Data analysis was performed using StarDriver software. In order to determine the experimental error, each sample was analysed three times and an average was taken of the two closest values. Due to the limitations of the technique, the surface area values are expressed to the nearest integer.

#### **2.3.5 Temperature-Programmed Reduction (TPR)**

Temperature-programmed reduction is a technique used to analyse the redox properties of a material. Specifically in this case, the reducibility of a material with increasing temperature. This is a useful technique in the context of catalysis, since the redox properties of a material can be crucial in determining its ability to interact with other species.

##### *2.3.5.1 Principle*

Temperature-programmed reduction works by measuring changes to the concentration of  $H_2$  in an inert carrier gas after it has been passed over a sample at increasing temperature. During the reduction of metal oxides,  $H_2$  undergoes dissociative adsorption on the surface of a particle resulting in a reduction of the metal. If rapid adsorption of  $H_2$  takes place, then the surface of the particle becomes a shell of reduced metal. Oxygen ions are removed by the inward diffusion of hydrogen atoms from the metal/metal oxide interface (forming hydroxyl species) and the outward diffusion of oxygen ions from the metal oxide to the metal/gas interface. The reduced metal shell therefore grows inwards, while the inner core metal oxide gradually shrinks, causing the metal/metal oxide interface (as well as the reaction rate,  $\alpha$ ) to

decrease. This is known as the shrinking core or contracting sphere model, and is illustrated in figure 2.3 a). An alternative model is the nucleation model (figure 2.3 b)). If the adsorption of  $H_2$  is slow, then the inward diffusion of hydrogen and the outward diffusion of oxygen ions begins to occur before the entire surface of the particle has been reduced. In this case the metal/metal oxide interface increases in size as the reaction takes place, resulting in the reaction rate increasing until eventually the model resembles the contracting sphere model, and the rate subsequently decreases<sup>9</sup>.

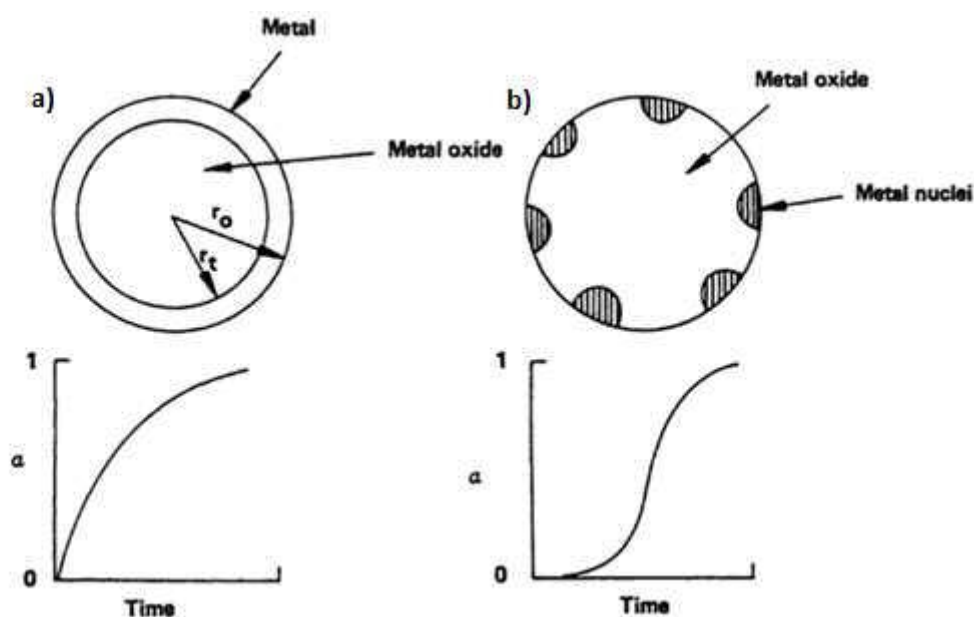


**Figure 2.3** Diagram of metal oxide reduction by a) contracting sphere model and b) nucleation model, and their corresponding reaction rates  $\alpha$ , over time<sup>9</sup>

The more reducible a sample, the greater the amount of  $H_2$  that will undergo dissociative adsorption, and so changes to the concentration of  $H_2$  in the gas stream are an indication of the reducibility of the sample over time. Changes to the concentration of  $H_2$  in the carrier gas causes changes to its thermal conductivity, and so can be detected by a thermal conductivity detector (TCD). A TPR profile plots the relative intensity of  $H_2$  consumption over time.

### 2.3.5.2 Experimental

TPR analysis was performed on a Thermo TPD/R/O 1100 Series. The sample (0.05 g) was heated from 30-900 °C at a rate of 10 °C min<sup>-1</sup> under a 20 ml min<sup>-1</sup> flow of 10% $H_2$ /Ar. The experiment was repeated for each catalyst to ensure the peak reduction temperature was within an error of  $\pm 5$  °C. When comparing temperatures between catalysts, differences of less than 10 °C were not considered significant.

## 2.4 Catalyst Testing – Thermogravimetric Analysis (TGA)

Soot oxidation activity was tested using thermogravimetric analysis on a Setaram Labsys TG-DTA/DSC instrument, shown in figure 2.4. A catalyst/soot ratio of 10:3 by mass was used in each case. 20 mg of catalyst and 6 mg of soot were mixed and placed in a crucible. In order to test thermal stability, catalyst samples were retrieved and mixed with fresh soot and the test repeated. In this case, the mass of soot used was dependent on the mass of catalyst that could be retrieved, abiding by the 10:3 ratio.



**Figure 2.4** Setaram Labsys TG-DTA/DSC used for soot oxidation testing

Catalysts were generally mixed by the “loose contact” method (catalyst and soot mixed by shaking and stirring with a spatula – low contact area), however some tests were carried out with catalyst and soot mixed by the “tight contact” method (compressed and mixed using pestle and mortar – high contact area). The two methods are known to give significantly different results, due to the difference in contact area<sup>10</sup>. While tight contact provides better reproducibility of results<sup>11</sup>, loose contact provides a better model for the contact between catalyst and soot in a particulate filter<sup>12,13</sup>.

Samples were heated from 30 °C to 900 °C at 5 °C min<sup>-1</sup>, typically under and atmosphere of flowing air. Major loss of mass in the sample during a test was attributed to oxidation of soot.

Setsoft software was used to collect TGA data. The derivative of the TG plot was used to determine the extrapolated onset, peak and final temperature of soot oxidation for each test. Each catalyst was tested for soot oxidation on at least two occasions, or until the peak and extrapolated onset temperatures (the most reliable measurements) were consistent to within  $\pm 5$  °C. As in the case of TPR; when comparing soot oxidation temperatures between catalysts, differences of less than 10 °C were not considered significant.

## 2.5 References

1. T. Bere, Cardiff University, 2016.
2. W. H. Bragg and W. L. Bragg, *Proc. R. Soc. Lond. Ser. Contain. Pap. Math. Phys. Character*, 1913, 88, 428–438.
3. S. B. Duckett and B. C. Gilbert, *Foundations of Spectroscopy*, Oxford University Press, Incorporated, 2000.
4. J. P. Glusker and K. N. Trueblood, *Crystal Structure Analysis: A Primer*, Oxford University Press, 2010.
5. J. W. Niemantsverdriet, *Spectroscopy in Catalysis*, John Wiley & Sons, 2007.
6. S. Brunauer, P. H. Emmett and E. Teller, *J. Am. Chem. Soc.*, 1938, 60, 309–319.
7. I. Langmuir, *J. Am. Chem. Soc.*, 1918, 40, 1361–1403.
8. G. C. Bond, *Heterogeneous Catalysis: Principles and Applications*, Oxford University Press, Oxford Oxfordshire ; New York, 2nd Revised edition edition., 1987.
9. A. Jones, *Temperature-Programmed Reduction for Solid Materials Characterization*, CRC Press, 1986.
10. J. P. A. Neeft, M. Makkee and J. A. Moulijn, *Fuel*, 1998, 77, 111–119.
11. M. A. Peralta, M. S. Gross, B. S. Sánchez and C. A. Querini, *Chem. Eng. J.*, 2009, 152, 234–241.
12. J. P. A. Neeft, O. P. van Pruissen, M. Makkee and J. A. Moulijn, *Appl. Catal. B Environ.*, 1997, 12, 21–31.
13. B. A. A. L. van Setten, J. M. Schouten, M. Makkee and J. A. Moulijn, *Appl. Catal. B Environ.*, 2000, 28, 253–257.



### 3. Study into reproducibility of CZA supports and effects of altering the co-precipitation method

In this chapter,  $\text{CeO}_2\text{-ZrO}_2\text{-Al}_2\text{O}_3$  (CZA) mixed metal oxide catalysts were prepared by the co-precipitation method. As described in Chapter 1, it has been extensively reported that ceria is an active soot oxidation catalyst due to its redox properties, which allow it to store and release oxygen depending on the surrounding conditions. These properties are improved by the introduction of zirconia into its lattice, which also provide greater thermal stability<sup>1-6</sup>. Incorporation of alumina has shown to increase surface area as well improve the thermal stability of ceria and ceria-zirconia catalysts without lowering catalytic activity<sup>7</sup>. Co-precipitation is a popular method of catalyst preparation, and there are numerous examples of its usage in the formation of ceria-zirconia catalysts for various purposes, including soot oxidation<sup>8-12</sup>. In the first instance, the preparation conditions were those of the best performing CZA catalyst from a previous project conducted at Cardiff University<sup>13</sup>. This specified a catalyst with a Ce:Zr:Al molar ratio of 7:3:10, and was used as the benchmark by which to compare the activity of the initial CZA catalysts. Certain characterisation techniques and soot oxidation testing found that there were discrepancies between batches of catalyst, and so an automated system was used in order to standardise the preparation method for future studies. The CZA catalysts prepared by this method were found to have much higher activity, which was explained by the increased concentration of sodium compounds, by-products of the preparation method that proved difficult to remove. This led to an investigation into the effects of sodium carbonate in the preparation method, first by attempting to remove it by increasing washing during filtration, and later by replacing it with alternative alkali-metal carbonates,  $\text{K}_2\text{CO}_3$  and  $\text{Cs}_2\text{CO}_3$ .

### 3.1 Manual co-precipitation of $\text{Ce}_{0.35}\text{Zr}_{0.15}\text{Al}_{0.5}\text{O}_{1.75}$ supports

In this section, 3 ceria-zirconia-alumina mixed metal oxide catalysts were prepared in a 7:3:10 molar ratio by a 'manual' co-precipitation method as described in 2.2.1. The catalysts in this section are referred to as CZA1, CZA2 and CZA3.

#### 3.1.1 Characterisation

Figure 3.1 shows the XRD patterns for the CZA catalysts prepared by the 'manual' co-precipitation method.

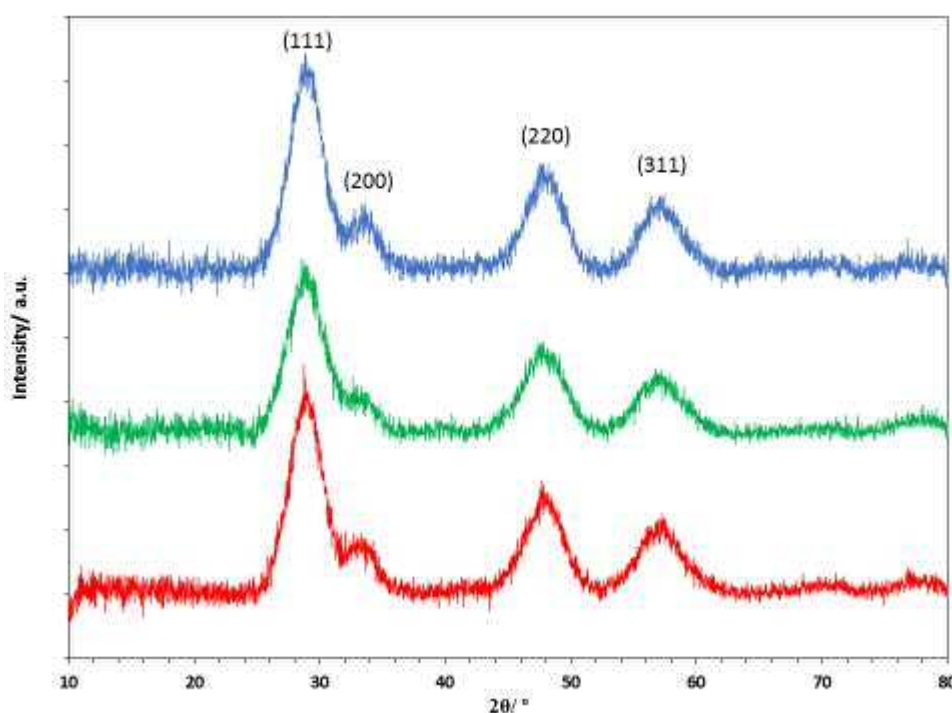


**Figure 3.1** X-ray diffractograms of CZA1 (blue), CZA2 (green) and CZA3 (red)

The reflections at around  $2\theta = 29^\circ$ ,  $33^\circ$ ,  $48^\circ$  and  $57^\circ$  are typical of a fluorite structured material with an fcc cell corresponding to the (111), (200), (220) and (311) planes respectively, and indicated the presence of  $\text{CeO}_2$ <sup>14</sup> (JCPDS card no. 071-4199). The lack of any other crystalline phases suggested that  $\text{ZrO}_2$  and  $\text{Al}_2\text{O}_3$  had been incorporated into the ceria lattice, and that homogenous  $\text{CeO}_2\text{-ZrO}_2\text{-Al}_2\text{O}_3$  materials had been produced in each case. As shown in table 3.1, the peak positions of the CZA materials each showed a shift to higher  $2\theta$  than the reference for pure ceria. This indicated a contraction to the ceria lattice due to the smaller

ionic radius of  $Zr^{4+}$  ions as compared to  $Ce^{4+}$  ions<sup>1</sup>. The crystallite sizes were calculated by the Scherrer equation from the most intense reflection, and were comparable between batches.

**Table 3.1** Peak positions and crystallite sizes of CMA catalysts determined by XRD

Catalyst	2 theta (°)				Crystallite size (nm)
	(111)	(200)	(220)	(311)	
Ceria*	28.5	33.1	47.5	56.3	-
CZA1	28.8	33.3	47.9	57.1	2.7
CZA2	28.9	33.3	47.7	57.1	2.5
CZA3	28.9	33.3	47.8	57.1	2.5

\*2 theta values of ceria referenced from JCPDS database (card no. 071-4199)

Raman spectroscopy is also a useful technique in characterising ceria-based materials, as the cubic fluorite structure of ceria in the  $Fm\bar{3}m$  space group has only one allowed Raman active mode ( $F_{2g}$ ) caused by the symmetric O-Ce-O stretching mode<sup>15,16</sup>. This produces a band reported to be centred at  $460\text{cm}^{-1}$ <sup>17,18</sup>. Raman spectroscopy was used in order to complement the findings of XRD and the spectra for CZA1, 2 and 3 are displayed in figure 3.2.

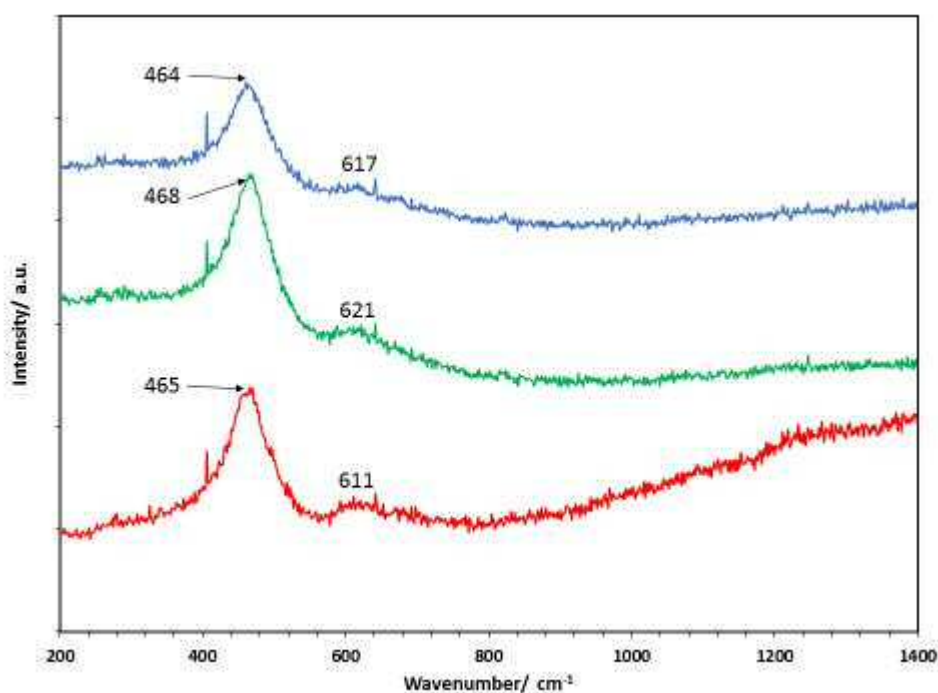


**Figure 3.2** Raman spectra of CZA1 (blue), CZA2 (green) and CZA3 (red)

The spectra for CZA1, 2 and 3 showed peaks at  $464\text{ cm}^{-1}$ ,  $468\text{ cm}^{-1}$  and  $465\text{ cm}^{-1}$  respectively, representing the  $F_{2g}$  Raman-active mode. In each case the peak was shifted to a slightly higher frequency than for pure  $\text{CeO}_2$ , which provided evidence of a decrease in the lattice parameter of ceria due to the incorporation of  $\text{Zr}^{4+}$  ions<sup>17,18</sup>. The broad peak at  $600\text{--}620\text{ cm}^{-1}$  can be attributed to non-degenerate Raman inactive longitudinal optical mode of ceria which occurs due to distortion of ceria symmetry, likely caused by oxygen vacancies within the ceria lattice<sup>18</sup>. These vacancies favour oxygen mobility within the structure, which is thought to lead to an improvement in soot oxidation activity<sup>19</sup>.

Temperature-programmed reduction analysis (TPR) was carried out on the CZA supports to determine their reducibility. The ability of cerium to undergo facile reduction is thought to be key to its properties as a soot oxidation catalyst<sup>3</sup>. The reduction of  $\text{Ce}^{4+}$  to  $\text{Ce}^{3+}$  allows the release of oxygen from the ceria lattice, allowing it to be readily available for soot oxidation<sup>1</sup>.

The TPR profiles shown in figure 3.3 provided a stark indication that the materials produced by the co-precipitation method were inconsistent. Ceria typically provides a bimodal TPR profile, with a sharp peak representing the reduction of surface  $\text{Ce}^{4+}$  to  $\text{Ce}^{3+}$  at around  $425\text{ }^\circ\text{C}$ , and a broad peak above  $800\text{ }^\circ\text{C}$  representing the reduction of cerium ions from within the bulk structure<sup>20,21</sup>. However, this pattern was not observed with the CZA materials prepared here.

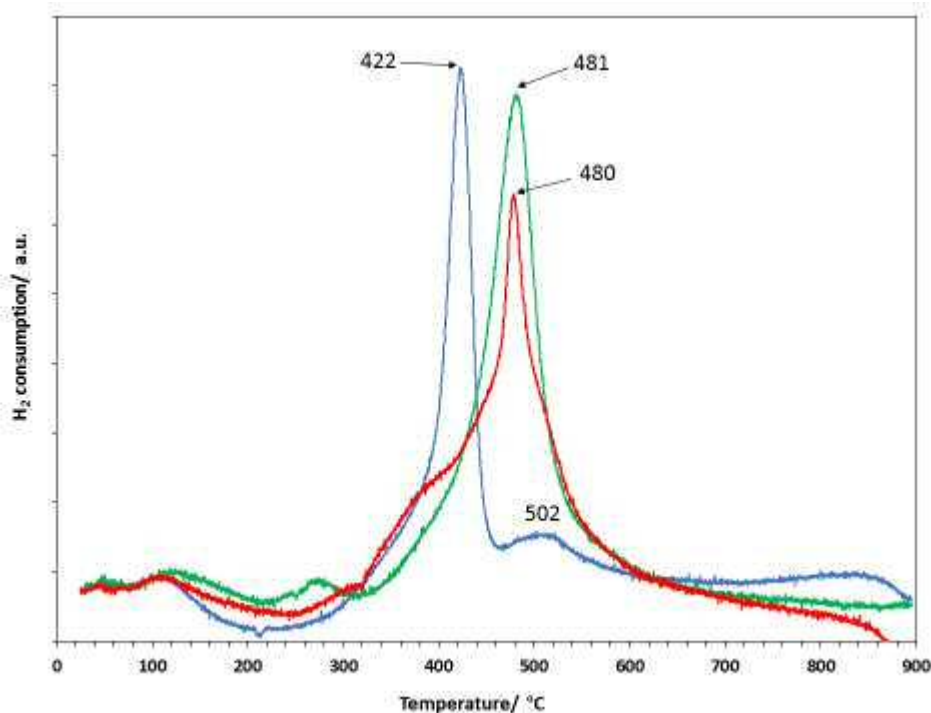


**Figure 3.3** TPR profiles of CZA1 (blue), CZA2 (green) and CZA3 (red)

The TPR profile of CZA1 showed a sharp peak at 422 °C typical of surface cerium reduction. Another smaller peak centred at 502 °C was also observed. This peak is at too low a temperature and not sufficiently broad to be identified as bulk cerium reduction. The surface reduction peaks of both CZA2 and CZA3 were at considerably higher temperatures, both peaking at around 480°C, however a shoulder could be observed on the CZA3 peak in the 310-410 °C region. The disparity between reduction profiles indicated that reduction of surface cerium was not uniform between batches, and the presence of shoulder peaks in temperature ranges not untypical of surface cerium reduction (in the cases of CZA1 and CZA3) could even suggest that there was lack of uniformity within the same batch.

**Table 3.2** BET surface areas of ‘manual’ CZA supports

<b>Catalyst</b>	<b>Surface area (m<sup>2</sup>g<sup>-1</sup>)</b>
<b>CZA1</b>	<b>180 (±1)</b>
<b>CZA2</b>	<b>173 (±5)</b>
<b>CZA3</b>	<b>215 (±5)</b>

Table 3.2 shows the surface areas of the CZA materials obtained by BET analysis. It was observed that the surface area of CZA3 was significantly higher than those of CZA1 and CZA2. The surface areas provided further evidence that the materials produced by the co-precipitation method were inconsistent.

### 3.1.2 Soot oxidation testing

Thermogravimetric analysis (TGA) was used to test the activity of the catalysts for soot oxidation. TGA is a useful tool as it measures changes in the mass of a sample as a function of temperature. In the case of a soot sample, a decrease in mass is attributed to the conversion of the solid carbonaceous species into gaseous  $\text{CO}/\text{CO}_2$ , i.e. soot oxidation. Figure 3.4 demonstrates a typical thermogravimetric (TG) plot and corresponding derivative (dTG) plot, in this case of a 6 mg sample of diesel soot heated from 30 to 900 °C at 5 °Cmin<sup>-1</sup> under flowing air.

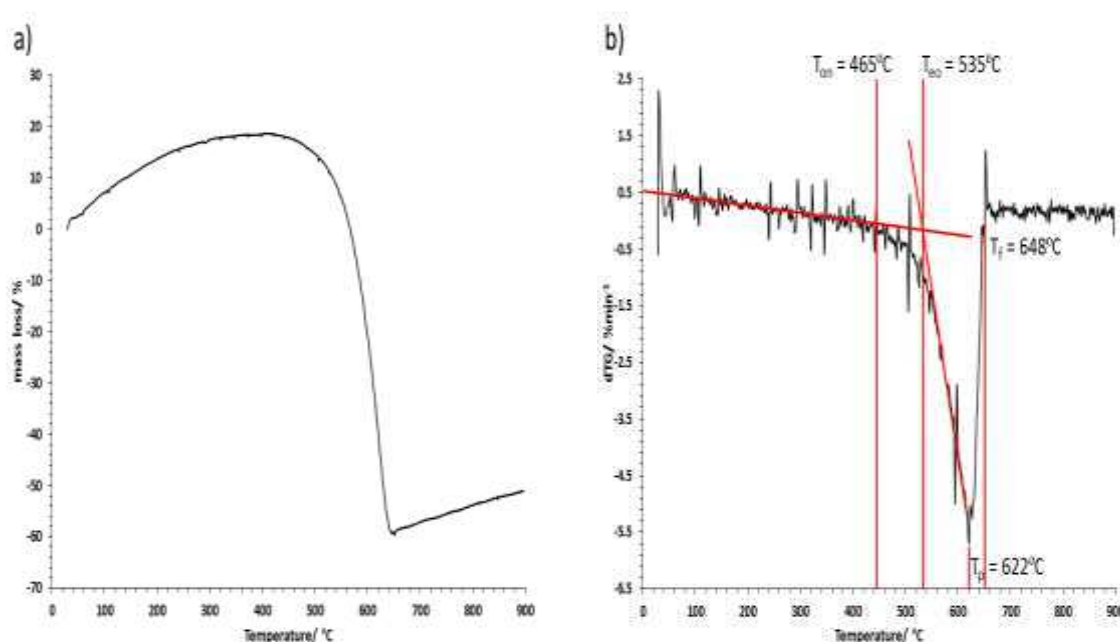


**Figure 3.4** a) TG plot of 6mg diesel soot sample, and b) derivative of same plot – demonstrating the positions of the onset, extrapolated onset, peak and final temperatures

The plots demonstrate that the oxidation of soot does not occur at one specific temperature but rather proceeds over a range temperatures. As shown in figure 3.4b), the derivative plot provides a curve from which the key points of the soot oxidation process can be obtained, namely the temperature at which soot oxidation begins, is at its maximum rate, and when it is completed. These markers are known as the onset temperature ( $T_{on}$ ), peak temperature ( $T_p$ ), and final temperature ( $T_f$ ) of soot oxidation. The sensitivity of the instrumentation means that small external disturbances can cause the dTG plot to be noisy, and can often make it difficult to determine an accurate onset temperature. Therefore a fourth measurement, the extrapolated onset temperature ( $T_{eo}$ ) can be used as a more accurate comparison. As shown

in the derivative plot, this is obtained by calculating the intersect point between the steepest gradient of the curve and the baseline. In this work, when comparing activity between catalysts, primacy is given to the peak temperature, since this is the temperature at which the catalyst is deemed to be operating at its maximum effectiveness. The dTG plots provide a better visual comparison between samples than the corresponding TG plots, and therefore are presented in this work. The original TG plots can be found in the appendix.

Thermogravimetric measurements can also be affected by a phenomenon known as the 'buoyancy effect', which can cause an apparent increase in a sample weight, due to convection currents occurring as the temperature of the gas surrounding the sample increases<sup>22</sup>. This phenomenon can be seen in figure 3.4a), as an increase in weight of almost 20% is observed prior to the onset of soot oxidation, making the baseline difficult to determine. However since the effect is linear the dTG plot can take this into account, and a baseline can still be established, albeit non-perpendicular to the y-axis.

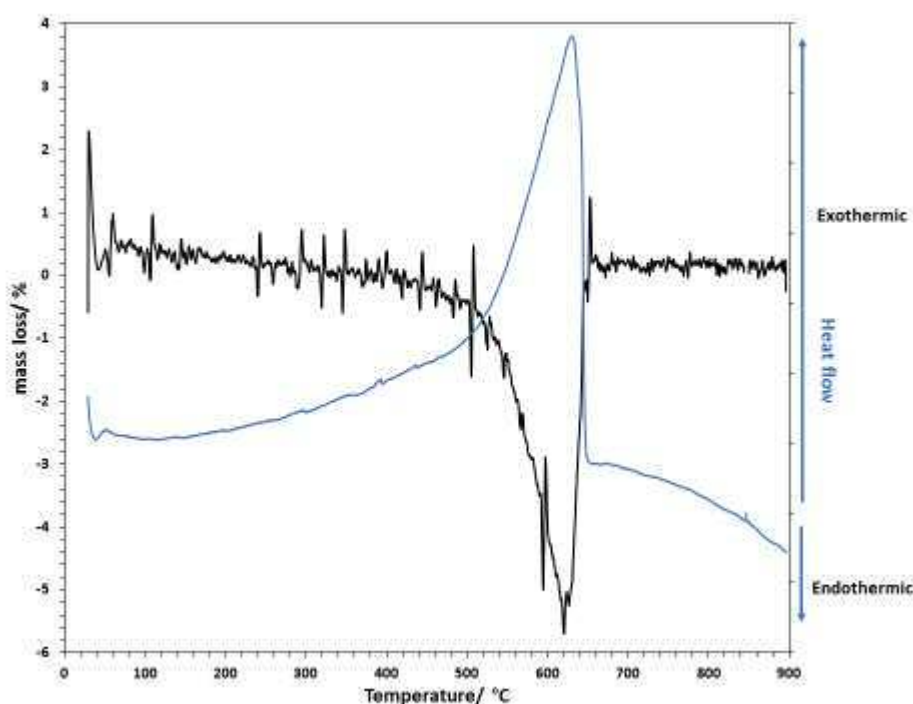


**Figure 3.5** dTG plot (black) and heat flow (blue) of 6mg diesel soot sample against temperature

The same equipment can be used to obtain differential thermal analysis (DTA) plots, which display the heat flow of the sample against the temperature of the furnace. Figure 3.5 shows the heat flow plot of the same soot sample, superimposed over the dTG plot for comparison.

The increase in heat flow corresponds to the loss of mass due to soot oxidation, demonstrating that soot oxidation is an exothermic process.

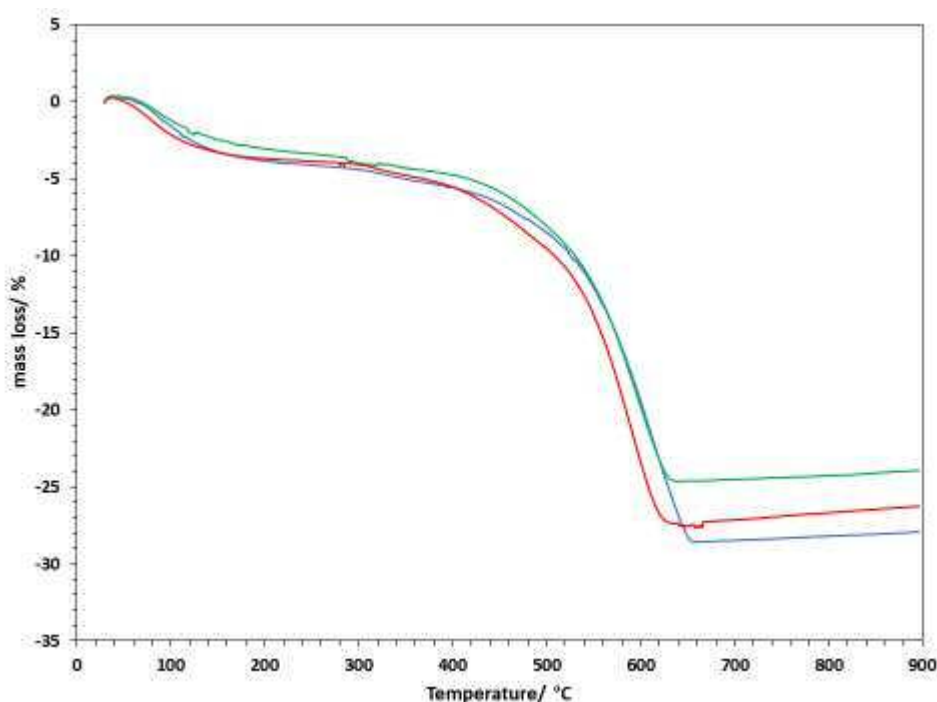


**Figure 3.6** TGA plots of catalyst/soot mixtures containing: CZA1 (blue), CZA2 (green) and CZA3 (red)

The CZA catalysts were tested for soot oxidation by running samples of catalyst/soot mixtures in a 10:3 ratio by mass through TGA analysis. Figure 3.6 shows the percentage mass loss of these mixtures as a function of temperature, from 30-900 °C. The initial loss of mass observed up to around 100 °C was attributed to the removal of surface water adsorbed on the surface of the catalyst. The remaining loss of mass accounted for between 20-25% of the total mass of the sample, in rough agreement with the 10:3 ratio (~23.1%) and so, along with the physical lack of soot observed in the sample post-analysis, this could reasonably be attributed to the complete oxidation of soot.

The derivative plots shown in figure 3.7 (offset by 1 %min<sup>-1</sup> for comparison) were able to provide further insight into the catalysed soot oxidation process, and the soot oxidation temperatures shown in table 3.3 were established from these plots, those for uncatalysed soot are also included for comparison. Also included for comparison are the soot oxidation temperatures of the benchmark CZA 7:3:10 catalyst previously prepared at Cardiff University<sup>13</sup>.



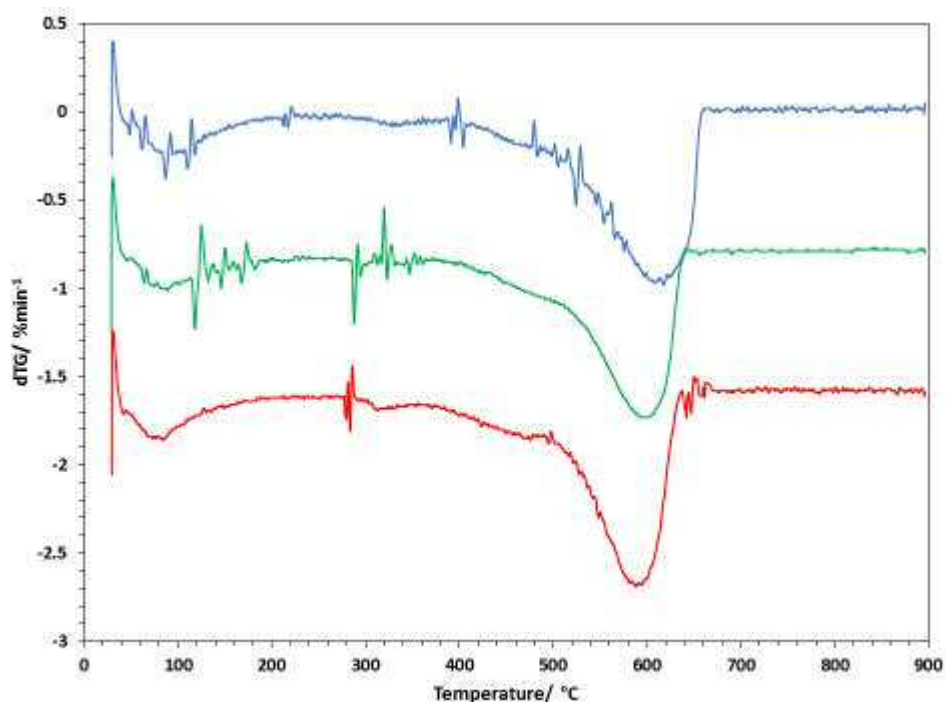


**Figure 3.7** dTG plots of catalyst/soot mixtures containing: CZA1 (blue), CZA2 (green) and CZA3 (red), offset for comparison

In summary, the CZA catalysts all showed activity for soot oxidation by lowering several of the key temperature markers. In each case the onset of soot oxidation occurred at or below 400 °C, a significant decrease in temperature compared to uncatalysed soot oxidation. Each of the CZA catalysts were also able to decrease both the extrapolated onset and peak soot oxidation temperatures. Complete soot oxidation was achieved at a lower temperature with both CZA2 and CZA3. The least successful catalyst was observed to be CZA1, as the onset, peak and final soot oxidation temperatures were significantly higher than with the other catalysts.

**Table 3.3** Soot oxidation temperatures of samples mixed with CZA catalysts

Catalyst	$T_{on}$ (°C)	$T_{eo}$ (°C)	$T_p$ (°C)	$T_f$ (°C)
<b>Soot (no catalyst)</b>	465	535	<b>622</b>	648
<b>Benchmark CZA</b>	407*	507*	<b>597*</b>	634*
<b>CZA1</b>	400	491	<b>608</b>	658
<b>CZA2</b>	383	499	<b>592</b>	640
<b>CZA3</b>	370	498	<b>588</b>	635

\* Values taken from R. Ramdas, Cardiff University<sup>13</sup>

Table 3.3 shows that the catalysed reactions caused a greater decrease in the initial onset temperature than the other temperature markers. This was most pronounced in the case of CZA3, where the onset temperature of soot oxidation decreased by 95 °C, whereas it only lowered the extrapolated onset, peak, and final temperatures by 37 °C, 34 °C and 13 °C respectively. The shape of the dTG profiles appeared to show a shoulder to the main soot oxidation peak – again, most pronounced with CZA3. This may be evidence that two separate processes were occurring. The first caused a slow rate of soot oxidation, not previously seen in the uncatalysed reaction, and the second, a more rapid soot oxidation process, comparable to the one in the uncatalysed reaction, but at a slightly lower temperature.

The temperature range over which this initial soot oxidation took place was between 370-500 °C (at which point it was usurped by the major soot oxidation peak), this is in rough agreement with the reduction peaks of the catalysts observed in the TPR shown in figure 3.3, which is evidence that the reduction of cerium and subsequent release of lattice oxygen was responsible. This mass loss could be explained by the oxidation of soot particles in close contact with the surface of the catalysts. Previous studies have shown that under tight contact conditions, the oxidation of the hydrocarbon fraction of the soot can be catalysed at a lower temperature than the majority carbon fraction<sup>23</sup>. The remaining soot was then oxidised at the higher temperature by atmospheric oxygen as in the uncatalysed reaction, the slightly lower temperature could be attributed to the initiation of soot oxidation and the exotherm it produced by the catalysed soot oxidation.

The catalysts showed similar soot oxidation temperatures to the benchmark catalyst, indicating that the preparation method had been successfully replicated.

### **3.2 Automated co-precipitation of $\text{Ce}_{0.35}\text{Zr}_{0.15}\text{Al}_{0.5}\text{O}_{1.75}$ supports – comparison with manually prepared supports**

The co-precipitation method employed in the preparation of the CZA catalysts was deemed to be the cause of the discrepancies observed between batches, in particular their reduction profiles and soot oxidation activities. The requirement to maintain constant pH and temperature by varying the rates of both nitrate and carbonate reagents manually meant that

inconsistencies in the rates of addition were inevitable between batches. In order to eradicate these inconsistencies and ensure that all future co-precipitated materials were reproducible, it was decided to standardise the preparation method by using an autotitrator to control the rates of addition of the reagents and to monitor more precisely the pH throughout.

This section compares the CZA material prepared by the standardised autotitrator method described in section 2.2.2.1 (referred to as 'auto-CZA') with those of the 'manual' co-precipitation CZA materials presented in the section above.

### 3.2.1 Characterisation

Figure 3.8 again shows the XRD patterns of the 'manual'-CZA materials, as well as that of the 'auto'-CZA.

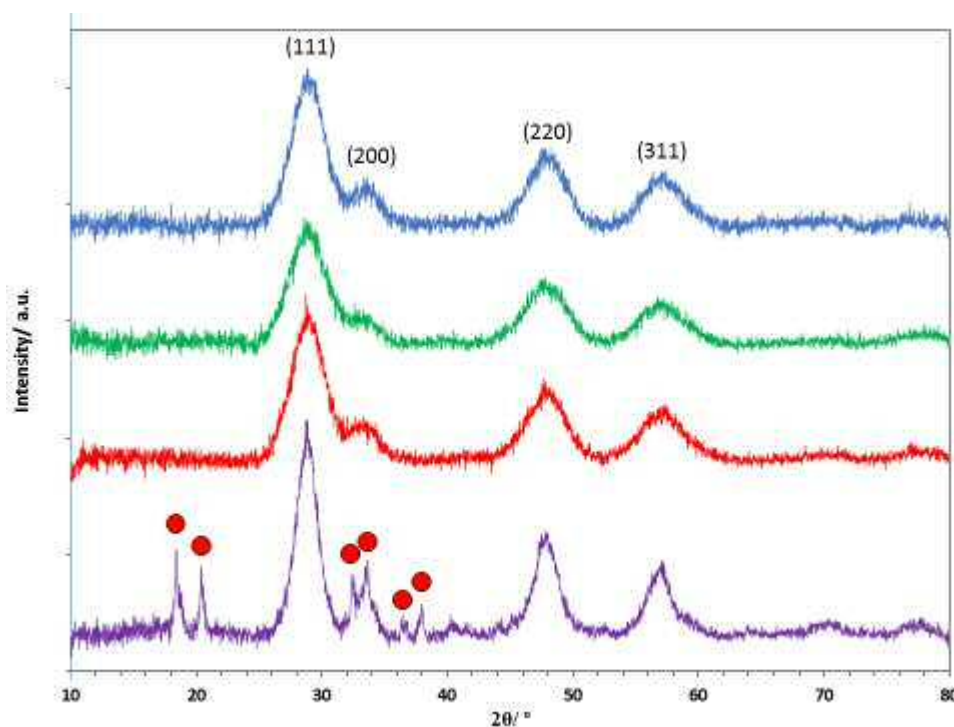


**Figure 3.8** X-ray diffractograms of manual co-precipitated CZA supports (blue, green, red) and automated CZA (purple)

The familiar reflections for the (111), (200), (220) and (311) planes of the fluorite structure were present in the XRD of the auto-CZA material, and their positions were unchanged. It is obvious from first glance that the XRD pattern of the auto-CZA material contained several additional peaks that were not present when the materials were prepared by the manual co-precipitation method. These have been highlighted in figure 3.8 by the red circles and

appeared at  $2\theta = 18.4^\circ, 20.4^\circ, 32.6^\circ, 33.7^\circ, 36.4^\circ, 38.0^\circ$ . While further characterisation (which is described in further detail below) identified an increased presence of sodium species within the material, no definitive match could be found to identify these XRD reflections.

**Table 3.4** Crystallite sizes calculated by Scherrer equation

<b>Catalyst</b>	<b>Crystallite size (nm)</b>
<b>CZA1</b>	2.7
<b>CZA2</b>	2.5
<b>CZA3</b>	2.5
<b>Auto-CZA</b>	3.6

It was also clear that the intensities of the main reflections were greater and peak widths narrower for the 'auto'-CZA material. Table 3.4 shows the crystallite sizes calculated from the reflections of the three 'manual' CZA catalysts and the 'auto'-CZA catalyst. The crystallite size for 'auto'-CZA were significantly larger than those of the 'manual'-CZA materials, likely due to the increased reaction time caused by the upscaling of the preparation method.

The Raman spectrum of 'auto'-CZA displayed in figure 3.9 also confirms the presence of ceria by the appearance of the peak belonging to the  $F_{2g}$  mode. As annotated, the frequency of this peak is shifted to a higher frequency than those of the 'manual'-CZA materials. This would suggest a greater incorporation of zirconium ions into the ceria lattice, causing greater deformation to the structure.

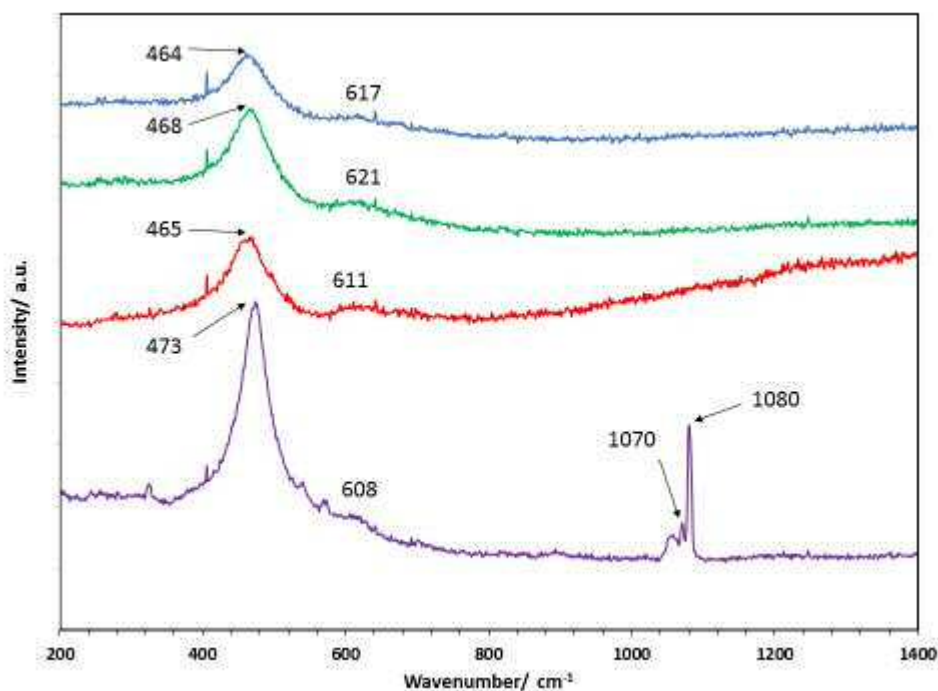


**Figure 3.9** Raman spectra of manual CZA supports (blue, green, red) and automated CZA (purple)

Also observed was the peak attributed to ceria oxygen vacancies in the 600-620  $\text{cm}^{-1}$  region. As in the XRD profiles, the Raman of 'auto'-CZA also showed peaks that not previously observed. Raman spectra of sodium nitrate and sodium carbonate (shown in the appendix) confirmed them to be responsible for the peaks at 1070  $\text{cm}^{-1}$  and 1080  $\text{cm}^{-1}$  respectively. This provided evidence that sodium species had been incorporated into the structure of the material during the preparation method, which was not observed using the previous method.

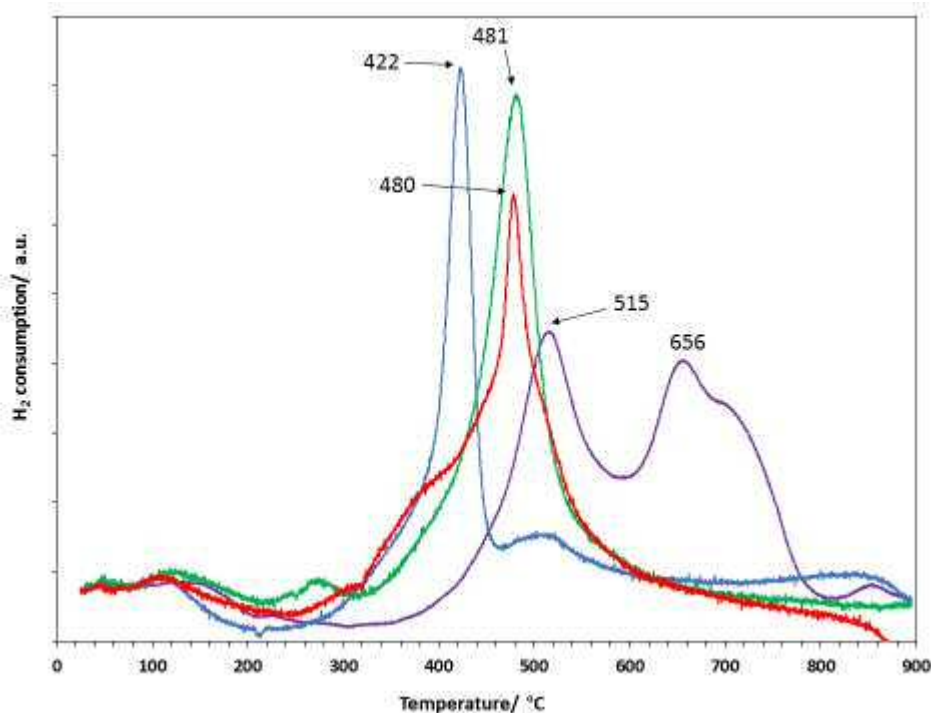


**Figure 3.10** TPR profiles of manual CZA (blue, green, red) and automated CZA (purple)

In contrast to the manual-CZA materials, the TPR profile of the 'auto'-CZA material in figure 3.10 showed a bimodal profile, with the main surface cerium peak at 515 °C. The intensity of this peak was considerably lower than those of the manual-CZA materials, and this was explained by BET analysis which indicated a much lower surface area for this material, displayed in table 3.5. XPS analysis (described in greater detail below) also showed a significant decrease in the atomic concentration of cerium on the surface of the material (see table 3.5), and this also contributed to the loss of intensity of this peak.

The surface reduction peak showed considerable overlap with a second peak, centred at 656 °C, which itself appeared to contain a shoulder. This area could be attributed to the reduction of bulk cerium ions, as reported in literature<sup>24</sup>. However, the presence of sodium carbonate as established by Raman suggested that this may have been caused by the decomposition of surface carbonates to CO and H<sub>2</sub>O, which was observed by Aneggi *et al.* when reporting on the effect of alkali metal loadings on ceria<sup>25</sup>. This would explain why no similar peak was observed for the three manually prepared catalysts.

X-ray photoelectron spectroscopy (XPS) was used in order to further investigate differences between the manual and automated CZA materials. The elements detected by XPS are shown in table 3.5, which also provides their concentrations in terms of atomic percentage.

**Table 3.5** Surface properties of ‘manual’ and ‘auto’-CZA catalysts provided by XPS and BET analyses

Catalyst	Surface atomic conc. (%)							Surface area (m <sup>2</sup> g <sup>-1</sup> )
	Ce 3d	Zr 3d	Al 2p	O 1s	C 1s	N 1s	Na 1s	
<b>Manual-CZA</b>	5.21	1.85	14.10	50.25	28.13	-	<b>0.46</b>	215 (±5)
<b>Auto-CZA</b>	2.69	1.16	8.80	45.23	33.82	0.49	<b>7.60</b>	23 (±1)

The XPS analysis showed that there was a significant increase in sodium concentration on the surface of the CZA catalyst when the automated method was used over the manual method, which is clear from the increased intensity of a peak at 1071eV shown in figure 3.11 a). Figure 3.11 b) shows the peaks attributed to O 1s; in both cases a peak at 529 eV can be observed, which is attributed to lattice oxygen present in CeO<sub>2</sub> and ZrO<sub>2</sub><sup>26</sup>. The main peak in this spectrum is attributed to oxygen from the alumina component, and is centred at 531 eV in both the ‘manual’- and ‘auto’-CZA spectra. An additional peak was observed at 533 eV in the ‘auto’-CZA spectrum, possibly indicating the presence of oxygen from a carbonate source, usually found at 532.5 eV. There was also an additional peak at ~536 eV observed in this spectrum which was attributed to Na auger<sup>27</sup>. The increase in intensity of the C 1s peak at 289.5 eV in figure 3.11 c) also indicated the increased presence of carbon from carbonate source in the ‘auto’-CZA as compared with the ‘manual’-CZA material. A small percentage of nitrogen was also detected on the ‘auto’-CZA which was not detected on the ‘manual’-CZA analysis. These observations provided further evidence of the increased presence of sodium species in the form of carbonate and nitrate when the automated method was used over the manual method.

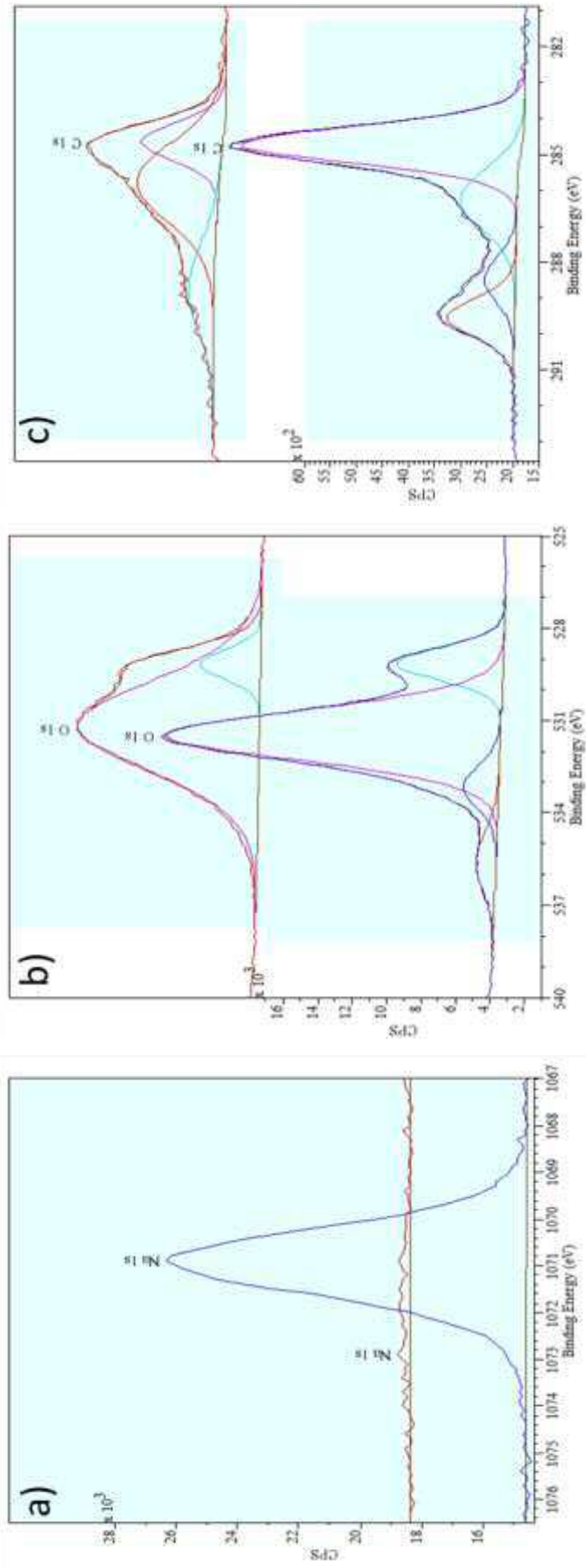


**Figure 3.11** Comparison of x-ray photoelectron spectra of manual-CZA (top) & auto-CZA (bottom) for; **a)** Na 1s, **b)** O 1s, **c)** C 1s



### 3.2.2 Soot oxidation testing

The 'auto'-CZA catalyst was tested for soot oxidation using TGA. The dTG plot in figure 3.12 shows clearly that soot oxidation took place at a considerably lower temperature when mixed with this catalyst compared to the three manually prepared catalysts shown previously. This is confirmed by several of the key temperature markers, highlighted in table 3.6.

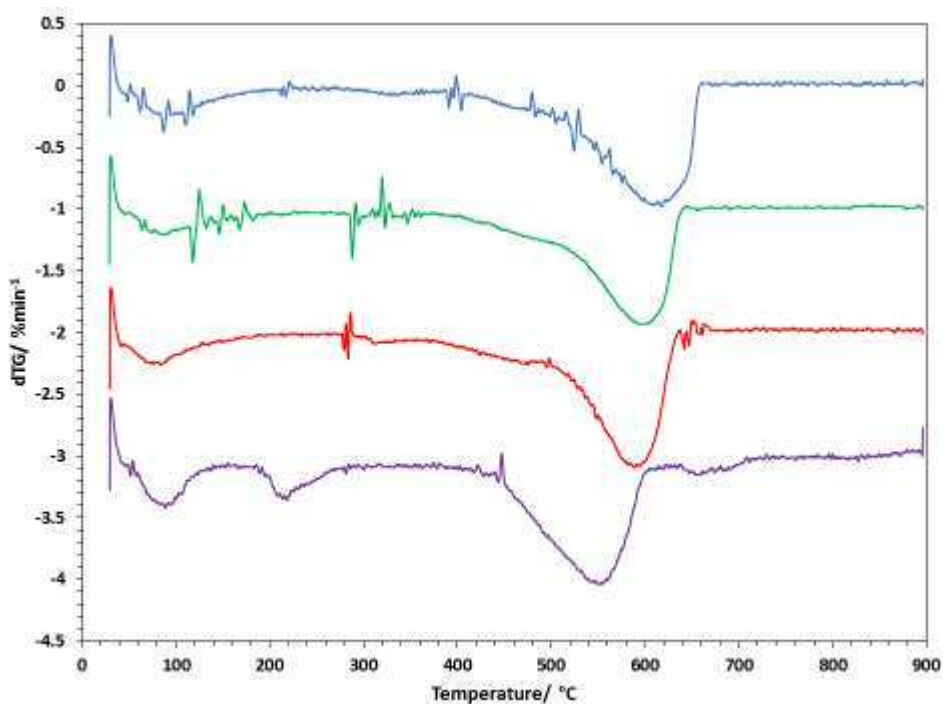


**Figure 3.12** dTG plots of catalyst/soot mixtures containing: manual CZA supports (blue, green, red) and automated CZA (purple)

The peak soot oxidation temperature when mixed with this catalyst was almost 40 °C lower than even the best performing 'manual'-CZA catalyst, and was over 70 °C lower than the uncatalysed reaction. The extrapolated onset and final temperatures were also considerably lower than the previous catalysed reactions, however the onset temperature was not lowered correspondingly. The superior soot oxidation activity of this catalyst could be explained by the increase in sodium content, which was shown by characterisation. It is well established from literature that alkali metals are active soot oxidation catalysts, and are able to enhance the soot oxidation properties of ceria-based catalysts by introducing carbonate intermediates and increasing contact between catalyst and soot<sup>3,25</sup>.

**Table 3.6** Soot oxidation temperatures of samples mixed with CZA catalysts

Catalyst	T <sub>o</sub> (°C)	T <sub>eo</sub> (°C)	T <sub>p</sub> (°C)	T <sub>f</sub> (°C)
Soot (no catalyst)	465	535	<b>622</b>	651
<b>CZA1</b>	400	491	<b>608</b>	658
<b>CZA2</b>	383	499	<b>592</b>	640
<b>CZA3</b>	370	498	<b>588</b>	635
<b>Auto-CZA</b>	405	431	<b>549</b>	607

In contrast with the manually prepared CZA catalysts, the ‘auto’-CZA catalyst did not provide evidence of a separate minor soot oxidation – which could be attributed to the oxidation of hydrocarbons as explained in the previous section – hence the higher onset temperature. This could be linked to the findings of the TPR, which suggested that less reduction of surface cerium was taking place, and at a higher temperature, resulting in lower availability of labile oxygen from the lattice to oxidise close-contact hydrocarbon particles at this temperature. However, it could be suggested that the alkali metal improved contact with soot overall, resulting in a decrease to the overall soot oxidation temperature.

### 3.3 Varying the automated preparation method of Ce<sub>0.35</sub>Zr<sub>0.15</sub>Al<sub>0.5</sub>O<sub>1.75</sub> supports

It was deemed that the increase in sodium species observed in the ‘auto’-CZA material was a consequence of the upscaling of the co-precipitation method. This meant that an increase in the volume of sodium carbonate was used in the method, however there had not been a corresponding upscale in the level of washing (0.5 L warm deionised water) to remove these species during the filtration stage of the process. Since the result of this was an improvement in catalytic activity, it was decided to investigate this further, first by attempting to remove sodium from the catalyst by incrementally increasing the washing, and subsequently by substituting sodium for alternative alkali metal carbonates (potassium and caesium).

### 3.3.1 Investigation into varying washing of Na-CZA catalysts

In order to investigate the effect of increasing washing on the CZA catalysts prepared by the automated co-precipitation method, three more catalysts were prepared by the method described in section 2.2.2.1, this time washed with 1.0, 1.5 and 2.0 litres of warm deionised water during filtration rather than the 0.5 litres used previously. The catalysts are referred to as Na-CZA followed by the volume of water used during washing, to distinguish them from each other. The original 'auto'-CZA catalyst presented in the previous section was used for comparison, and in this case is referred to as Na-CZA 0.5 L.

#### 3.3.1.1 Characterisation

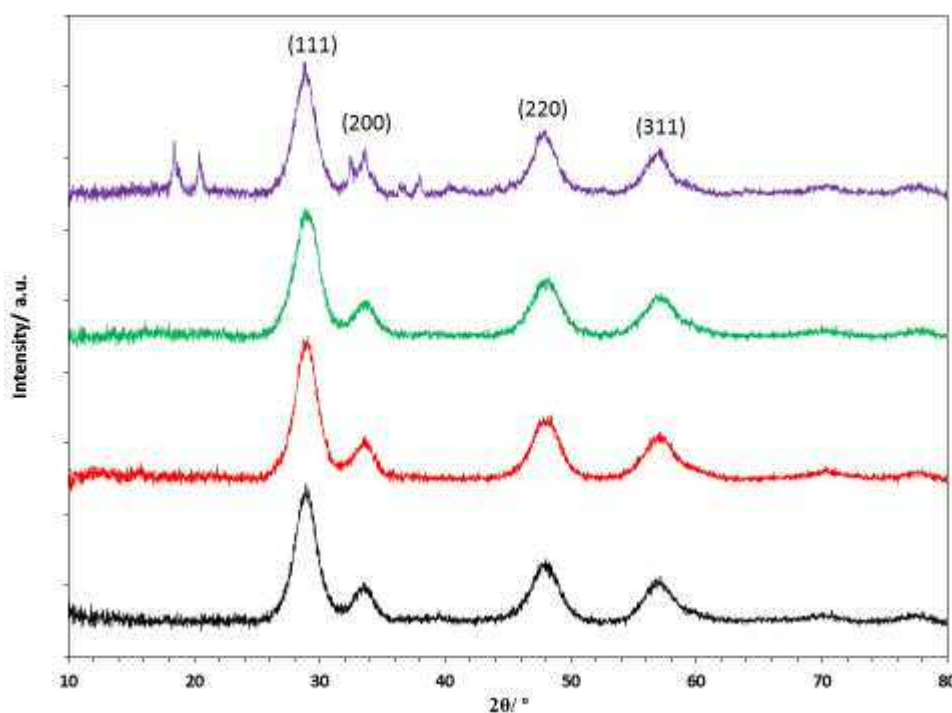


**Figure 3.13** X-ray diffractograms of Na-CZA0.5L (purple), Na-CZA1.0L (green), Na-CZA1.0L (red) and Na-CZA2.0L (black)

The XRD patterns of the Na-CZA catalysts in figure 3.13 showed that the peaks seen previously were not present when washing was increased to at least 1 litre. This suggested that increasing washing had been successful in removing these species from the catalyst material. The ceria reflections were once again present at the same  $2\theta$  angles, indicating the same crystal structure was present in each case. The crystallite sizes of this phase were again

calculated by the Scherrer equation from the main (111) reflection, and are shown in table 3.7.

**Table 3.7** Crystallite sizes of Na-CZA catalysts (calculated by Scherrer equation from XRD)

Catalyst	Crystallite size (nm)
Na-CZA 0.5L	4.1
Na-CZA 1.0L	4.1
Na-CZA 1.5L	4.6
Na-CZA 2.0L	4.3

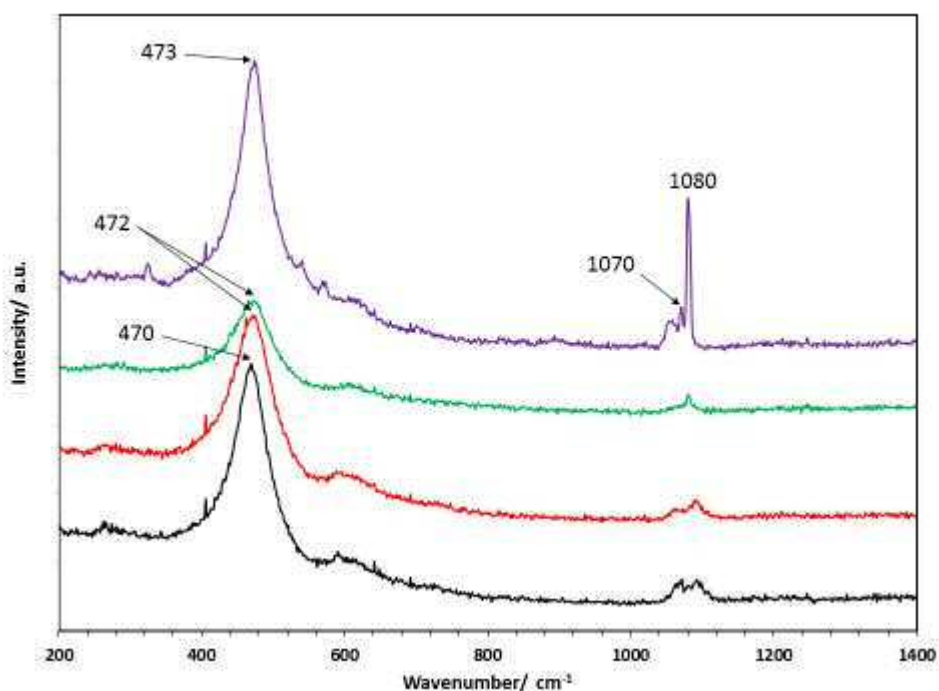


**Figure 3.14** Raman spectra of Na-CZA0.5L (purple), Na-CZA1.0L (green), Na-CZA1.5L (red) and Na-CZA2.0L (black)

The Raman spectra shown in figure 3.14 complemented the findings of XRD. The  $F_{2g}$  mode of ceria was again present and the shift from  $460\text{ cm}^{-1}$  was also observed, indicating incorporation of  $\text{ZrO}_2$ . There was significant decrease in the intensity of the sodium nitrate and sodium carbonate peaks at  $1070\text{ cm}^{-1}$  and  $1080\text{ cm}^{-1}$  when washing was increased from 0.5 L to 1.0 L and above. This suggested that washing was effective at removing these species but was not able to eradicate them fully, as XRD had suggested.

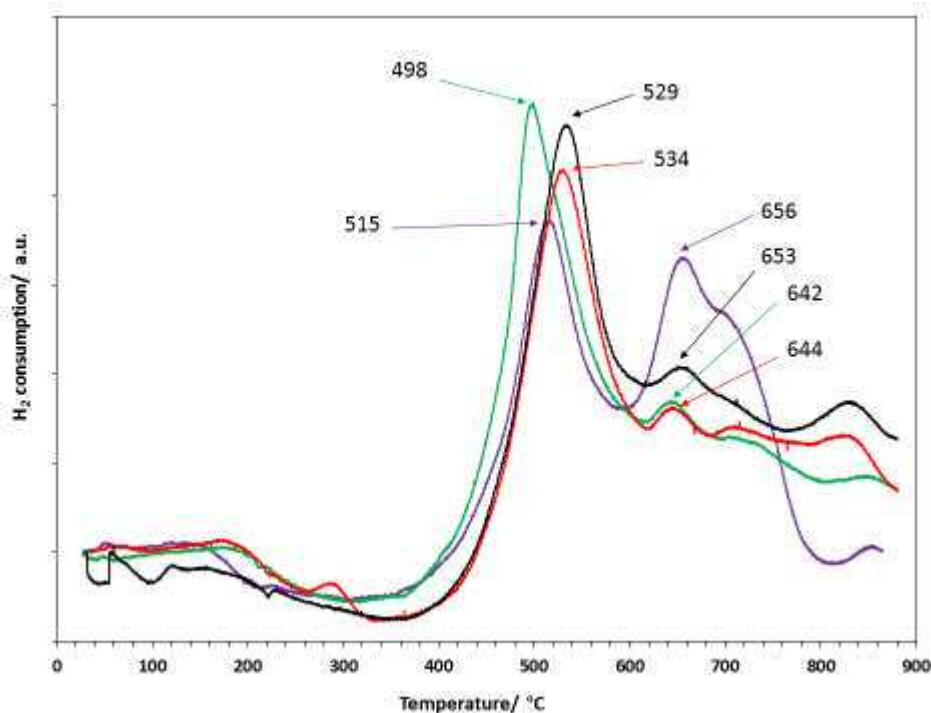


**Figure 3.15** TPR profiles of Na-CZA0.5L (purple), Na-CZA1.0L (green), Na-CZA1.5L (red) and Na-CZA2.0L (black)

The TPR profiles in figure 3.15 showed that increasing washing also had an effect on the reduction properties of the CZA materials. An increase in the intensity of surface cerium reduction was observed when washing was increased from 0.5L to  $\geq 1.0$  L. However, there was no trend to suggest that increasing washing above 1.0 L had any further effect on this. The BET and XPS analyses of these catalysts provided the surface areas and surface elemental composition in table 3.8, which showed an increase in the surface areas and increase in surface cerium concentration as compared with Na-CZA0.5L, indicating that more cerium was available at the surface to undergo reduction. The increase in surface area may have resulted from the removal of carbonates from the surface of the catalysts, also evidenced in XPS by the considerable decrease in the percentage of carbon on the surfaces, as well as the decrease in the  $\text{Na}_2\text{CO}_3$  peak observed in Raman mentioned previously. The temperature at which peak reduction took place was comparable in the case of Na-CZA 1.5L and 2.0L at around 530 °C, however it was observed that this peak was at a lower temperature in the case of Na-CZA 1.0L. The broad TPR peak between 600-800 °C which was previously attributed to both bulk cerium reduction and decomposition of carbonates in Na-CZA0.5L, can be seen to have decreased in intensity when washing was increased above 1.0 L, which could also be attributed to the removal of carbonates from these catalysts.

Table 3.8 shows the atomic percentages of elements detected by XPS analysis. Washing above 1 litre caused a significant decrease in carbon, and reduced nitrogen to an undetectable level on the surfaces of the catalysts. This suggested, in agreement with the XRD and Raman, that the carbonate and nitrate species previously detected had been removed by increasing the volume of washing. However, this did not correspond to a decrease in the levels of sodium on the surface of the catalysts. Even when taking into account the removal of carbon and nitrogen, the level of sodium on the surface of the catalysts actually increased considerably when washing was increased from 0.5 to 1 litre, and a less pronounced increase then occurred when washing was increased from 1 to 1.5 litres, and again from 1.5 to 2 litres. It is possible that with increasing washing, while removing the nitrates and carbonates substantially, the sodium may have been displaced from within the catalyst structure and simply deposited on the surface.

**Table 3.8** Surface properties of Na-CZA catalysts provided by XPS and BET analyses

Catalyst	Atomic conc. (%)						Surface area (m <sup>2</sup> g <sup>-1</sup> )	
	Ce 3d	Zr 3d	Al 2p	O 1s	C 1s	N 1s		Na 1s
<b>Na-CZA 0.5L</b>	2.69	1.16	8.80	45.23	<b>33.82</b>	0.49	<b>7.60</b>	23 (±1)
<b>Na-CZA 1.0L</b>	6.51	1.71	11.92	46.74	<b>17.62</b>	-	<b>15.48</b>	65 (±1)
<b>Na-CZA 1.5L</b>	5.13	1.15	14.10	45.80	<b>17.43</b>	-	<b>16.40</b>	58 (±2)
<b>Na-CZA 2.0L</b>	4.96	1.15	14.47	46.51	<b>16.06</b>	-	<b>16.83</b>	47 (±2)

### 3.3.3.2 Soot oxidation testing

Due to the continued presence of sodium on the catalysts' surfaces, it was expected that the improvement in soot oxidation observed between the 'auto'-CZA and 'manual'-CZA catalysts would be sustained. However, a possible issue with alkali metals for soot oxidation catalysis is that they have been reported to be thermally unstable, forming volatile species at high temperatures which result in their removal from the catalyst and a subsequent loss in activity<sup>3,25</sup>. For this reason catalysts were also tested for thermal durability, which was achieved by retrieving samples after soot oxidation testing up to 900 °C, and repeating the test with fresh soot.

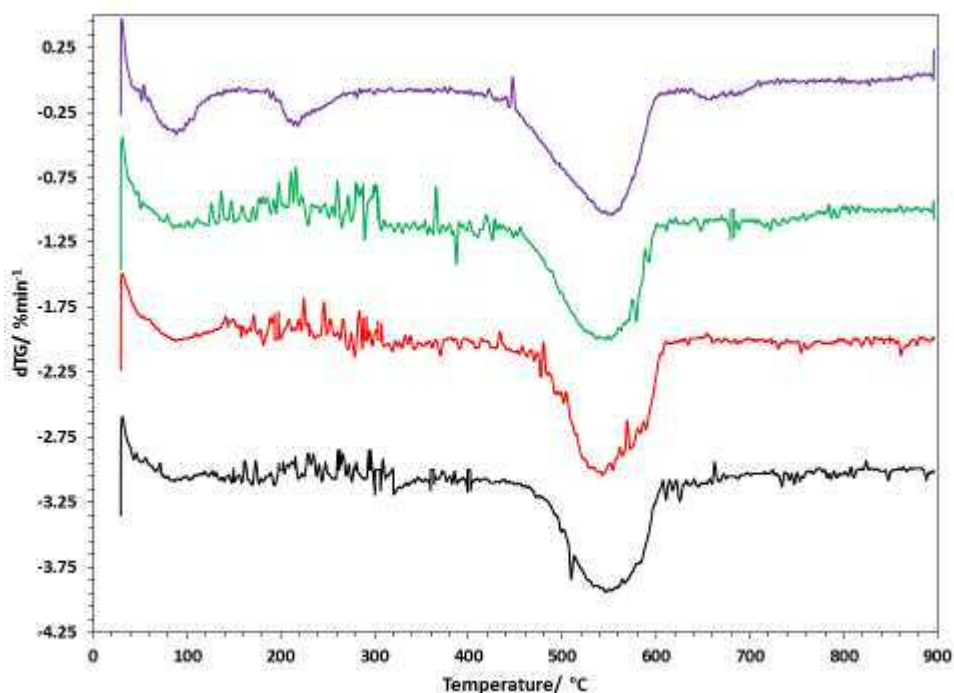


**Figure 3.16** dTG plots of catalyst/soot mixtures containing: Na-CZA0.5L (purple), Na-CZA1.0L (green), Na-CZA1.5L (red) and Na-CZA2.0L (black)

The dTG plots of each of the catalyst's first runs are shown in figure 3.16, and the soot oxidation temperatures extracted from these plots are presented in table 3.9. The soot oxidation temperatures of the catalysts washed with  $\geq 1.0$  L were fairly consistent in each case. Their peak and final temperatures were also consistent with those achieved with Na-CZA 0.5L, while their onset temperatures were higher in comparison.

**Table 3.9** Soot oxidation temperatures of samples mixed with Na-CZA catalysts on their first and second use

Catalyst	$T_o$ (°C)		$T_{eo}$ (°C)		$T_p$ (°C)		$T_f$ (°C)	
	1 <sup>st</sup> run	2 <sup>nd</sup> run	1 <sup>st</sup> run	2 <sup>nd</sup> run	1 <sup>st</sup> run	2 <sup>nd</sup> run	1 <sup>st</sup> run	2 <sup>nd</sup> run
<b>Soot (no catalyst)</b>	465		535		<b>622</b>		651	
<b>Na-CZA 0.5L</b>	405	402	431	476	<b>549</b>	<b>544</b>	607	587
<b>Na-CZA 1.0L</b>	438	456	454	463	<b>547</b>	<b>534</b>	601	585
<b>Na-CZA 1.5L</b>	440	448	473	460	<b>543</b>	<b>541</b>	609	588
<b>Na-CZA 2.0L</b>	437	435	468	470	<b>547</b>	<b>544</b>	607	599

The dTG plots in figure 3.17 show the soot oxidation temperatures of the Na-CZA catalysts on first and second use. In each case, it was observed that the peak soot oxidation temperatures (shown in table 3.9) did not change significantly between first and second use, and this indicated that the catalysts all had good thermal stability up to 900 °C.

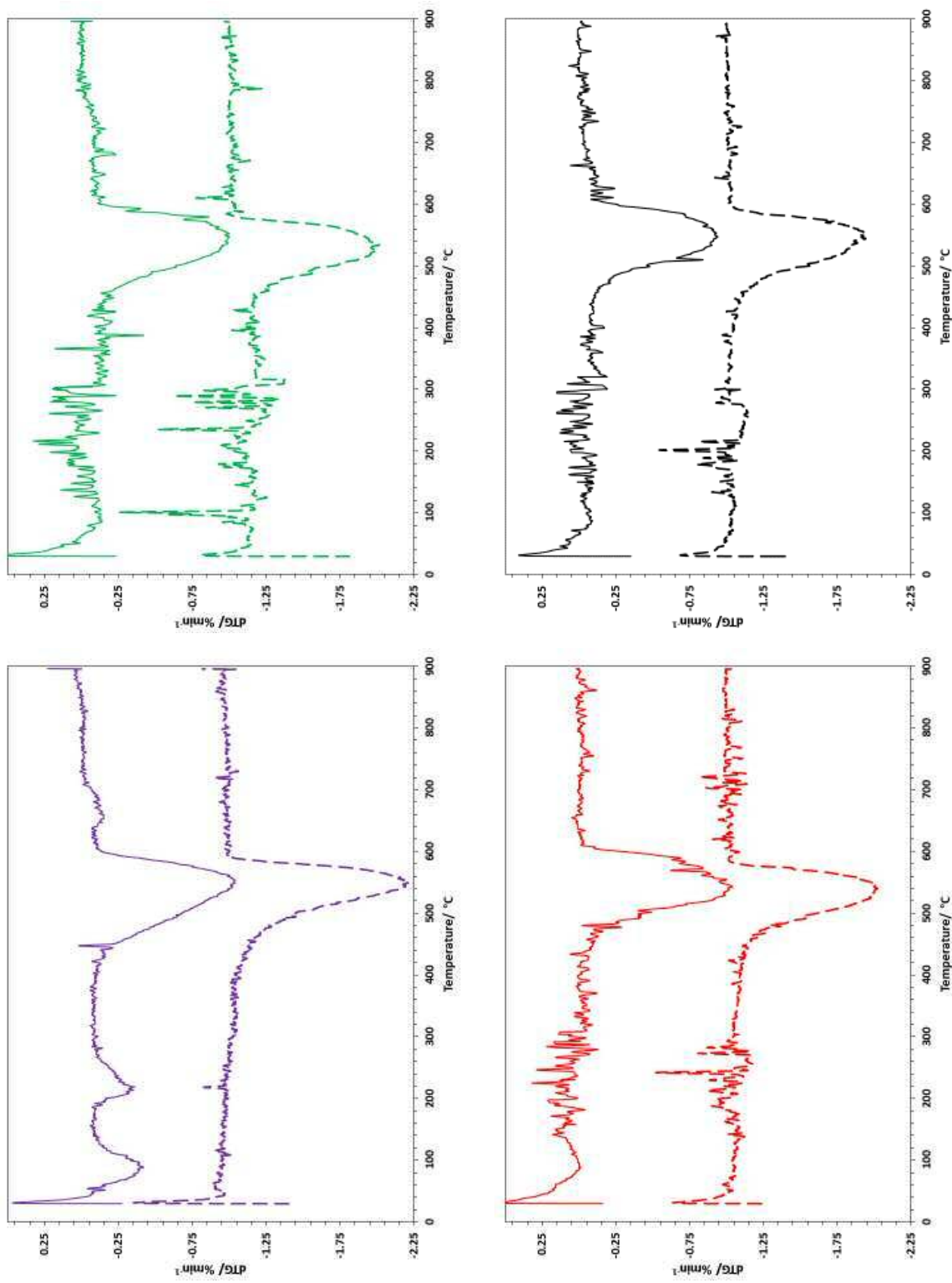


**Figure 3.17** dTG plots of catalyst/soot mixtures containing: Na-CZA0.5L (purple), Na-CZA1.0L (green), Na-CZA1.5L (red) and Na-CZA2.0L (black) on the first run (solid line) and second run (dashed line)



It was concluded that an increase in washing was clearly effective at removing the carbonate and nitrate species from the Na-CZA structures, however the XPS analysis suggested that sodium itself persisted on the surfaces of the catalysts, and soot oxidation testing showed that their catalytic activity was unaffected.

The purpose of this line of investigation was to attempt to remove or reduce sodium so as to establish whether it was responsible for the improved catalytic activity reported when switching from the manual to the automated co-precipitation method. Since increasing washing had neither the desired effect of removing sodium, nor an effect on the activity of the catalysts, it was not possible to achieve this. It was decided to use an alternative approach, by removing sodium from the catalyst preparation entirely.

### 3.3.2 Alternative alkali metal carbonates as precipitating agent (potassium and caesium)

CZA catalysts were prepared using potassium and caesium carbonates rather than sodium carbonate as the precipitating agent. In order to compare the effects of these metals on the activity of the CZA catalysts, both were washed with only 0.5 L of water during filtration.

These catalysts are referred to as K-CZA0.5L and Cs-CZA0.5L. Both were tested for soot oxidation and compared with the results for Na-CZA 0.5L from the previous section.

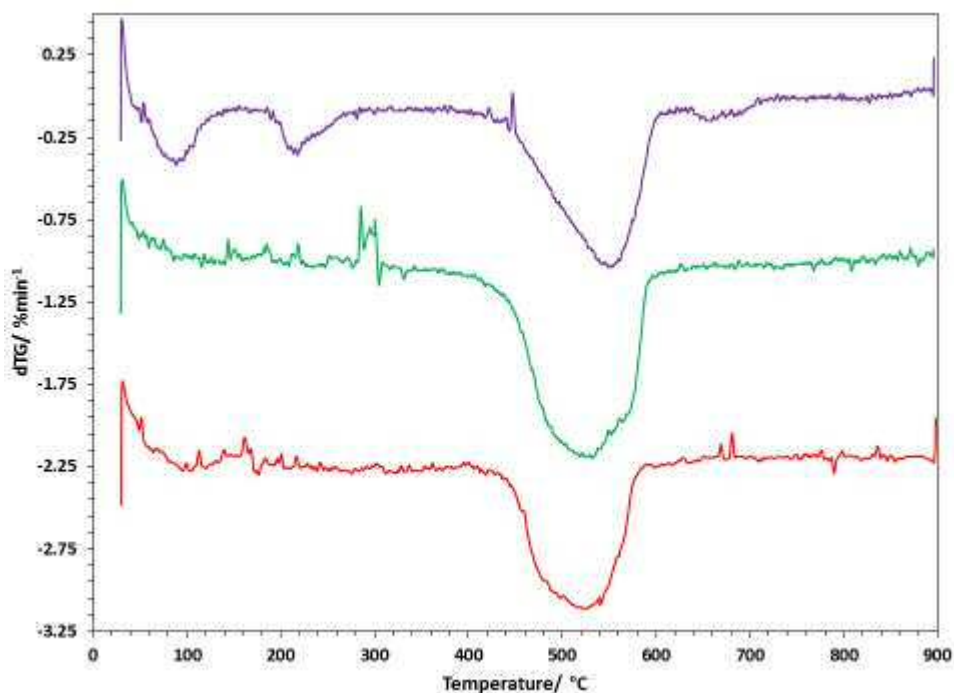


**Figure 3.18** dTG plots of catalyst/soot mixtures containing: Na-CZA0.5L (purple), K-CZA0.5L (green), Cs-CZA0.5L (red)

The dTG plots in figure 3.18 demonstrate that the substitution of sodium carbonate for the potassium and caesium analogues during the preparation method resulted in a further improvement in soot oxidation activity. From table 3.10 it can be seen that peak soot oxidation temperatures with K-CZA0.5L and Cs-CZA0.5L were lowered by around 25 °C compared with Na-CZA0.5L. As mentioned previously, there have been numerous reports of alkali metals being active soot oxidation catalysts, and have shown that activity increases tending down the group due to the trend in decreasing electronegativity, allowing for stronger electrostatic attraction between alkali metal and oxygen and maintaining higher dispersion on the catalyst<sup>25,28</sup>. Since the presence of alkali metals in this case is due to a by-product of the preparation method rather than a controlled addition to the catalyst, a direct correlation between activity and each alkali metal should not be made. However, it is clear that the use of potassium and caesium carbonates rather than sodium carbonate led to an improvement in activity.

**Table 3.10** Soot oxidation temperatures of samples mixed with Na-CZA, K-CZA and Cs-CZA

Catalyst	T <sub>o</sub> (°C)	T <sub>eo</sub> (°C)	T <sub>p</sub> (°C)	T <sub>f</sub> (°C)
<b>Soot (no catalyst)</b>	465	535	<b>622</b>	651
<b>Na-CZA 0.5L</b>	405	431	<b>549</b>	607
<b>K-CZA 0.5L</b>	407	437	<b>529</b>	596
<b>Cs-CZA 0.5L</b>	400	441	<b>524</b>	589

### 3.3.3 Investigation into varying washing of K-CZA catalysts

It was again decided to investigate removing the alkali metal from the CZA catalyst, this time by increasing washing from 0.5 L to 2.0 L during the preparation using potassium carbonate. The higher solubility of potassium carbonate in water over sodium carbonate<sup>29</sup> suggested it could be removed from the catalyst more readily, and that a comparison could be made between CZA catalysts prepared by the automated co-precipitation method both with and without the presence of alkali metals. This catalyst is referred to as K-CZA2.0L, and the K-CZA0.5L catalyst is again used as a comparison in this section.

## 3.3.3.1 Characterisation

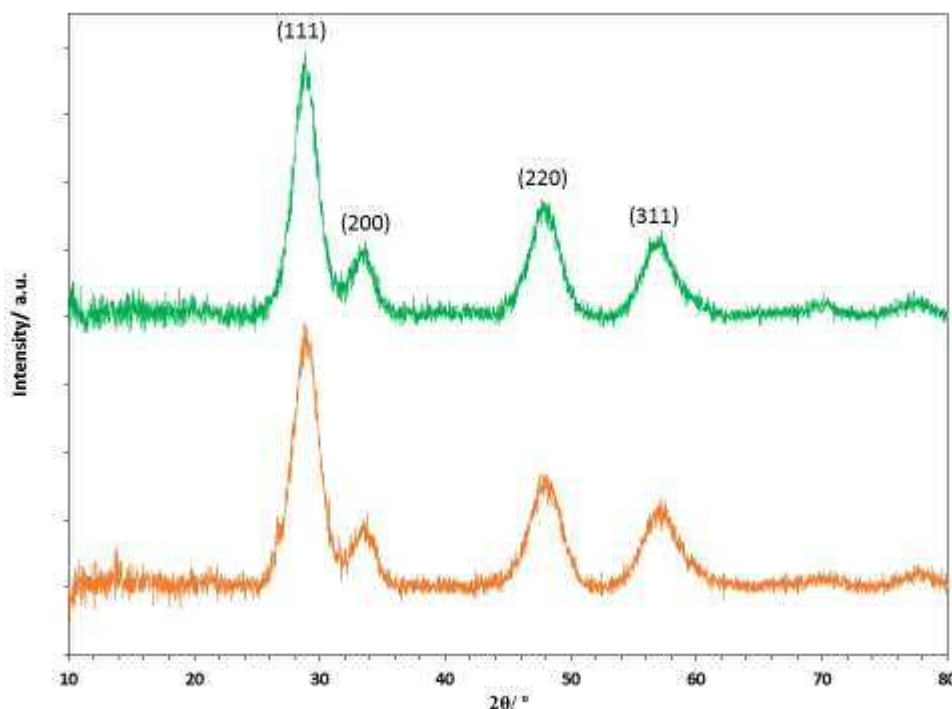


**Figure 3.19** X-ray diffractograms of K-CZA0.5L (green) and K-CZA2.0L (orange)

The XRD patterns of the K-CZA catalysts shown in figure 3.19 both showed the familiar reflections seen in the Na-CZA materials, again indicating the fluorite-type structure of  $\text{CeO}_2$ . The peak positions and intensities were consistent between both batches, and crystallite sizes were also unaltered. Interestingly, no additional peaks were observed in K-CZA0.5L as had been the case in Na-CZA0.5L, which may have been an indication of the more facile removal of potassium species than sodium species.

The crystallite sizes, shown in table 3.11, were slightly lower than the equivalent Na-CZA catalysts, but were still higher than seen for the original ‘manual’-CZA catalysts.

**Table 3.11** Crystallite sizes of K-CZA catalysts (calculated by Scherrer equation from XRD)

Catalyst	Crystallite size (nm)
K-CZA 0.5L	3.8
K-CZA 2.0L	3.7

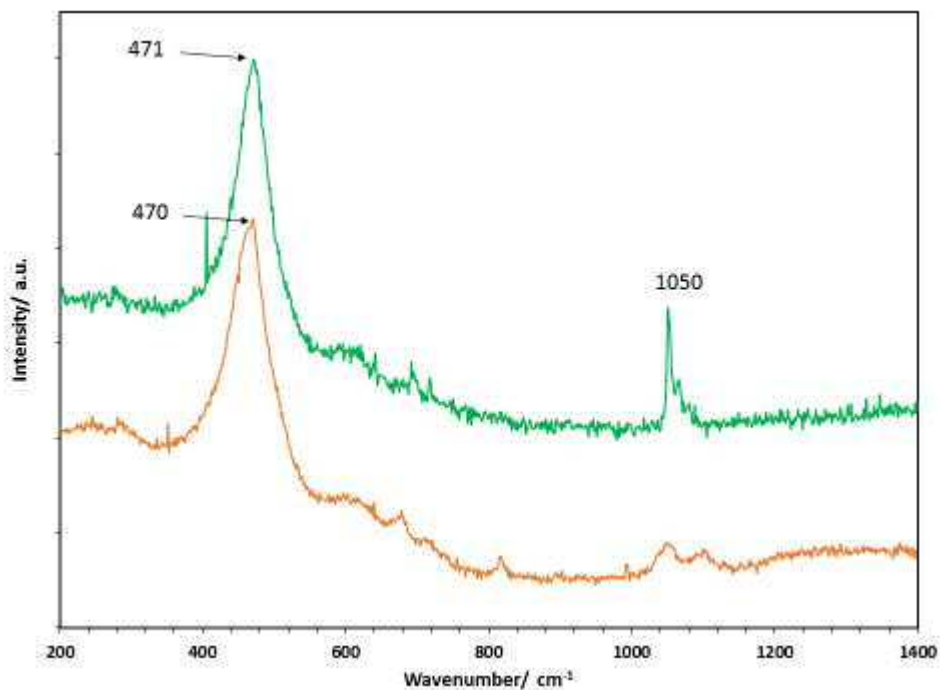


**Figure 3.20** Raman spectra of K-CZA0.5L (green), K-CZA2.0L (orange)

The Raman spectra of the K-CZA catalysts in figure 3.20 also confirmed the presence of ceria. The shift of the  $f_{2g}$  mode peak to around  $470\text{ cm}^{-1}$  again indicated the incorporation of zirconia. The peak at  $1050\text{ cm}^{-1}$  on the K-CZA0.5L spectrum was identified as belonging to potassium carbonate, and this peak was seen to decrease significantly in intensity when washing was increased to 2.0 L, again indicating that washing was effective at removing the potassium species from the catalyst.

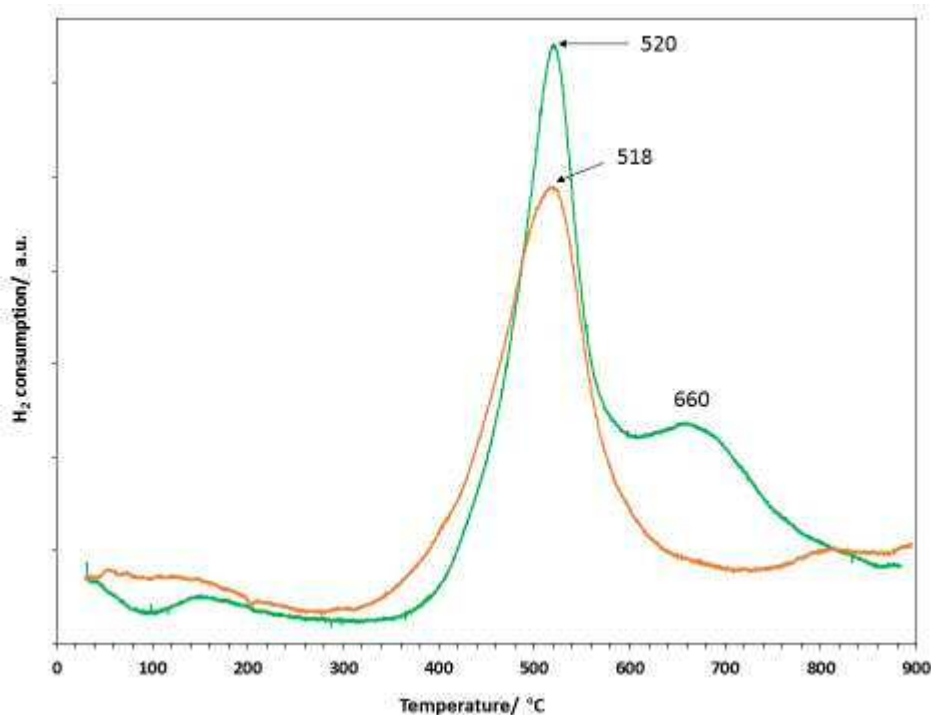


**Figure 3.21** TPR profiles of K-CZA0.5L (green) and K-CZA2.0L (orange)

The TPR profiles of the K-CZA catalysts are shown in figure 3.21. Both show the familiar peak attributed to the reduction of surface  $\text{Ce}^{4+}$  at around 520 °C, which were in agreement with the temperature range observed of the equivalent peaks found in the TPR profiles of the Na-CZA materials in figure 3.15.

Similar to the Na-CZA materials, K-CZA 0.5L showed a secondary, broad peak centred at 660 °C, attributed to the decomposition of carbonate species. In this case, the peak can be attributed to the presence of residual potassium carbonate from the catalyst preparation. This peak is not present when washing was increased in K-CZA 2.0L, again indicating the removal of the potassium species by washing.

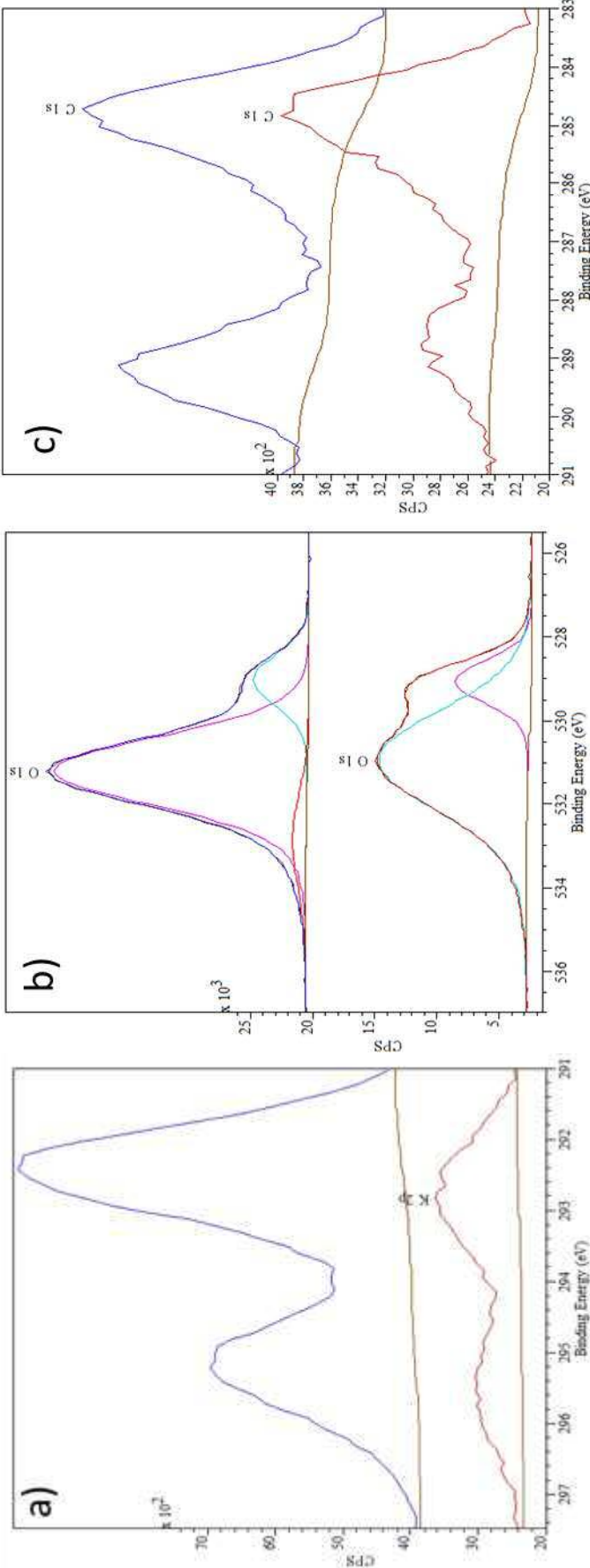


Figure 3.22 Comparison of x-ray photoelectron spectra of K-CZA0.5L (top) and K-CZA2.0L (bottom) for; a) K 2p, b) O 1s, c) C 1s

Surface analysis by XPS and BET also showed that a physical change occurred to the K-CZA catalysts when washing was increased, summarised in table 3.12. Surface area was seen to increase significantly upon increased washing, and the concentration of surface potassium provided by XPS was seen to decrease significantly. Figure 3.22a) shows K 2p peaks with binding energies 295.6 eV and 292.8 eV, attributed to potassium present from its carbonate form<sup>30</sup>. The spectra in figure 3.22b) show the peaks belonging to O 1s. In the case of K-CZA2.0L, the peaks are centred at 529 eV and 531 eV indicating the presence of oxygen from ceria/zirconia and alumina respectively; however in the spectrum belonging to K-CZA0.5L, there is an additional peak centred at around 532.5 eV which attributed to the presence of oxygen in carbonate form. The increased presence of carbonate in K-CZA0.5L is also evidenced in the C 1s spectra in figure 3.22c), which shows a larger intensity peak centred at around 289 eV.

**Table 3.12** Surface properties of K-CZA catalysts provided by XPS and BET analyses

Catalyst	Surface atomic conc. (%)					K 2p	Surface area (m <sup>2</sup> g <sup>-1</sup> )
	Ce 3d	Zr 3d	Al 2p	O 1s	C 1s		
<b>K-CZA 0.5L</b>	3.62	0.68	12.25	56.05	18.69	<b>8.72</b>	37 (±2)
<b>K-CZA 2.0L</b>	8.02	1.59	17.52	54.05	16.25	<b>2.57</b>	171 (±3)

As previously described in the case of the Na-CZA catalysts, the correlation between low surface area and higher alkali metal concentration could be explained by the metal plugging the micropores on the catalyst surface. Thus, removing the potassium in this case resulted in a significant increase in surface area.

### 3.3.3.2 Soot oxidation testing

The K-CZA 2.0L catalyst was tested for soot oxidation and compared with that of the K-CZA 0.5L catalyst shown in the previous section. Unlike the results of the Na-CZA catalysts, the dTG plots in figure 3.23 show that increasing washing when using  $K_2CO_3$  as the precipitating agent had a substantial impact on the soot oxidation activities of the CZA materials.

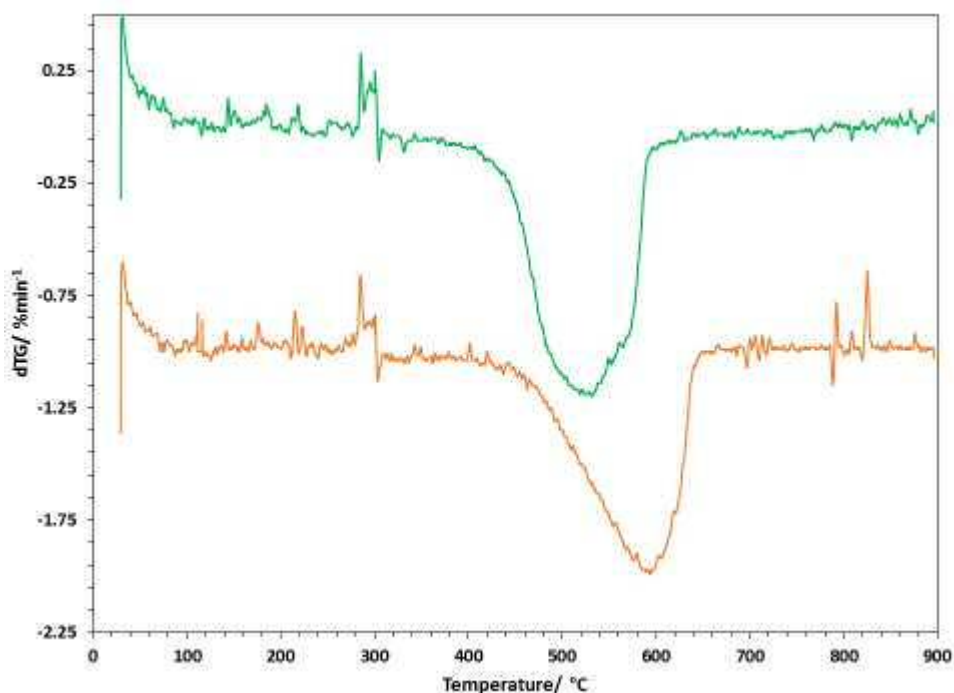


**Figure 3.23** dTG plots of catalyst/soot mixtures containing: K-CZA0.5L (green) and K-CZA2.0L (orange)

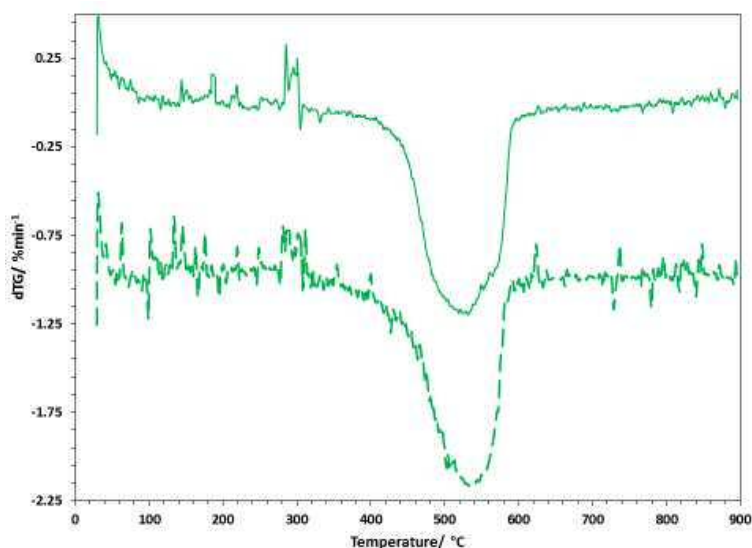
The soot oxidation temperature increased significantly when washing was increased from 0.5L to 2.0 L. The peak soot oxidation temperature (shown in table 3.13) increased by over 60 °C, while the  $T_f$  was around 50 °C higher when washing was increased. The slope of the peaks suggested that soot oxidation occurred more rapidly in the case of K-CZA0.5L, whereas soot oxidation was slower to reach its maximum rate in the case of K-CZA2.0L. The greater presence of potassium on the surface of K-CZA0.5L compared to that of K-CZA2.0L as confirmed by XPS analysis explained the discrepancy in soot oxidation temperatures between the two.



**Table 3.13** Soot oxidation temperatures of samples mixed with K-CZA catalysts on their first and second use

Catalyst	$T_o$ (°C)		$T_{eo}$ (°C)		$T_p$ (°C)		$T_f$ (°C)	
	1 <sup>st</sup> run	2 <sup>nd</sup> run	1 <sup>st</sup> run	2 <sup>nd</sup> run	1 <sup>st</sup> run	2 <sup>nd</sup> run	1 <sup>st</sup> run	2 <sup>nd</sup> run
<b>Soot (no catalyst)</b>	465		535		<b>622</b>		648	
<b>K-CZA 0.5L</b>	407	360	437	436	<b>529</b>	<b>534</b>	596	590
<b>K-CZA 2.0L</b>	422	423	456	482	<b>594</b>	<b>590</b>	648	635

The durability of the catalysts were tested in the same way as the Na-CZA catalysts described previously, and are shown in figure 3.24 and 3.25. Table 3.13 shows that the temperature range over which soot oxidation occurred when mixed with K-CZA2.0L was not affected on second use. While onset and peak soot oxidation temperatures were not affected, the increase in extrapolated onset temperature suggested that the initial soot oxidation was slower on second use, but subsequently accelerated towards peak oxidation at a greater rate. The peak temperature of oxidation with K-CZA0.5L increased slightly on second use, however the overall range of temperatures over which soot oxidation took place was not adversely affected. This suggested that, as previously shown with sodium, potassium was stable on the CZA catalyst.

**Figure 3.24** dTG plots of catalyst/soot mixtures containing K-CZA0.5L on the first run (solid line) and second run (dashed line)

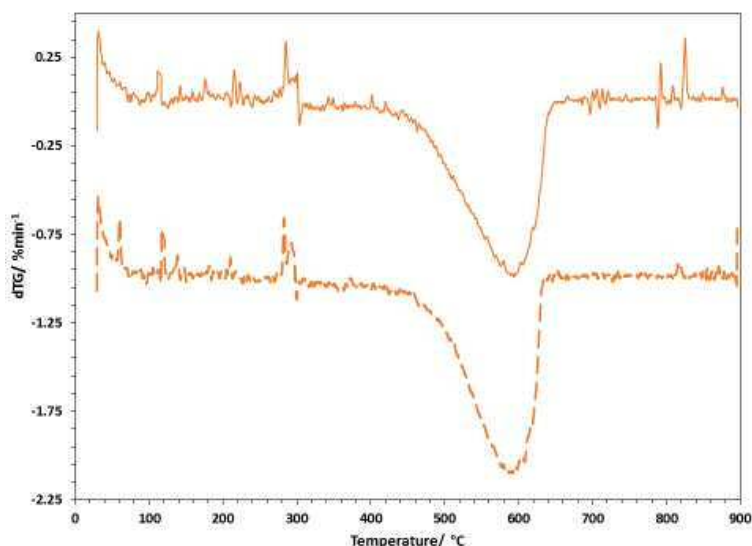


**Figure 3.25** dTG plots of catalyst/soot mixtures containing K-CZA2.0L on the first run (solid line) and second run (dashed line)

### 3.4 Conclusions

The work detailed in this chapter originated from the initial attempts at reproducing an active CZA catalyst previously prepared at this institute. In terms of soot oxidation activity, an equally active CZA catalyst was successfully produced. It was also interesting to note from the shape of the soot oxidation curves that two distinct processes may have been taking place, one involving labile lattice oxygen oxidising soot (possibly the hydrocarbon fraction) within close contact of the catalyst, and a separate process utilising the atmospheric oxygen flowed over the sample.

The catalyst was prepared several times in order to establish the reproducibility of the preparation method, however several characterisation techniques and catalyst testing found that there were discrepancies between batches, which were attributed to the inconsistent nature of the preparation method. By adopting an automated mechanical system to undertake the co-precipitation of the CZA catalyst, it was found that soot oxidation improved considerably compared to the same catalysts prepared manually. Characterisation suggested that there was an increased level of sodium – in particular sodium carbonate, the precipitating agent used in the preparation method – in the automated CZA compared to the inferior manually prepared catalyst. Since alkali metals have been widely reported as active soot oxidation catalysts, this opened up an interesting avenue of investigation into the role of the

precipitating agent on the activity of the CZA catalyst. It was suggested that increasing washing during the filtration step of the catalyst preparation could reduce the level of sodium and confirm the link between the high activity and the presence of sodium. XRD and Raman spectroscopy suggested that increasing washing above 1.0 litre was effective at removing carbonate and nitrate species from the CZA materials, however XPS indicated that sodium on the surface of the catalysts was not diminished by increasing washing. Soot oxidation temperatures were fairly consistent when catalysed by each of these materials, and were all equally effective on repeated use.

Changes to soot oxidation activity were observed when sodium carbonate was replaced with alternative alkali metal carbonates as the precipitating agent. Low-volume washing of CZA catalysts prepared with potassium and caesium carbonate as precipitating agents showed a further decrease in the peak soot oxidation temperature compared with their sodium carbonate counterpart. Since potassium and caesium have previously shown to be more active soot oxidation catalysts than sodium<sup>25</sup>, this provided evidence of a link between precipitating agent and soot oxidation.

Further evidence was established by increasing washing on the CZA catalysts prepared using potassium carbonate. In this case, washing was considerably more effective at removing potassium than it had been for sodium, evidenced by the relative levels of potassium detected by XPS. In this case, soot oxidation activity deteriorated considerably upon decreasing potassium, to a similar level found in the manually prepared CZA catalysts from the initial study.

Therefore the introduction of alkali metals in the form of the precipitating agent during the automated co-precipitation method was able to significantly enhance the soot oxidation properties of CZA catalysts. In terms of repeated use for soot oxidation, CZA catalysts prepared with both sodium and potassium maintained their activity and so were considered to be thermally stable. However, the ease with which potassium was removed by washing with water compared to sodium during the preparation of the catalysts must also be considered. High temperature thermal aging of ceria-based catalysts in the presence of water has previously shown to result in significant loss of alkali metal content<sup>25</sup>, therefore it would be interesting to investigate the stability of the alkali metals on the CZA materials presented in this chapter in a similar manner.

### 3.5 References

1. A. Trovarelli, *Comments Inorg. Chem.*, 1999, **20**, 263–284.
2. S. Liu, X. Wu, D. Weng and R. Ran, *J. Rare Earths*, 2015, **33**, 567–590.
3. A. Bueno-López, *Appl. Catal. B Environ.*, 2014, **146**, 1–11.
4. I. Atribak, B. Azambre, A. Bueno López and A. García-García, *Appl. Catal. B Environ.*, 2009, **92**, 126–137.
5. E. Aneggi, C. de Leitenburg and A. Trovarelli, *Catal. Today*, 2012, **181**, 108–115.
6. J. Li, X. Liu, W. Zhan, Y. Guo, Y. Guo and G. Lu, *Catal. Sci. Technol.*, 2016, **6**, 897–907.
7. T. Kanazawa, J. Suzuki, T. Takada, T. Suzuki, A. Morikawa, A. Suda, H. Sobukawa and M. Sugiura, in *Science and Technology in Catalysis 2002*, eds. M. Anpo, M. Onaka and H. Yamashita, Kodansha Ltd, Tokyo, 2003, vol. 145, pp. 415–418.
8. D. R. Sellick, A. Aranda, T. García, J. M. López, B. Solsona, A. M. Mastral, D. J. Morgan, A. F. Carley and S. H. Taylor, *Appl. Catal. B Environ.*, 2013, **132–133**, 98–106.
9. M. Machida, Y. Murata, K. Kishikawa, D. Zhang and K. Ikeue, *Chem. Mater.*, 2008, **20**, 4489–4494.
10. I. Atribak, A. Bueno-López and A. García-García, *J. Catal.*, 2008, **259**, 123–132.
11. L. Katta, P. Sudarsanam, G. Thrimurthulu and B. M. Reddy, *Appl. Catal. B Environ.*, 2010, **101**, 101–108.
12. V. Sánchez Escribano, E. Fernández López, M. Panizza, C. Resini, J. M. Gallardo Amores and G. Busca, *Solid State Sci.*, 2003, **5**, 1369–1376.
13. R. Ramdas, Thesis, Cardiff University, 2014.
14. D. Terribile, A. Trovarelli, J. Llorca, C. de Leitenburg and G. Dolcetti, *Catal. Today*, 1998, **43**, 79–88.
15. M. Yashima, H. Arashi, M. Kakihana and M. Yoshimura, *J. Am. Ceram. Soc.*, 1994, **77**, 1067–1071.
16. L. N. Ikryannikova, A. A. Aksenov, G. L. Markaryan, G. P. Murav'eva, B. G. Kostyuk, A. N. Kharlanov and E. V. Lunina, *Appl. Catal. Gen.*, 2001, **210**, 225–235.
17. V. G. Keramidas and W. B. White, *J. Chem. Phys.*, 1973, **59**, 1561–1562.
18. M. R. Benjaram, T. Gode and L. Katta, *Chin. J. Catal.*, 2011, **32**, 800–806.
19. P. Fornasiero, J. Kašpar and M. Graziani, *J. Catal.*, 1997, **167**, 576–580.
20. G. L. Markaryan, L. N. Ikryannikova, G. P. Muravieva, A. O. Turakulova, B. G. Kostyuk, E. V. Lunina, V. V. Lunin, E. Zhilinskaya and A. Aboukais, *Colloids Surf. Physicochem. Eng. Asp.*, 1999, **151**, 435–447.
21. A. Bueno-López, K. Krishna, M. Makkee and J. A. Moulijn, *J. Catal.*, 2005, **230**, 237–248.
22. A. E. Newkirk, *Anal. Chem.*, 1960, **32**, 1558–1563.
23. G. Neri, L. Bonaccorsi, A. Donato, C. Milone, M. G. Musolino and A. M. Visco, *Appl. Catal. B Environ.*, 1997, **11**, 217–231.
24. P. Fornasiero, G. Balducci, R. Di Monte, J. Kašpar, V. Sergo, G. Gubitosa, A. Ferrero and M. Graziani, *J. Catal.*, 1996, **164**, 173–183.
25. E. Aneggi, C. de Leitenburg, G. Dolcetti and A. Trovarelli, *Catal. Today*, 2008, **136**, 3–10.

26. H. Liang, S. Wu, Y. Hong, S. Li, Y. Chen, X. Yu and D. Ye, *Catal. Lett.*, 2014, **144**, 685–690.
27. XPS Interpretation of Sodium, <http://xpssimplified.com/elements/sodium.php>
28. Z. H. Zhu, G. Q. Lu and R. T. Yang, *J. Catal.*, 2000, **192**, 77–87.
29. A. Burrows, J. Holman, A. Parsons, G. Pilling and G. Price, *Chemistry<sup>3</sup>: Introducing inorganic, organic and physical chemistry*, OUP Oxford, Oxford, 2 edition., 2013.
30. Q. Li, X. Wang, Y. Xin, Z. Zhang, Y. Zhang, C. Hao, M. Meng, L. Zheng and L. Zheng, *Sci. Rep.*, 2014, **4**, 4725.

## 4. Rare-Earth metal dopants in ceria-alumina catalyst supports

The importance of introducing foreign cations into the ceria lattice in order to improve its catalytic and thermal properties has been long-established and well-documented<sup>1-3</sup>. The previous chapter discussed the use of zirconium in this respect, and also served to establish an effective method of producing ceria-based mixed-metal oxide catalysts. In this chapter, the method employed to prepare ceria-zirconia-alumina catalysts was again used in order to investigate the use of rare-Earth metal dopants (lanthanum, praseodymium and neodymium) as alternatives to zirconium.

As with zirconium, the use of rare-Earth metals to dope ceria catalysts has been widely reported<sup>1,4-6</sup>. The effects of incorporating rare-Earth metals into the structure of ceria differs from that of zirconium due to the differences in their physical and chemical properties. Whereas zirconium exists in the +4 oxidation state, and is therefore isovalent to the Ce<sup>4+</sup> ions in CeO<sub>2</sub>, the rare-Earth elements in this study exist in the +3 oxidation state (Pr is stable in both +4 and +3 states<sup>5</sup>). The incorporation of these ions into the ceria structure has been reported to cause lattice stress, induced by the need to maintain charge neutrality, which forces the reduction of cerium ions and thus the creation of greater oxygen vacancies<sup>6</sup>. The other significant difference is the size of the ionic radii compared to Ce<sup>4+</sup>. While the incorporation of the smaller Zr<sup>4+</sup> ions causes a contraction of the ceria lattice<sup>7</sup>, the rare-Earth metals cause an expansion to the lattice due to their larger ionic radii<sup>6</sup>.

This investigation aimed to establish whether the soot oxidation activity observed by the CZA catalysts in chapter 3 could be enhanced by replacing zirconium with the aforementioned rare-Earth metals. This initially involved maintaining the same 7:3:10 molar ratio of Ce:M:Al (where M = zirconium/rare-Earth metal) as in the previous chapter so as to allow for a direct comparison. As well as replacing zirconium outright, a catalyst containing a 7:1.5:1.5:10 molar ratio of Ce:La:Zr:Al was also prepared in order to investigate whether a synergistic effect between the two dopant metals could be established. These catalysts are referred to as CZA, CLZA, CLA, CPA and CNA (C = ceria, Z = zirconia, L = lanthana, P = praseodymia, N = neodymia,

A = alumina), and collectively as CMA. A further study into the effects of varying the Ce:M:Al ratio (5:5:10 and 3:7:10) was also conducted with all of the above combinations (in each case the La:Zr ratio of CLZA remained 1:1). Although a previous study at Cardiff University had established the 7:3:10 ratio as the optimum for CZA<sup>8</sup>, the changes to the preparation method described in chapter 3 justified repeating this study, which also allowed for a fair comparison between each of the CZA catalysts and the corresponding rare-Earth metal-containing catalysts.

The investigation concluded that the catalysts containing neodymium were the most active for soot oxidation. These catalysts exhibited similar activity to the other CMA catalysts during their initial testing, however on repeated use their activities improved significantly, which suggested the catalysts could be improved by exposure to higher temperatures. An investigation into the calcination conditions of CNA catalysts was therefore carried out. A CNA catalyst calcined at 750 °C under flowing air was found to be the most active catalyst prepared in this chapter.

## 4.1 Rare-Earth metal alternatives to zirconium in ceria-alumina catalyst supports

In this section, 5 catalysts were prepared by an automated co-precipitation method as described in section 2.2.2.2. Each catalyst contained a Ce:M:Al molar ratio of 7:3:10, where M = Zr, La, La+Zr (in a 1:1 ratio), Pr, Nd. These are referred to as CZA, CLA, CLZA, CPA, CNA.

### 4.1.1 Characterisation

Each of the catalysts were characterised in a similar fashion to those in chapter 3. Figure 4.1 shows the x-ray diffractograms of the CMA materials.

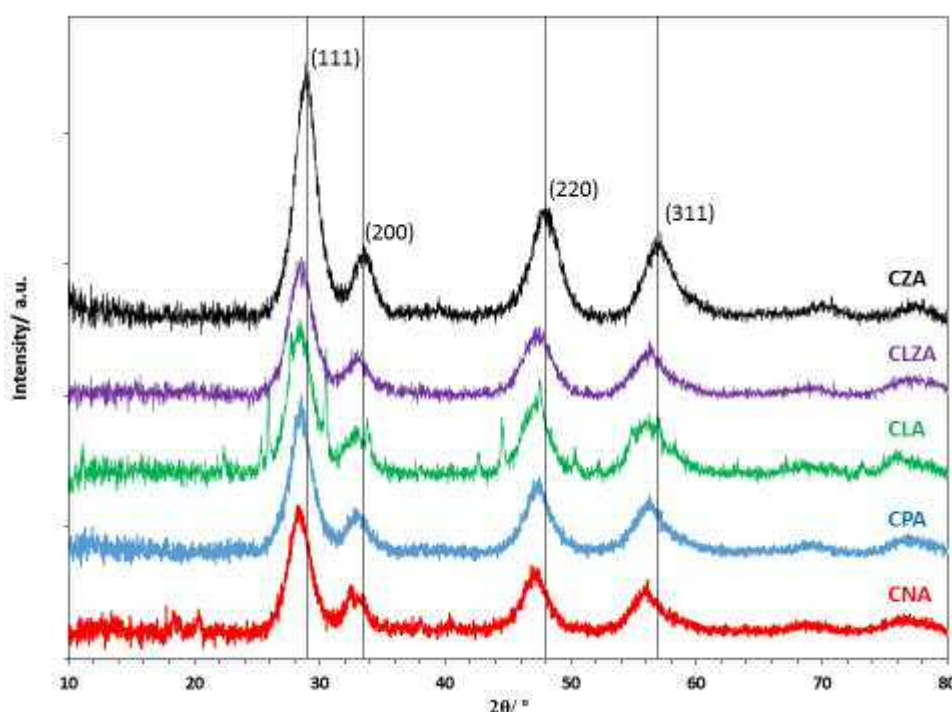


**Figure 4.1** X-ray diffractograms of CZA (black), CLZA (purple), CLA (green), CPA (blue) and CNA (red). The black lines are included to emphasise the shift in ceria peak positions relative to those of CZA

As explained in the previous chapter, ceria is a fluorite-type structure with an fcc cell containing the (111), (200), (220) and (311) planes. The reflections corresponding to these planes were observed in the diffractograms of each of the CMA catalysts. The substitution of lanthanum, praseodymium and neodymium in place of zirconium caused the 2 theta values of these reflections to decrease, summarised in table 4.1. As previously stated, the presence of zirconium causes the contraction of the ceria lattice due to the difference in ionic radii ( $\text{Ce}^{4+} \sim 0.97 \text{ \AA}$  and  $\text{Zr}^{4+} \sim 0.84 \text{ \AA}$ ), resulting in a shift to higher 2 theta values. The partial substitution



of  $Zr^{4+}$  for  $La^{3+}$  (ionic radius  $\sim 1.10 \text{ \AA}^9$ ) in the case of CLZA negated this effect, and the 2 theta values observed were similar to those of pure ceria (referenced from JCPDS database, card no. 071-4199). The 2 theta values of CLA and CNA (ionic radius of  $Nd^{3+} \sim 1.15 \text{ \AA}^{10}$ ) were observed to decrease compared to pure ceria, indicating an expansion of the lattice. The 2 theta values of the reflections in the case of CPA indicated that no lattice expansion had taken place. This would suggest that the praseodymium present within the structure was predominantly in the form of  $Pr^{4+}$ , as it has a similar ionic radius to  $Ce^{4+}$  ( $\sim 0.96 \text{ \AA}^{11}$ ). However the shift to a lower 2 theta value of the (200) reflection suggested there may have been some lattice expansion, which would be explained by the presence of  $Pr^{3+}$  which has a larger ionic radius of  $\sim 1.13 \text{ \AA}^{11}$ . The crystallite sizes for the ceria phase in each of the catalysts are shown in table 4.1, which were calculated by the Scherrer equation from the (111) reflections. It was observed that the crystallite size decreased when zirconium was replaced with rare-Earth metals.

Several additional reflections were observed in the case of CLA, most prominently at  $25.8^\circ$ ,  $30.3^\circ$ ,  $44.5^\circ$  and  $47.5^\circ$ . These were all matched with a reference for lanthanum oxide carbonate, ( $La_2O_2CO_3$  JCPDS card no. 37-0804).

**Table 4.1** Peak positions and crystallite sizes of CMA catalysts determined by XRD

Catalyst	2 theta ( $^\circ$ )				Crystallite size (nm)
	(111)	(200)	(220)	(311)	
<b>Ceria*</b>	28.5	33.1	47.5	56.3	-
<b>CZA</b>	28.9	33.5	48.0	57.1	4.1
<b>CLZA</b>	28.5	33.0	47.4	56.4	3.6
<b>CLA</b>	28.3	32.9	47.2	56.0	3.4
<b>CPA</b>	28.5	32.9	47.5	56.3	3.5
<b>CNA</b>	28.3	32.8	47.2	56.0	3.4

\*2 theta values of ceria referenced from JCPDS database (card no. 071-4199)

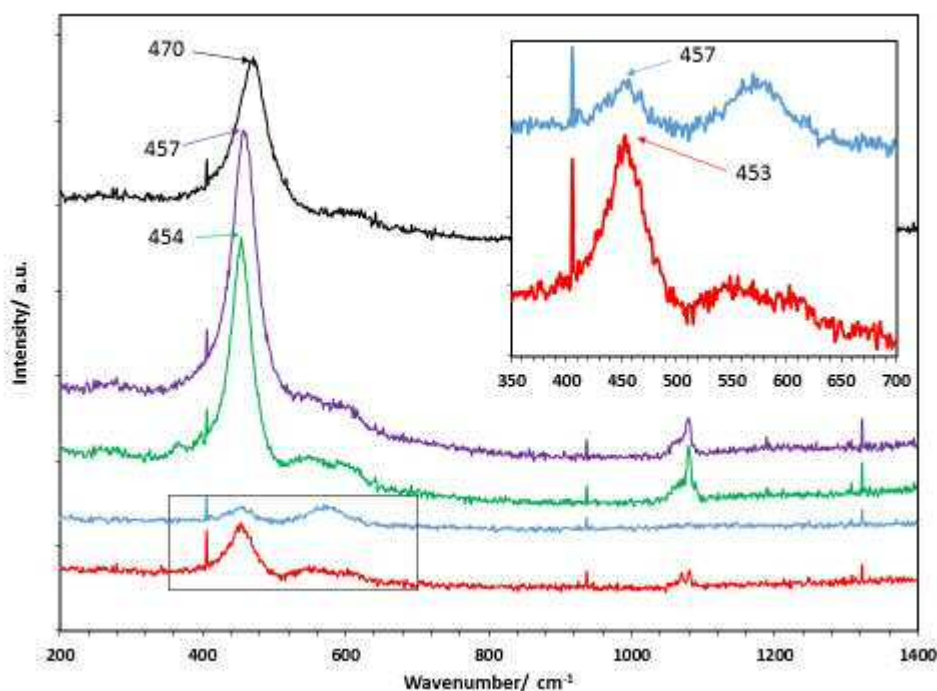


**Figure 4.2** Raman spectra of CZA (black), CLZA (purple), CLA (green), CPA (blue) and CNA (red). Inset, expanded view of CPA and CNA major peaks between 350 and 700 $\text{cm}^{-1}$

The CMA samples were analysed by Raman spectroscopy, and are shown in figure 4.2. The peak representing the  $F_{2g}$  Raman-active mode of ceria was observed in each of the spectra, however the position and intensity of the peak was seen to vary depending on the dopant metal used. As mentioned in the previous chapter, the incorporation of  $Zr^{4+}$  ions causes a decrease in the lattice parameter of  $CeO_2$ , which in turn results in an increase in the frequency of the  $F_{2g}$  mode from around  $460\text{ cm}^{-1}$ <sup>12,13</sup>. In the case of the CZA sample shown in figure 4.2 this resulted in a peak at  $470\text{ cm}^{-1}$ . However due to the relatively large ionic radii of the RE metals compared to  $Zr^{4+}$ , in each case their incorporation had the opposite effect, increasing the lattice parameter and thus decreasing the Raman frequency of the active ceria mode. The pattern for which this took place was much in agreement with the findings of the XRD. The decrease in frequency was most pronounced in the cases of CLA and CNA, shifting to  $454\text{ cm}^{-1}$  and  $453\text{ cm}^{-1}$  respectively, likely due to the disruption to the ceria lattice caused by the bulky  $La^{3+}$  and  $Nd^{3+}$  ions mentioned previously. In the cases of CLZA and CPA, the disruption caused by the presence of bulky  $La^{3+}$  and  $Pr^{3+}$  ions was likely tempered by that of the smaller  $Zr^{4+}$  and  $Pr^{4+}$  ions respectively, to a frequency of only  $457\text{ cm}^{-1}$ . It was also observed that the intensity of the  $F_{2g}$  peak was considerably lower in the cases of CPA and CNA compared to the other catalysts. For CPA, the intensity of the peak at  $510\text{-}630\text{ cm}^{-1}$  relative to the main ceria peak

suggested a greater proportion of oxygen vacancies had been formed in CPA than the other catalysts. This is a widely reported phenomenon in Ce-Pr materials, due to the ease with which praseodymium is able to reduce from +4 to +3 oxidation state, aiding the formation of Ce<sup>3+</sup> and thus oxygen vacancies<sup>6,14</sup>.

X-ray photoelectron spectroscopy and BET surface area analysis were performed on the catalysts in order to determine their surface properties. The atomic percentages of the elements detected by XPS were quantified and can be found in table 4.2 as well as the surface areas determined by BET analysis.

There were significant variations observed in the surface areas of the CMA catalysts. As reported in the previous chapter, the presence of high levels of sodium (as confirmed by XPS) may have lowered the surface areas of the catalysts by plugging micropores, and so the values may not reflect the physical change incurred by varying the dopant metal.

**Table 4.2** Surface properties of CMA catalysts provided by XPS and BET analyses

Catalyst	Atomic conc. (%)						Surface area	
	Ce 3d	Zr 3d	RE*	Al 2p	O 1s	C 1s	Na 1s	(m <sup>2</sup> g <sup>-1</sup> )
<b>CZA</b>	6.22	1.27	-	17.03	51.51	7.25	16.73	36 (±1)
<b>CLZA</b>	5.49	0.40	1.46	19.59	51.15	6.62	15.29	40 (±1)
<b>CLA</b>	3.36	-	1.66	18.18	51.31	7.55	17.94	21 (±1)
<b>CPA</b>	5.40	-	1.82	20.67	52.33	6.14	13.65	30 (±1)
<b>CNA</b>	3.29	-	1.11	21.03	53.75	6.04	14.78	30 (±1)

\*RE = La 3d/Pr 3d/Nd 3d

In each case cerium, the dopant metal(s) and aluminium accounted for around a quarter of the elemental composition of the surface detectable by XPS. The ratios of these elements are provided in table 4.3. Compared with the ratios used during the preparation method, it was observed that each of the catalysts had an excess of aluminium on their surfaces. Apart from CLA, there was also an excess of cerium over the dopant metal, in particular in the case of CZA. The zirconium content on the surface of CLZA was also much lower than expected, demonstrated by the Zr/La ratio, which deviated considerably from the equimolar ratio used during the preparation of the catalyst.

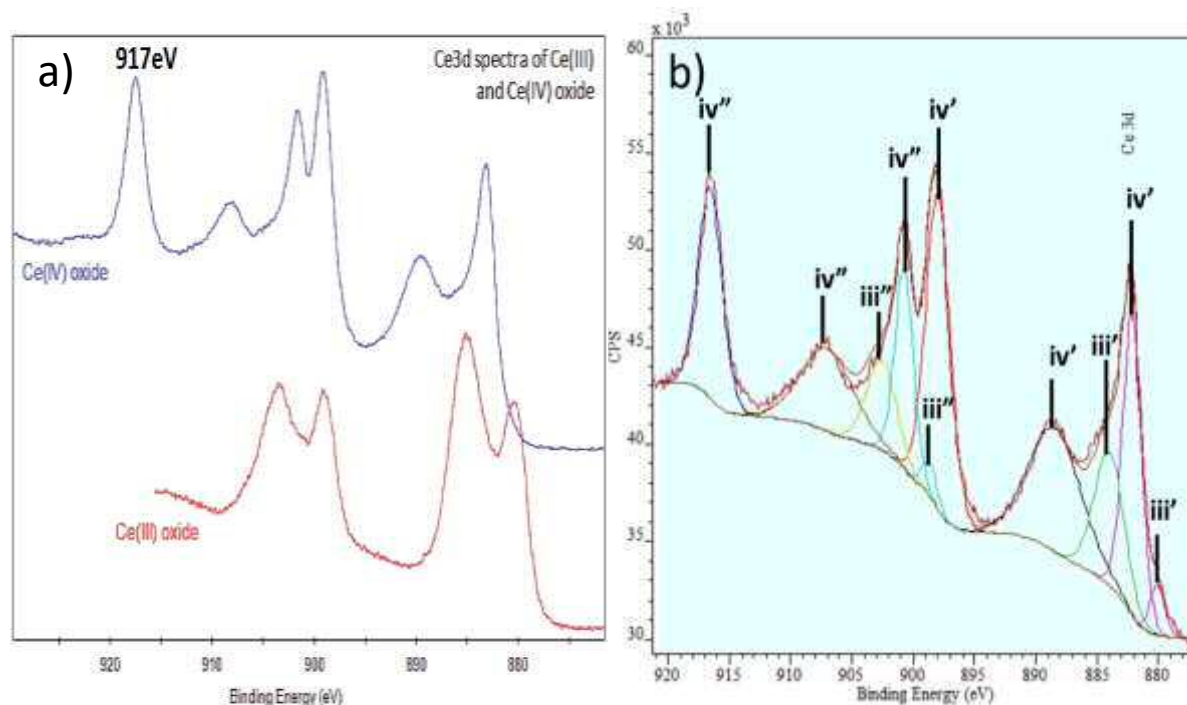


**Figure 4.3** (a) example of XPS spectra of Ce3d region<sup>15</sup>, (b) Ce 3d region of CLA 7:3:10

Analysis of the Ce 3d region was able to provide information regarding the oxidation state of cerium on the surfaces of the catalysts and hence the ability of the dopant to increase the number of oxygen vacancies. As shown in figure 4.3 a)<sup>15</sup> the number of peaks and their positions vary depending on whether cerium is in the (IV) or (III) oxidation state. The peaks in the Ce 3d region are assigned into the 3d 3/2 and 3d 5/2 components which are further split into spin-orbital multiplets. In the case of Ce(IV) there are three states, and in Ce(III) there are two, with Ce(IV) easily distinguishable by its peak at 917 eV<sup>6</sup>. The spectra of the Ce 3d region of the CMA catalysts provided evidence that cerium was predominantly in the (IV) oxidation state, however the presence of Ce(III) peaks were also detected to various extents. CLA was found to have the most intense Ce(III) peaks relative to Ce(IV), and is shown in figure 4.3b). The Ce 3d spectra of the other catalysts can be found in the appendix. The peaks marked iv' and iii' belong to the 3d 5/2 component of Ce(IV) and Ce(III) respectively, and those marked iv'' and iii'' belong to the 3d 3/2 component. The relative intensities of the peaks of both states were calculated and the ratios are provided in table 4.3. These show that the proportion of Ce(III) increased significantly when zirconium was totally replaced with lanthanum and a slight increase was also observed upon partial substitution. In contrast, the presence of Pr and Nd slightly lowered the proportion of Ce(III) compared to CZA.

**Table 4.3** Atomic ratio of metals on CMA catalyst surfaces

Catalyst	Ce : M : Al	Ce : M	Zr : La	Ce(III) : Ce(IV)
<b>Preparation method</b>	7.0 : 3.0 : 10.0	7.0 : 3.0	1:1	
<b>CZA</b>	5.1 : 1.0 : 13.9	8.3 : 1.7	-	0.14 : 1
<b>CLZA</b>	4.1 : 1.4 : 14.5	7.4 : 2.6	0.27 : 1	0.17 : 1
<b>CLA</b>	4.0 : 2.0 : 14.0	6.7 : 3.3	-	0.25 : 1
<b>CPA</b>	3.9 : 1.3 : 14.8	7.5 : 2.5	-	0.10 : 1
<b>CNA</b>	2.6 : 0.9 : 16.5	7.5 : 2.5	-	0.11 : 1

M = Zr/La,Zr/La/Pr/Nd

Temperature-programmed reduction was performed on the catalysts in order to determine the effects of varying the dopant metal had on the reducibility of Ce<sup>4+</sup> ions. Each of the catalysts' TPR profiles (figure 4.4) showed at least two distinct curves, the first centred at just over 500 °C and the second at around 650 °C, with considerable overlap between both. A third peak was observed in the case of CLA centred at 707 °C, while a significant shoulder peak appeared at a similar temperature in the profile of CZA. The initial peaks centred at around 510-530 °C were attributed solely to the reduction of surface Ce<sup>4+</sup> ions in the case of CZA, CLZA, CLA and CNA, as the other cations are non-reducible<sup>1</sup>. In the case of CPA, reduction of Pr<sup>4+</sup> to Pr<sup>3+</sup> could occur under these conditions<sup>5</sup>; however its reduction profile provided no evidence that two distinct reductions took place.

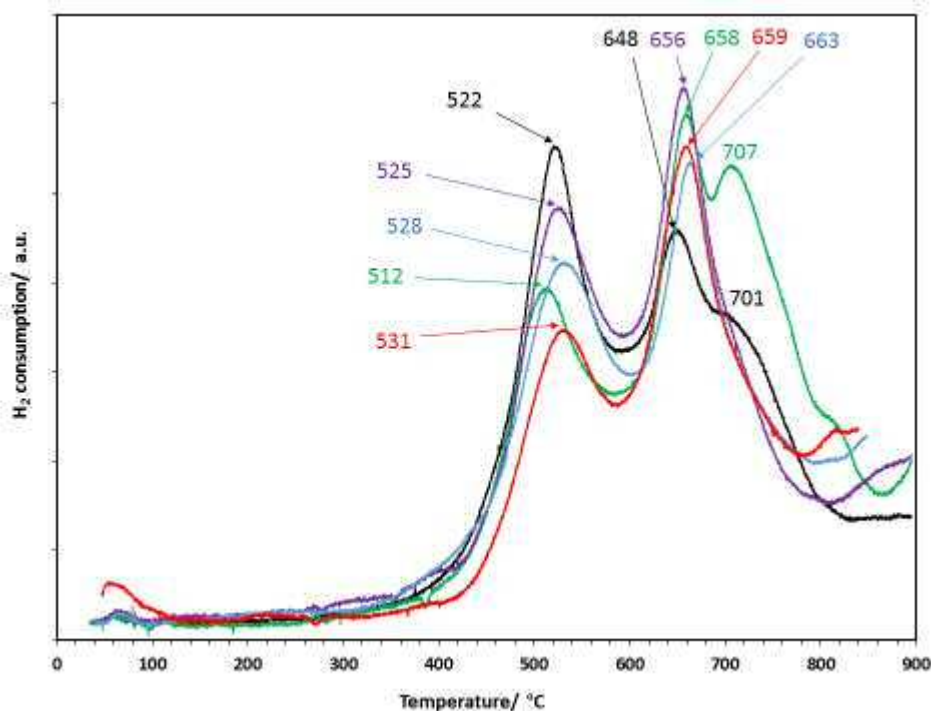


**Figure 4.4** TPR profiles of CZA (black), CLZA (purple), CLA (green), CPA (blue) and CNA (red)

The temperature of peak intensity for the surface cerium reduction occurred at around 520-530 °C, except for CLA which peaked in intensity at 512 °C. The areas under these peaks were calculated in order to determine the relative reducibility of the catalysts' surface cerium ions. Table 4.4 shows the areas of the surface  $\text{Ce}^{4+}$  reduction peaks relative to the largest peak, belonging to CZA. This showed reduction of  $\text{Ce}^{4+}$  ions on the surfaces of CLZA and CPA were comparable to that of CZA (although the contribution of  $\text{Pr}^{4+}$  reduction could not be determined in the case of CPA), and that the same reduction occurred to a much lesser extent in the case of CLA and CNA.

**Table 4.4** Summary of surface reduction properties of CMA catalysts

Catalyst	Peak surface reduction temp (°C)	Relative intensity	
		Peak	Area
CZA	522	1	1
CLZA	525	0.87	0.98
CLA	512	0.70	0.71
CPA*	528	0.75	0.94
CNA	531	0.61	0.67

\*Figures for CPA may include reduction of  $\text{Pr}^{4+}$

Thermogravimetric analysis revealed that a mass loss occurred between 650 °C and 750 °C in each of the catalysts, as shown in the dTG plots in figure 4.5. This could be attributed to the decomposition of polycarbonates and other contaminants within the bulk structure of the catalysts<sup>16</sup>, possibly as a result of sodium species that were unable to be removed during the washing and calcination stages of catalyst preparation. In the case of CLA this could also be linked to the presence of the lanthanum carbonate species detected by XRD<sup>17</sup>. It is likely that the peaks observed at a similar temperature range on the TPR plots were also caused by this, since the decomposition of carbonates to CO<sub>2</sub> and H<sub>2</sub>O would result in H<sub>2</sub> consumption<sup>18</sup>.

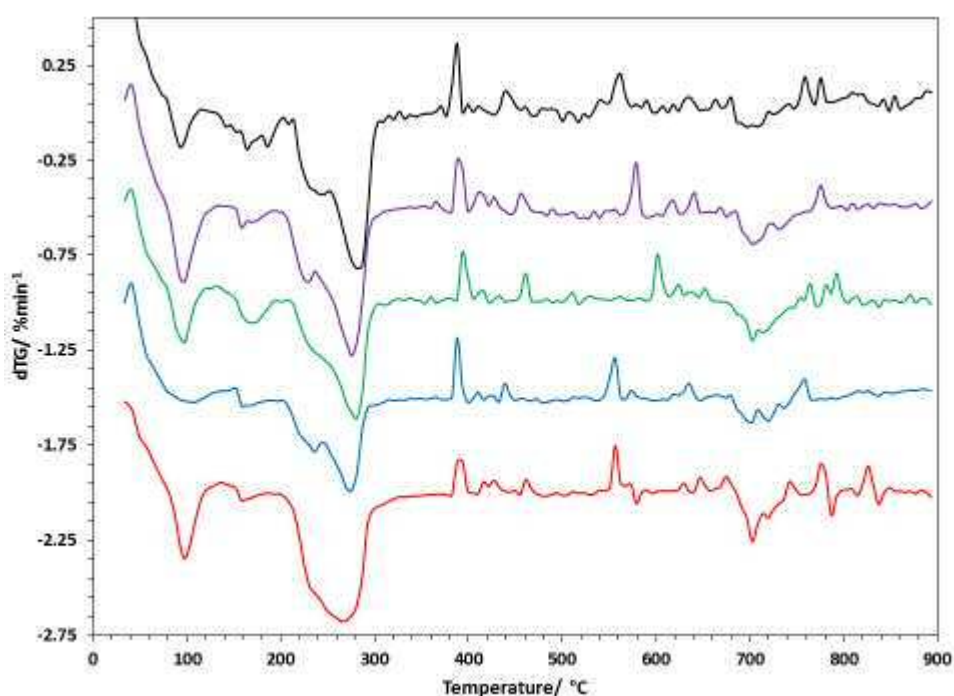


**Figure 4.5** dTG plots of CZA (black), CLZA (purple), CLA (green), CPA (blue) and CNA (red)

#### 4.1.2 Soot oxidation testing

Each of the catalysts were tested for soot oxidation using thermogravimetric analysis as in Chapter 3. The dTG plots of these tests are shown in figure 4.6, offset by 1 %min<sup>-1</sup> for ease of comparison, and the key soot oxidation temperatures extracted from these plots are presented in table 4.5.

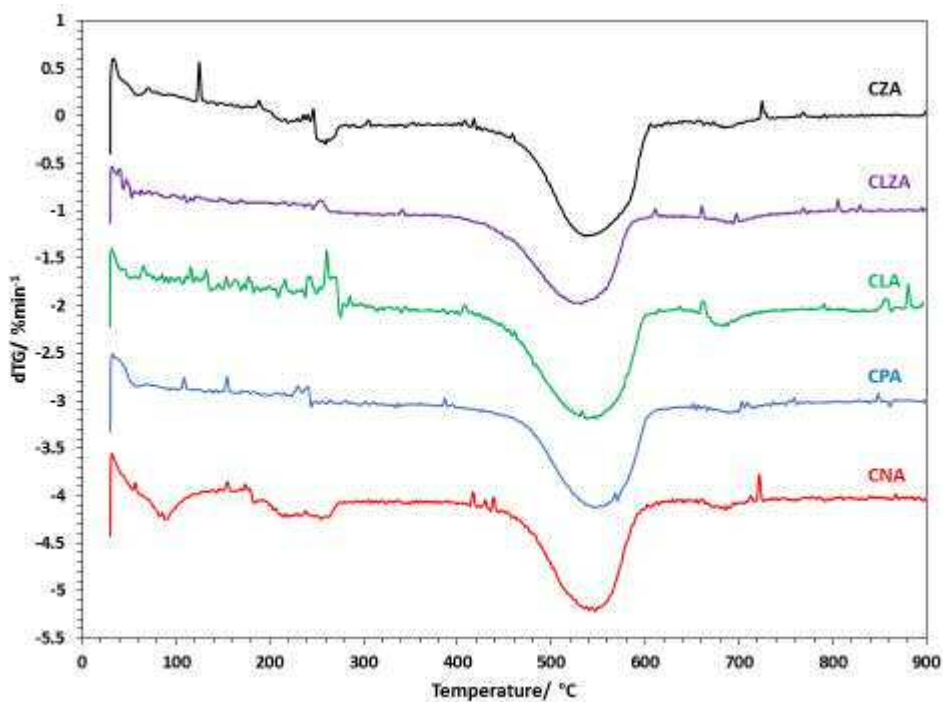


**Figure 4.6** dTG plots of catalyst/soot mixtures containing: CZA (black), CLZA (purple), CLA (green), CPA (blue) and CNA (red)

Each of the CMA materials were found to be catalytically active for soot oxidation, decreasing the onset, peak and final temperatures in each case. The lowest peak soot oxidation temperature was observed in the presence of CLZA, which was at least 10°C lower than with any of the other catalysts, and the only one able to lower this temperature below 540 °C. The lowest extrapolated onset temperature was also observed with this catalyst, followed by CLA, both of which were considerably lower than CZA, CPA and CNA which were all above 460°C. In each case soot oxidation was observed to begin slowly before accelerating rapidly towards a peak rate. Since the rate of soot oxidation was so low during this initial stage, the  $T_{eo}$  was deemed a more significant measure of the catalysts' soot oxidation activity than the  $T_o$ .



**Table 4.5** Soot oxidation temperatures of samples mixed with CMA catalysts on their first and second use

Catalyst	T <sub>o</sub> (°C)		T <sub>eo</sub> (°C)		T <sub>p</sub> (°C)		T <sub>f</sub> (°C)	
	1 <sup>st</sup> run	2 <sup>nd</sup> run	1 <sup>st</sup> run	2 <sup>nd</sup> run	1 <sup>st</sup> run	2 <sup>nd</sup> run	1 <sup>st</sup> run	2 <sup>nd</sup> run
<b>Soot (no catalyst)</b>	465		535		<b>622</b>		651	
<b>CZA</b>	410	389	461	436	<b>542</b>	<b>538</b>	605	597
<b>CLZA</b>	399	391	439	449	<b>531</b>	<b>534</b>	607	610
<b>CLA</b>	415	380	448	430	<b>541</b>	<b>539</b>	615	598
<b>CPA</b>	398	393	463	470	<b>544</b>	<b>549</b>	616	603
<b>CNA</b>	405	383	464	451	<b>547</b>	<b>525</b>	617	581

The thermal stability of the catalysts was tested by repeating soot oxidation testing with the used samples. The dTG plots comparing the soot oxidation on first and second use are shown in figure 4.7. From the data extracted from these plots in table 4.5 it was observed that the catalysts were able to maintain their soot oxidation activity, with no significant increase in temperature from the first run. Interestingly in the case of CNA, the soot oxidation temperature was seen to decrease compared to the initial testing, which suggested an increase in catalytic activity on second use. This improvement, in which peak soot oxidation was reached at a temperature of 525 °C – the lowest observed in any of the catalysts – was investigated further and is discussed in sections 4.6 and 4.7 of this chapter.

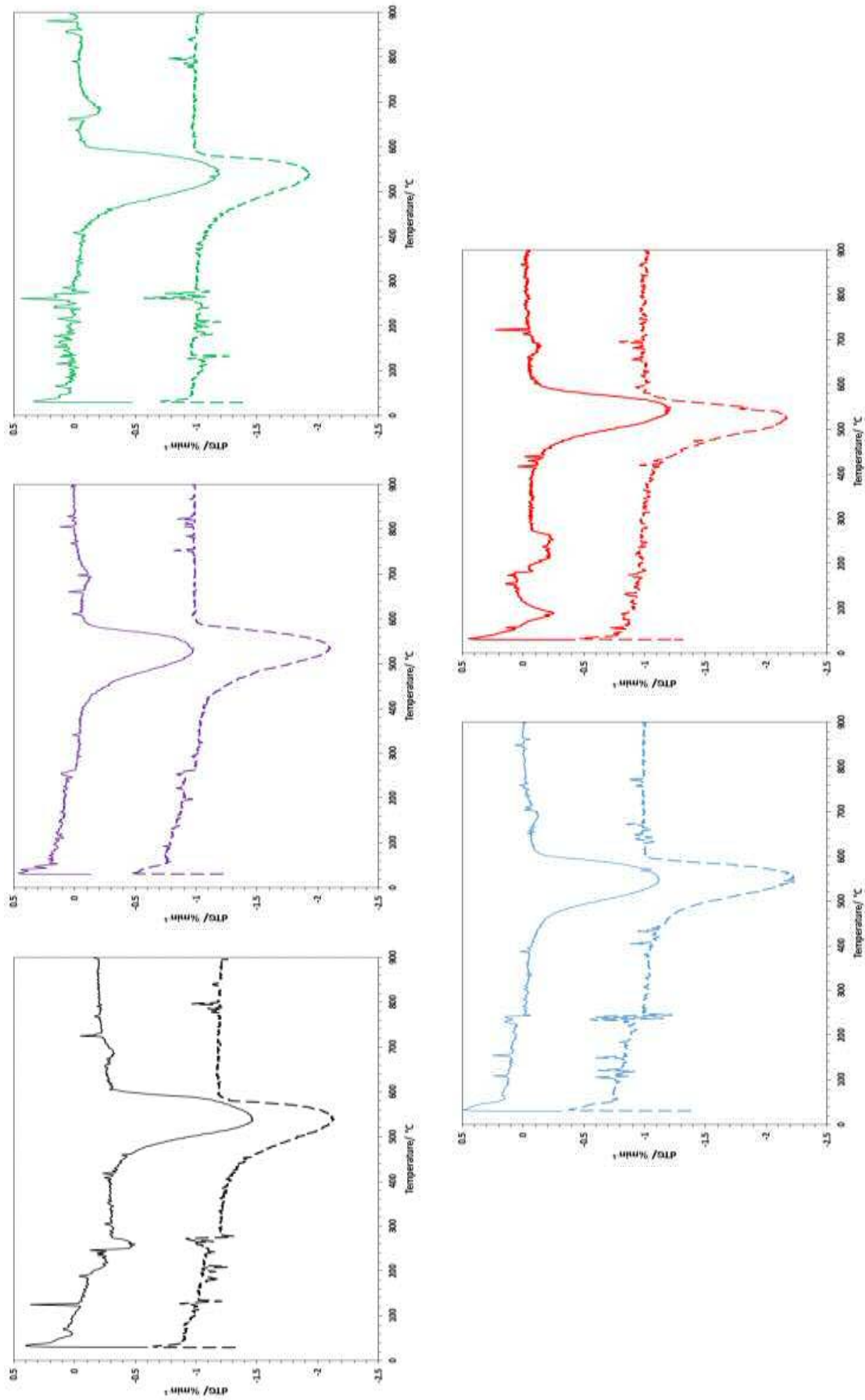


**Figure 4.7** dTG plots of catalyst/soot mixtures containing: CZA (black), CLZA (blue), CPA (purple), CLA (green), CNA (red) on the first run (solid line) and second run (dashed line)

## 4.2 Varying Ce:Zr ratio of CZA

Two additional CZA catalysts – in 5:5:10 and 3:7:10 ratios – were prepared by the same co-precipitation method as above. These were characterised and tested for comparison with the CZA catalyst in section 4.1. The catalysts are referred to according to their Ce:Zr:Al ratios.

### 4.2.1 Characterisation

Each of the catalysts were characterised and tested as in the previous section.

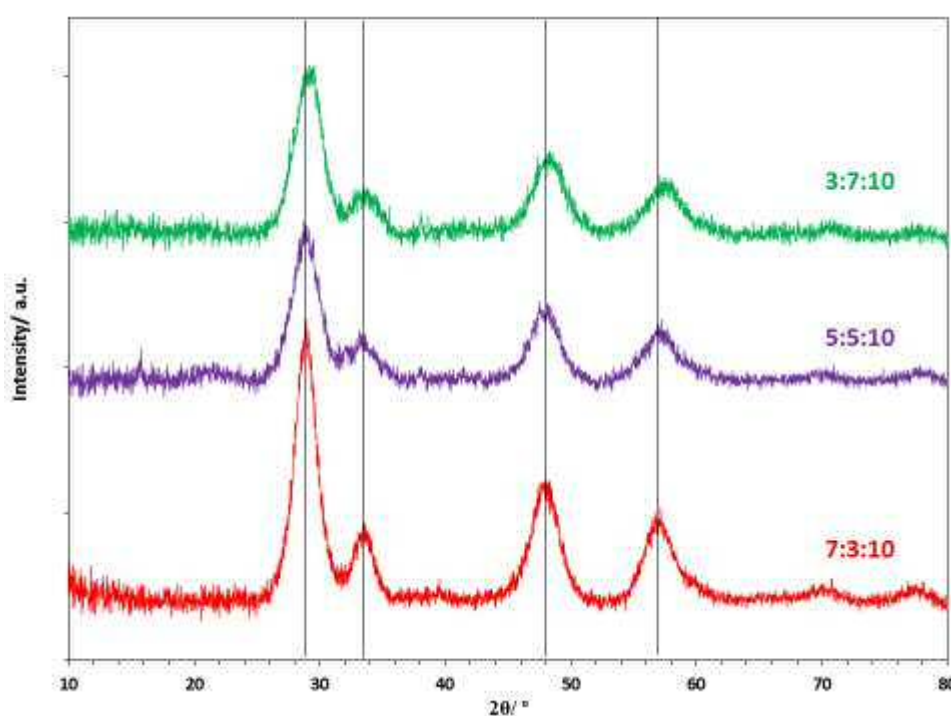


**Figure 4.8** X-ray diffractograms of CZA catalysts; 3:7:10 (green), 5:5:10 (purple) and 7:3:10 (red). Black lines indicate peak shift from CZA 7:3:10

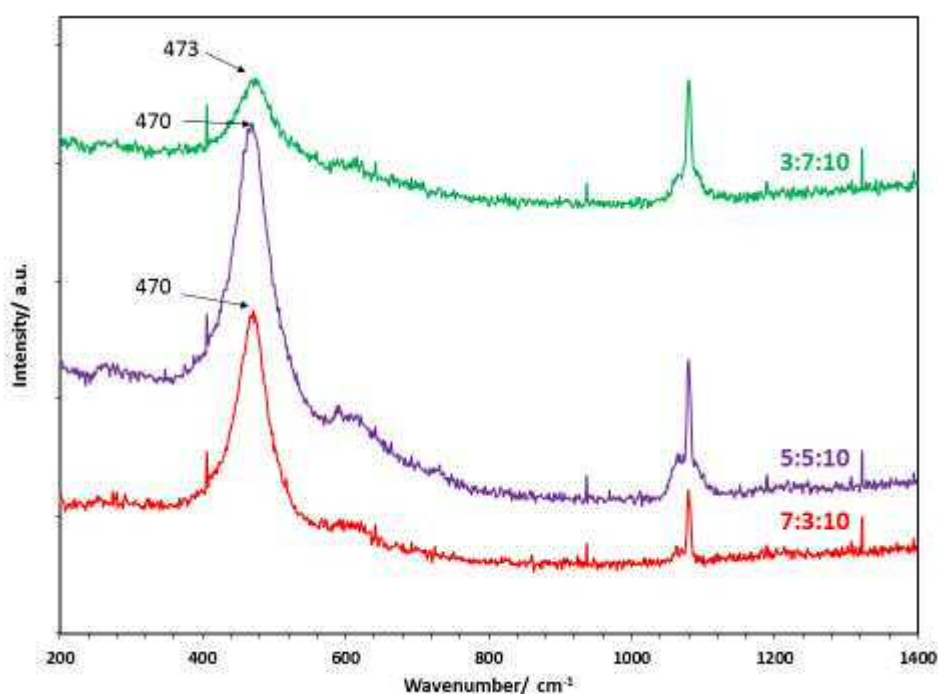
The familiar ceria reflections were observed in each of the X-ray diffractograms of the CZA catalysts in figure 4.8, however the increase in zirconium content resulted in shifts to higher  $2\theta$  values, as shown in table 4.6. As mentioned in the previous section, this is caused by contraction of the ceria lattice brought about by the incorporation of the smaller  $Zr^{4+}$  ions<sup>7</sup>. It was also observed that an increase in the zirconium content resulted in a decrease to the ceria crystallite. No evidence of additional phases was observed, indicating homogeneity of the ceria-zirconia structure in each case.

**Table 4.6** Peak positions and crystallite sizes of CZA catalysts determined by XRD

Catalyst	2 theta (°)				Crystallite size (nm)
	(111)	(200)	(220)	(311)	
Ceria*	28.5	33.1	47.5	56.3	-
7:3:10	28.9	33.5	48.0	57.1	4.1
5:5:10	28.9	33.5	48.1	57.3	3.4
3:7:10	29.2	33.6	48.3	57.5	3.3

\*2 theta values of ceria referenced from JCPDS database (card no. 071-4199)

The  $F_{2g}$  mode of ceria was observed in each of the Raman spectra of the CZA catalysts, as labelled in figure 4.9. As stated previously, the incorporation of zirconium causes a contraction of the ceria lattice, increasing the frequency of the Ce-O stretching mode. This peak was centred at  $470\text{ cm}^{-1}$  for both CZA 7:3:10 and 5:5:10, shifted from the  $460\text{ cm}^{-1}$  value reported for pure ceria<sup>12,13</sup>. The peak for CZA 3:7:10 was shifted further; centred at  $473\text{ cm}^{-1}$ , indicating a greater incorporation of zirconium. The intensity of this peak was also significantly lower in the case of CZA 3:7:10, reflecting the decrease in ceria ratio.

**Figure 4.9** Raman spectra of CZA catalysts; 3:7:10 (green), 5:5:10 (purple) and 7:3:10 (red)

Further analysis by XPS and BET was carried out in order to characterise the surface properties of the CZA catalysts. The elemental composition and areas of the catalysts' surfaces are provided in table 4.7. It was observed that CZA 5:5:10 had a lower surface area than CZA 7:3:10 and 3:7:10. Other than the expected increase/decrease in cerium and zirconium, varying the Ce:Zr ratio did not have a significant effect on the elemental composition of the catalysts' surfaces.

**Table 4.7** Surface properties of CZA catalysts provided by XPS and BET analyses

Catalyst	Atomic conc. (%)						Surface area (m <sup>2</sup> g <sup>-1</sup> )
	Ce 3d	Zr 3d	Al 2p	O 1s	C 1s	Na 1s	
<b>7:3:10</b>	6.22	1.27	17.03	51.51	7.25	16.73	36 (±1)
<b>5:5:10</b>	4.05	1.43	18.34	51.30	7.18	17.70	21 (±0)
<b>3:7:10</b>	2.68	2.56	19.14	49.80	6.37	19.45	37 (±1)

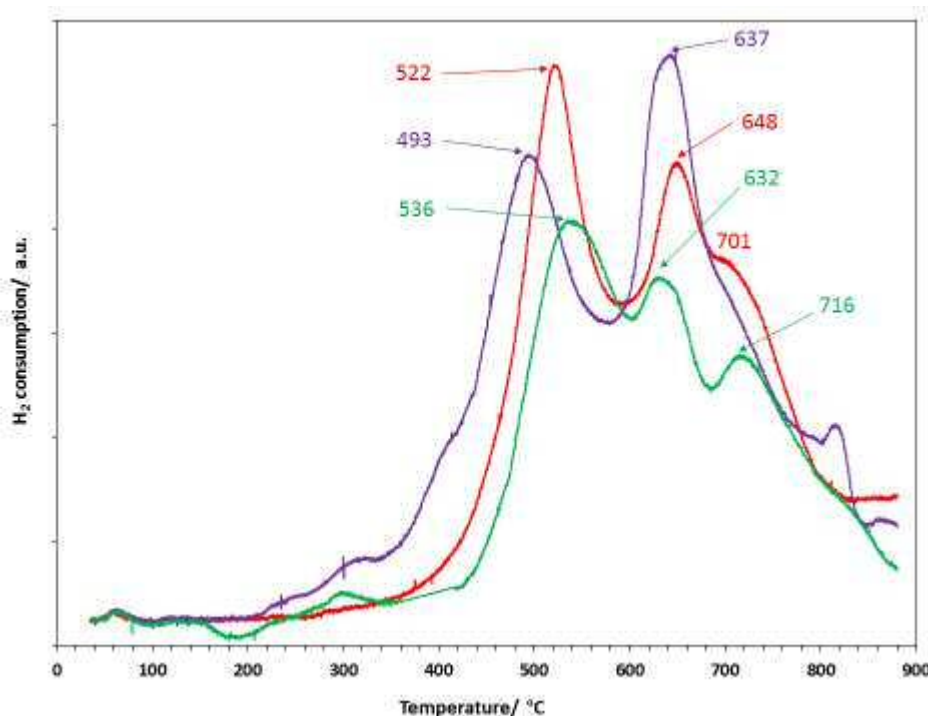
As with CZA 7:3:10, table 4.8 shows that the proportion of zirconium was lower in each case than anticipated from the catalyst preparation, while the proportion of aluminium greater than expected. The Ce 3d regions showed that the proportion of Ce(III) was similar in both CZA 7:3:10 and 3:7:10, however an increase was observed in the case of CZA 5:5:10.

**Table 4.8** Atomic ratio of metals on CZA catalyst surfaces

Catalyst	Ce:Zr:Al	Ce:Zr	Ce(III):Ce(IV)
<b>CZA 7:3:10</b>	5.1 : 1.0 : 13.9	8.3 : 1.7	0.14 : 1
<b>CZA 5:5:10</b>	3.4 : 1.2 : 15.4	7.3 : 2.7	0.17 : 1
<b>CZA 3:7:10</b>	2.2 : 2.1 : 15.7	5.1 : 4.9	0.13 : 1

The TPR profiles of the CZA catalysts are shown in figure 4.10. It was observed in each case that the catalysts produced multiple reduction peaks. An initial peak in the range of 350 °C to 600 °C was attributed to the reduction of surface cerium ions, and the peaks ranging from 600-800 °C were a combination of the reduction of cerium ions from within the bulk

structures, as well as the decomposition of carbonates and other impurities from the materials<sup>18</sup>.



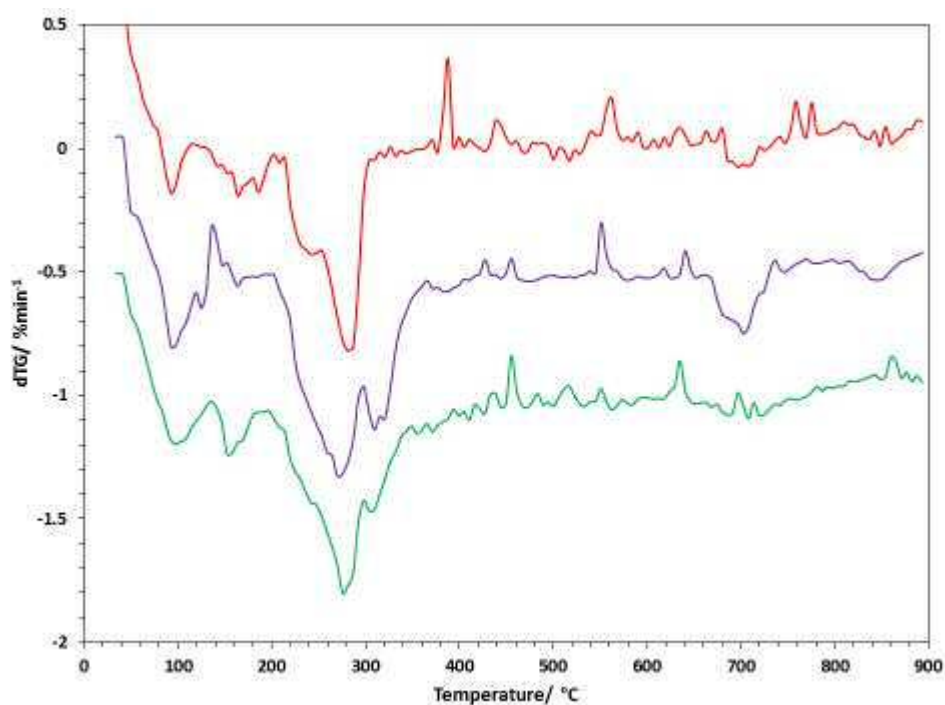
**Figure 4.10** TPR profiles of CZA catalysts; 3:7:10 (green), 5:5:10 (purple) and 7:3:10 (red)

Table 4.9 summarises the data obtained for surface cerium reduction from the TPR profiles. The lowest temperature of surface  $\text{Ce}^{4+}$  reduction was observed in CZA 5:5:10, which reached peak intensity at 493 °C, significantly lower than CZA 7:3:10 (522 °C) and 3:7:10 (536 °C). The intensity at peak reduction was highest for CZA 7:3:10, followed by 5:5:10 and 3:7:10 respectively. However when the total area of the curves were calculated it was observed that CZA 5:5:10 was the most reducible of the CZA catalysts.

**Table 4.9** Summary of surface reduction properties of CZA catalysts

Catalyst	Peak reduction temp (°C)	Relative intensity	
		Peak	Total Area
<b>7:3:10</b>	522	1	<b>1</b>
<b>5:5:10</b>	493	0.83	<b>1.13</b>
<b>3:7:10</b>	536	0.72	<b>0.80</b>

The peaks observed in the 650-800 °C region consisted of a major peak, centred at 648 °C, 637 °C and 632 °C for CZA 7:3:10, 5:5:10 and 3:7:10 respectively. This peak contained a prominent shoulder, centred at 701 °C for CZA 7:3:10, and a less prominent shoulder in a similar region for CZA 5:5:10. In the case of CZA 3:7:10, there was less overlap between peaks in this region, therefore revealing a distinct peak centred at 716 °C.



**Figure 4.11** dTG plots of CZA catalysts; 7:3:10 (red) 5:5:10 (purple) and 3:7:10 (green)

As explained in section 4.1.1, it was difficult to determine to what extent the apparent reduction taking place in this temperature range could be attributed to the reduction of bulk cerium ions. Once again, thermogravimetric analysis was performed on the catalysts which, as can be seen from the dTG plots in figure 4.11, revealed that a mass loss in the temperature range 650-750 °C occurred in each case. As mentioned previously, this mass loss can be attributed to the decomposition of polycarbonates and other impurities within the bulk structure<sup>16</sup>. The loss of mass at this temperature range was most prominent in the case of CZA 5:5:10, and could explain the high intensity of the TPR peak observed between 600-750 °C relative to the other CZA catalysts, due to the reduction of the carbonate species to CO<sub>2</sub> and H<sub>2</sub>O<sup>18</sup>.

### 4.2.2 Soot oxidation testing

The CZA catalysts were each tested for soot oxidation by thermogravimetric analysis. The derivative plots are presented in figure 4.12, with each of the samples offset by  $1\ \text{\%min}^{-1}$  for ease of comparison.

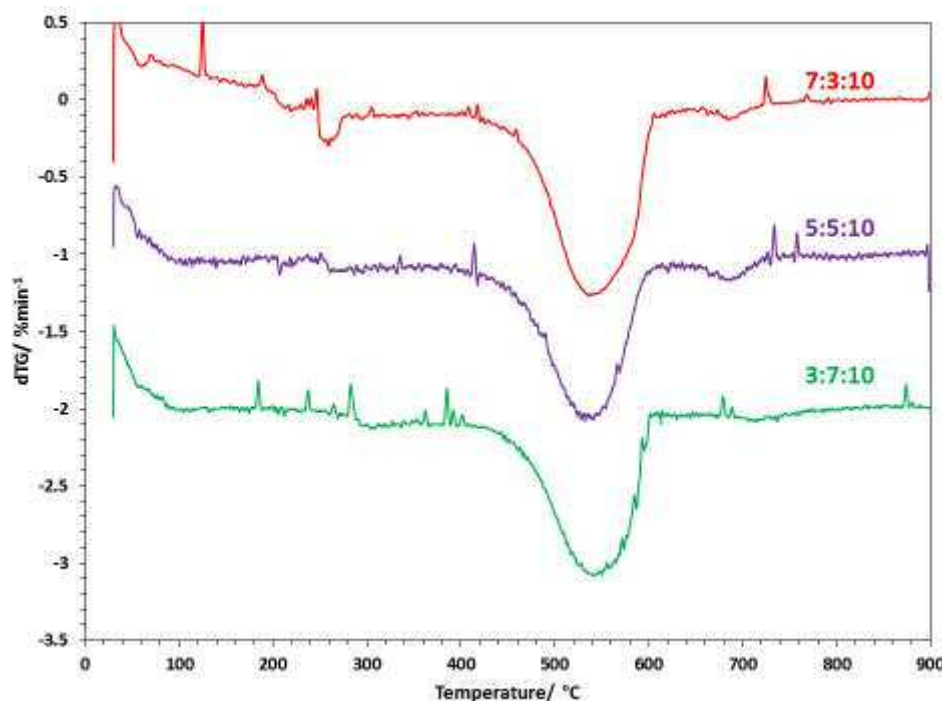


**Figure 4.12** dTG plots of catalyst/soot mixtures containing CZA: 7:3:10 (red), 5:5:10 (purple) and 3:7:10 (green)

The greatest decrease in soot oxidation temperature was observed in the case of CZA 5:5:10 which, as shown in table 4.10, lowered the onset and peak temperatures by around  $10\ \text{°C}$  further than CZA 7:3:10 and 3:7:10. This improvement in catalytic activity was attributed to the findings of TPR, which established that  $\text{Ce}^{4+}$  ions on the surface of CZA 5:5:10 were able to reduce at lower temperatures and higher intensity than the other CZA catalysts. This allowed the redox mechanism described in chapter 1 to take place at a lower temperature, increasing the concentration of liberated lattice oxygen at the catalyst/soot interface and allowing the capture and conversion of  $\text{O}_2$  from the gas-phase into more reactive oxygen species<sup>19,20</sup>.



**Table 4.10** Soot oxidation temperatures of samples mixed with CZA catalysts on their first and second use

Catalyst	$T_o$ (°C)		$T_{eo}$ (°C)		$T_p$ (°C)		$T_f$ (°C)	
	1 <sup>st</sup> run	2 <sup>nd</sup> run	1 <sup>st</sup> run	2 <sup>nd</sup> run	1 <sup>st</sup> run	2 <sup>nd</sup> run	1 <sup>st</sup> run	2 <sup>nd</sup> run
Soot (no catalyst)	465		535		622		651	
7:3:10	410	389	461	436	542	538	605	597
5:5:10	396	400	452	456	532	532	607	597
3:7:10	415	408	465	474	542	543	601	594

The test was repeated with fresh soot in order to determine the catalysts durability on repeated use. The dTG plots of these tests are shown in figure 4.13.

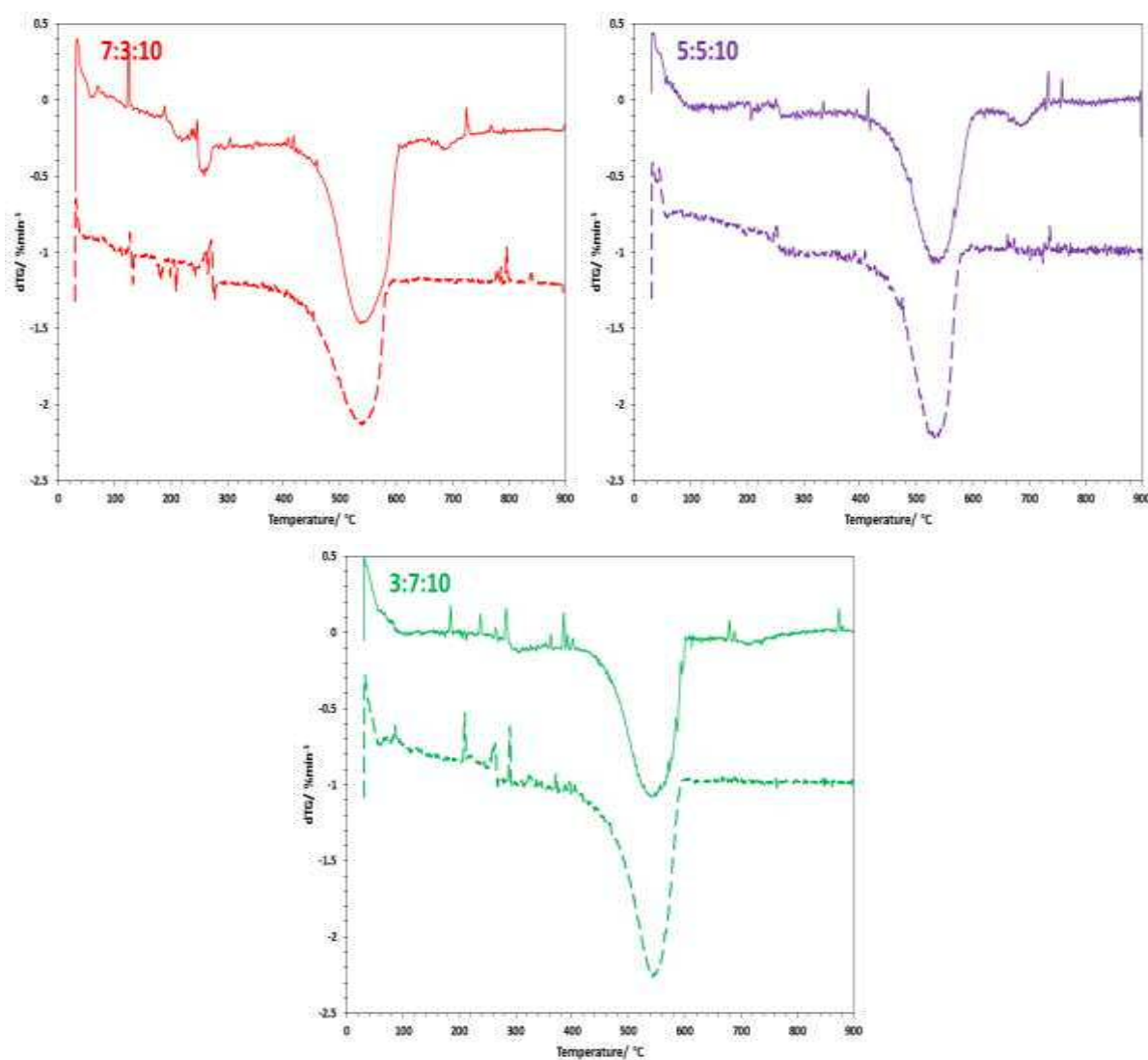


**Figure 4.13** dTG plots of catalyst/soot mixtures containing: CZA: 7:3:10 (red), 5:5:10 (purple) and 3:7:10 (green), on the first run (solid line) and second run (dashed line)

Each of the catalysts showed good thermal stability, managing to maintain similar soot oxidation temperatures on their second run as in their first, with the  $T_{e0}$  of CZA 3:7:10 showing the only meaningful increase. This provided evidence that the higher activity of CZA 5:5:10 compared to the other catalysts could be sustained over multiple usage.

### 4.3 Varying Ce:(La,Zr) ratio of CLZA

Two additional CLZA catalysts – in Ce:(La,Zr):Al ratios of 5:5:10 and 3:7:10 (La:Zr 1:1 in each case) – were prepared by the same co-precipitation method as above. These were characterised and tested for comparison with the CLZA catalyst in section 4.1. The catalysts are referred to according to their Ce:(La,Zr):Al ratios.

#### 4.3.1 Characterisation

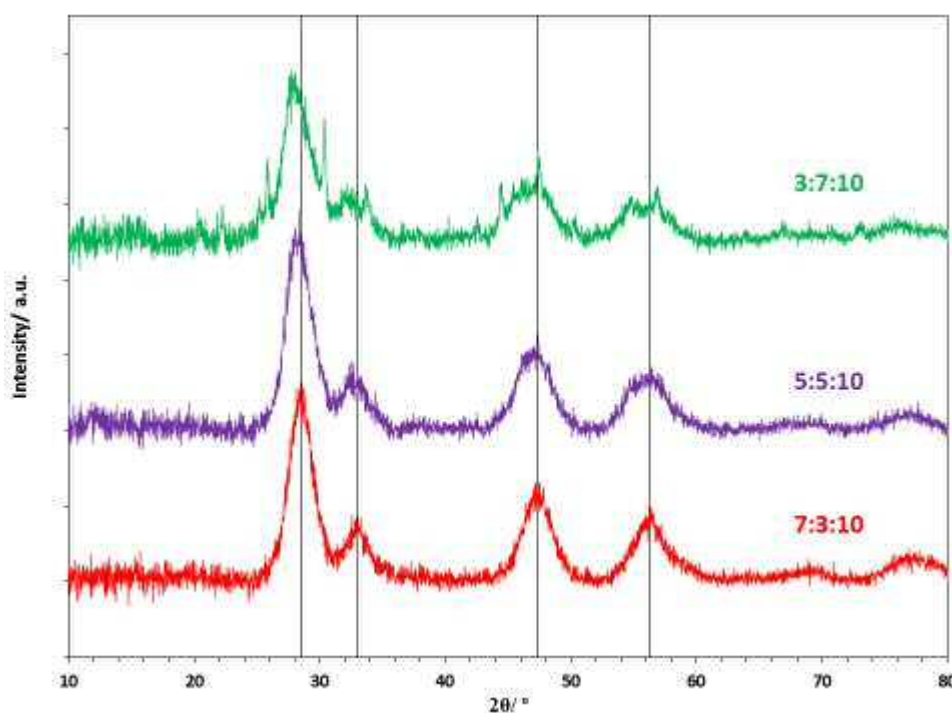


**Figure 4.14** X-ray diffractograms of CLZA catalysts; 3:7:10 (green), 5:5:10 (purple) and 7:3:10 (red). Black lines indicate peak shift from CLZA 7:3:10

The diffractograms of the CLZA catalysts are shown in figure 4.14. As mentioned in section 4.1.1, replacing  $Ce^{4+}$  ions (ionic radius  $\sim 0.96 \text{ \AA}$ ), with  $La^{3+}$  ions (ionic radius  $\sim 1.17 \text{ \AA}$ ) causes expansion of the ceria lattice, while the presence of  $Zr^{4+}$  ions (ionic radius  $\sim 0.84 \text{ \AA}$ ) has the reverse effect. In the case of CLZA 7:3:10 it was shown that this resulted in the positions of

the (111), (200), (220) and (311) reflections remaining similar to those of CeO<sub>2</sub>. This indicated there was no net expansion/contraction to the ceria lattice, which was explained by the effects of La<sup>3+</sup> and Zr<sup>4+</sup> ions negating each other. However, increasing the ratio of lanthanum and zirconium over cerium resulted in the reflections shifting to lower 2 theta values (summarised in table 4.11), indicating overall ceria lattice expansion. This suggested that the increase in lanthanum within the material had a greater effect on the lattice parameter of ceria than the equivalent increase in zirconium. As in the case of CZA, a reduction in the cerium content within the materials corresponded to a decrease in the crystallite size.

Additional reflections were observed in the case of CLZA 3:7:10, most prominently at 22.3°, 25.8°, 30.3°, 44.5°, 47.5° and 56.8°. As in the case of CLA 7:3:10 described in section 4.1.1, these were matched with a reference for lanthanum oxide carbonate (La<sub>2</sub>O<sub>2</sub>CO<sub>3</sub> JCPDS card no. 37-0804). This revealed that lanthanum was present in a separate phase from ceria, however was only detectable by XRD at higher lanthanum concentrations.

**Table 4.11** Peak positions and crystallite sizes of CLZA catalysts determined by XRD

Catalyst	2 theta (°)				Crystallite size (nm)
	(111)	(200)	(220)	(311)	
<b>Ceria*</b>	28.5	33.1	47.5	56.3	-
<b>7:3:10</b>	28.5	33.0	47.4	56.4	4.1
<b>5:5:10</b>	28.2	32.8	47.2	56.1	3.9
<b>3:7:10</b>	28.0	32.6	46.9	55.9	2.6

\*2 theta values of ceria referenced from JCPDS database (card no. 071-4199)

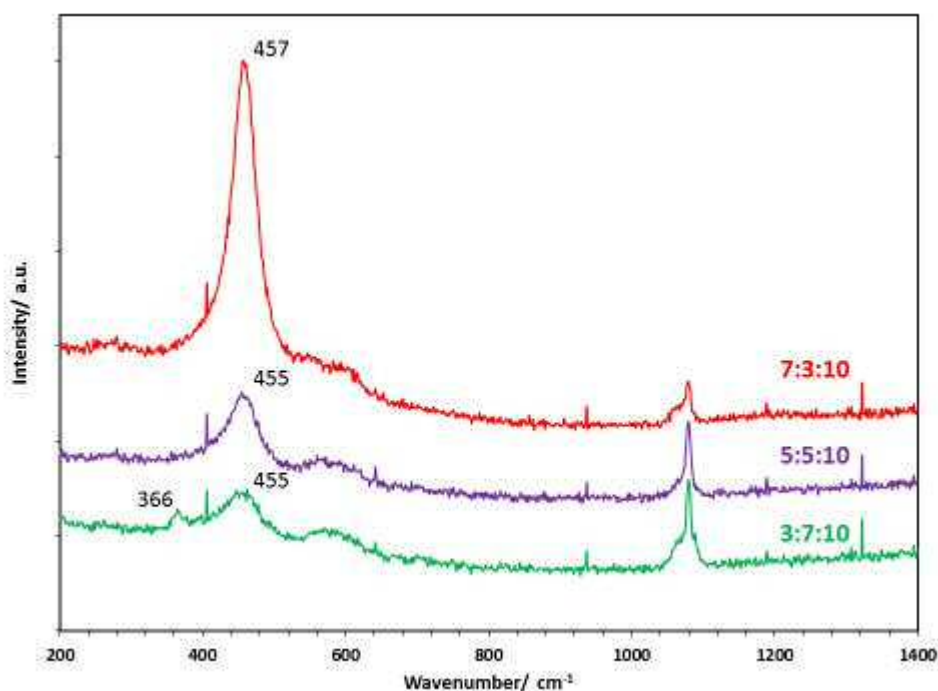


**Figure 4.15** Raman spectra of CLZA catalysts; 3:7:10 (green), 5:5:10 (purple) and 7:3:10 (red)

The Raman spectra of the CLZA catalysts shown in figure 4.15 also demonstrated the influence of the lanthanum ions on the lattice parameter of ceria. In each case the familiar  $F_{2g}$  mode belonging to ceria was shifted to a lower frequency than that found in pure ceria ( $460\text{ cm}^{-1}$ ). In CLZA 7:3:10 this peak was centred at  $457\text{ cm}^{-1}$ , and a further shift to  $455\text{ cm}^{-1}$  was observed when the lanthanum content was increased further in CLZA 5:5:10 and 3:7:10. It was also observed that the intensity of this peak diminished as a result of the decreasing ceria content of the catalysts. A low intensity band was observed at  $366\text{ cm}^{-1}$  in the spectrum of CLZA 3:7:10, which could be attributed to  $\text{La}_2\text{O}_2\text{CO}_3$ , as detected by XRD<sup>21,22</sup>.

The catalysts were analysed by XPS and BET in order to determine their surface properties, the elemental compositions and surface areas are provided in table 4.12. It was again determined that the presence of sodium impurities (confirmed by XPS) were more likely responsible for the variations in surface area than any trend concerning the composition of dopant metals. The quantification of the elements showed that cerium, zirconium, lanthanum and aluminium accounted for around a quarter of the composition of the surface in each case.

**Table 4.12** Surface properties of CLZA catalysts provided by XPS and BET analyses

Catalyst	Atomic conc. (%)							Surface area (m <sup>2</sup> g <sup>-1</sup> )
	Ce 3d	Zr 3d	La 3d	Al 2p	O 1s	C 1s	Na 1s	
<b>7:3:10</b>	5.49	0.40	1.46	19.59	51.15	6.62	15.29	40 (±1)
<b>5:5:10</b>	3.43	0.64	2.53	18.35	51.98	6.44	16.63	46 (±0)
<b>3:7:10</b>	2.59	0.59	2.57	18.96	51.43	6.73	17.13	36 (±0)

The ratios of the metals showed there was a large excess of aluminium on the surfaces of the CLZA catalysts. An excess of Ce over (La,Zr) was observed on each of the catalysts, however the La:Zr ratio suggested this was due to a deficiency in zirconium on the surface rather than lanthanum. The proportion of cerium in the +3 oxidation remained constant between CLZA 7:3:10 and 5:5:10, however decreased in favour of Ce(IV) in CLZA 3:7:10.

**Table 4.13** Atomic ratio of metals on CLZA catalyst surfaces

Catalyst	Ce:(La,Zr):Al	Ce:(La,Zr)	La:Zr	Ce(III)/Ce(IV)
<b>CLZA 7:3:10</b>	4.1 : 1.4 : 14.5	7.4 : 2.6	1 : 0.27	0.17 : 1
<b>CLZA 5:5:10</b>	2.8 : 2.5 : 14.7	5.2 : 4.8	1 : 0.25	0.17 : 1
<b>CLZA 3:7:10</b>	2.1 : 2.6 : 15.3	4.5 : 5.5	1 : 0.23	0.13 : 1

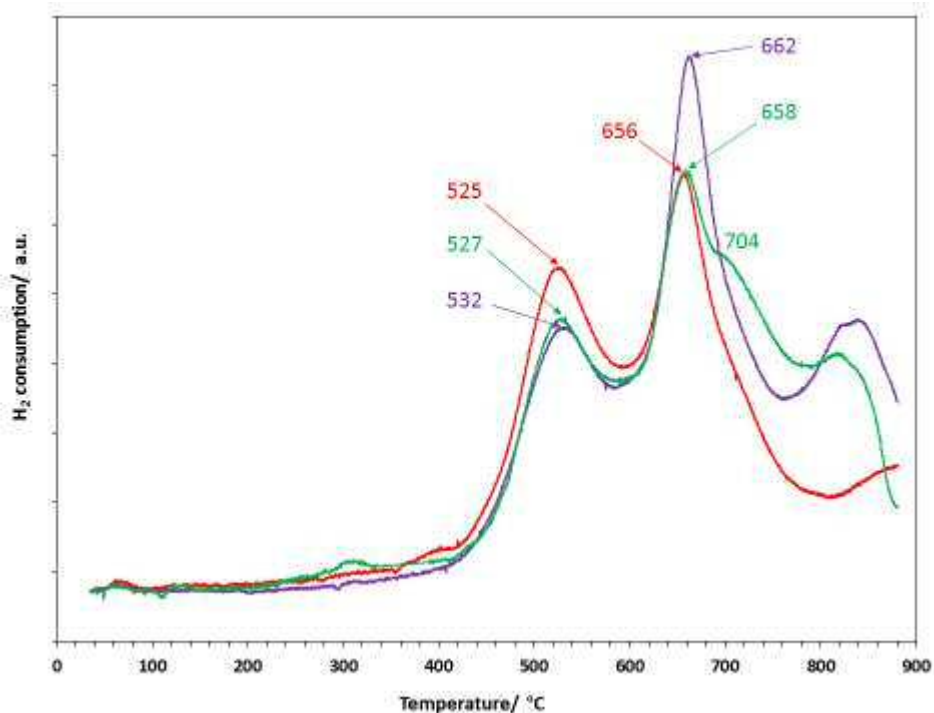


**Figure 4.16** TPR profiles of CLZA catalysts; 3:7:10 (green), 5:5:10 (purple) and 7:3:10 (red)

The TPR profiles of the CLZA catalysts are provided in figure 4.16 and are annotated with the peak temperatures. As with the previous catalysts presented in this chapter, two distinct but partially overlapping curves were observed in each of the catalysts. The initial curve, centred at around 530 °C was attributed to reduction of surface  $\text{Ce}^{4+}$  ions; while the second curve, centred at around 660 °C was believed to be the result of a combination of bulk  $\text{Ce}^{4+}$  reduction, as well as the decomposition of impurities within the catalyst structures.

**Table 4.14** Summary of surface reduction properties of CLZA catalysts

Catalyst	Peak reduction	Relative intensity	
	temp (°C)	Peak	Total Area
<b>7:3:10</b>	525	0.87	<b>0.98</b>
<b>5:5:10</b>	532	0.70	<b>0.83</b>
<b>3:7:10</b>	527	0.73	<b>0.84</b>

The data obtained from the surface cerium reduction peaks are summarised in table 4.14, all of which were calculated relative to the surface  $\text{Ce}^{4+}$  reduction peak of CZA 7:3:10 from section 4.1.1. Peak reduction occurred at similar temperatures in each case, within a narrow

range of 525-532 °C. Unlike CZA, the trend in reducibility did not follow the trend in surface cerium concentration, with CLZA 5:5:10 and 3:7:10 showing similar reduction profiles despite the difference in quantities of cerium. This observation suggested that increasing the La,Zr content of the material increased the ability of  $\text{Ce}^{4+}$  ions to reduce to  $\text{Ce}^{3+}$ .

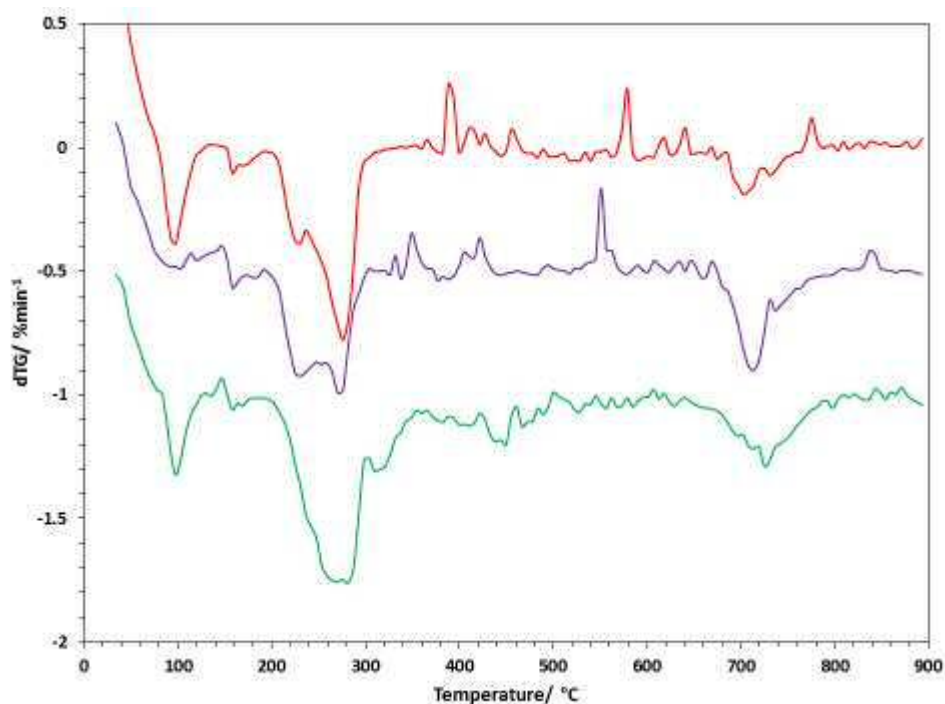


**Figure 4.17** dTG plots of CLZA catalysts; 7:3:10 (red) 5:5:10 (purple) and 3:7:10 (green)

As with the CZA catalysts in section 4.2.1, the thermogravimetric analysis of the CLZA catalysts, provided in the form of the derivative plots in figure 4.17, showed a mass loss between 650-750 °C. This was attributed to the decomposition of impurities from the bulk structures of the catalysts, including carbonate species. As with the CZA catalysts, this decomposition was also attributed to the reduction peak observed between 600-750 °C in the TPR profiles of the catalysts. This is supported by the relative intensities of these reduction peaks, which were comparable for both CLZA 7:3:10 and 3:7:10 corresponding to a similar mass loss in the dTG plots of the catalysts. It was observed that this reduction peak was of higher intensity in the case of CLZA 5:5:10, and this also corresponded to a greater loss of mass in this temperature range observed in the dTG plot. The shoulder peak at 704 °C in the TPR profile of CLZA 3:7:10 may be of the same origin as peaks observed at a similar temperature in the TPR profiles of the CLA catalyst in figure 4.4. This was linked to the presence of  $\text{La}_2\text{O}_2\text{CO}_3$ , and is discussed in greater detail in section 4.4.1.

### 4.3.2 Soot oxidation testing

The CLZA catalysts were each tested for soot oxidation by thermogravimetric analysis in the usual manner. The derivative plots are presented in figure 4.18, with each of the samples offset by  $1\% \text{min}^{-1}$  for ease of comparison.

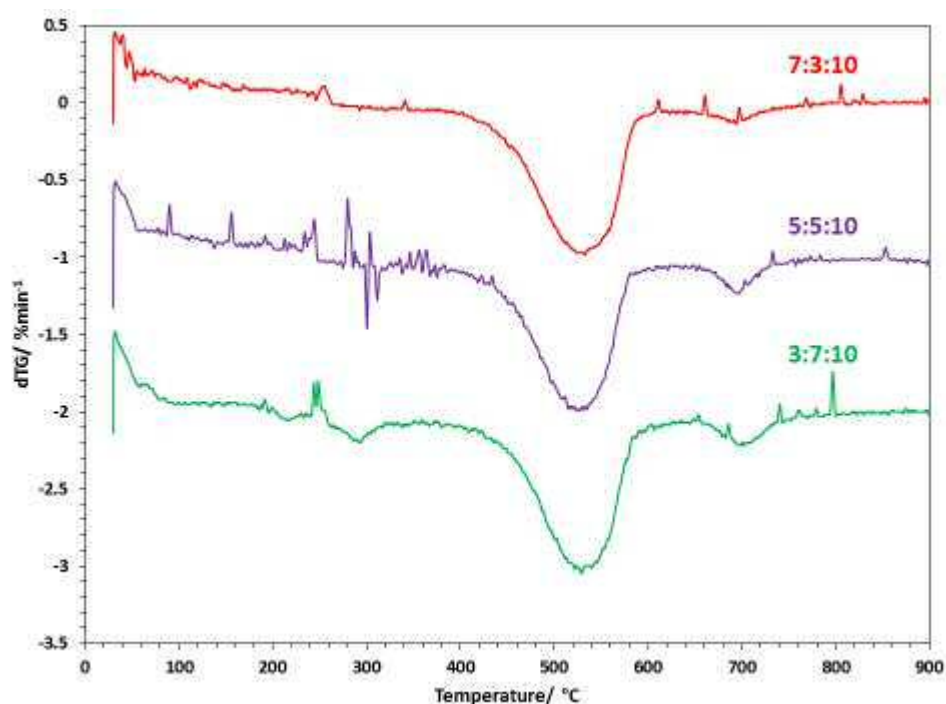


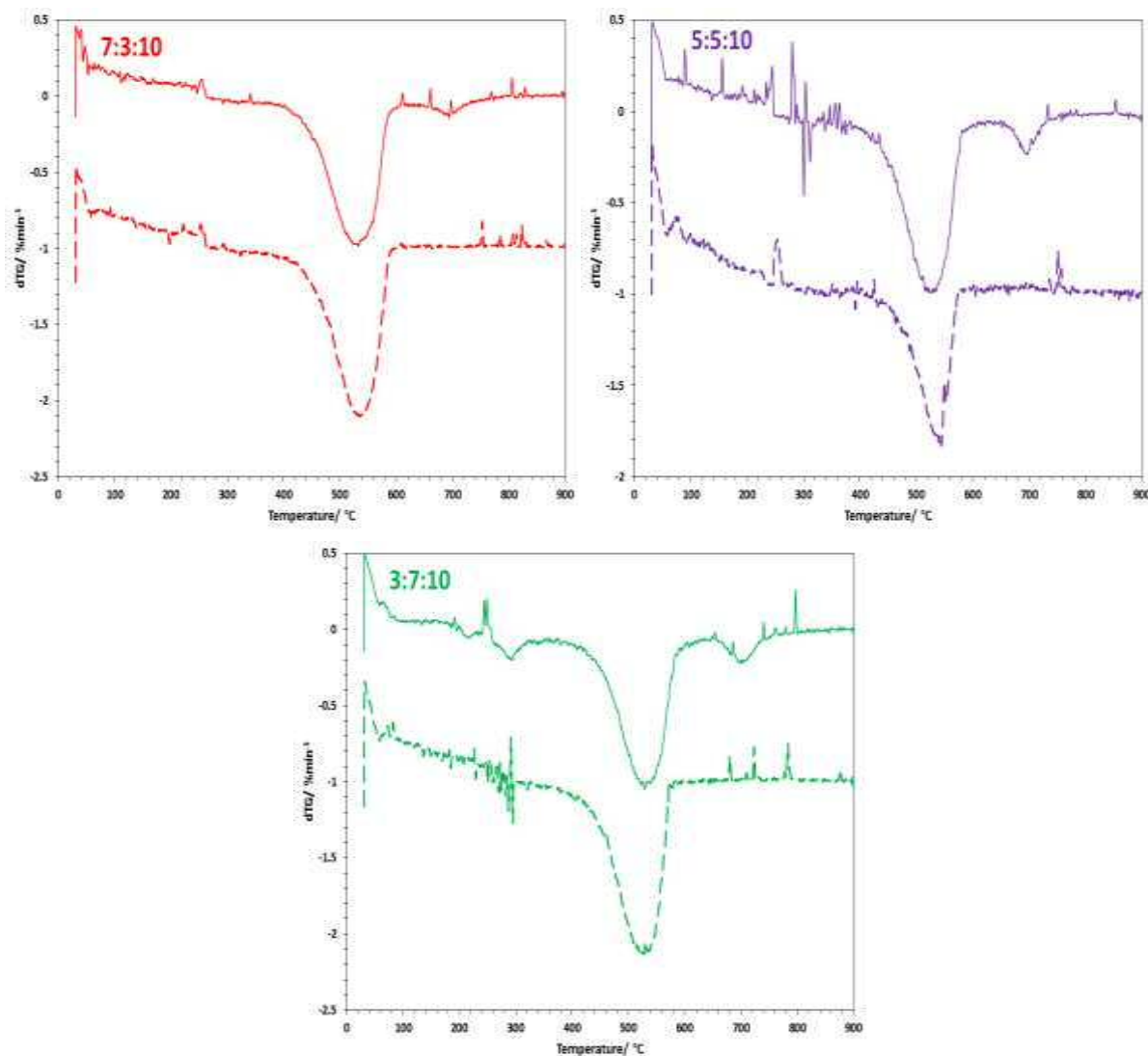
**Figure 4.18** dTG plots of catalyst/soot mixtures containing CLZA: 7:3:10 (red), 5:5:10 (purple) and 3:7:10 (green)

The dTG plots showed that the change in Ce:(Zr,La) ratio had little effect on the soot oxidation activity of the catalysts. The data provided in table 4.15 showed that peak soot oxidation took place at similar temperatures for each of the catalysts, at around 530 °C. The onset and extrapolated onset temperatures were also comparable for each of the catalysts. Interestingly, all three of the CLZA catalysts showed similar activity to CZA 5:5:10 presented in the previous section. In that case, the improved activity was attributed to its low-temperature, high-intensity reduction profile. However the TPR profiles of the CLZA catalysts were unremarkable by comparison, which suggested this was not the only contributing factor to improved catalytic activity.



**Table 4.15** Soot oxidation temperatures of samples mixed with CLZA catalysts on their first and second use

Catalyst	$T_o$ (°C)		$T_{eo}$ (°C)		$T_p$ (°C)		$T_f$ (°C)	
	1 <sup>st</sup> run	2 <sup>nd</sup> run	1 <sup>st</sup> run	2 <sup>nd</sup> run	1 <sup>st</sup> run	2 <sup>nd</sup> run	1 <sup>st</sup> run	2 <sup>nd</sup> run
<b>Soot (no catalyst)</b>	465		535		<b>622</b>		651	
<b>7:3:10</b>	399	391	439	449	<b>531</b>	<b>534</b>	607	603
<b>5:5:10</b>	400	416	440	467	<b>528</b>	<b>539</b>	600	579
<b>3:7:10</b>	393	377	449	438	<b>528</b>	<b>527</b>	603	585

**Figure 4.19** dTG plots of catalyst/soot mixtures containing: CLZA 7:3:10 (red), 5:5:10 (purple) and 3:7:10 (green), on the first run (solid line) and second run (dashed line)

Upon second use (figure 4.19), it was found that CLZA 3:7:10 showed comparable soot oxidation activity to its first use, showing a decrease in onset temperatures and maintaining the peak soot oxidation temperature. However CLZA 5:5:10 demonstrated a loss of activity

on second use. The onset, extrapolated onset and peak temperatures all increased by at least 10 °C compared to the first use with this catalyst.

#### 4.4 Varying Ce:La ratio of CLA

Two additional CLA catalysts – in 5:5:10 and 3:7:10 ratios – were prepared by the same co-precipitation method as above. These were characterised and tested for comparison with the CLA catalyst in section 4.1. The catalysts are referred to according to their Ce:La:Al ratios.

##### 4.4.1 Characterisation

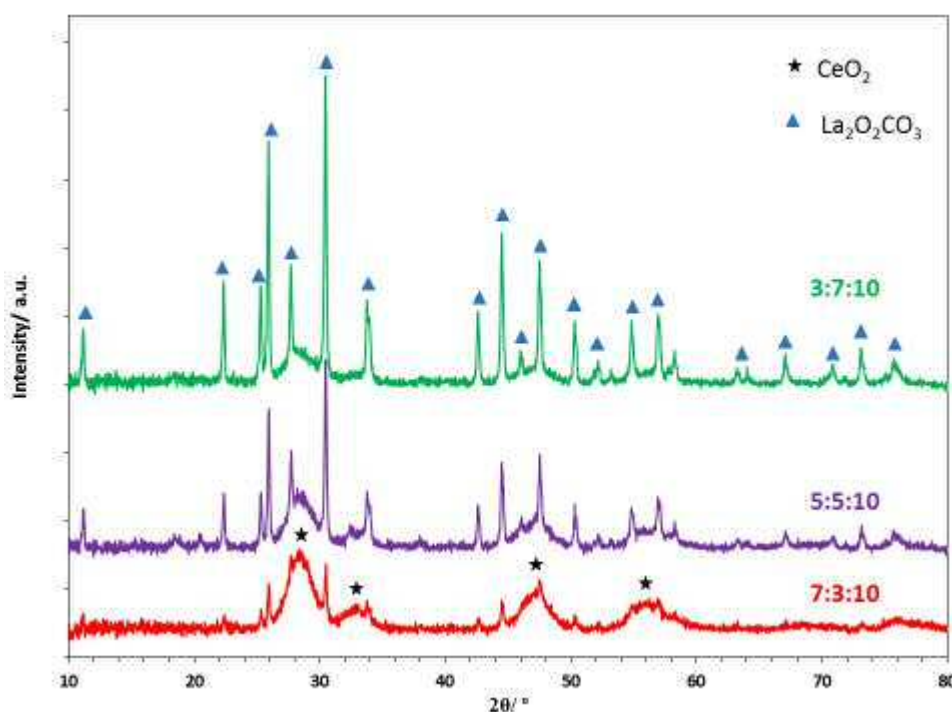


**Figure 4.20** X-ray diffractograms of CLA catalysts; 3:7:10 (green), 5:5:10 (purple) and 7:3:10 (red).

The X-ray diffractograms of the CLA catalysts observed in figure 4.20 indicated the presence of two distinct crystalline phases, the intensities of which varied corresponding to the cerium/lanthanum ratio. The cubic fluorite reflections of ceria were observed at around 28°, 33°, 47° and 56°. It was observed that as the cerium content decreased in favour of lanthanum, these reflections diminished in intensity. Due to the low intensity of the reflections and their overlapping with reflections of the second phase, it was difficult to determine whether there were significant shifts in the 2 theta values between the catalysts.

As in the case of CLZA 3:7:10 mentioned previously, the second phase (the reflections of which are denoted by the blue triangles) was identified as lanthanum dioxycarbonate,  $\text{La}_2\text{O}_2\text{CO}_3$  (JCPDS card no. 37-0804). It was observed that these reflections were sharp, indicating a highly crystalline phase, which increased in intensity from CLA 7:3:10 through to CLA 3:7:10 corresponding to the increase in the lanthanum content. The presence of this phase suggested that lanthanum carbonate formed during co-precipitation was not fully decomposed to lanthanum oxide during the calcination process<sup>17</sup>. As with CLZA, this indicated that the catalysts with higher lanthanum concentrations did not contain a homogenous mixed metal oxide crystalline phase.

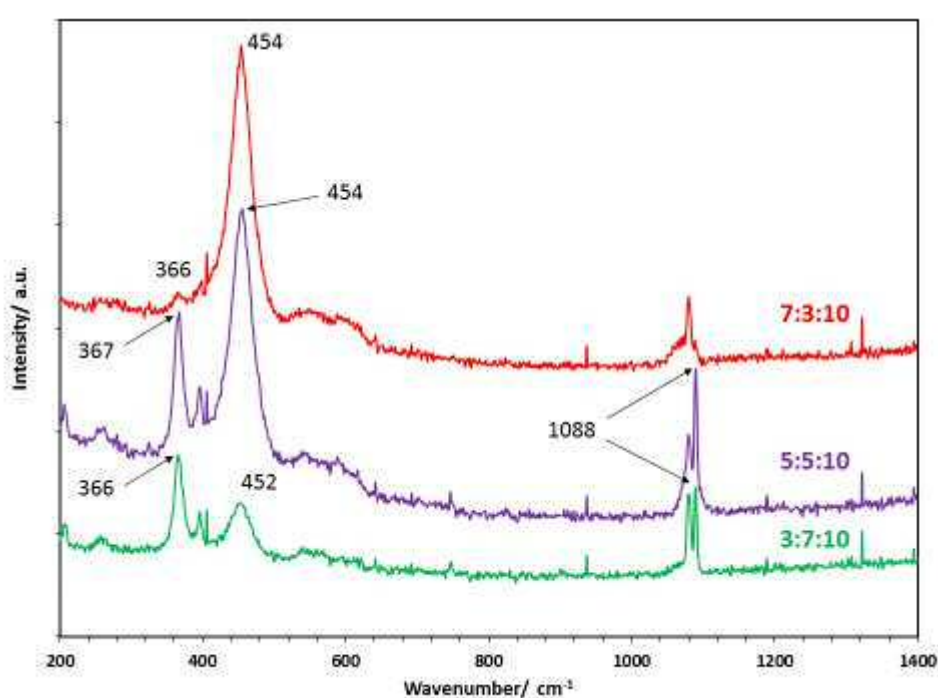


**Figure 4.21** Raman spectra of CLA catalysts; 3:7:10 (green), 5:5:10 (purple) and 7:3:10 (red)

The CLA catalysts were also characterised by Raman, and their spectra are displayed in figure 4.21. Each of the catalysts produced the typical  $\text{F}_{2g}$  mode of ceria. In the case of CLA 7:3:10 and 5:5:10, this peak was centred at 454  $\text{cm}^{-1}$  shifted from the 460  $\text{cm}^{-1}$  value of pure ceria, and for CLA 3:7:10 a further shift to 452  $\text{cm}^{-1}$  indicating disruption of the ceria lattice due to the incorporation of  $\text{La}^{3+}$  ions. There was also a significant decrease in the intensity of this peak in the case of CLA 3:7:10 compared to the others, reflecting the decrease in ceria content within the material.

The Raman spectra of CLA 5:5:10 and 3:7:10 were able to support the findings of the XRD in detecting the presence of  $\text{La}_2\text{O}_2\text{CO}_3$  within the catalyst structures. The peaks at  $366\text{ cm}^{-1}$  and  $1088\text{ cm}^{-1}$  have been reported as typical of  $\text{La}_2\text{O}_2\text{CO}_3$ <sup>21,22</sup>. A smaller peak detected at  $405\text{ cm}^{-1}$  could be attributed to lanthanum oxide,  $\text{La}_2\text{O}_3$ <sup>21</sup>.

The surface properties of the CLA catalysts from XPS and BET analyses are summarised in table 4.16. No trend was observed for the catalysts' surface areas which, as mentioned previously, were most likely influenced by the presence of sodium species plugging pores on the catalyst surface. Other than the expected variations in cerium and lanthanum, no significant changes in elemental composition were observed between the catalysts.

**Table 4.16** Surface properties of CLA catalysts provided by XPS and BET analyses

Catalyst	Atomic conc. (%)						Surface area ( $\text{m}^2\text{g}^{-1}$ )
	Ce 3d	La 3d	Al 2p	O 1s	C 1s	Na 1s	
<b>7:3:10</b>	3.36	1.66	18.18	51.31	7.55	17.94	21 ( $\pm 2$ )
<b>5:5:10</b>	3.03	2.60	18.00	51.19	7.86	17.32	26 ( $\pm 0$ )
<b>3:7:10</b>	2.56	4.32	18.41	51.07	7.15	16.49	23 ( $\pm 0$ )

From the Ce/La/Al ratios calculated from XPS in table 4.17 it was found that there was an excess of aluminium on the surfaces of each of the catalysts. No pattern in the Ce/La ratios could be established, with CLA 7:3:10 containing an excess of lanthanum over cerium, and the reverse being the case for CLA 5:5:10 and 3:7:10. A decrease in the proportion of cerium in the +3 oxidation state was observed as lanthanum was increased, however it remained higher than observed in the CZA and CLZA catalysts.

**Table 4.17** Atomic ratio of metals on CLA catalyst surfaces

Catalyst	Ce:La:Al	Ce:La	Ce(III):Ce(IV)
<b>CLA 7:3:10</b>	4.0 : 2.0 : 14.0	6.7 : 3.3	0.25 : 1
<b>CLA 5:5:10</b>	2.6 : 2.2 : 15.2	5.4 : 4.6	0.21 : 1
<b>CLA 3:7:10</b>	2.0 : 3.4 : 14.6	3.7 : 6.3	0.20 : 1

The TPR analysis conducted on the CLA catalysts provided interesting reduction profiles, which are shown in figure 4.22. As with the catalysts presented in the previous sections, a

reduction curve between 400 °C and 600 °C was observed for each of the CLA catalysts, attributed to the reduction of surface  $\text{Ce}^{4+}$  to  $\text{Ce}^{3+}$ . A second peak centred at around 660 °C, also typical of the catalysts presented so far in this chapter and attributed to the decomposition of structural impurities was also observed for each CLA catalyst. However the most striking observation from the TPR profiles of these catalysts was the presence of a third reduction curve between 700 °C and 900 °C, which showed a significant increase in intensity with increasing lanthanum content.

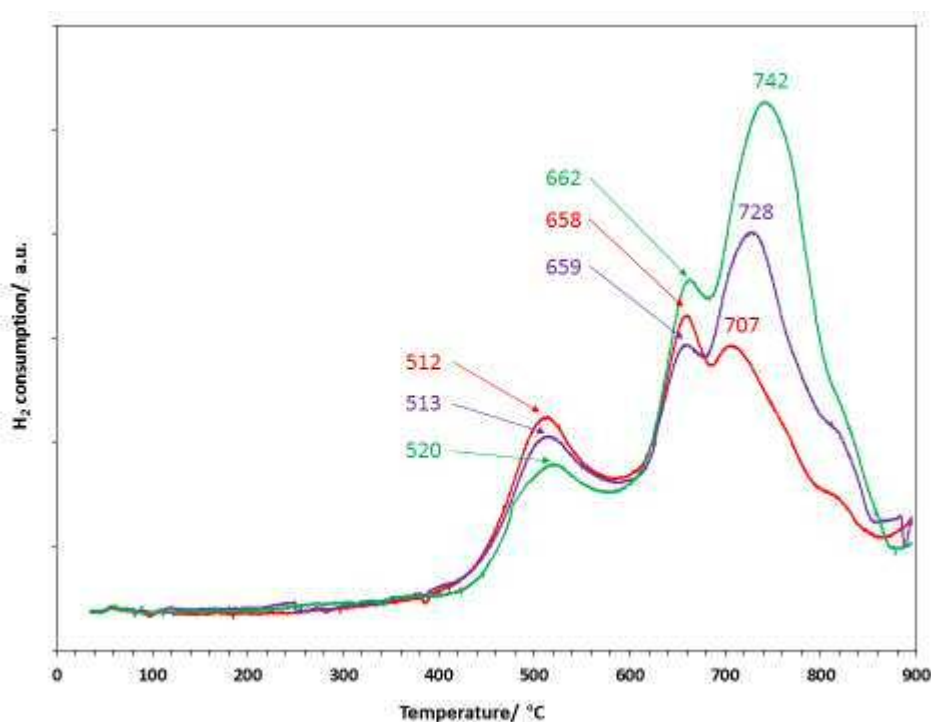


**Figure 4.22** TPR profiles of CLA catalysts; 3:7:10 (green), 5:5:10 (purple) and 7:3:10 (red)

It was observed that the surface reduction peaks centred at 512 °C, 513 °C and 520 °C for CLA 7:3:10, 5:5:10 and 3:7:10 respectively decreased in intensity as the proportion of cerium decreased, summarised in table 4.18, relative to CZA 7:3:10.

**Table 4.18** Summary of surface reduction properties of CLA catalysts

Catalyst	Peak reduction temp (°C)	Relative intensity	
		Peak	Area
<b>7:3:10</b>	512	0.70	<b>0.71</b>
<b>5:5:10</b>	513	0.63	<b>0.70</b>
<b>3:7:10</b>	520	0.53	<b>0.63</b>

Thermogravimetric analysis of the CLA catalysts was carried out in order to determine the extent of impurity decomposition. The results are provided in figure 4.23 in the form of the derivative TG plots.

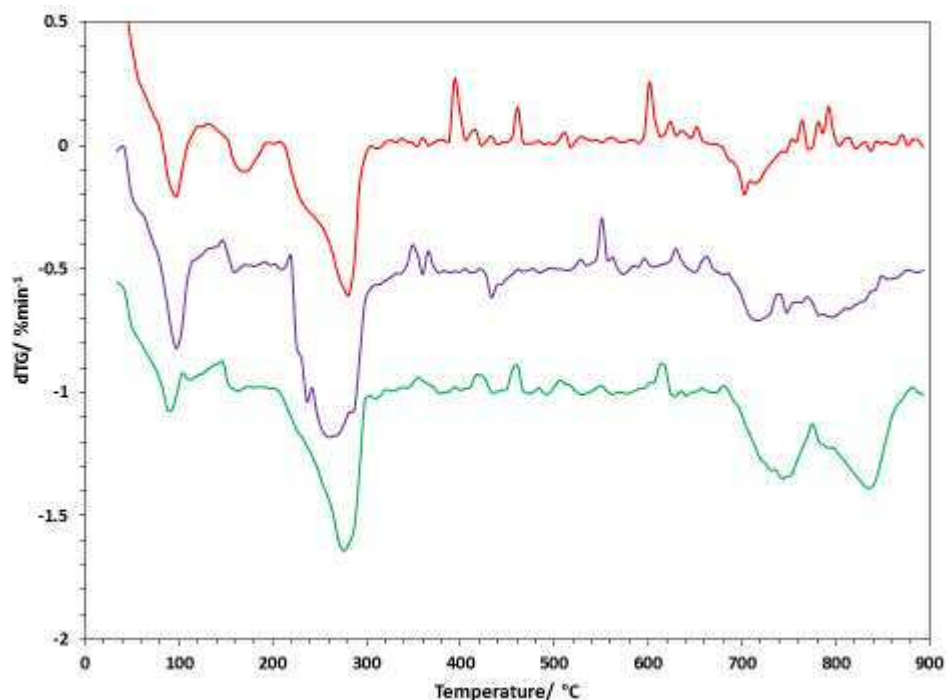
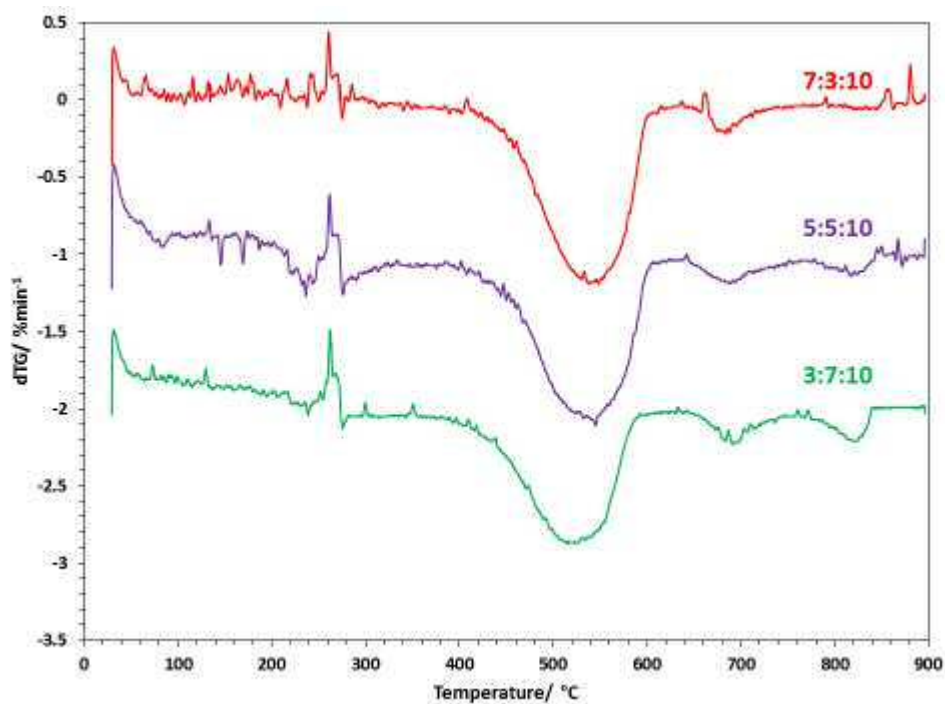


**Figure 4.23** dTG plots of CLA catalysts; 7:3:10 (red), 5:5:10 (purple) and 3:7:10 (green)

As with CZA and CLZA, a loss of mass was observed between 650 °C and 750 °C, and this was attributed to the same loss of impurity as in those cases. Again, this was evidence of the peaks at around 660 °C on the TPR plots belonging to the decomposition of carbonates. This mass loss was observed to be most intense in the case of CLA 3:7:10, and least intense in CLA 5:5:10, matching the trend of the TPR peaks. Interestingly, in CLA 5:5:10 and more intensely in CLA 3:7:10 a separate mass loss occurred between 780 °C and 880 °C. The increasing presence of this mass loss corresponded to an increase in the proportion of lanthanum within the catalyst, and could be attributed to the decomposition of the  $\text{La}_2\text{O}_2\text{CO}_3$  (established from XRD and Raman) to  $\text{La}_2\text{O}_3$ <sup>17</sup>. This would also explain the increasing intensity of the third peak centred between 700 °C and 750 °C on the TPR profiles of the catalysts, owing to the consumption of  $\text{H}_2$  associated with the decomposition of carbonate species to  $\text{CO}_2$  and  $\text{H}_2\text{O}$ .

#### 4.4.2 Soot oxidation testing

The CLA catalysts were each tested for soot oxidation by thermogravimetric analysis in the usual manner. The derivative plots are presented in figure 4.24, with each of the samples offset by  $1\% \text{min}^{-1}$  for ease of comparison.

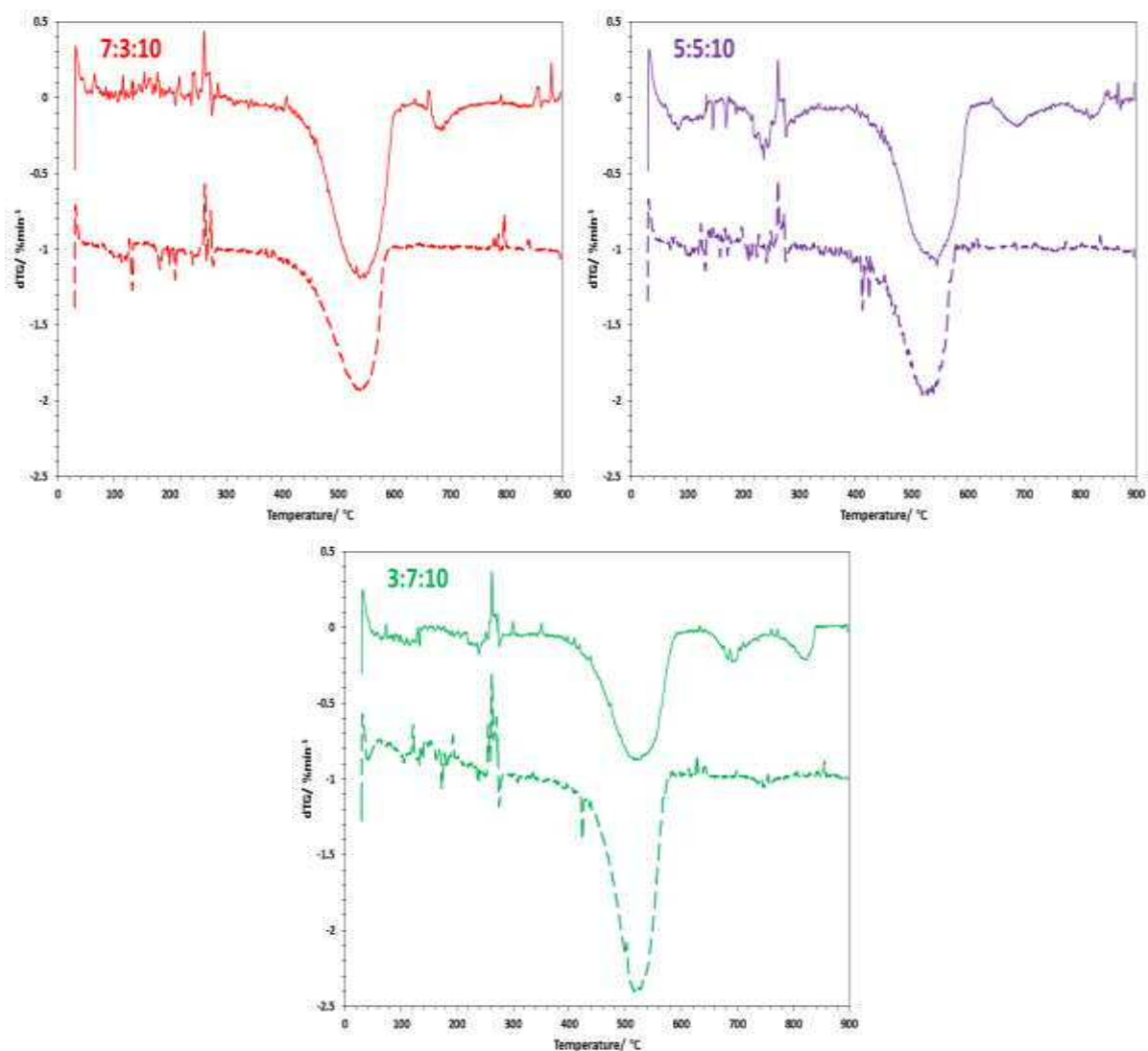


**Figure 4.24** dTG plots of catalyst/soot mixtures containing CLA: 7:3:10 (red), 5:5:10 (purple) and 3:7:10 (green)

It was observed that an increase in the lanthanum content of the catalysts resulted in an increase in soot oxidation activity. As can be seen from table 4.19, the onset, peak and final temperatures all followed this trend, with CLA 3:7:10 decreasing the soot oxidation temperature  $20\text{ }^{\circ}\text{C}$  further than CLA 7:3:10. As with CLZA, this was despite the TPR measurements suggesting the reducibility of the catalysts in this temperature region was unremarkable compared to the less active catalysts presented in this work, which again suggested this was not the determining factor.

**Table 4.19** Soot oxidation temperatures of samples mixed with CLA catalysts on their first and second use

Catalyst	$T_o$ (°C)		$T_{eo}$ (°C)		$T_p$ (°C)		$T_f$ (°C)	
	1 <sup>st</sup> run	2 <sup>nd</sup> run	1 <sup>st</sup> run	2 <sup>nd</sup> run	1 <sup>st</sup> run	2 <sup>nd</sup> run	1 <sup>st</sup> run	2 <sup>nd</sup> run
Soot (no catalyst)	465		535		622		651	
7:3:10	415	380	448	430	541	539	615	598
5:5:10	396	391	444	437	533	528	604	579
3:7:10	391	389	426	449	520	520	591	583

**Figure 4.25** dTG plots of catalyst/soot mixtures containing CLA: 7:3:10 (red), 5:5:10 (purple) and 3:7:10 (green), on the first run (solid line) and second run (dashed line)

The thermal stability of the catalysts was tested by rerunning the tested samples. The dTG plots of the 2<sup>nd</sup> runs are shown in figure 4.25 compared to their corresponding first run, and the soot oxidation temperatures extracted from these can be found in table 4.19. These



showed that the catalysts were able to maintain their activity, confirming the stability of the catalysts after subjection to high temperatures.

## 4.5 Varying Ce:Pr ratio of CPA

Two additional CPA catalysts – in 5:5:10 and 3:7:10 ratios – were prepared by the same co-precipitation method as above. These were characterised and tested for comparison with the CPA catalyst in section 4.1. The catalysts are referred to according to their Ce:Pr:Al ratios.

### 4.5.1 Characterisation

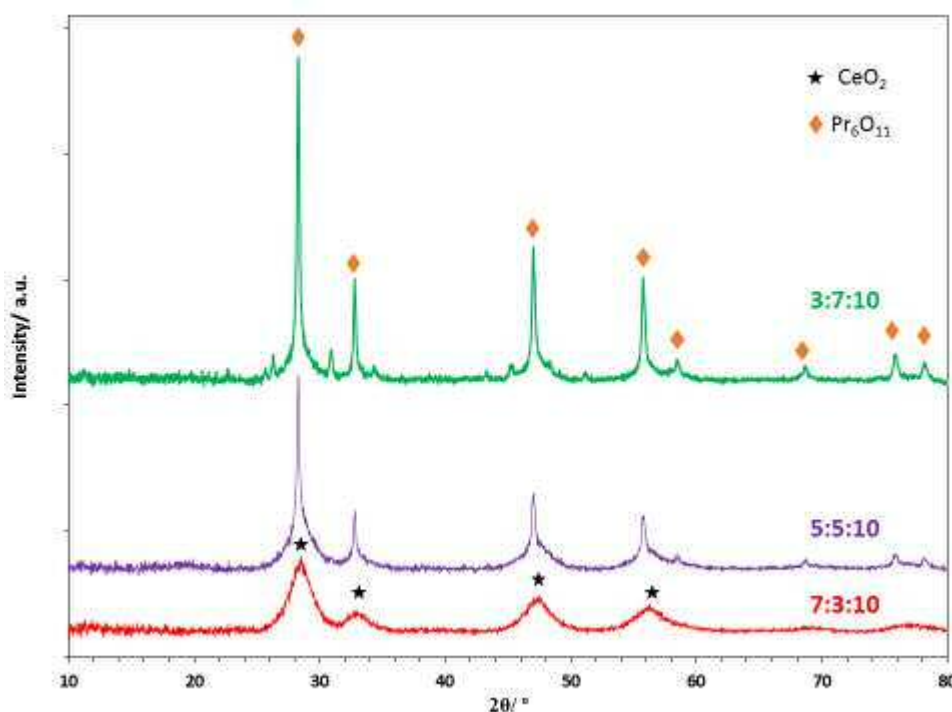


**Figure 4.26** X-ray diffractograms of CPA catalysts; 3:7:10 (green), 5:5:10 (purple) and 7:3:10 (red)

The increase in the molar content of praseodymium over cerium resulted in a change in the crystalline structure of the catalysts, observed in the X-ray diffractograms in figure 4.26. As mentioned in section 4.1.1, the diffractogram of CPA 7:3:10 provided the typical cubic fluorite reflections at  $28.5^\circ$ ,  $32.9^\circ$ ,  $47.5^\circ$  and  $56.3^\circ$  associated with  $\text{CeO}_2$ . These reflections are seen to reduce in intensity in the diffractograms of CPA 5:5:10 and 3:7:10, corresponding to the decrease in the molar content of cerium. In addition, the diffractograms of these catalysts provided evidence of a separate crystalline phase, with reflections centred at  $28.3^\circ$ ,  $32.8^\circ$ ,  $47.0^\circ$ ,  $55.7^\circ$ ,  $58.4^\circ$ ,  $68.6^\circ$ ,  $75.8^\circ$  and  $78.1^\circ$  corresponding to the (111), (200), (220), (311), (222),

(400), (331) and (420) planes of the cubic fluorite structure of  $\text{Pr}_6\text{O}_{11}$  (identified by JCPDS database, card no. 00-042-1121). These reflections were of greatest intensity in the case of CPA 3:7:10, corresponding to the increase in the content of praseodymium. The overlapping of many of the  $\text{Pr}_6\text{O}_{11}$  reflections with those of  $\text{CeO}_2$  owed to the similarities of their fluorite-type structures. The presence of both phases at higher concentrations of praseodymium indicated that the catalysts did not consist of a homogenous mixed metal oxide phase.  $\text{Pr}_6\text{O}_{11}$  contains a mix of Pr(IV) and Pr(III) and therefore its presence provided evidence of praseodymium in both oxidation states.

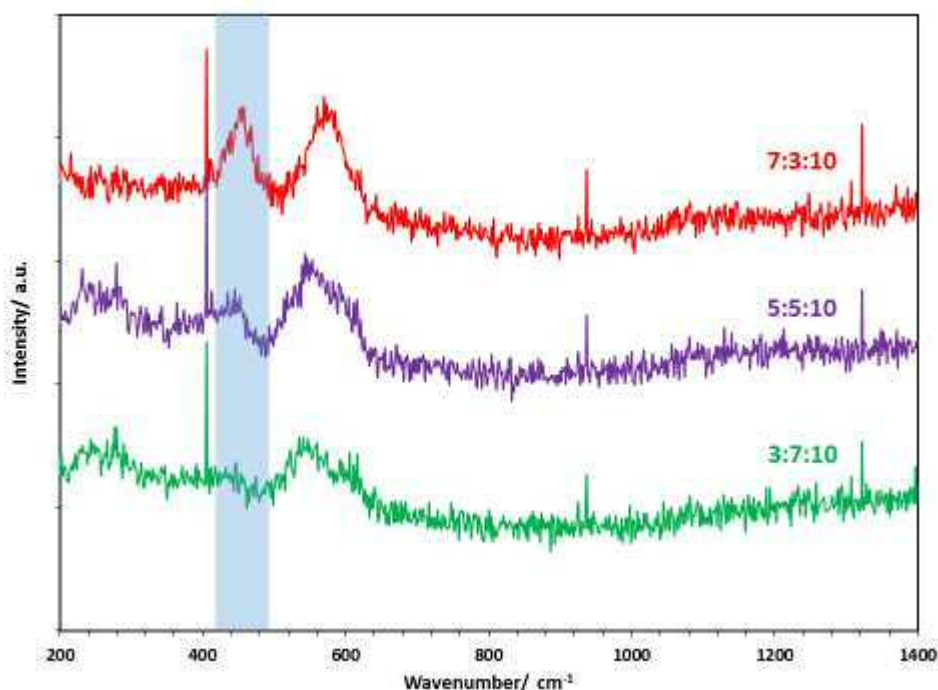


**Figure 4.27** Raman spectra of CPA catalysts; 3:7:10 (green), 5:5:10 (purple) and 7:3:10 (red)

The Raman spectra of the CPA catalysts, shown in figure 4.27, indicated that the intensities of the  $F_{2g}$  mode of ceria typically observed at around 460  $\text{cm}^{-1}$  (highlighted) were much lower than those observed in the other CMA catalysts. The intensity of this mode decreased further as the molar content of cerium was decreased. A broad peak at 500-650  $\text{cm}^{-1}$  was observed for each of the catalysts, attributed to lattice defects resulting from the formation of oxygen vacancies. The relative intensity of this peak compared to the  $F_{2g}$  peak of the other CMA catalysts suggested a much higher concentration of oxygen vacancies in the CPA catalysts. As mentioned previously, the high concentration of oxygen vacancies can be attributed to the ease with which Pr is able to cycle between oxidation states<sup>6,14</sup>.

The CPA catalysts were analysed by XPS and BET in order to determine their surface properties, which are summarised in table 4.20.

**Table 4.20** Surface properties of CPA catalysts provided by XPS and BET analyses

Catalyst	Atomic conc. (%)						Surface area (m <sup>2</sup> g <sup>-1</sup> )
	Ce 3d	Pr 3d	Al 2p	O 1s	C 1s	Na 1s	
<b>7:3:10</b>	5.40	1.82	20.67	52.33	6.14	13.64	30 (±1)
<b>5:5:10</b>	5.28	4.47	20.40	50.22	6.88	12.75	20 (±1)
<b>3:7:10</b>	3.59	6.61	19.67	49.95	6.94	13.24	21 (±0)

As observed in the other CMA catalysts, the ratios of the metals calculated in table 4.21 showed an excess of aluminium compared with cerium and praseodymium on the CPA surfaces. It was also observed that there was an excess of cerium compared with praseodymium on the surface in each case.

**Table 4.21** Atomic ratio of metals on CPA catalyst surfaces

Catalyst	Ce:Pr:Al	Ce:Pr	Ce(III):Ce(IV)	Pr(III):Pr(IV)
<b>CPA 7:3:10</b>	3.9 : 1.3 : 14.8	7.5 : 2.5	0.10 : 1	0.22 : 1
<b>CPA 5:5:10</b>	3.5 : 3.0 : 13.5	5.4 : 4.6	0.08 : 1	0.47 : 1
<b>CPA 3:7:10</b>	2.5 : 4.5 : 13.0	3.5 : 6.5	0.08 : 1	0.48 : 1

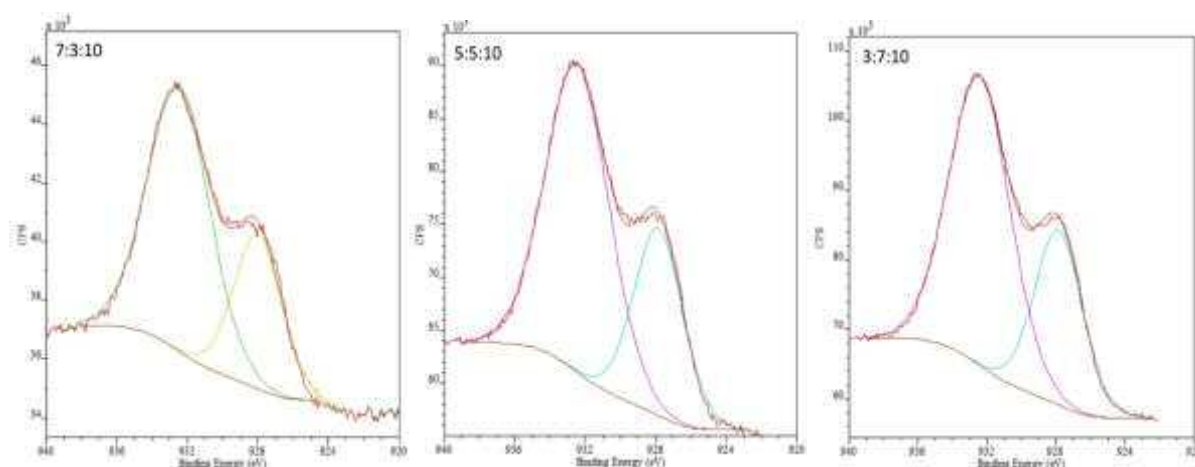


**Figure 4.28** Pr 3d region of XPS spectra of CPA catalysts

Figure 4.28 shows the XPS spectra of the Pr 3d region of the CPA catalysts. As suggested from XRD, the bimodal peak structure observed in each of the spectra confirmed the presence of

both Pr(IV) (at 932.4 eV) and Pr(III) at (927.8 eV) on the surface of the catalysts<sup>6</sup>. Table 4.21 shows the Pr(III)/(IV) ratios on the surfaces of each of the catalysts. It was observed that the majority of surface praseodymium was in the +4 oxidation state, however the proportion of Pr(III) was considerably higher in CPA 5:5:10 and 3:7:10 than observed in CPA 7:3:10. Also shown in the table are the relatively low ratios of Ce(III) on the surfaces of the CPA catalysts compared with the other materials presented in this chapter.

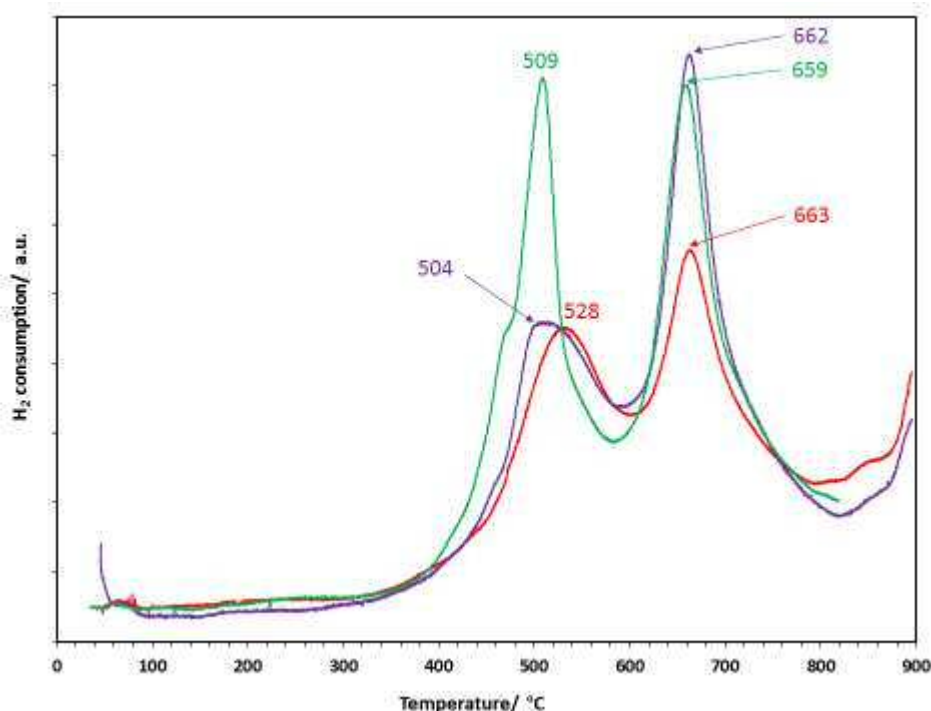


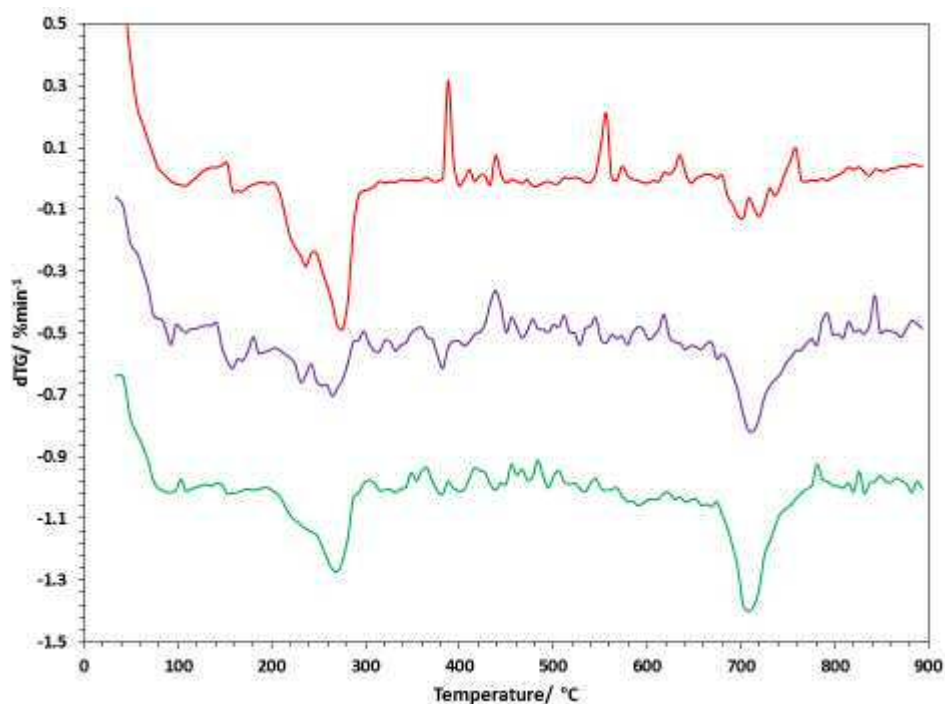
**Figure 4.29** TPR profiles of CPA catalysts; 3:7:10 (green), 5:5:10 (purple) and 7:3:10 (red)

The reduction profiles of the CPA catalysts are provided in figure 4.29. Each of the catalysts produced two distinct reduction curves, the first peaking at around 500 °C, and the second at around 660 °C. The lower temperature curve of CPA 7:3:10 resembled those of the other catalysts reported in this chapter, peaking at 528 °C, and thus this was attributed to the reduction of surface  $\text{Ce}^{4+}$  ions. However, as the proportion of praseodymium was increased, it was observed that this curve became distorted, increasing in intensity at a lower temperature (504 °C for CPA 5:5:10 and 509°C for CPA 3:7:10). This distortion was attributed to the reduction of  $\text{Pr}^{4+}$  taking place simultaneously with  $\text{Ce}^{4+}$  <sup>14</sup>.

**Table 4.22** Summary of surface reduction properties of CPA catalysts

Catalyst	Peak reduction	Relative intensity	
	temp (°C)	Peak	Area
<b>7:3:10</b>	528	0.75	<b>0.94</b>
<b>5:5:10</b>	504	0.77	<b>1.07</b>
<b>3:7:10</b>	509	1.43	<b>1.27</b>

The thermogravimetric analysis of the catalysts again provided evidence of a mass loss between 650 °C and 750 °C corresponding to the decomposition of trapped carbonate species within the bulk structures of the catalysts. The dTG plots in figure 4.30 showed that the mass loss was greater in CPA 5:5:10 and 3:7:10 than in CPA 7:3:10. This corresponded to the increase in the intensity of the second reduction curves of both CPA 5:5:10 and 3:7:10 compared to CPA 7:3:10 observed in the TPR profiles in figure 4.29.

**Figure 4.30** dTG plots of CPA catalysts; 7:3:10 (red) 5:5:10 (purple) and 3:7:10 (green)

#### 4.5.2 Soot oxidation testing

The results of soot oxidation testing by TGA are expressed as the dTG plots in figure 4.31.

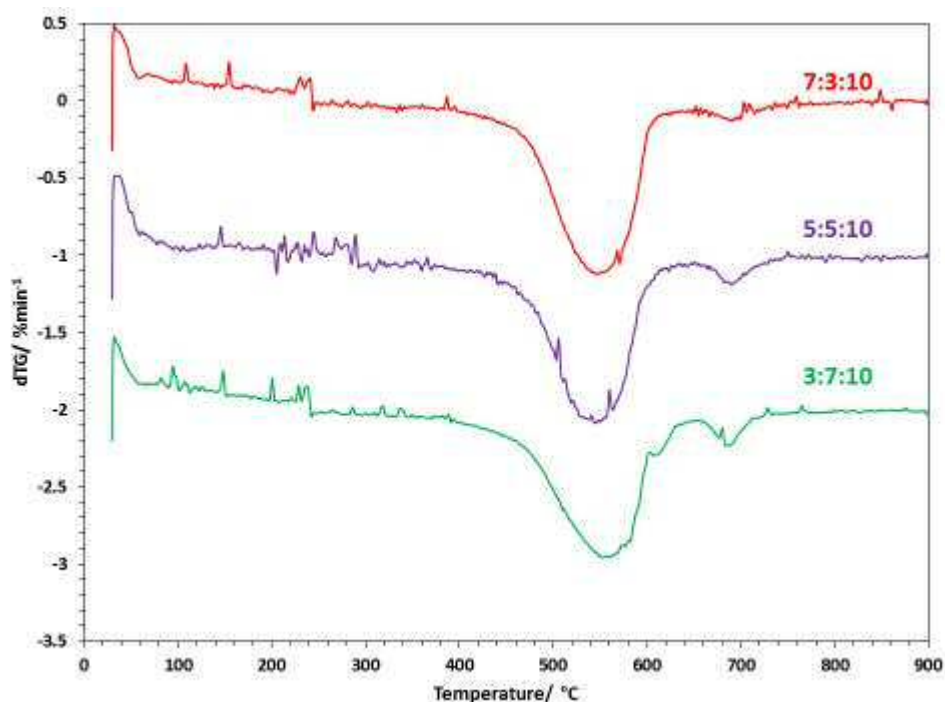


**Figure 4.31** dTG plots of catalyst/soot mixtures containing CPA: 7:3:10 (red), 5:5:10 (purple) and 3:7:10 (green). The presence of reducible praseodymium ions established from TPR did not equate to an improvement in catalytic activity for soot oxidation. This can be seen from table 4.23, which showed that the peak soot oxidation temperature was not lowered below 540 °C – on the contrary, it was observed that this temperature increased slightly in the case of CPA 3:7:10 to above 550 °C. A study by Machida *et al.* determined that while  $\text{Pr}_6\text{O}_{11}$  had a higher oxygen release/storage potential,  $\text{CeO}_2$  was able to generate superoxide  $\text{O}_2^-$  radicals which are highly reactive with soot<sup>20</sup>. Therefore despite the TPR profiles of the CPA catalysts showing that an increase in praseodymium resulted in an increase in the release of oxygen, the lower reactivity of this oxygen meant that this did not result in an increase in catalytic activity.

**Table 4.23** Soot oxidation temperatures of samples mixed with CPA catalysts on their first and second use

Catalyst	$T_o$ (°C)		$T_{eo}$ (°C)		$T_p$ (°C)		$T_f$ (°C)	
	1 <sup>st</sup> run	2 <sup>nd</sup> run	1 <sup>st</sup> run	2 <sup>nd</sup> run	1 <sup>st</sup> run	2 <sup>nd</sup> run	1 <sup>st</sup> run	2 <sup>nd</sup> run
<b>Soot (no catalyst)</b>	465		535		622		651	
<b>7:3:10</b>	406	393	463	470	<b>544</b>	<b>549</b>	616	603
<b>5:5:10</b>	386	403	468	479	<b>544</b>	<b>547</b>	631	603
<b>3:7:10</b>	391	396	458	477	<b>553</b>	<b>548</b>	- *	613

\* $T_f$  coincided with decomposition of impurities – difficult to establish accurate temperature

The soot oxidation temperatures when catalysed by the used samples are shown in table 4.23, which were extracted from the dTG plots in figure 4.32. This showed that the majority of soot oxidation took place within a narrower temperature range, with a higher  $T_{e0}$  and lower  $T_f$ , while the peak temperature was not altered significantly.

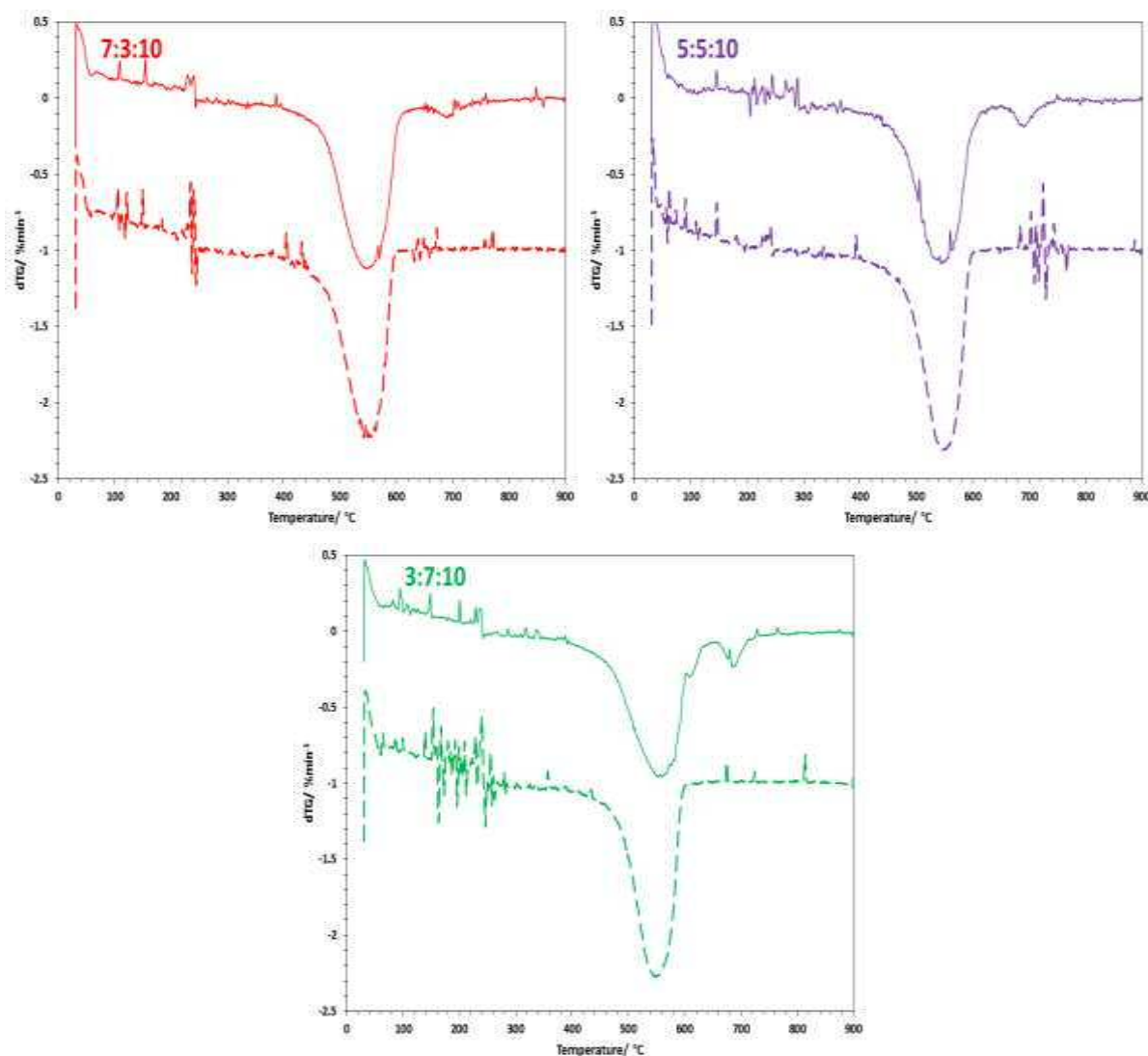


**Figure 4.32** dTG plots of catalyst/soot mixtures containing CPA: 7:3:10 (red), 5:5:10 (purple) and 3:7:10 (green), on the first run (solid line) and second run (dashed line)

#### 4.6 Varying Ce:Nd ratio of CNA

Two additional CNA catalysts – in 5:5:10 and 3:7:10 ratios – were prepared by the same co-precipitation method as above. These were characterised and tested for comparison with the CNA catalyst in section 4.1. The catalysts are referred to according to their Ce:Nd:Al ratios.

## 4.6.1 Characterisation

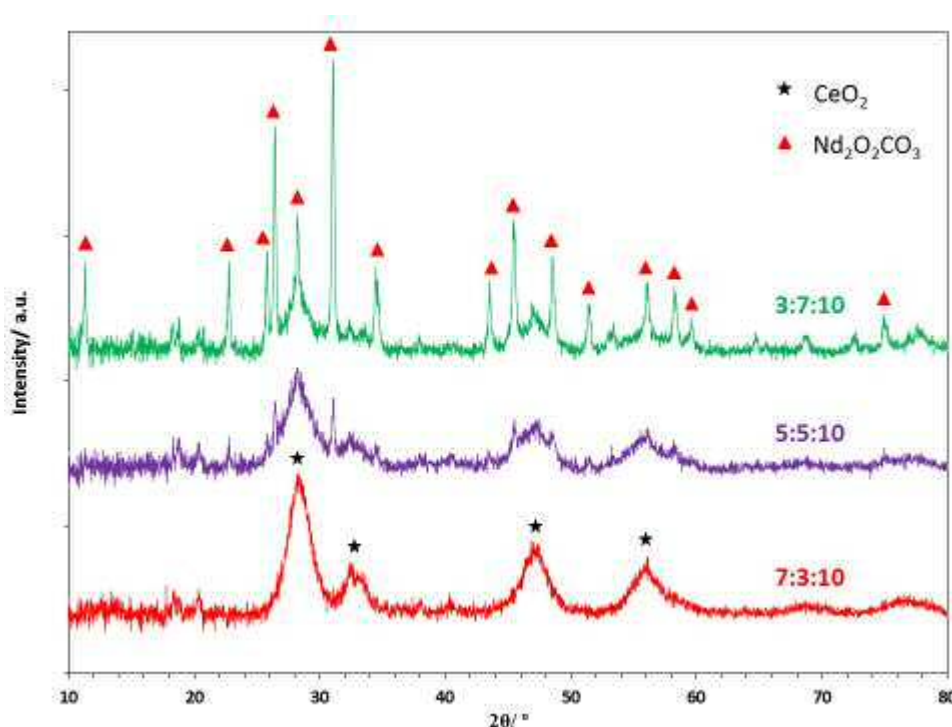
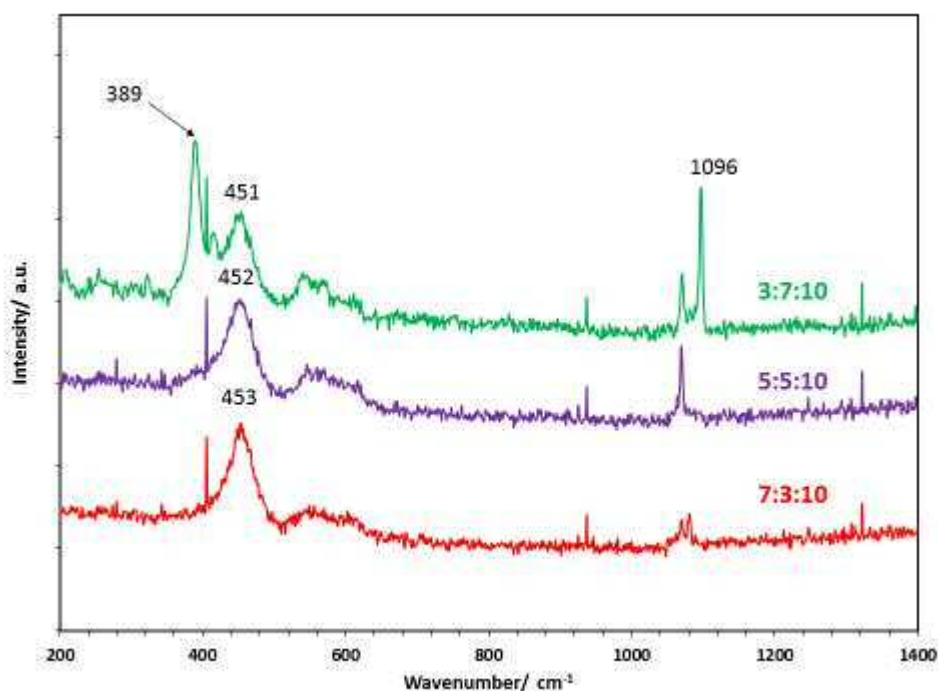


Figure 4.33 X-ray diffractograms of CNA catalysts; 3:7:10 (green), 5:5:10 (purple) and 7:3:10 (red)

The CNA catalysts displayed similar diffractograms to those of CLA found in section 4.4.1. The diffractogram of CNA 7:3:10 contained the cubic fluorite reflections of ceria, as discussed in 4.1.1. The decrease in cerium content in CNA 5:5:10 and 3:7:10 led to a decrease in the intensity of these reflections. The sharp reflections denoted by red triangles in figure 4.33 were also detected in these catalysts, and were attributed to neodymium dioxycarbonate,  $\text{Nd}_2\text{O}_2\text{CO}_3$  (JCPDS card No. 23-0421), the neodymium analog of the lanthanum phase detected in the corresponding CLA catalysts. The intensities of these reflections increased in CNA 3:7:10 corresponding to the increase in neodymium concentration. As with CLA, the presence of this phase suggested the calcination conditions were not sufficient to fully decompose neodymium carbonate,  $\text{Nd}_2(\text{CO}_3)_3$  formed during co-precipitation, to neodymium oxide,  $\text{Nd}_2\text{O}_3$ <sup>23</sup>. As with the catalysts which contained a high content of lanthanum and praseodymium, the presence of two phases demonstrated that the catalysts did not consist of a single homogenous mixed metal oxide phase.





**Figure 4.34** Raman spectra of CNA catalysts; 3:7:10 (green), 5:5:10 (purple) and 7:3:10 (red)

The Raman spectra of the CNA catalysts shown in figure 4.34 each contained the  $F_{2g}$  mode attributed to ceria. As annotated, the centre of this peak was seen to shift to lower frequency upon increasing neodymium content, from  $453\text{ cm}^{-1}$  in CNA 7:3:10 to  $451\text{ cm}^{-1}$  in CNA 3:7:10, indicating greater incorporation of  $\text{Nd}^{3+}$  ions into the ceria lattice and decreasing the frequency of the Ce-O stretching mode. In agreement with the findings of XRD, the prominent peak observed at  $1096\text{ cm}^{-1}$  was attributed to the carbonate group found in  $\text{Nd}_2\text{O}_2\text{CO}_3^{24}$ .

The surface properties of the catalysts were analysed by XPS and BET. Quantification of the surface composition (table 4.24) determined that cerium, neodymium and aluminium accounted for around a quarter of the elements in each of the catalysts. No changes were observed to the positions and intensities of the peaks in the Ce 3d region when the proportion of neodymium was increased, demonstrating that Ce(IV) remained the predominant form of cerium on the surfaces of the catalysts.

**Table 4.24** Surface properties of CNA catalysts provided by XPS and BET analyses

Catalyst	Atomic conc. (%)						Surface area (m <sup>2</sup> g <sup>-1</sup> )
	Ce 3d	Nd 3d	Al 2p	O 1s	C 1s	Na 1s	
<b>7:3:10</b>	3.29	1.11	21.03	53.75	6.04	14.78	30 (±1)
<b>5:5:10</b>	3.42	1.76	20.53	53.21	6.85	14.23	34 (±1)
<b>3:7:10</b>	2.05	2.58	20.69	53.36	6.47	14.85	28 (±1)

As with the other CMA catalysts presented in this chapter, the metal ratios showed that aluminium was in excess compared with cerium and neodymium on the surface of each of the catalysts relative to the initial molar ratio (table 4.25). It was also observed that there was a higher proportion of cerium than neodymium on the surface of each of the catalysts than anticipated from the preparation method. No significant change to the relative intensities of the cerium peaks was observed in the Ce 3d region of the spectra, indicating that the proportion of Ce(III) remained low.

**Table 4.25** Atomic ratio of metals on CNA catalyst surfaces

Catalyst	Ce:Nd:Al	Ce:Nd	Ce(III):Ce(IV)
<b>CNA 7:3:10</b>	2.6 : 0.9 : 16.5	7.5 : 2.5	0.11 : 1
<b>CNA 5:5:10</b>	2.7 : 1.3 : 16.0	6.7 : 3.3	0.10 : 1
<b>CNA 3:7:10</b>	1.6 : 2.0 : 16.3	4.5 : 5.5	0.11 : 1

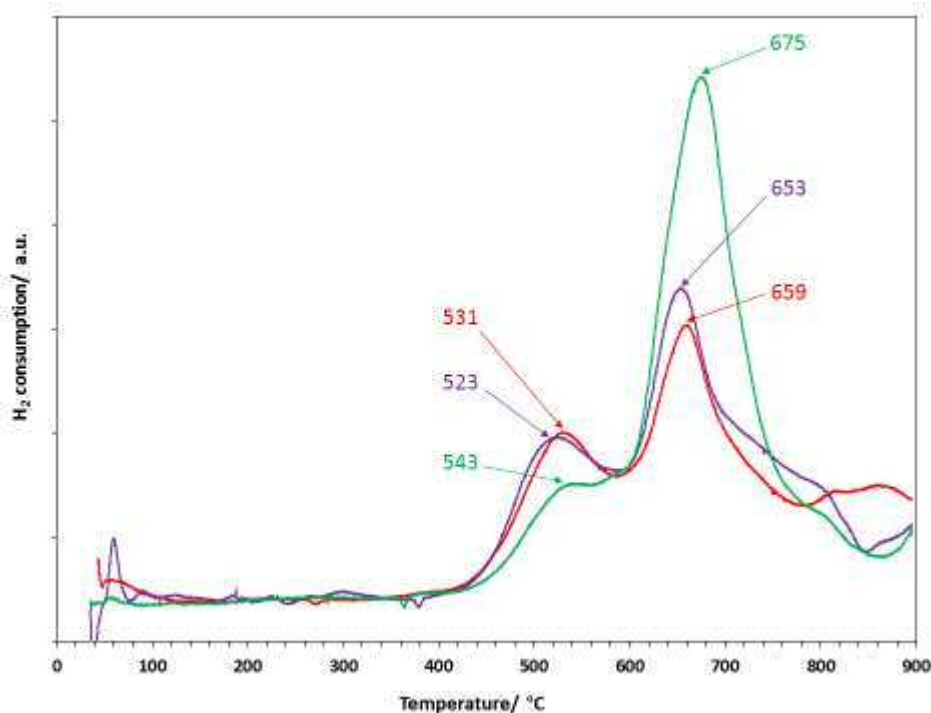


**Figure 4.35** TPR profiles of CNA catalysts; 3:7:10 (green), 5:5:10 (purple) and 7:3:10 (red)

Each of the CNA catalysts showed a bimodal reduction profile in figure 4.35. The lower temperature curve was once again attributed to the reduction of surface  $\text{Ce}^{4+}$  ions. Thermogravimetric analysis suggested the higher temperature curve was caused by the decomposition of carbonate species within the bulk structure of the catalysts, described in greater detail below, however there may also have been a contribution by the reduction of bulk  $\text{Ce}^{4+}$  ions. A significant disparity between the peak temperatures was observed for the surface cerium reduction curves. CNA 5:5:10 had the lowest peak reduction temperature at 523 °C, while CNA 3:7:10 had the highest at 543 °C. CNA 7:3:10 and 5:5:10 showed comparable surface reduction intensities, which could be explained by the similar proportion of cerium on the surface. This would also explain the decrease in intensity observed in the case of CNA 3:7:10, which had a significantly lower proportion of cerium.

**Table 4.26** Summary of surface reduction properties of CNA catalysts

Catalyst	Peak reduction	Relative intensity	
	temp (°C)	Peak	Area
<b>7:3:10</b>	531	0.61	<b>0.67</b>
<b>5:5:10</b>	523	0.59	<b>0.65</b>
<b>3:7:10</b>	543	0.43	<b>0.54</b>

The thermogravimetric analysis of the CNA catalysts in figure 4.36 showed a mass loss above 700 °C attributed to the decomposition of impurities and carbonates within the bulk structure of the catalysts, as reported in the previous sections of this chapter.

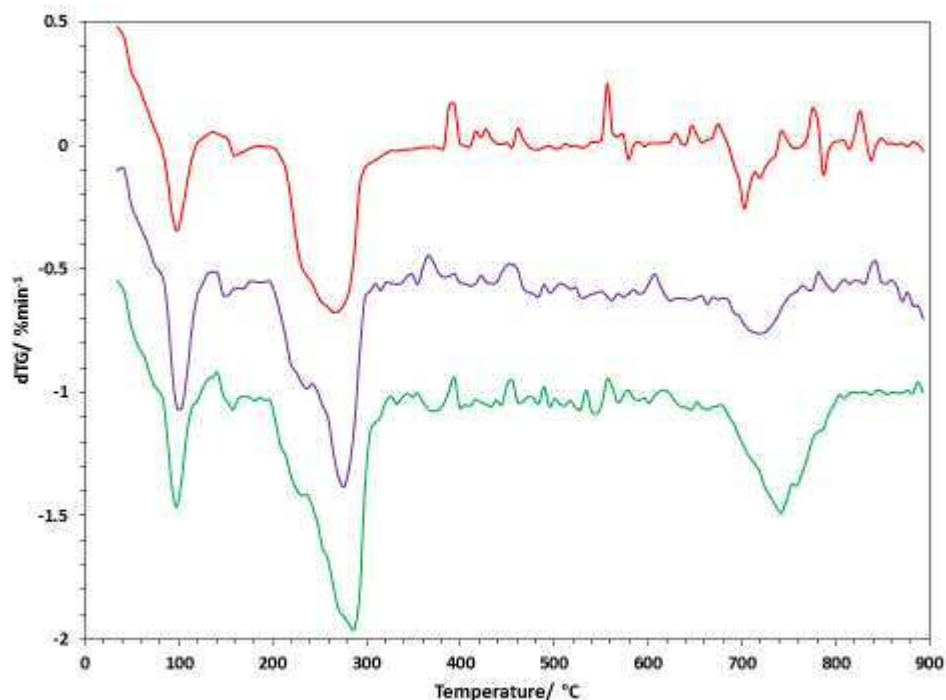


**Figure 4.36** dTG plots of CNA catalysts; 7:3:10 (red) 5:5:10 (purple) and 3:7:10 (green)

In the case of CNA 7:3:10 and 5:5:10, this occurred between around 700 °C to 750 °C and were of similar intensity, peaking at around 720 °C. For CNA 3:7:10, the mass loss occurred over a greater temperature range (700-800 °C, peaking at 740 °C), and was significantly higher in intensity. This matched the trend observed for the second reduction curve of the TPR profiles, with CNA 7:3:10 and 5:5:10 showing similar intensities and peak temperatures, whereas CNA 3:7:10 was significantly higher in intensity, also with a higher peak temperature. This increase was attributed to the decomposition of  $\text{Nd}_2\text{O}_2\text{CO}_3^{23}$ , which XRD and Raman indicated had the greatest presence in CNA 3:7:10.

#### 4.6.2 Soot oxidation testing

The CNA catalysts were each tested for soot oxidation by thermogravimetric analysis in the usual manner. The derivative plots are presented in figure 4.37, with each of the samples offset by  $1\% \text{min}^{-1}$  for ease of comparison.

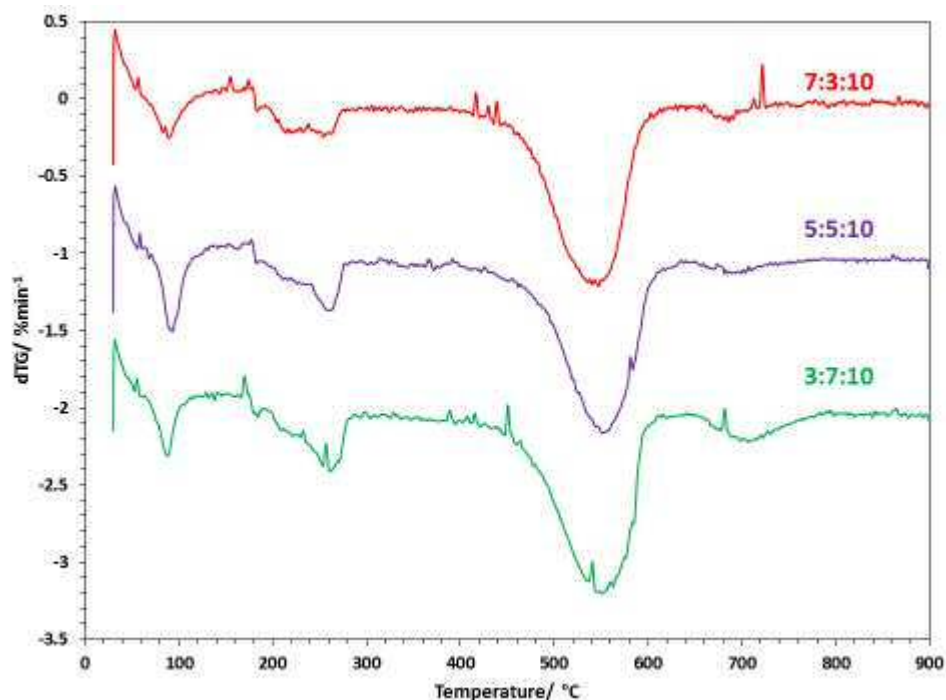


**Figure 4.37** dTG plot comparison of catalyst/soot mixtures in; synthetic air (solid lines), and N<sub>2</sub> (dashed lines) containing: CNA: 7:3:10 (red), 5:5:10 (purple) and 3:7:10 (green)

As seen in table 4.27, varying the Ce:Nd ratio had little effect on the activity of the CNA catalysts, with a peak soot oxidation temperature of around 550 °C in each case. As a group, the CNA catalysts performed worse than those containing zirconium and the other rare-Earth metals.

**Table 4.27** Soot oxidation temperatures of samples mixed with CNA catalysts

Catalyst	T <sub>o</sub> (°C)	T <sub>eo</sub> (°C)	T <sub>p</sub> (°C)	T <sub>f</sub> (°C)
Soot (no catalyst)	465	535	<b>622</b>	651
<b>7:3:10</b>	411	464	<b>547</b>	617
<b>5:5:10</b>	419	475	<b>550</b>	633
<b>3:7:10</b>	418	467	<b>551</b>	610

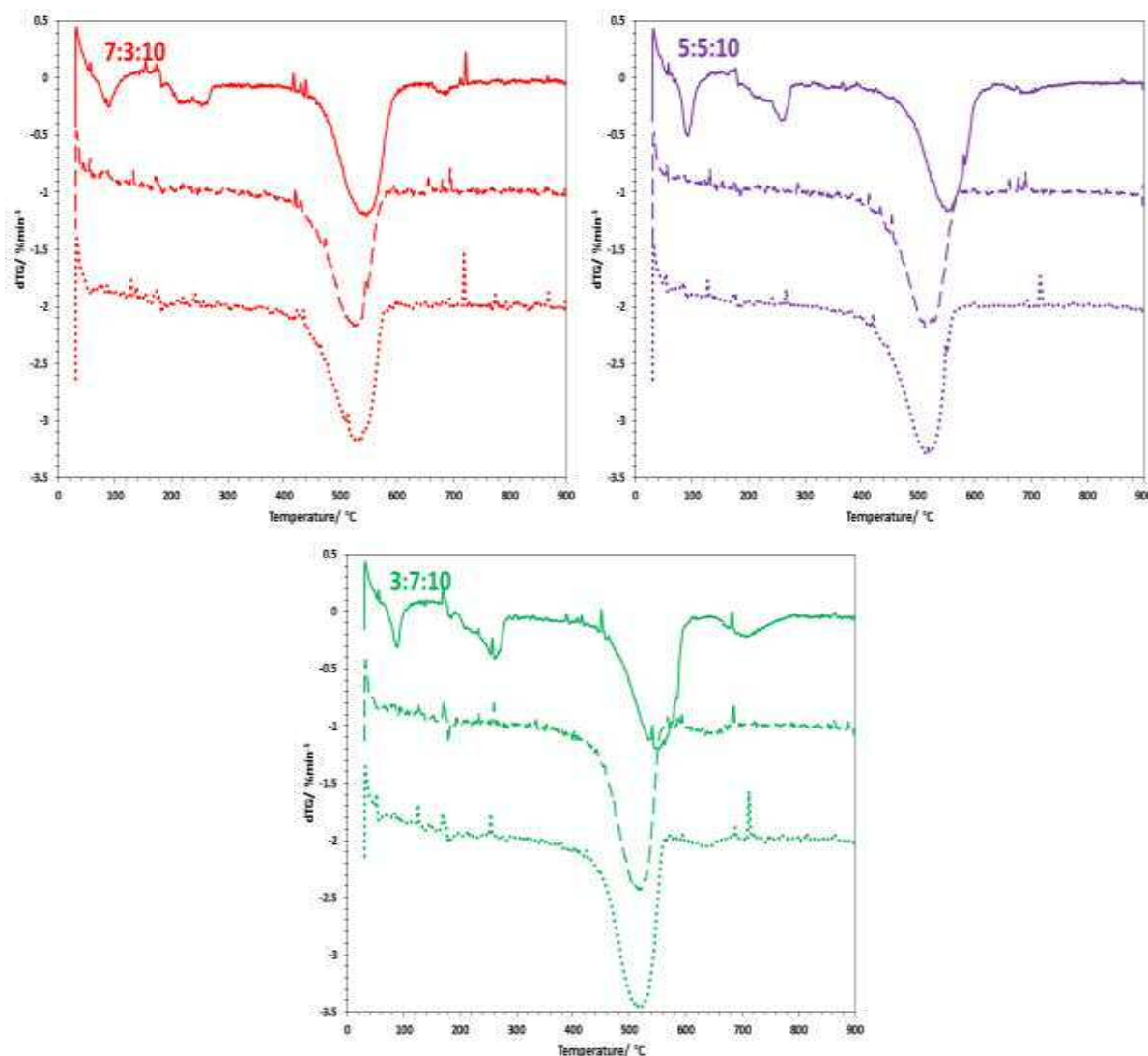


**Figure 4.38** dTG plots of catalyst/soot mixtures containing CNA: 7:3:10 (red), 5:5:10 (purple) and 3:7:10 (green); on the first run (solid line), second run (dashed line) and third run (dotted line)

Each of the catalysts' samples were reused in order to determine their thermal stability. As was observed in the case of CNA 7:3:10 in section 4.1.2, each of the CNA catalysts were significantly more active on 2<sup>nd</sup> use than they had been on their first. This can be seen from the dTG plots in figure 4.38, and the soot oxidation data extracted from them in table 4.28, which showed that the soot oxidation temperature decreased by every marker for each of the catalysts. Remarkably, the peak soot oxidation temperature decreased by over 20 °C, 35 °C and 30 °C for CNA 7:3:10, 5:5:10 and 3:7:10 respectively. In stark contrast to their activity in their initial runs, this represented the most active group of catalysts presented so far in this chapter; CNA 5:5:10 and 3:7:10 demonstrated the lowest peak soot oxidation temperatures of any individual catalyst.

The catalysts were subjected to a 3<sup>rd</sup> round of testing in order to determine whether their improved activity could be sustained, the results of which are also provided in figure 4.38 and table 4.28. The 3<sup>rd</sup> runs confirmed the thermal stability of the improved CNA catalysts, with the peak soot oxidation temperatures remaining at the lower temperatures.

**Table 4.28** Soot oxidation temperatures of samples mixed with CNA catalysts on their first, second and third use

Catalyst	T <sub>o</sub> (°C)			T <sub>eo</sub> (°C)			T <sub>p</sub> (°C)			T <sub>f</sub> (°C)		
	1 <sup>st</sup>	2 <sup>nd</sup>	3 <sup>rd</sup>	1 <sup>st</sup>	2 <sup>nd</sup>	3 <sup>rd</sup>	1 <sup>st</sup>	2 <sup>nd</sup>	3 <sup>rd</sup>	1 <sup>st</sup>	2 <sup>nd</sup>	3 <sup>rd</sup>
	run	run	run	run	run	run	run	run	run	run	run	run
<b>Soot</b>	465			535			<b>622</b>			651		
<b>7:3:10</b>	411	383	398	464	451	441	<b>547</b>	<b>525</b>	<b>528</b>	617	581	579
<b>5:5:10</b>	419	389	356	475	439	434	<b>550</b>	<b>514</b>	<b>515</b>	633	575	590
<b>3:7:10</b>	418	383	383	467	444	445	<b>551</b>	<b>519</b>	<b>515</b>	610	567	562

The results suggested a significant structural change must have taken place to the catalysts after subjection to high temperatures, resulting in a considerable improvement in catalytic activity which was sustained upon repeated use. The soot oxidation temperature was lowered further than had been observed with any of the corresponding CZA, CLZA, CLA or CPA catalysts. It was therefore decided to investigate the effects the thermal treatment had on the materials during catalyst preparation.

#### 4.7 Varying calcination conditions of CNA catalysts

Three new batches of CNA 7:3:10 were prepared, each of which were calcined at 750 °C. This temperature was chosen due to the results of the thermogravimetric analysis of the CNA catalysts in figure 4.36 (section 4.6.1) which showed a mass loss at this temperature which was attributed to the decomposition of impurities, (possibly Nd<sub>2</sub>O<sub>2</sub>CO<sub>3</sub> detected by XRD and Raman) which may have contributed to the improvement of the catalysts.

The three batches were calcined under three different atmospheres. Since the original CNA catalysts were calcined under static air, this atmosphere was chosen in order to establish whether the higher temperature alone was sufficient to improve the catalyst. Flowing air was the atmosphere used under the soot oxidation tests of the TGA, therefore this atmosphere

was used in order to replicate those conditions. An atmosphere of 10% $H_2$ /Ar was used in order to replicate the reducing effect of the soot on the catalysts during testing.

The three catalysts, referred to as "CNA 750°C Static Air", "CNA 750°C Flowing Air" and "CNA 750°C  $H_2$ /Ar" were characterised and tested and compared with the same analyses of CNA 7:3:10 from section 4.6.1 which is referred to as "CNA 500°C Static Air" in this section. A sample of the same catalyst pre-calcination was also analysed for comparison.

#### 4.7.1 Characterisation

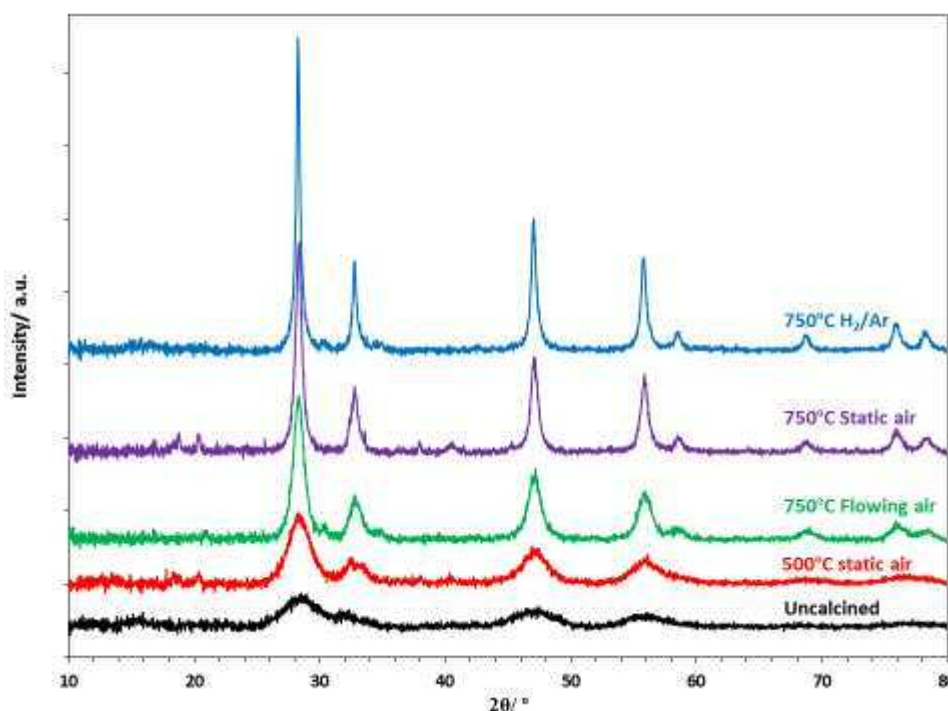


Figure 4.39 X-ray diffractograms of calcined CNA catalysts

The diffractograms of the CNA catalysts shown in figure 4.39 showed that upon calcination, the intensity of the cubic fluorite reflections of ceria increased, indicating a more crystalline phase. Increasing the calcination temperature from 500 °C to 750 °C resulted in a further increase, to the extent that ceria reflections at 59.1°, 69.5°, 76.7° and 79.1° – belonging to the (222), (400), (331) and (420) planes respectively – were distinguishable from the background interference. This increase in crystallinity is reflected in the crystallite sizes calculated from the (111) reflections, shown in table 4.29, which show a significant increase upon higher temperature calcination, especially in the case of "CNA 750°C  $H_2$ /Ar". The reflections were



observed to decrease to a slightly lower  $2\theta$  angle compared to pure ceria, in agreement with the findings discussed in section 4.1.1.

**Table 4.29** Peak positions and crystallite sizes of CNA catalysts determined by XRD

Catalyst	2 theta (°)				Crystallite size (nm)
	(111)	(200)	(220)	(311)	
Ceria*	28.5	33.1	47.5	56.3	-
Uncalcined	28.4	-	47.2	56.1	2.1
500°C Static air	28.3	32.8	47.2	56.0	3.4
750°C Static air	28.3	32.8	47.1	55.9	11.9
750°C Flowing air	28.3	32.8	47.2	55.9	8.1
750°C H <sub>2</sub> /Ar	28.3	32.8	47.0	55.8	16.9

\*2 theta values of ceria referenced from JCPDS database (card no. 071-4199)

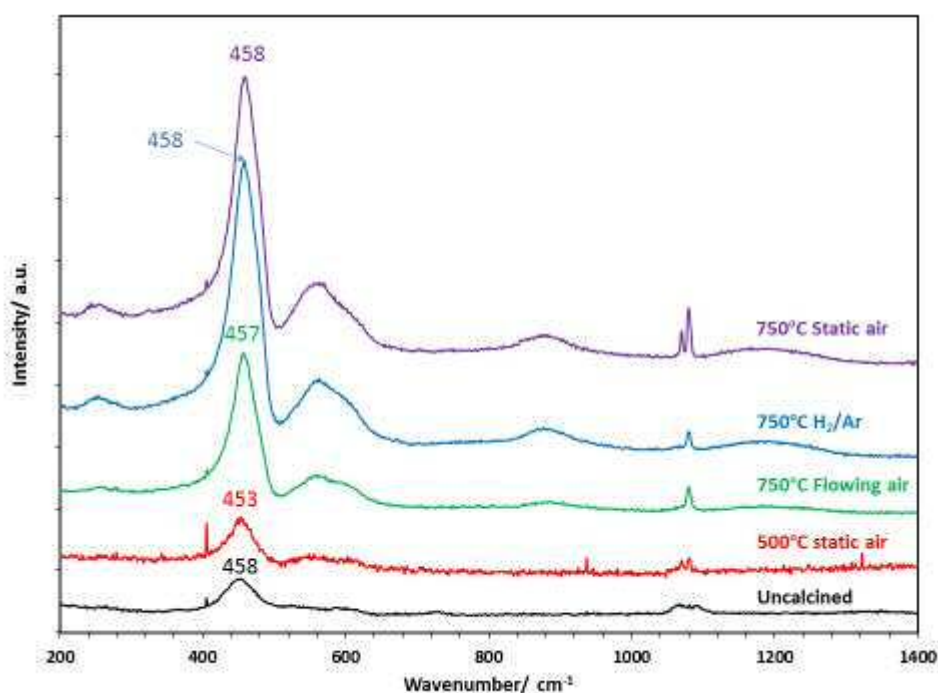


**Figure 4.40** Raman spectra of CNA catalysts

Raman spectra of the catalysts are provided in figure 4.40. An increase in calcination temperature resulted in an increase in the intensity of the  $F_{2g}$  mode attributed to ceria. As with XRD, this was attributed to the increased crystallite size of the ceria phase in these

catalysts. The peak positions of these catalysts were also observed to be shifted to a lower wavenumber than pure ceria, although not to the same extent as “CNA 500°C Static Air”.

**Table 4.30** Surface properties of CNA catalysts provided by XPS and BET analyses

Catalyst	Atomic conc. (%)					Surface area	
	Ce 3d	Nd 3d	Al 2p	O 1s	C 1s	Na 1s	(m <sup>2</sup> g <sup>-1</sup> )
Uncalcined	6.48	1.40	17.82	51.94	9.84	12.52	87 (±3)
500°C Static air	3.29	1.11	21.03	53.75	6.04	14.78	30 (±1)
750°C Static air	0.42	0.53	12.65	46.61	10.91	28.89	5 (±0)
750°C Flowing air	2.42	0.91	24.38	46.32	5.96	20.03	14 (±0)
750°C H <sub>2</sub> /Ar	1.84	0.73	27.96	45.06	4.35	20.06	10 (±0)

The surface properties of the catalysts were analysed by XPS and BET, and are summarised in table 4.30. It was observed that the surface area decreased upon calcination, and was lower when calcined at 750 °C than 500 °C. The decline of surface area was attributed to sintering of ceria at higher temperatures<sup>25</sup>. This was observed to the greatest extent in the case of “CNA 750°C Static”, which had the lowest surface area of the catalysts presented in this section and those in previous sections. Elemental quantification by XPS showed that – with the exception of “CNA 750°C Static” – in keeping with the other CMA catalysts presented in this chapter, cerium, neodymium and aluminium accounted for around 25-30 % of the surface of the catalysts. As mentioned, this was not the case for “CNA 750°C Static”, of which Ce, Nd & Al accounted for only around half this percentage, likely due to the high proportion of carbon and sodium also observed on the surface.

**Table 4.31** Atomic ratio of metals on CNA catalyst surfaces

Catalyst	Ce:Nd:Al	Ce:Nd	Ce(III):Ce(IV)
<b>Preparation method</b>	7 : 3 : 10	7 : 3	-
<b>Uncalcined</b>	5.0 : 1.1 : 13.9	8.2 : 1.8	0.25 : 1
<b>500°C Static air</b>	2.6 : 0.9 : 16.5	7.5 : 2.5	0.11 : 1
<b>750°C Static air</b>	0.6 : 0.8 : 18.6	4.4 : 6.6	0.08 : 1
<b>750°C Flowing air</b>	1.7 : 0.7 : 17.6	7.3 : 2.7	0.28 : 1
<b>750°C H<sub>2</sub>/Ar</b>	1.2 : 0.5 : 18.3	7.2 : 2.8	0.29 : 1

As seen from the atomic ratios of the metals in table 4.31, there was an excess of aluminium on the surfaces of each of the catalysts compared to the original molar ratio used in the preparation method. An excess of cerium over neodymium was also observed, most notably in the uncalcined catalyst. "CNA 750°C Static" was again the exception to this, showing a considerable cerium deficiency. Another interesting observation was the proportion of Ce(III) on the surfaces of the catalysts. The uncalcined catalyst showed a high proportion of Ce(III) over Ce(IV) compared to many of the catalysts reported in this chapter. While calcination at 750 °C under flowing atmospheres maintained this high proportion, calcination under static air resulted in a decrease to the Ce(III) content.

The C 1s and O 1s regions of the catalysts' XPS spectra are shown in figures 4.41 and 4.42, overleaf.

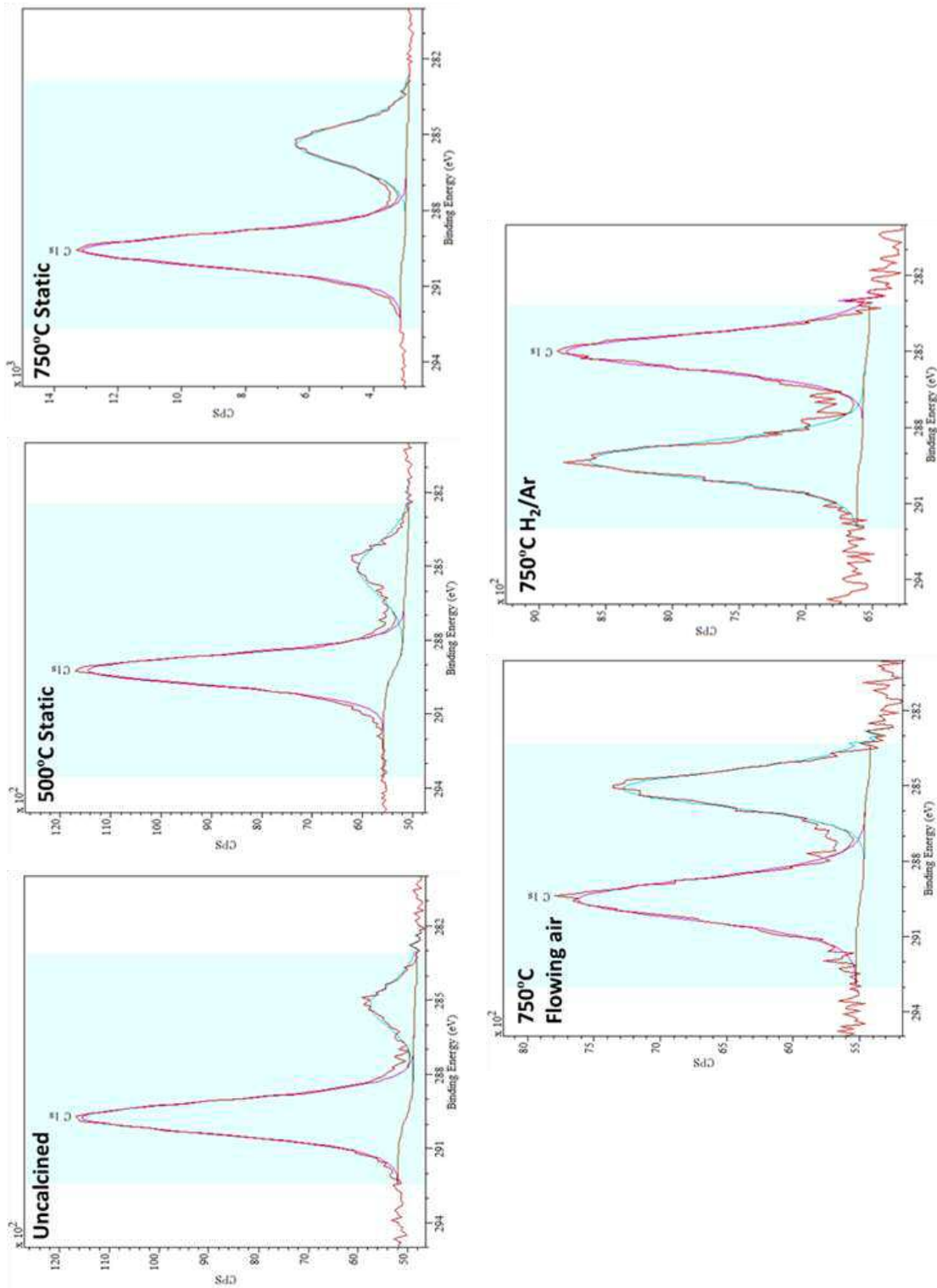


Figure 4.41 C 1s spectra of CNA 7:3:10 catalysts

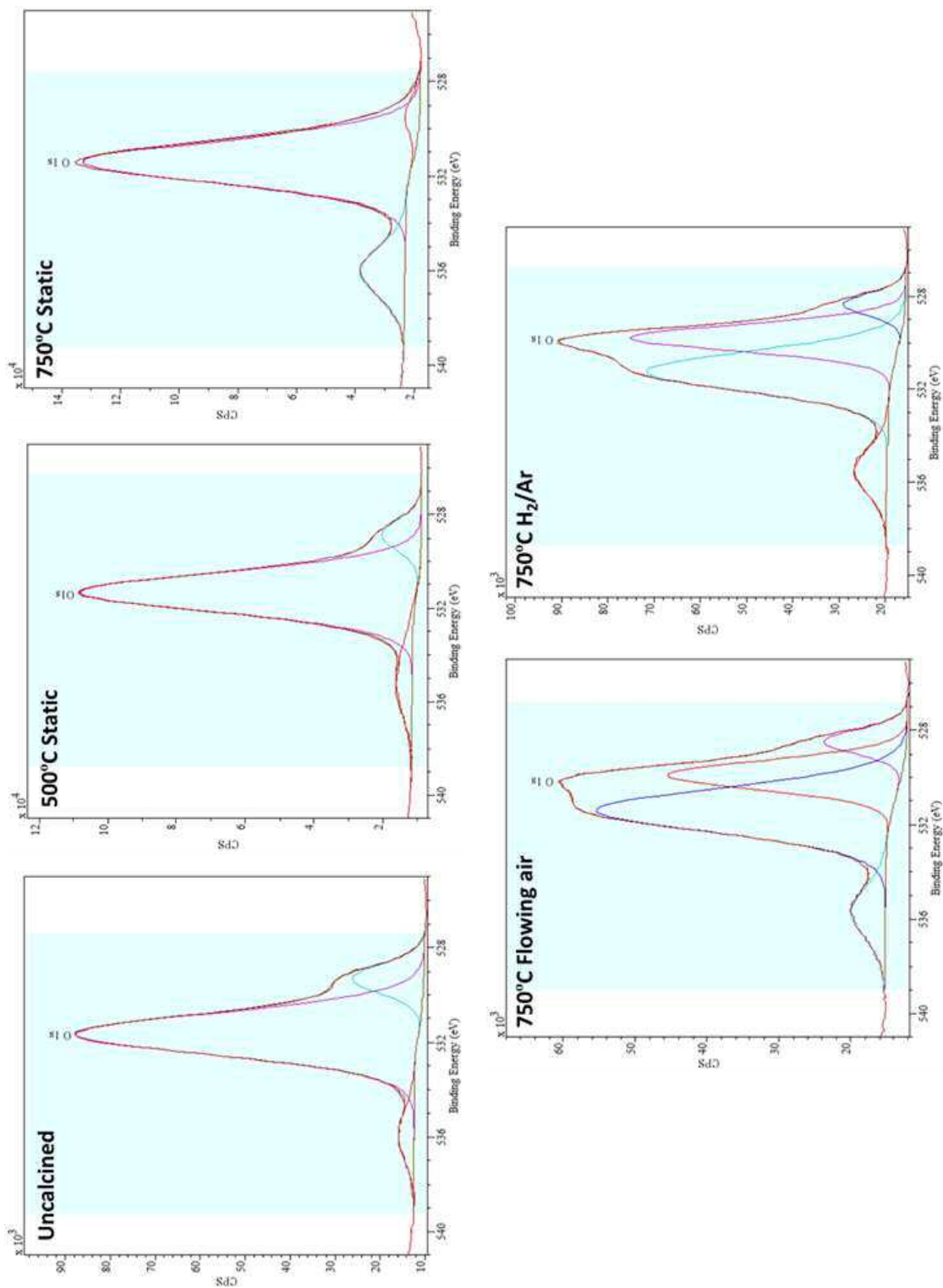
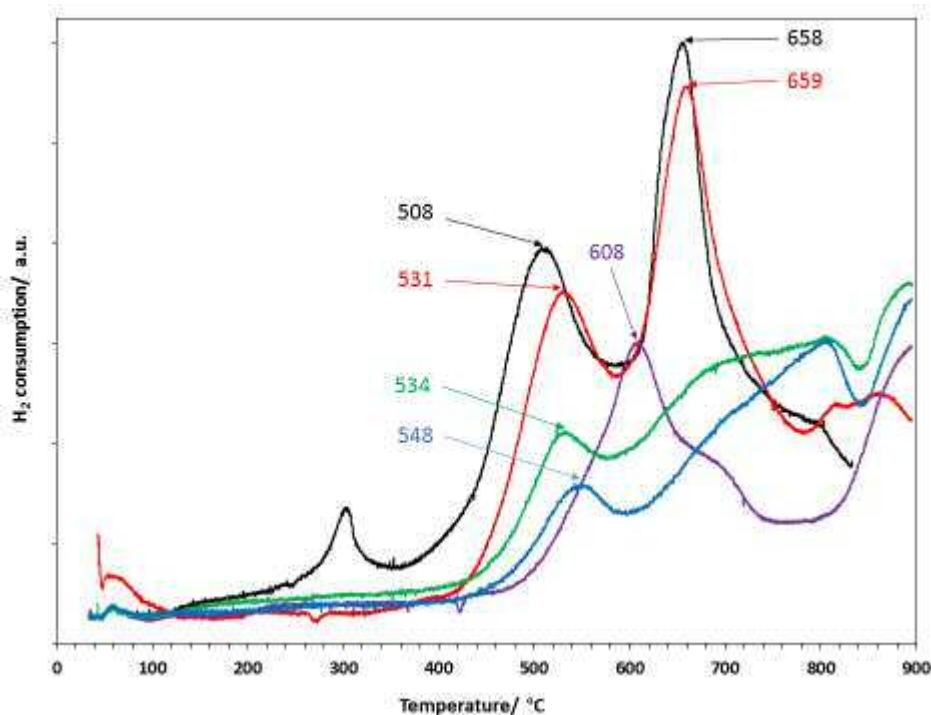


Figure 4.42 O 1s spectra of CNA 7:3:10 catalysts

The C 1s regions all showed two distinct peaks at 285 eV and 289 eV attributed to adventitious and carbonate sources of carbon respectively. The areas of these peaks were quantified and are shown in table 4.32. It was observed that the proportion of carbon in the carbonate form was highest in the uncalcined catalyst, and decreased significantly when calcined at 750 °C under flowing air and H<sub>2</sub>/Ar. The peaks in the O 1s region were assigned to three groups. The peaks in the 528.5-530 eV region are attributed to metal-oxide bonds (lattice oxygen), the peaks at 531.5 eV were attributed to oxygen from alumina and carbonates, and the peaks at ~536 eV were attributed to Na auger<sup>26</sup>. As table. 4.32 shows, the proportion of oxygen in the alumina/carbonate region is significantly lower in the cases of “CNA 750°C Flowing Air” and “CNA 750°C H<sub>2</sub>/Ar”. The presence of a splitting of the metal-oxide component in the O 1s regions of “CNA 750°C Flowing Air” and “CNA 750°C H<sub>2</sub>/Ar” could have indicated that cerium oxide and neodymium oxide produced two separate signals, due to the decomposition of Nd<sub>2</sub>O<sub>2</sub>CO<sub>3</sub>. The observations in the C 1s and O 1s regions suggested that a higher temperature and a flowing atmosphere during calcination resulted in a decrease in the presence of carbonates and increase in neodymium oxide. This may provide evidence of the decomposition of the Nd<sub>2</sub>O<sub>2</sub>CO<sub>3</sub> phase that was detected in the CNA catalysts in section 4.6.1.

**Table 4.32** Relative peak areas (%) of O 1s and C 1s regions

Catalyst	Atomic conc. (%) (O 1s)		Atomic conc. (%) (C 1s)	
	Lattice O <sup>2-</sup>	Al <sub>2</sub> O <sub>3</sub> /CO <sub>3</sub> <sup>2-</sup>	Adventitious	CO <sub>3</sub> <sup>2-</sup>
Uncalcined	13	87	15	85
500°C static	8	92	21	79
750°C static	4	96	29	71
750°C flowing air	9	31	59	43
750°C H <sub>2</sub> /Ar	7	40	53	49



**Figure 4.43** TPR profiles of CNA 7:3:10 catalysts: Uncalcined (black), 500°C static air (red), 750°C static air (purple), 750°C flowing air (green), 750°C 10% $H_2$ /Ar (blue)

Figure 4.43 shows that the reduction profiles of the catalyst were greatly affected by changes in calcination conditions. The peak at around 660 °C observed in the uncalcined catalyst was the same as that observed previously for “CNA 500°C Static”, which was attributed in section 4.6.1 to the decomposition of carbonates and other impurities. This peak was not observed in any of the catalysts calcined at 750 °C, suggesting these species had been removed during calcination. The removal of this peak revealed a broad curve between 600 °C and 850 °C in “CNA 750°C Flowing Air” and “CNA 750°C  $H_2$ /Ar”, which was attributed to the reduction of bulk  $Ce^{4+}$  ions<sup>1</sup>. The calcination conditions also had an effect on the reduction of  $Ce^{4+}$  ions. As seen in table 4.33, the reduction of surface cerium took place at the lowest temperature and greatest intensity in the uncalcined catalyst. The surface reduction curves of the catalysts calcined under static air both showed similar intensities, however when calcined at 750 °C the temperature at which reduction took place was considerably higher. The other catalysts calcined at 750 °C did not show as great an increase in reduction temperature, however the overall intensity of the surface reduction curves were significantly lower. The deterioration in surface  $Ce^{4+}$  reduction for the catalysts calcined at 750 °C was attributed to their lower surface areas and high crystallinity, which impeded their reduction capabilities.

**Table 4.33** Surface cerium reduction properties of CNA catalysts

Catalyst	Peak reduction	Intensity*	
	temp (°C)	Peak	Area
Uncalcined	508	0.69	<b>0.86</b>
500°C Static air	531	0.61	<b>0.67</b>
750°C Static air	608	0.51	<b>0.68</b>
750°C Flowing Air	534	0.35	<b>0.46</b>
750°C H <sub>2</sub> /Ar	548	0.25	<b>0.33</b>

\*Relative to CZA 7:3:10 (Section 4.1.1)

#### 4.7.2 Soot oxidation testing

The CNA catalysts were each tested for soot oxidation by thermogravimetric analysis in the usual manner. The derivative plots are presented in figure 4.44, with each of the samples offset by 1 %min<sup>-1</sup> for ease of comparison.

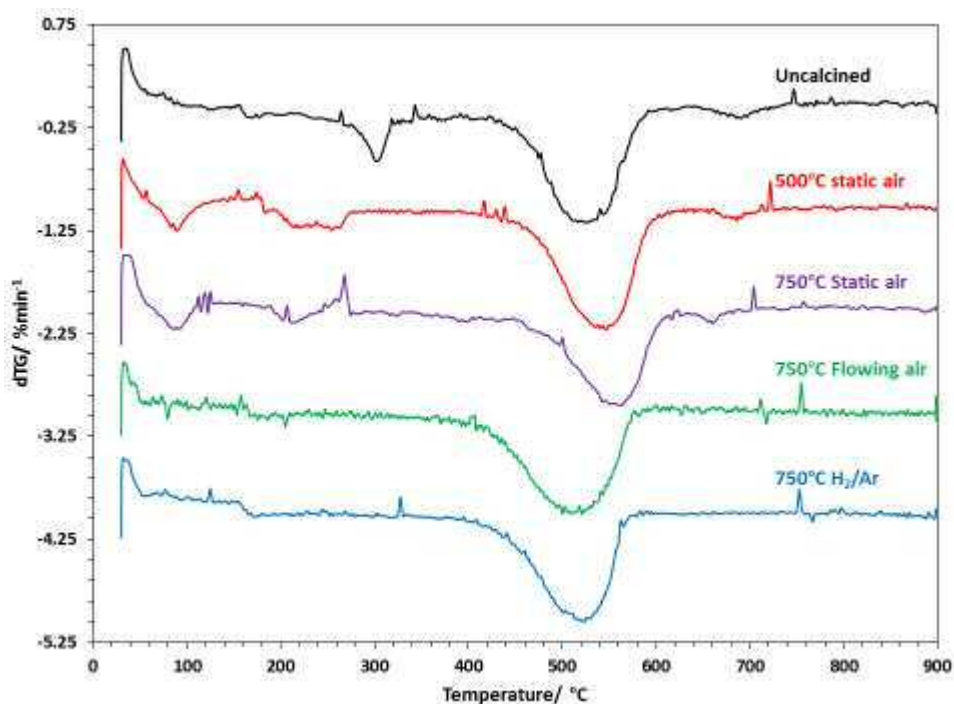


**Figure 4.44** dTG plots of catalyst/soot mixtures containing CNA: Uncalcined (black), 500°C static air (red), 750°C static air (purple), 750°C flowing air (green), 750°C 10%H<sub>2</sub>/Ar (blue)

Testing revealed that the calcination conditions were highly influential in the soot oxidation activity of the CNA catalyst. As indicated in table 4.34, the increase in calcination temperature under static air from 500 °C to 750 °C resulted in a decrease in activity, with the peak soot



oxidation temperature rising to almost 560 °C in the case of the latter. Significantly, the onset temperature was considerably higher, which could be explained by the higher temperature reduction peak observed in the TPR profile of this catalyst described above. Interestingly, it was also observed that the activity of both these catalysts decreased after calcination, with the uncalcined material able to achieve peak soot oxidation at a considerably lower temperature than both. The catalysts calcined under flowing air and H<sub>2</sub>/Ar were considerably more active than the aforementioned “static air” catalysts, with the former being the most active of the two. The soot oxidation temperatures of these catalysts were similar to the rerun CNA catalysts described in section 4.6.2.

**Table 4.34** Soot oxidation temperatures of samples mixed with CNA catalysts on their first and second use

Catalyst	T <sub>o</sub> (°C)		T <sub>eo</sub> (°C)		T <sub>p</sub> (°C)		T <sub>f</sub> (°C)	
	1 <sup>st</sup> run	2 <sup>nd</sup> run	1 <sup>st</sup> run	2 <sup>nd</sup> run	1 <sup>st</sup> run	2 <sup>nd</sup> run	1 <sup>st</sup> run	2 <sup>nd</sup> run
<b>Soot (no catalyst)</b>	465		535		<b>622</b>		651	
<b>Uncalcined</b>	428		455		<b>523</b>		592	
<b>500°C Static air</b>	405	383	464	451	<b>547</b>	<b>525</b>	617	581
<b>750°C Static air</b>	457	411	472	454	<b>559</b>	<b>533</b>	623	578
<b>750°C Flowing air</b>	369	364	419	433	<b>512</b>	<b>516</b>	587	575
<b>750°C H<sub>2</sub>/Ar</b>	378	396	434	436	<b>523</b>	<b>523</b>	584	583

The calcined catalysts were subjected to a second round of soot oxidation testing to determine their thermal durability, which are shown in figure 4.45. As observed with the CNA catalysts in the previous section, “CNA 750°C Static” performed much better on its second run, decreasing the soot oxidation temperature at each marker by at least 25 °C. The other two catalysts calcined at 750 °C were both able to maintain the high activity displayed during the first round of testing.

This suggested that a flowing atmosphere, either during calcination or soot oxidation testing, was essential to the improvement in activity observed. The higher activity of “CNA 750°C Flowing Air” suggested that an oxidative flowing atmosphere was more beneficial than a reductive atmosphere.

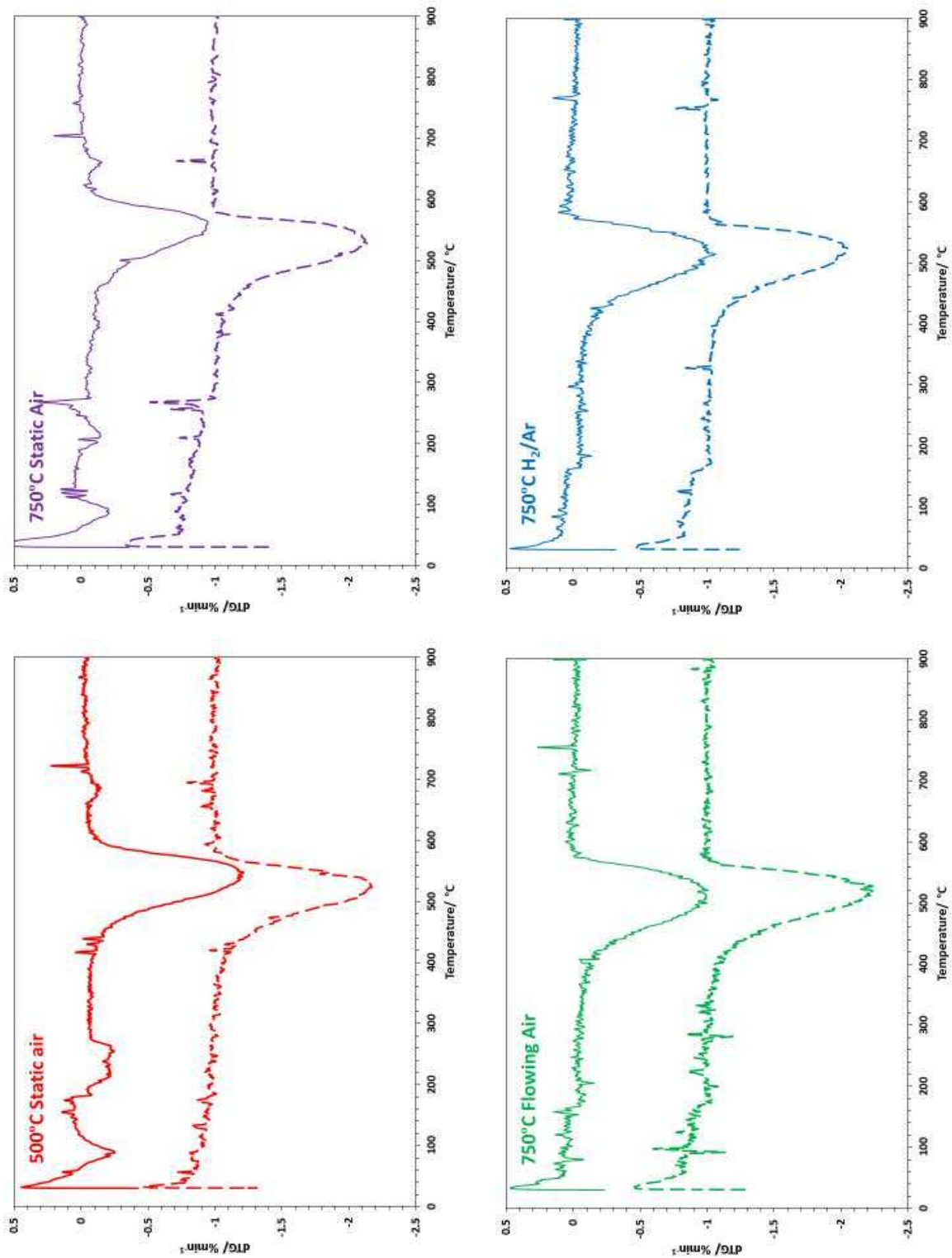


**Figure 4.45** DTG plots of catalyst/soot mixtures containing CNA: 500°C static air (red), 750°C static air (purple), 750°C flowing air (green), 750°C 10% H<sub>2</sub>/Ar (blue) on the first run (solid line) and second run (dashed line)

## 4.8 Summary and conclusions

In this chapter the use of rare-Earth metals as an alternative to zirconium were investigated as dopants in ceria-alumina catalysts. Zirconium, lanthanum, an equimolar mix of the two, praseodymium and neodymium were mixed in 7:3, 5:5 and 3:7 ratios with cerium in order to determine the optimum composition for an active and stable soot oxidation catalyst. A catalyst prepared using a 3:7:10 Ce:La:Al ratio was found to be the most active during the first round of testing, and proved to be thermally durable by maintaining this high activity during its second testing. Each of the CNA catalysts were found to be considerably more active during their second tests, leading to a subsequent investigation into the calcination conditions of the CNA 7:3:10 catalyst. This investigation led to the discovery of the most active catalyst presented in this chapter – CNA in a 7:3:10 ratio calcined at 750 °C in flowing air.

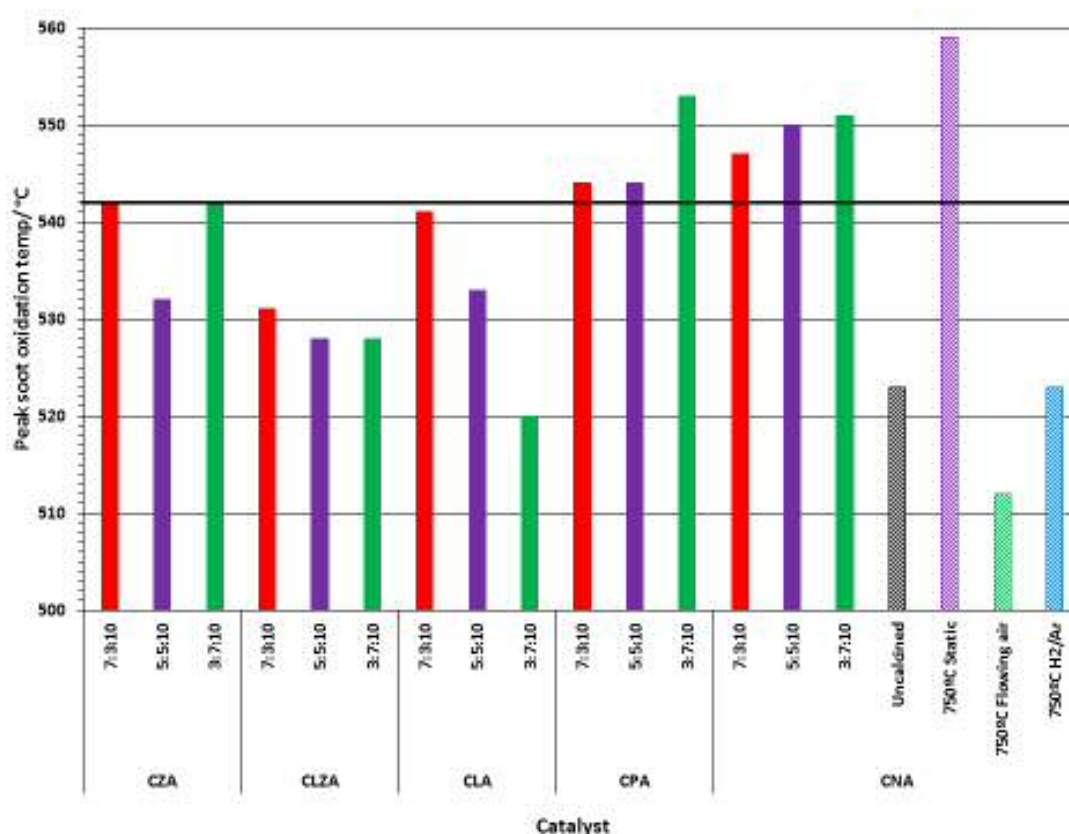


**Figure 4.46** Peak soot oxidation temperatures mixed with CMA catalysts (black line indicates the peak soot oxidation temperature with CZA 7:3:10)

A summary of the peak soot oxidation temperatures achieved with each of the CMA catalysts is shown in figure 4.46. The black line indicates the peak soot oxidation temperature with CZA 7:3:10, the benchmark from the previous chapter. From this chart we can see that the

catalysts containing lanthanum were generally more active than CZA, while those containing praseodymium and neodymium (during their first run) were less active.

The characterisation of the catalysts by XRD and Raman indicated that, as expected, the dopant metals altered the parameters of the ceria lattice due to their ionic radii. In the case of CZA this resulted in a lattice contraction due to the relatively small ionic radius of  $Zr^{4+}$ , whereas lattice expansion was observed in the catalysts containing rare-Earth metals due to the relatively large ionic radii of  $La^{3+}$ ,  $Pr^{3+}$  and  $Nd^{3+}$ . This was observed to the greatest extent in the CLA and CNA catalysts, which were doped only with the larger  $La^{3+}$  and  $Nd^{3+}$  ions, but less so in CLZA and CPA which also contained the smaller  $Zr^{4+}$  and  $Pr^{4+}$  ions respectively. These analyses also indicated the presence of a separate phase to ceria in the catalysts containing higher concentrations of rare-Earth elements. CLA, CLZA and CNA were found to contain a metal-oxycarbonate phase, while CPA showed evidence of a strong  $Pr_6O_{11}$  phase. The increase of these phases corresponding to an increase in dopant metal content suggested that unlike CZA, the rare-Earth metals were unable to form a homogenous crystalline phase with ceria, the contrast possibly due to the greater difficulty of larger ions to fully integrate into the lattice structure.

The temperature-programmed reduction profiles of the catalysts showed a distinct peak attributed to the reduction of surface  $Ce^{4+}$  ions, and a further peak(s) at a higher temperature which was attributed to the reduction of bulk cerium ions as well as the decomposition of carbonates and other impurities. The intensity of the surface reduction peak was lower in most of the catalysts than CZA 7:3:10 and was found to decrease as the proportion of cerium decreased. The exceptions to this were CZA 5:5:10; which had a higher intensity and a lower peak temperature surface reduction than CZA 7:3:10, and the CPA catalysts; which showed an increase in reducibility as the proportion of cerium decreased and praseodymium increased due to the reduction of  $Pr^{4+}$  ions.

Figure 4.47 a) and b) respectively, show the relative intensities of surface reduction and the peak reduction temperatures of the catalysts compared to the peak soot oxidation temperatures achieved.

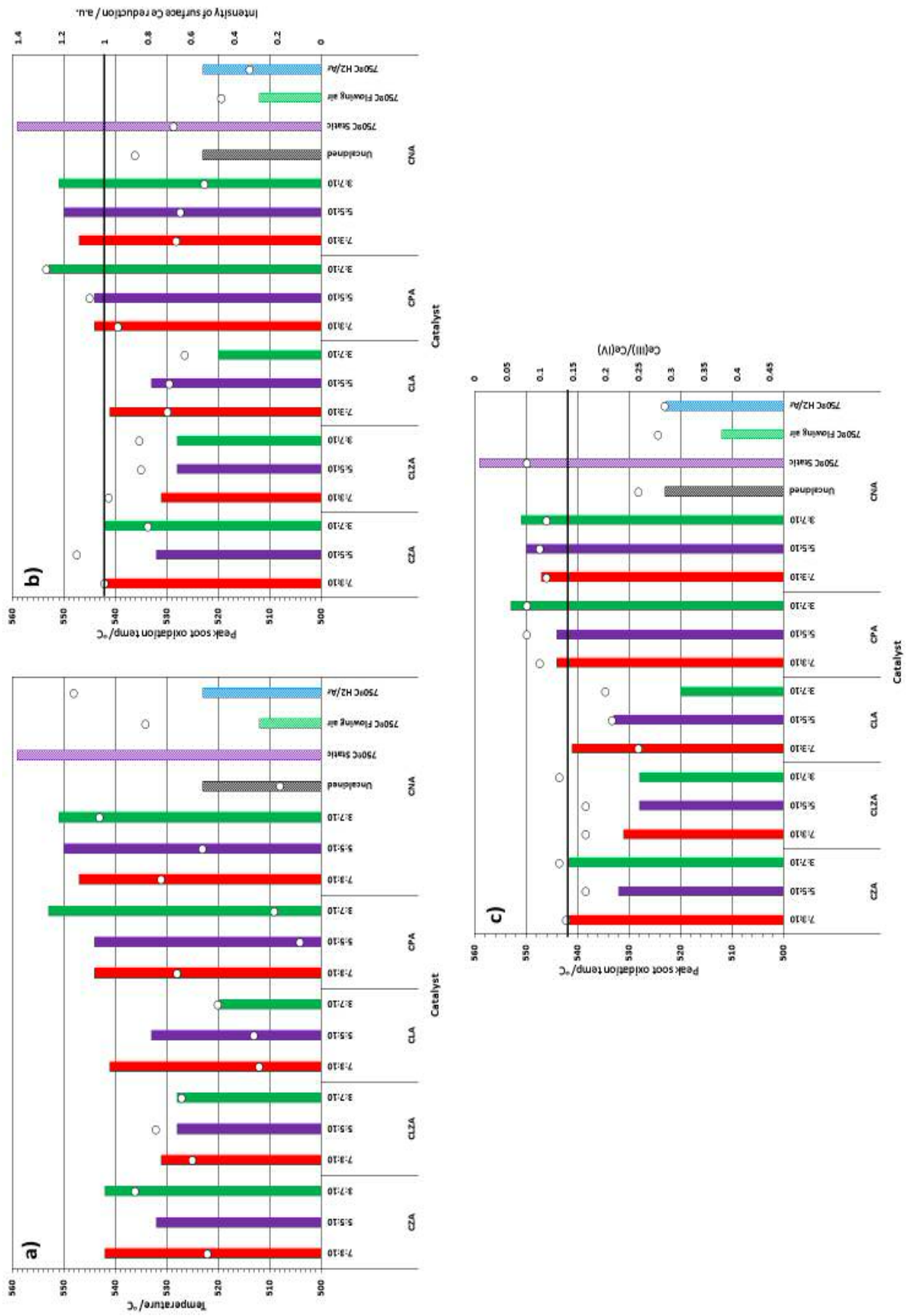


**Figure 4.47** Comparison of peak soot oxidation temperatures (bars) with **a)** peak surface reduction temperatures, **b)** peak surface reduction intensities and **c)** surface Ce(III)/Ce(IV) ratios (white circles) (black lines indicate the peak soot oxidation temperature with CZA 7:3:10)

In the case of CZA 5:5:10, the decrease in temperature (at 493 °C, beyond the scale of the chart) and increase in intensity of reduction compared to CZA 7:3:10 resulted in a decrease in the soot oxidation temperature between the two catalysts. The reverse was observed in the case of “CNA 750°C Static”, which underwent a less intense reduction at a significantly higher temperature (608 °C), and which resulted in a considerably higher soot oxidation temperature. However these were the two extreme cases, and a universal link between surface reduction and the soot oxidation activity of the remaining catalysts was not established. As mentioned in section 4.5, in the case of CPA 5:5:10 and 3:7:10, although the reduction of  $\text{Pr}^{4+}$  resulted in an overall increase in the reduction on the surfaces and at a lower temperature, there is evidence in literature which suggests the oxygen released by this reduction is not as reactive as the species released during reduction of  $\text{Ce}^{4+}$ <sup>20</sup>. Therefore the increase in oxygen released did not result in a decrease in the soot oxidation temperature.

Another consideration was the proportion of cerium in the +3 oxidation state on the surfaces of the catalysts provided by XPS. This is an indication of the quantity of oxygen vacancies on the catalysts' surfaces, which could enhance the redox properties of ceria. As shown in figure 4.47 c), there was again no consistent trend between this and peak soot oxidation temperature. However it was interesting to note that in almost all cases those catalysts containing a higher proportion of Ce(III) on their surfaces than CZA 7:3:10 tended to show a lower soot oxidation temperature, whereas those with a lower Ce(III) proportion tended to result in higher soot oxidation temperatures. This was particularly relevant to the CNA 7:3:10 catalysts of varying calcination conditions, which showed a considerable improvement in activity corresponding to a higher proportion of Ce(III), despite “CNA 750°C Flowing air” and “CNA 750°C H<sub>2</sub>/Ar” having shown low intensity surface  $\text{Ce}^{4+}$  reduction in their TPR profiles.

In conclusion, the activity of ceria catalysts showed greatest improvement when doped with lanthanum and, under the correct calcination conditions, neodymium. From XPS studies it was determined that these catalysts had a high proportion of Ce(III) present on their surfaces compared to the original CZA catalyst. This indicated an increase in oxygen vacancies which enhanced the redox properties of the catalyst, allowing more rapid exchange of oxygen at the phase boundary, which could subsequently be utilised for soot oxidation. This was likely brought about by distortion to the ceria lattice caused by the introduction of bulky aliovalent  $\text{La}^{3+}$  and  $\text{Nd}^{3+}$  ions, confirmed by XRD and Raman. The study into praseodymium-doped ceria

catalysts showed that despite increasing the reducibility of the catalyst, this did not result in an improvement in activity. This emphasised the importance of the “quality” (reactivity) rather than “quantity” of oxygen species available for soot oxidation at the catalyst surface.

It was observed from the study into the CNA 7:3:10 catalysts that calcination at a higher temperature and under flowing atmospheres resulted in much more active catalysts. But for time constraints, it would have been interesting to extend this study to the other CMA catalysts presented in this chapter, particularly to the CLA catalysts which had many structural similarities to CNA. However only the CNA catalysts showed such significant improvement subsequent to testing under the TGA conditions, and therefore it was deemed unlikely that an improvement to catalytic activity would have been observed to this extent.

## 4.9 References

1. A. Bueno-López, *Appl. Catal. B Environ.*, 2014, **146**, 1–11.
2. J. Kašpar, P. Fornasiero and M. Graziani, *Catal. Today*, 1999, **50**, 285–298.
3. P. Fornasiero, G. Balducci, R. Di Monte, J. Kašpar, V. Sergo, G. Gubitosa, A. Ferrero and M. Graziani, *J. Catal.*, 1996, **164**, 173–183.
4. P. Dulgheru and J. A. Sullivan, *Top. Catal.*, 2013, **56**, 504–510.
5. K. Harada, T. Oishi, S. Hamamoto and T. Ishihara, *J. Phys. Chem. C*, 2014, **118**, 559–568.
6. D. Mukherjee, B. G. Rao and B. M. Reddy, *Appl. Catal. B Environ.*, 2016, **197**, 105–115.
7. I. Atribak, A. Bueno-López and A. García-García, *J. Catal.*, 2008, **259**, 123–132.
8. R. Ramdas, Thesis, Cardiff University, 2014.
9. L. Katta, P. Sudarsanam, G. Thrimurthulu and B. M. Reddy, *Appl. Catal. B Environ.*, 2010, **101**, 101–108.
10. J. Guo, Z. Shi, D. Wu, H. Yin, M. Gong and Y. Chen, *J. Alloys Compd.*, 2015, **621**, 104–115.
11. S. Liu, X. Wu, D. Weng and R. Ran, *J. Rare Earths*, 2015, **33**, 567–590.
12. V. G. Keramidas and W. B. White, *J. Chem. Phys.*, 1973, **59**, 1561–1562.
13. M. R. Benjaram, T. Gode and L. Katta, *Chin. J. Catal.*, 2011, **32**, 800–806.
14. N. Guillén-Hurtado, A. García-García and A. Bueno-López, *Appl. Catal. B Environ.*, 2015, **174–175**, 60–66.
15. Thermo Scientific XPS: Knowledge Base, <http://xpssimplified.com/elements/cerium>
16. B. Azambre, S. Collura, P. Darcy, J. M. Trichard, P. Da Costa, A. García-García and A. Bueno-López, *Fuel Process. Technol.*, 2011, **92**, 363–371.
17. A. N. Shirsat, M. Ali, K. N. G. Kaimal, S. R. Bharadwaj and D. Das, *Thermochim. Acta*, 2003, **399**, 167–170.
18. E. Aneggi, C. de Leitenburg, G. Dolcetti and A. Trovarelli, *Catal. Today*, 2008, **136**, 3–10.

19. C. F. Oliveira, F. A. C. Garcia, D. R. Araújo, J. L. Macedo, S. C. L. Dias and J. A. Dias, *Appl. Catal. Gen.*, 2012, **413–414**, 292–300.
20. M. Machida, Y. Murata, K. Kishikawa, D. Zhang and K. Ikeue, *Chem. Mater.*, 2008, **20**, 4489–4494.
21. A. Orera, G. Larraz and M. L. Sanjuán, *J. Eur. Ceram. Soc.*, 2013, **33**, 2103–2110.
22. R. P. Turcotte, J. O. Sawyer and L. Eyring, *Inorg. Chem.*, 1969, **8**, 238–246.
23. C. Artini, M. M. Carnasciali, G. A. Costa, R. Masini, E. Franceschi and F. Locardi, *J. Therm. Anal. Calorim.*, 2013, **112**, 499–503.
24. C. Artini, *J. Alloys Compd.*, 2009, **477**, 532–536.
25. K. Krishna, A. Bueno-López, M. Makkee and J. A. Moulijn, *Appl. Catal. B Environ.*, 2007, **75**, 189–200.
26. Oxygen, <http://sites.cardiff.ac.uk/xpsaccess/reference/oxygen/>.



## 5. Alkali and transition metal catalysts on ceria-based supports

The main focus of the project thus far has been on enhancing the properties of ceria in order to improve its catalytic activity by introducing various foreign elements into its structure. The main role of these foreign elements was not to act directly as soot oxidation catalysts, but rather to improve the soot oxidation capabilities of ceria by influencing its structural and physical properties, so called “ceria amplifiers”<sup>1</sup>. The co-precipitation method of catalyst preparation has been used in order to ensure incorporation of the foreign metals throughout the ceria structure, so as to enhance its surface and bulk properties. However it has also been observed during this study that other active species – namely alkali metals – can be used in conjunction with ceria in order to improve the overall ability of the material to catalyse soot oxidation; termed “ceria synergy”<sup>1</sup>.

As stated in Chapter 1, there have been studies into a broad range of soot oxidation catalysts supported on various materials. In this chapter, the ceria-based materials presented in the previous chapter were utilised as supports for various species which have been reported to exhibit activity for soot oxidation. The aim of this investigation was to provide stable supports for these active species whilst also enhancing the catalytic activity of the supports themselves, resulting in highly active soot oxidation catalysts. A wet impregnation method, described in Chapter 2, was used to prepare each of the catalysts.

Initially, this expanded on a previous study at Cardiff University which utilised a combination of silver and potassium on a CZA support<sup>2</sup>. Although scientifically significant, the use of silver for real-world application is controversial due to its reported tendency to sinter<sup>3</sup>. Various other transition metals were therefore screened on a CZA support as potential substitutes for silver, of which copper was found to be the most promising. The use of copper was subsequently expanded to the various other ceria supports presented in the previous chapter.

### 5.1 Silver and potassium on CZA catalyst supports

As discussed in Chapter 1, the high activity of silver and alkali metals for application in soot oxidation catalysts have been widely reported in literature, as well as in conjunction with ceria and doped-ceria catalysts. Silver, due to its ability to form highly reactive superoxide species

and its interactions with ceria inducing facile oxygen mobility<sup>4-6</sup>, and alkali metals due to their ability to form carbonate intermediates for the reaction of solid carbon to CO<sub>2</sub>, and their low-melting points allowing mobility and increased soot contact<sup>7-9</sup>. A previous study into the use of silver and potassium on a CZA support was undertaken at Cardiff University and established a synergistic effect took place. The optimum loadings were found to be 2 and 10 weight%, respectively, using AgNO<sub>3</sub> and K<sub>2</sub>CO<sub>3</sub> as the precursors<sup>2</sup>. This was based on observations of greatest cerium reduction intensity and lowest soot oxidation temperatures by 2%Ag as it was predominantly present as Ag<sup>0</sup> and thus interacted favourably with CeO<sub>2</sub>. The 10%K loading also produced the lowest soot oxidation temperatures, with lower loadings having less impact and higher loadings decreasing the activity by lowering the concentration of cerium on the surface of the support.

However before applying the findings of that study to the various new ceria supports presented in Chapter 4, it was decided to impregnate both species separately on the CZA support produced by this study in order to establish the role each has in enhancing the activity of soot oxidation. These are referred to as 2%Ag/CZA and 10%K/CZA. The combination of both silver and potassium with the same respective loadings on the same CZA support was also prepared in order to establish the extent, if any of the synergistic effect between the two. This catalyst is referred to as 2%Ag,10%K/CZA. The results of characterisation and testing provided by these catalysts were compared with the bare CZA support in each case.

### 5.1.1 Characterisation

Each of the catalysts were characterised in a similar fashion to those in the previous chapter.

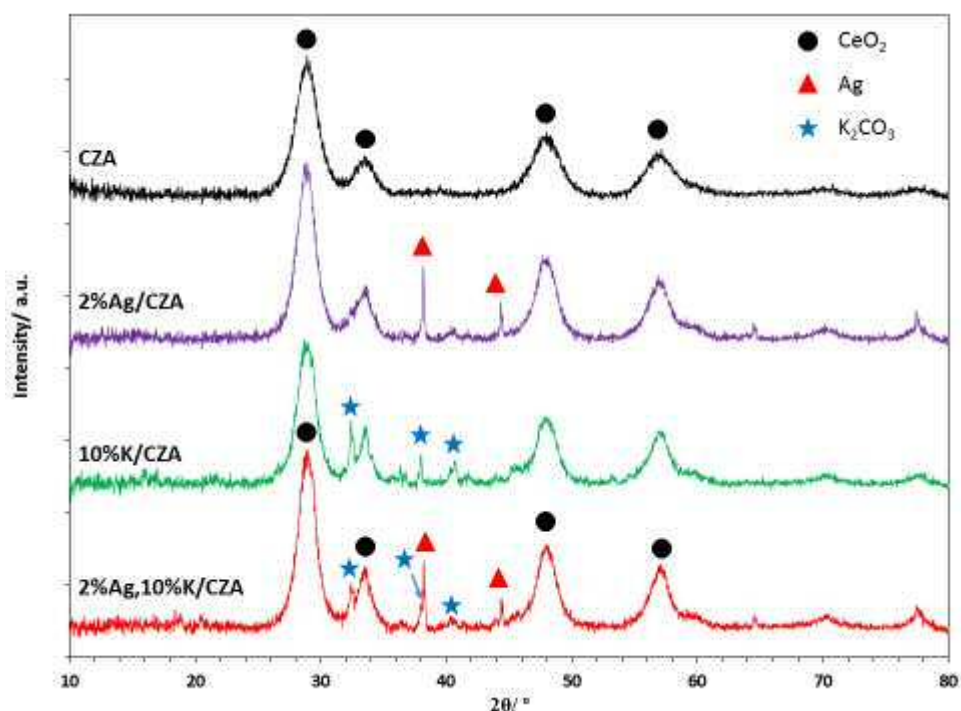


**Figure 5.1** X-ray diffractograms of CZA (black), 2%Ag/CZA (purple), 10%K/CZA (green) and 2%Ag,10%K/CZA (red)

The X-ray diffractograms of the catalysts in figure 5.1 each showed the typical fluorite-type structure of ceria, with reflections at  $28.9^\circ$ ,  $33.5^\circ$ ,  $48.0^\circ$ ,  $57.0^\circ$  attributed to the (111), (200), (220) and (311) planes respectively as established in the previous chapters. As noted, the positions of these reflections were consistent in each case. This suggested that the impregnation of silver, potassium and a combination of both did not cause a change to the lattice parameter of ceria in the manner observed when foreign cations were introduced by co-precipitation in the previous chapter. Additional reflections were also observed in the diffractograms of the impregnated catalysts. In 2%Ag/CZA, two prominent reflections were observed at  $38.2^\circ$  and  $44.4^\circ$ , identified as belonging to a cubic phase of metallic silver,  $\text{Ag}^0$  (JCPDS 65-2871). The diffractogram of 10%K/CZA showed several reflections attributed to monoclinic  $\text{K}_2\text{CO}_3$  at  $32.4^\circ$ ,  $38.0^\circ$  and  $40.6^\circ$  (JCPDS 16-820) which suggested that potassium remained in its precursor carbonate form, despite calcination. The diffractogram of 2%Ag,10%K/CZA displayed the reflections of both the silver and potassium phases described above.

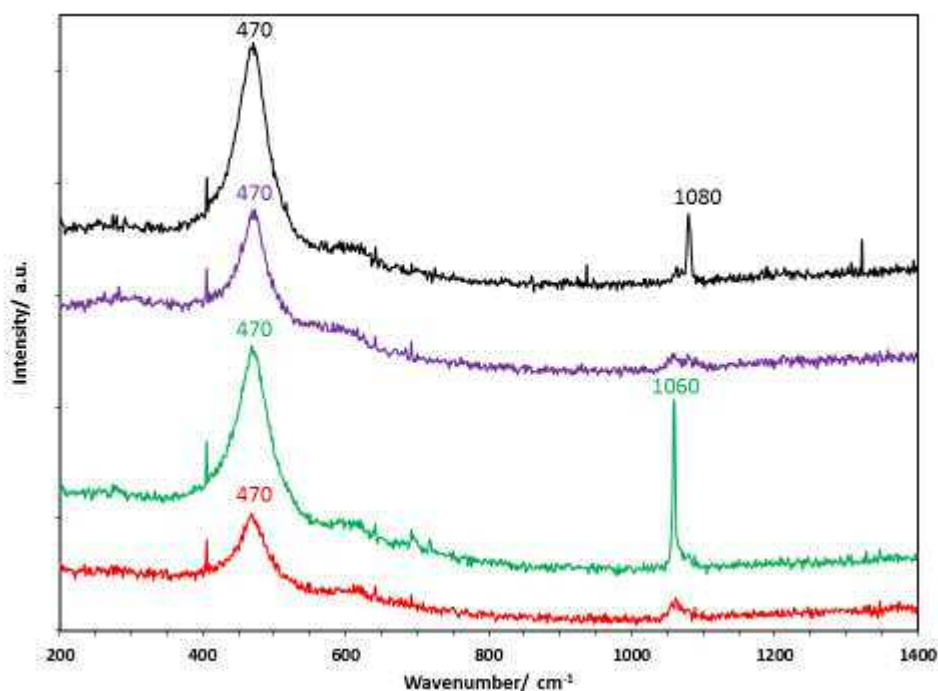


**Figure 5.2** Raman spectra of CZA (black), 2%Ag/CZA (purple), 10%K/CZA (green) and 2%Ag,10%K/CZA (red)

The Raman spectra of the catalysts in figure 5.2 each showed  $F_{2g}$  mode typical of the Ce-O bond of ceria. In each case the position of the peak remained consistent with the bare CZA support, at  $470\text{ cm}^{-1}$ . The spectrum of 10%K/CZA contained a sharp peak at  $1060\text{ cm}^{-1}$  which indicated the presence of  $K_2CO_3$ , in agreement with the findings of the XRD. However, this peak was not observed to this extent in the Raman spectrum of 2%Ag,10%K/CZA.

X-ray photoelectron spectroscopy and BET surface area analysis were performed on the catalysts in order to determine their surface properties.

Peaks in the Ag 3d (2%Ag/CZA, 2%Ag,10%K/CZA) and K 2p (10%K/CZA, 2%Ag,10%K/CZA) regions of the XPS spectra (examples in figure 5.3 shown from 2%Ag,10%K/CZA) confirmed the presence of the impregnated metals on the surfaces of the catalysts.

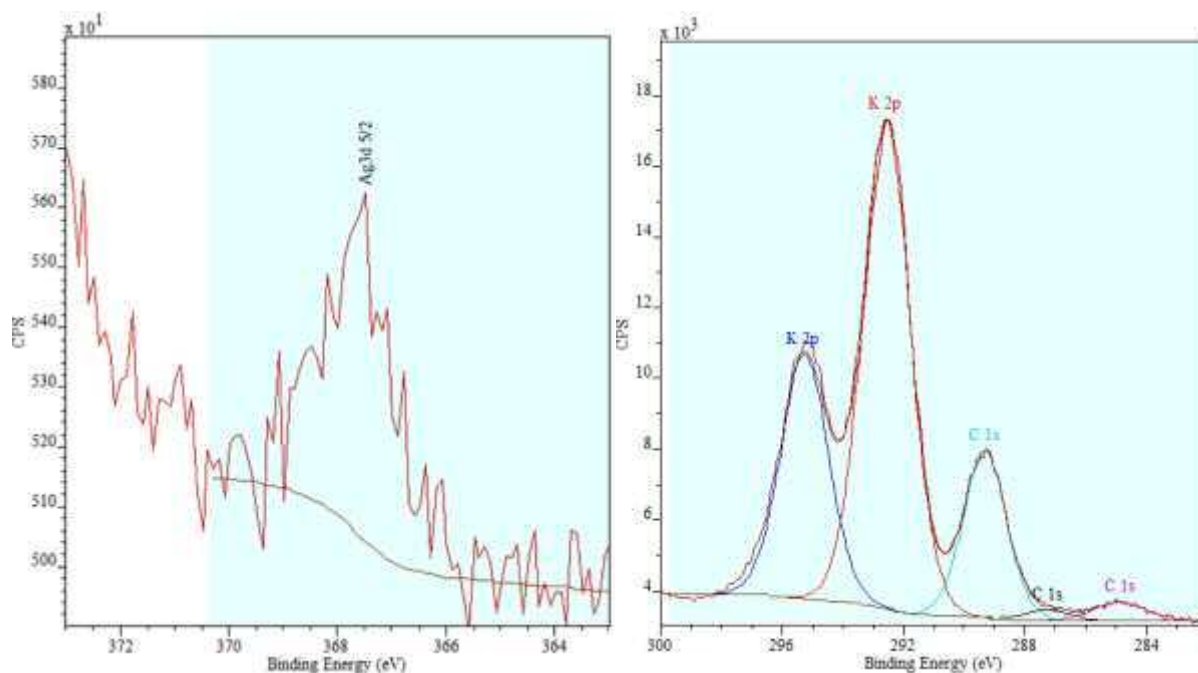
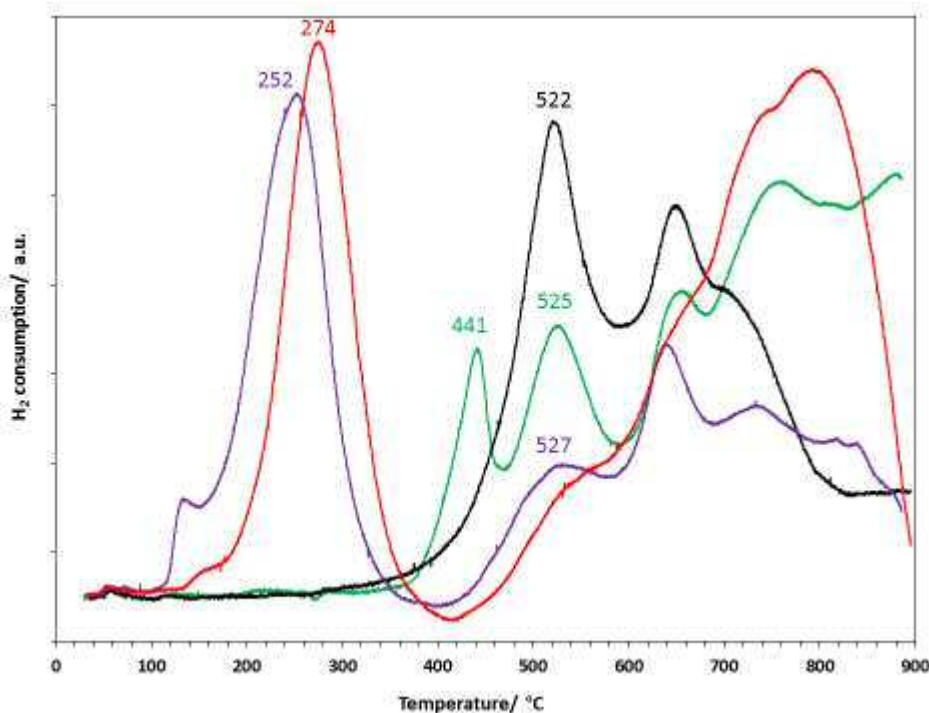


Figure 5.3 Ag 3d region and C 1s/K 2p region of 2%Ag,10%K/CZA

The concentrations of the surface elements were quantified and are shown in table 5.1. Few changes were observed to the composition of the surface of the CZA support, save for the presence of the impregnated metals and an increase in the concentration of carbon in the case of the catalysts impregnated with potassium. This provided further evidence of the presence of potassium carbonate in these catalysts as identified by XRD and Raman. BET analysis of the catalysts showed that the impregnation of the metals resulted in a decrease in surface area. The trend in decreasing surface areas corresponded to an increase in the quantity of impregnated materials (2%Ag<10%K<2%Ag,10%K) and could be explained by the plugging of pores on the surface of the support, as suggested in previous chapters.

Table 5.1 Surface properties of Ag and K/CZA catalysts provided by XPS and BET analyses

Catalyst	Atomic conc. (%)								Surface area (m <sup>2</sup> g <sup>-1</sup> )
	Ce 3d	Zr 3d	Al 2p	O 1s	C 1s	Na 1s	Ag 3d	K 2p	
<b>CZA</b>	6.22	1.27	17.03	51.51	7.25	16.73	-	-	36 (±1)
<b>2%Ag</b>	6.30	1.23	16.96	51.65	7.12	16.49	0.25	-	31 (±2)
<b>10%K</b>	5.79	1.10	14.82	48.48	11.91	15.73	-	2.17	27 (±0)
<b>2%Ag,10%</b>	6.02	1.15	11.87	51.50	11.57	15.99	0.21	1.70	20 (±0)



**Figure 5.4** TPR profiles of CZA (black), 2%Ag/CZA (purple), 10%K/CZA (green) and 2%Ag,10%K/CZA (red)

The TPR profiles of each of the catalysts are shown in figure 5.4, again with the bare CZA support included for comparison. In each case, a significant decrease in the intensity of the reduction peak at around 520 °C was observed between the impregnated catalysts and the bare support. In previous chapters this peak has been attributed to the reduction of surface  $\text{Ce}^{4+}$  ions. In the case of 2%Ag/CZA, the formation of a reduction peak at a much lower temperature of 252 °C was observed. This was attributed to a decrease in the temperature of surface  $\text{Ce}^{4+}$  reduction as a consequence of interactions with silver, which weaken Ce-O bonds and allow a more facile reduction<sup>10</sup>. It has also been extensively reported that a spillover process can take place whereby  $\text{H}_2$  is dissociated to H atoms by Ag and subsequently spills onto the surface of the support whereby it reduces the oxygen of ceria<sup>11–13</sup>.

This was corroborated by the decrease in the Ce reduction peak at around 525 °C observed for the bare CZA support. The residual reduction curve in this region suggested that not all the cerium on the surface of the support was interacting with Ag.

The impregnation of 10wt% potassium also significantly altered the TPR profile of CZA. In this case a splitting of the surface  $\text{Ce}^{4+}$  reduction peak was observed, which resulted in a separate reduction peak at 441 °C. A similar observation was made by Aneggi *et al.* with a similar

loading of K supported on CeO<sub>2</sub> (figure 5.5) however did not offer an explanation, only stating that potassium was responsible for the change<sup>8</sup>. Another notable change in the profile was a significant increase in reduction above 700 °C. This was also seen in the work by Aneggi, and was attributed to the decomposition of potassium carbonate (the presence of which was evidenced from XRD and Raman), similar to the decomposition of sodium carbonate reported in previous chapters of this work.

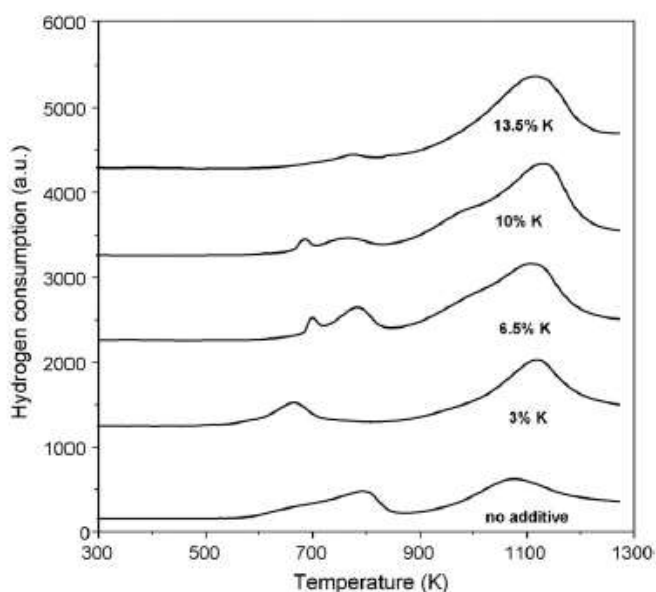


**Figure 5.5** TPR profiles of CeO<sub>2</sub> and CeO<sub>2</sub> doped with various potassium loadings<sup>8</sup>

The TPR profile of 2%Ag,10%K/CZA contained both the main features of the 2%Ag and 10%K/CZA profiles. The peak associated with reduction of Ce<sup>4+</sup> ions at a decreased temperature due to the presence of silver, and the large broad peak in the 600-800 °C region attributed to the decomposition of potassium carbonate were both observed.

### 5.1.2 Soot oxidation testing

Each of the catalysts were tested for soot oxidation using thermogravimetric analysis as in the previous chapters. The dTG plots of these tests are shown in figure 5.6, offset by 1 %min<sup>-1</sup> for ease of comparison, and the key soot oxidation temperatures extracted from these plots are presented in table 5.2.

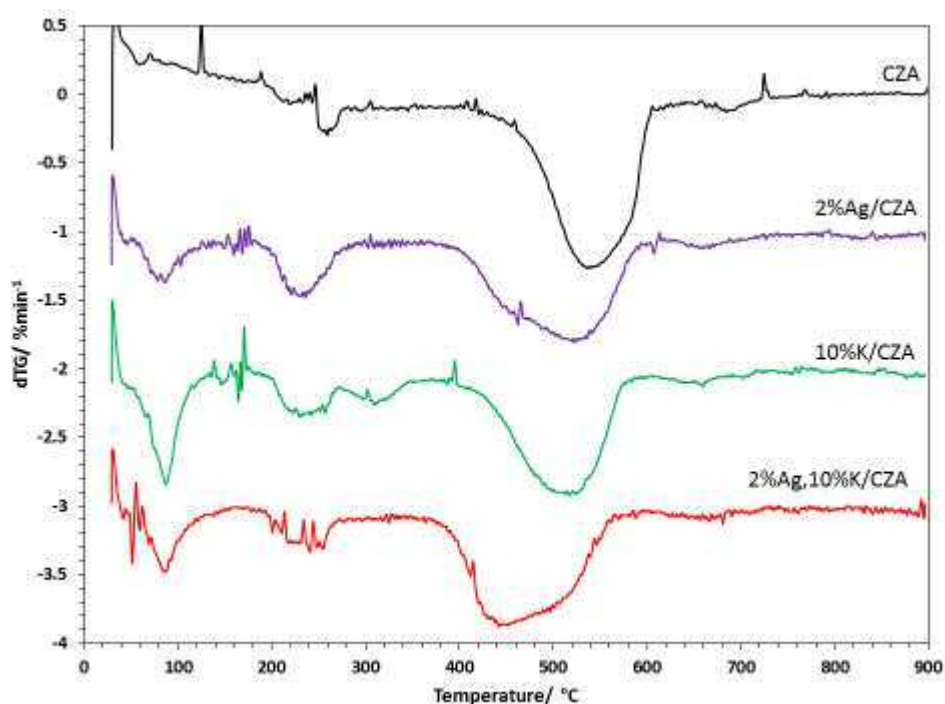


**Figure 5.6** DTG plots of catalyst/soot mixtures containing: CZA (black), 2%Ag/CZA (purple), 10%K/CZA (green) and 2%Ag,10%K/CZA (red)

It was observed from the results of testing that the impregnation of silver and potassium resulted in an increase in catalytic activity towards soot oxidation compared to the bare CZA support.

**Table 5.2** Soot oxidation temperatures of samples mixed with CZA catalysts on their first and second use

Catalyst	$T_o$ (°C)		$T_{eo}$ (°C)		$T_p$ (°C)		$T_f$ (°C)	
	1 <sup>st</sup> run	2 <sup>nd</sup> run	1 <sup>st</sup> run	2 <sup>nd</sup> run	1 <sup>st</sup> run	2 <sup>nd</sup> run	1 <sup>st</sup> run	2 <sup>nd</sup> run
<b>Soot (no catalyst)</b>	465		535		<b>622</b>		651	
<b>CZA</b>	410	389	461	436	<b>542</b>	<b>538</b>	605	597
<b>2%Ag/CZA</b>	372	396	401	453	<b>523</b>	<b>542</b>	594	587
<b>10%K/CZA</b>	397	384	424	429	<b>512</b>	<b>542</b>	587	590
<b>2%Ag,10%K/CZA</b>	363	376	388	442	<b>450</b>	<b>535</b>	564	589

In the case of 2%Ag/CZA, the shape of the derivative curve suggests that two distinct processes occurred during soot oxidation. Interestingly, the presence of a shoulder to the main derivative curve representing a lower temperature soot oxidation process is also observed when catalyst and soot are mixed in tight contact conditions. This phenomenon was



observed in a study by Neri *et al.*<sup>14</sup> into the activity of various metal oxide catalysts under tight contact conditions, and was attributed to the combustion of the hydrocarbons present in the soot.

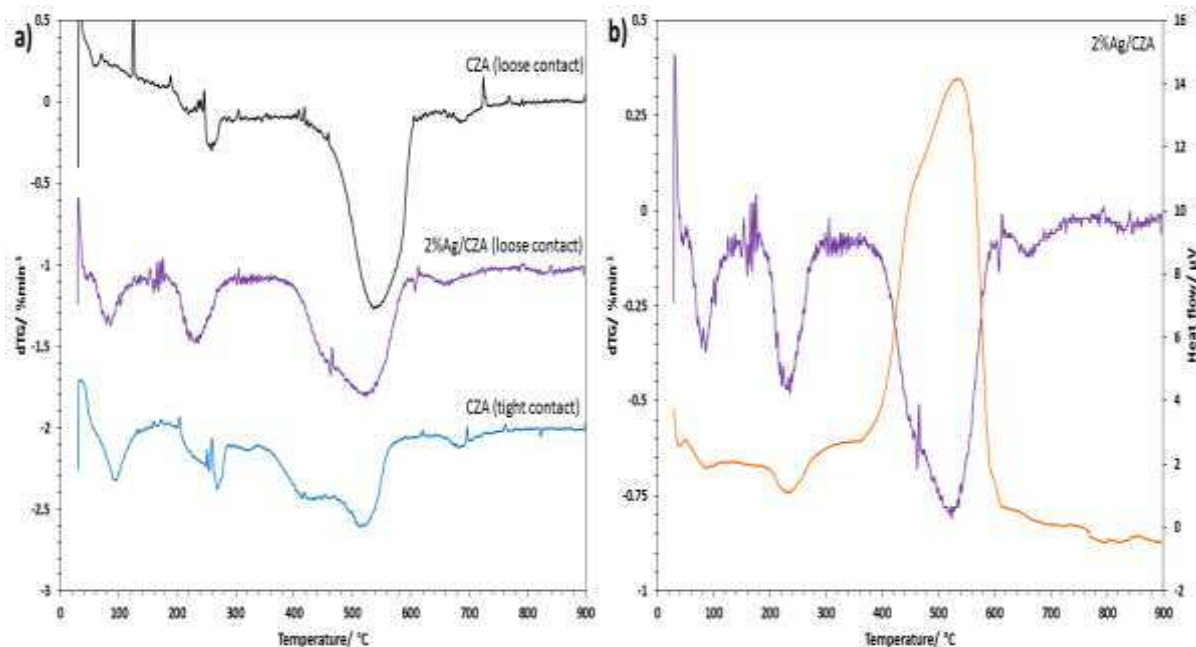


**Figure 5.7 a)** dTG plots of catalyst/soot mixtures containing: CZA (black), 2%Ag/CZA (purple) in loose contact, and CZA in tight contact (blue). **b)** Comparison of dTG and Heat flow plots of soot oxidation with 2%Ag/CZA

As seen in figure 5.7a) the dTG profile of soot oxidation in a tight contact mix with CZA bore much greater resemblance to the loose contact plot of 2%Ag/CZA than that of loose contact CZA. As explained in Chapter 1, contact is an important factor in the ability of a catalyst to oxidise soot, as closer contact allows for more facile transfer of oxygen from catalyst to soot, increasing the probability of a successful reaction. Tight contact mixing increases the proportion of soot within close enough proximity to the catalyst to allow this transfer to take place. The lower temperature (<500 °C) soot oxidation process observed under tight contact conditions can therefore be attributed to the higher proportion of hydrocarbons on the soot in close contact with the catalyst. Despite the much lower proportion of soot particles in close contact with 2%Ag/CZA due to loose contact mixing, a similar process appears to have taken place. This could be explained by the findings of TPR, in that interactions between  $\text{Ag}^0$  and  $\text{CeO}_2$  allowed for release of oxygen at lower temperatures than observed in the bare CZA support. As previously stated, it has also been reported extensively that Ag is able to form highly reactive superoxide  $\text{O}_2^-$  species which would result in rapid oxidation of the hydrocarbons in contact with the catalyst<sup>11–13</sup>. Kobayashi and Hikosaka observed a similar

two-curve dTG soot oxidation with Ag/CeO<sub>2</sub> catalysts which was attributed to separate catalysed and non-catalysed soot oxidation processes<sup>15</sup>. As shown by the heat flow plot in figure 5.7b), this initial process also resulted in an exotherm at the lower temperature which may have contributed to the oxidation of the remaining soot proceeding at a lower temperature. This resulted in the decrease of the peak soot oxidation temperature from 542 °C with the bare support to 523°C with 2%Ag/CZA. This represented a decrease of around 100 °C compared to the uncatalysed reaction.

Referring back to figure 5.6, the onset temperature of soot oxidation in the presence of 10%K/CZA showed a more modest decrease from the bare CZA support of about 10 °C. In this case there was no evidence of a distinct process taking place at a lower temperature from the major soot oxidation curve. However, this catalyst was able to lower the peak soot oxidation temperature even further than the silver catalyst described above. This suggested that while silver was capable of decreasing the soot oxidation temperature further, its effects were more localised which resulted in two distinct processes. In contrast potassium was better able to improve the major soot oxidation process. This was observed in a study by Shimokawa *et al.* which showed that Ag/CeO<sub>2</sub> was superior at oxidising soot in close contact than K/CeO<sub>2</sub>, however the former was superior at catalysing the complete oxidation of soot<sup>16</sup>. This was explained by the contact achieved between catalyst and soot. While silver was only able to catalyse soot with which it was in close contact, the mobility of potassium species on the surface of the support allowed for contact with a greater quantity of soot, resulting in a more comprehensive oxidation.

In the presence of the combined silver and potassium catalyst the soot oxidation temperature was observed to decrease even further. As with 2%Ag/CZA, the shape of the dTG curve indicated two soot oxidation processes taking place. However, on this occasion the lower temperature process (attributed to the presence of Ag<sup>0</sup>) was dominant, and occurred at a slightly lower temperature. This resulted in a further decrease to the T<sub>o</sub> and T<sub>eo</sub> by around 10 °C compared to the silver-only catalyst. More significantly, the dominance of this initial process resulted in a considerable decrease to the peak soot oxidation temperature to 450 °C. There was also a sizeable decrease in the final soot oxidation temperature, to below 570 °C. It is likely that this improvement to the catalytic activity can be attributed to a synergistic effect between silver and potassium on the catalyst surface.

The thermal durability of the catalysts was tested as in the previous chapters of this work. The dTG plots of these tests are shown in figure 5.8, compared with the original run of the corresponding catalyst. The data extracted from these plots is again presented in table 5.2.

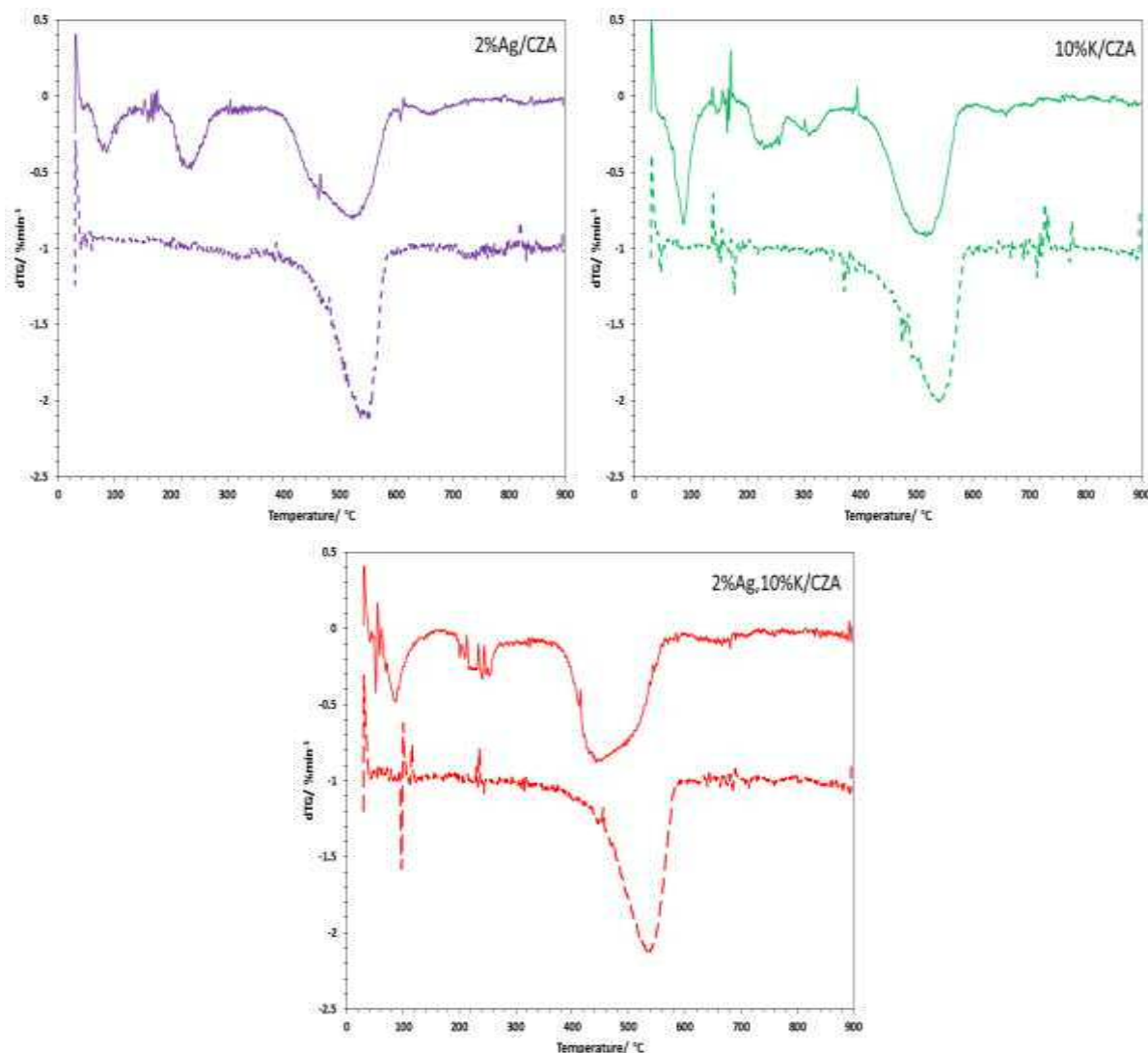


**Figure 5.8** dTG plots of catalyst/soot mixtures containing: 2%Ag/CZA (purple), 10%K/CZA (green) and 2%Ag,10%K/CZA (red) on the first run (solid line) and second run (dashed line)

The tests showed that the two-process phenomenon observed in the silver-containing catalysts during the first run was not observed on repeat testing. This resulted in an increase in the onset temperature of soot oxidation, and a considerable increase in the extrapolated onset temperature of over 50 °C. The peak soot oxidation temperature was also increased, in the case of 2%Ag/CZA by almost 20 °C and in the case of 2%Ag,10%K/CZA by over 80 °C, resulting in temperatures similar to those achieved by the bare CZA support. There are several possible reasons for the loss of activity observed on the catalysts' second runs. In the case of

both silver-containing catalysts, it is well-known that silver sinters at higher temperatures, which would contribute to its deactivation<sup>3</sup>.

The peak soot oxidation temperature of 10%K/CZA was also affected, returning to a similar temperature as the bare CZA support. The  $T_o$ ,  $T_{eo}$  and  $T_f$  were not significantly affected, however these temperatures were also similar to those of the bare CZA support on its second run, suggesting the positive effect of potassium on the activity of the catalyst had been considerably diminished. As stated in Chapter 3; despite their well-established soot oxidation properties, alkali metals have also been reported as unstable due to their poor hydrothermal resistance. The formation of volatile compounds at high temperatures and in the presence of water has shown to result in significant decrease in alkali-metal content and subsequent catalyst deactivation<sup>8</sup>. This contrasted with the co-precipitated catalyst containing  $K_2CO_3$  which was presented in Chapter 3, which showed similar soot oxidation activity to 10%K/CZA on its first run, but was also able to maintain this activity on its second run, suggesting that impregnated potassium was less stable than co-precipitated.

The results of the soot oxidation testing showed that the impregnation of silver and potassium on the CZA support increased catalytic activity on the first run. However, repeat testing showed that these catalysts were not thermally durable, as they were not able to maintain their activity after being subjected to high temperatures due to the reasons described above.

## 5.2 Silver and potassium on alternative ceria-based catalyst supports

Despite their poor thermal durability, the impregnation of silver and potassium on a CZA support has shown to be highly active for soot oxidation, both in the above section and in previous work conducted at Cardiff University<sup>2</sup>. In this section, the same method was applied to the various supports presented in section 4.1 from the previous chapter (Ce:M:Al 7:3:10, where M = La, La+Zr, Pr, Nd), in order to investigate its effect on different ceria-based supports, and whether an improvement to the thermal stability could be established. In particular, a study by Gao *et al.* which demonstrated an improvement in Ag thermal stability

by doping the ceria support with Nd offered some encouragement in this respect<sup>13</sup>. Collectively the catalysts are referred to as 2%Ag,10%K/CMA.

### 5.2.1 Characterisation

Each of the catalysts were characterised in a similar fashion to those in the above section.

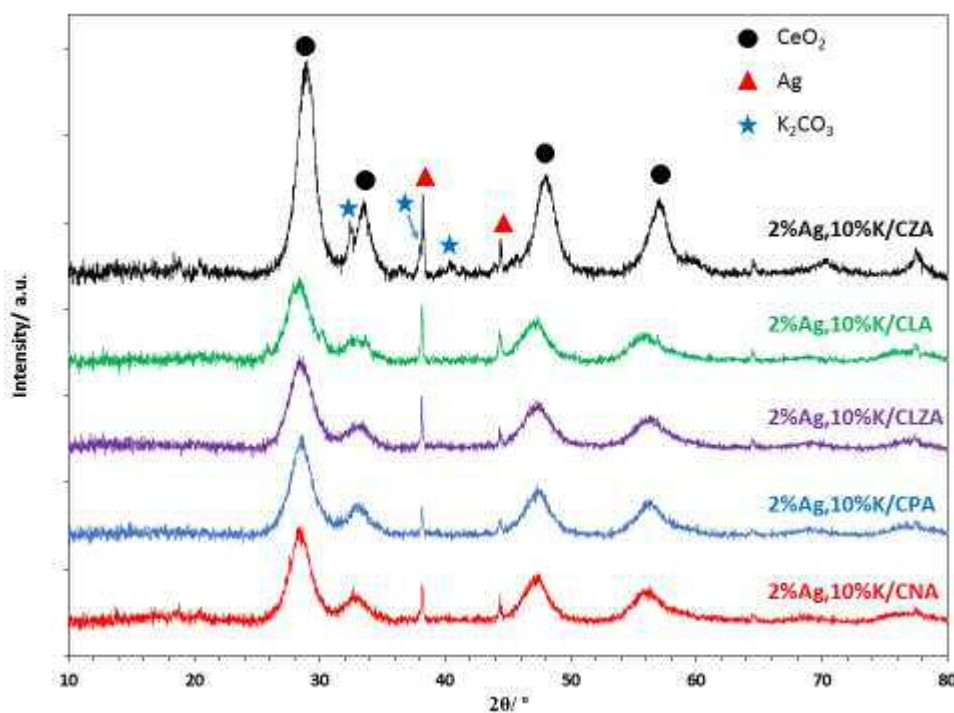


**Figure 5.9** X-ray diffractograms of 2%Ag,10%K on CZA (black), CLA (green), CLZA (purple), CPA (blue) and CNA (red)

The X-ray diffractograms of the 2%Ag,10%K/CMA catalysts in figure 5.9 showed the typical fluorite-type structure of ceria in each case. As observed in the case of 2%Ag,10%K/CZA, the  $2\theta$  values of the reflections attributed to the (111), (200), (220) and (311) planes of this phase each remained in the same positions as their respective bare supports (around  $28^\circ$ ,  $33^\circ$ ,  $47^\circ$  and  $56^\circ$  respectively). The reflections at  $38.2^\circ$  and  $44.4^\circ$  observed in 2%Ag,10%K/CZA and attributed to metallic silver were also present in the diffractograms of the other catalysts. However, the  $K_2CO_3$  reflections observed weakly at  $32.4^\circ$ ,  $38.0^\circ$  and  $40.6^\circ$  in the CZA version were not visible in the remaining 2%Ag,10%K/CMA catalysts.

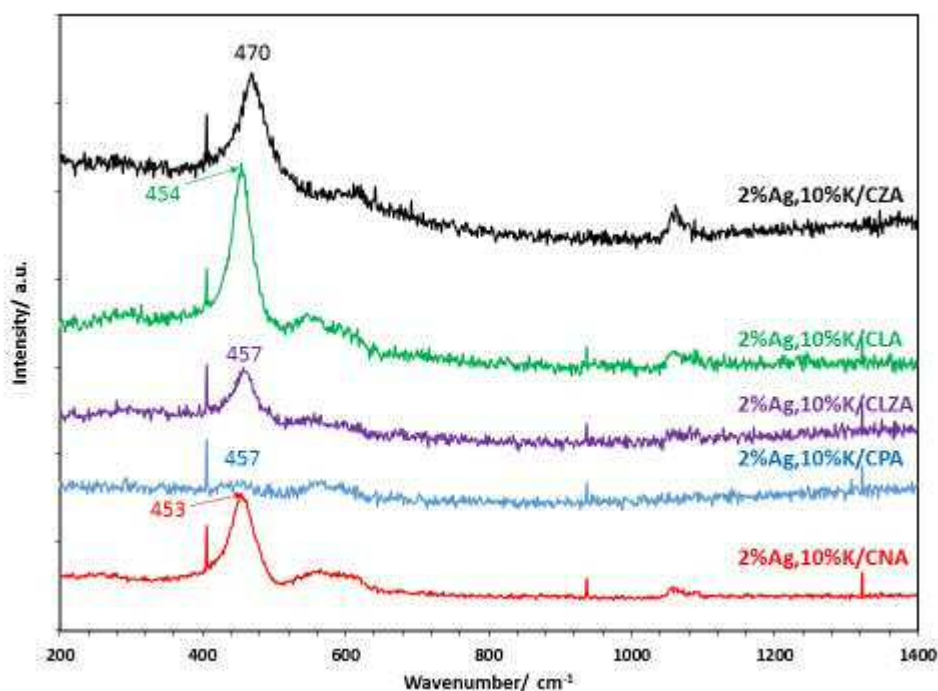


**Figure 5.10** Raman spectra of 2%Ag,10%K on CZA (black), CLA (green), CLZA (purple), CPA (blue) and CNA (red)

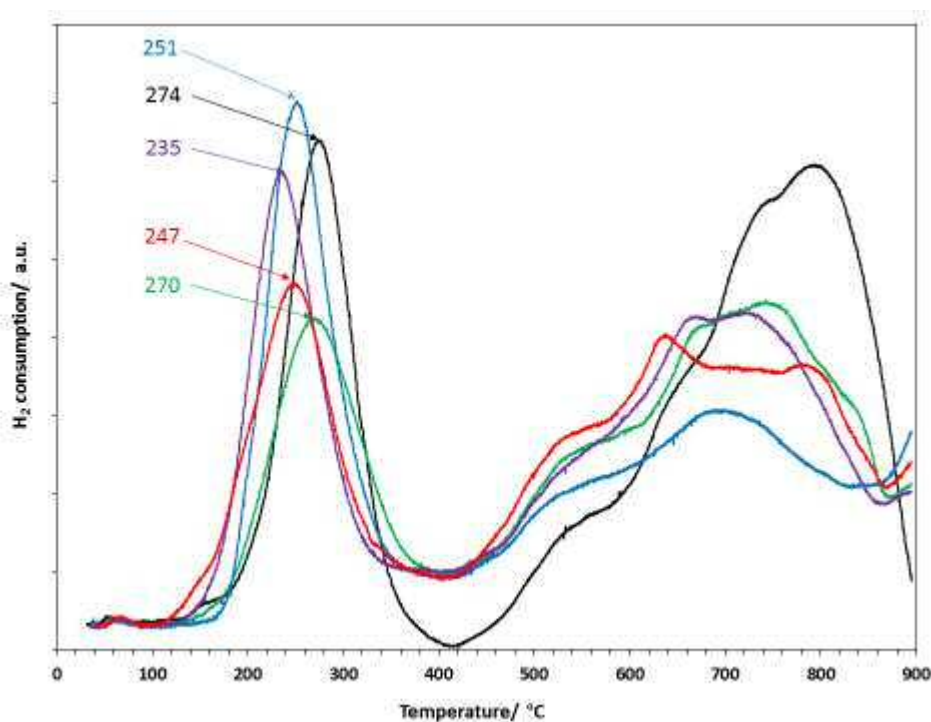
In agreement with XRD, the Raman spectra of the catalysts shown in figure 5.10 also showed no change in the peak positions of the main  $F_{2g}$  mode associated with ceria. As with 2%Ag,10%K/CZA, only a weak signal associated with  $K_2CO_3$  was observed at  $1060\text{ cm}^{-1}$  in the CLA, CLZA and CNA versions of the catalyst, while this signal was not detected at all in 2%Ag,10%K/CPA.

X-ray photoelectron spectroscopy and BET surface area analysis were performed on the catalysts in order to determine their surface properties. The Ag 3d and K 2p regions of the XPS spectra confirmed the presence of silver and potassium on the surfaces of the catalysts. The regions of all the elements were used to calculate the compositions of the surfaces, which are shown in table 5.3, which showed silver accounting for around 0.2% and potassium 1.5% of the atomic concentration of the surface in each case. As mentioned in the case of 2%Ag,10%K/CZA, the level of carbon on the surfaces of the catalysts had increased compared to the respective bare supports, again suggesting the potassium carbonate precursor had survived the calcination process. As was the case in the previous section, the impregnation of silver and potassium resulted in a decrease to the surface areas of the catalysts.

**Table 5.3** Surface properties of 2%Ag,10%K/CMA catalysts provided by XPS and BET analyses

Catalyst	Atomic conc. (%)								Surface area (m <sup>2</sup> g <sup>-1</sup> ) (bare support)
	Ce 3d	M*	Al 2p	O 1s	C 1s	Na 1s	Ag 3d	K 2p	
Ag,K/CZA	6.02	1.15	11.87	51.50	11.57	15.99	0.21	1.70	20 ±1 (36)
Ag,K/CLA	2.97	2.95	13.18	53.02	10.36	15.80	0.22	1.50	12 ±0 (21)
Ag,K/CLZA	3.76	2.08	12.64	54.53	10.58	14.77	0.19	1.45	17 ±1 (40)
Ag,K/CPA	3.07	1.82	14.86	53.81	10.72	14.20	0.18	1.34	14 ±0 (30)
Ag,K/CNA	2.65	2.45	13.52	54.04	10.60	15.04	0.23	1.47	13 ±0 (30)

The TPR profiles of the catalysts are provided in figure 5.12. The pattern observed in these profiles are each similar to that of 2%Ag,10%K/CZA, which was described in section 5.1.1, suggesting the impregnated species had a similar influence on the reduction of Ce<sup>4+</sup> ions in each case. This could be seen in the comparisons of the catalysts' TPR profiles and those of their respective supports in figure 5.13, which showed that the peak representing the reduction of surface Ce<sup>4+</sup> in each of the supports decreased in intensity and was replaced by the lower temperature reduction.

**Figure 5.12** TPR profiles of 2%Ag,10%K on CZA (black), CLA (green), CLZA (purple), CPA (blue) and CNA (red)

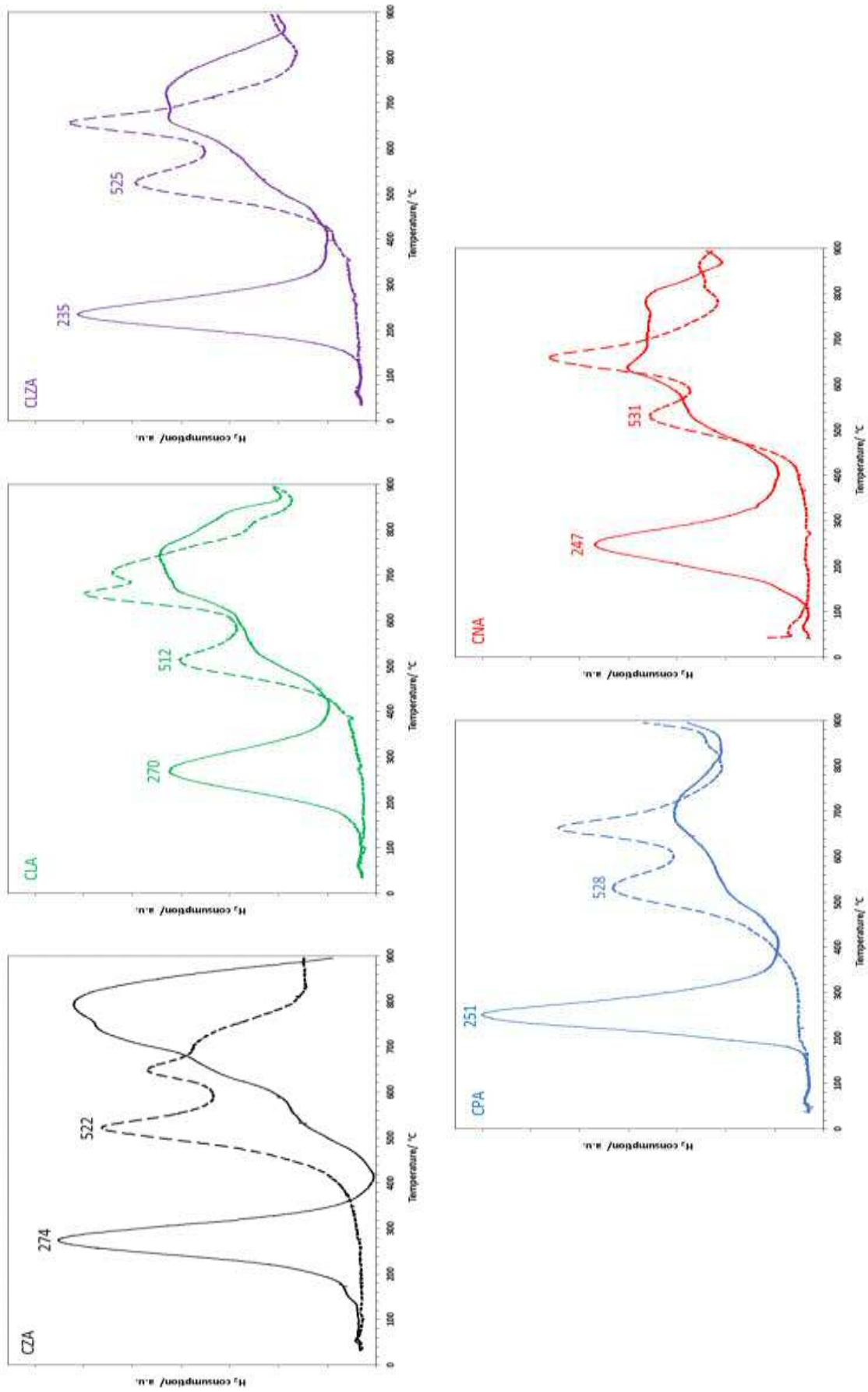


**Figure 5.13** TPR profiles of 2%Ag,10%K on CZA (black), CPA (blue) and CNA (red), (all solid lines) compared with their respective bare supports (dashed lines)



This was less pronounced in the case of CNA as this was the support with the lowest intensity cerium reduction to begin with. It can be seen with all the catalysts that the Ag-influenced cerium reduction curve was more intense than the reduction curves of the bare supports. The peak temperature of reduction varied considerably between the catalysts, ranging between 235 °C for CLZA and 274 °C for CZA, representing a decrease in peak reduction temperature of between 248 °C and 290 °C.

### 5.2.2 Soot oxidation testing

The 2%Ag,10%K/CMA catalysts were each tested for soot oxidation by thermogravimetric analysis in the usual manner. The derivative plots are presented in figure 5.14, with each of the samples offset by 1 %min<sup>-1</sup> for ease of comparison.

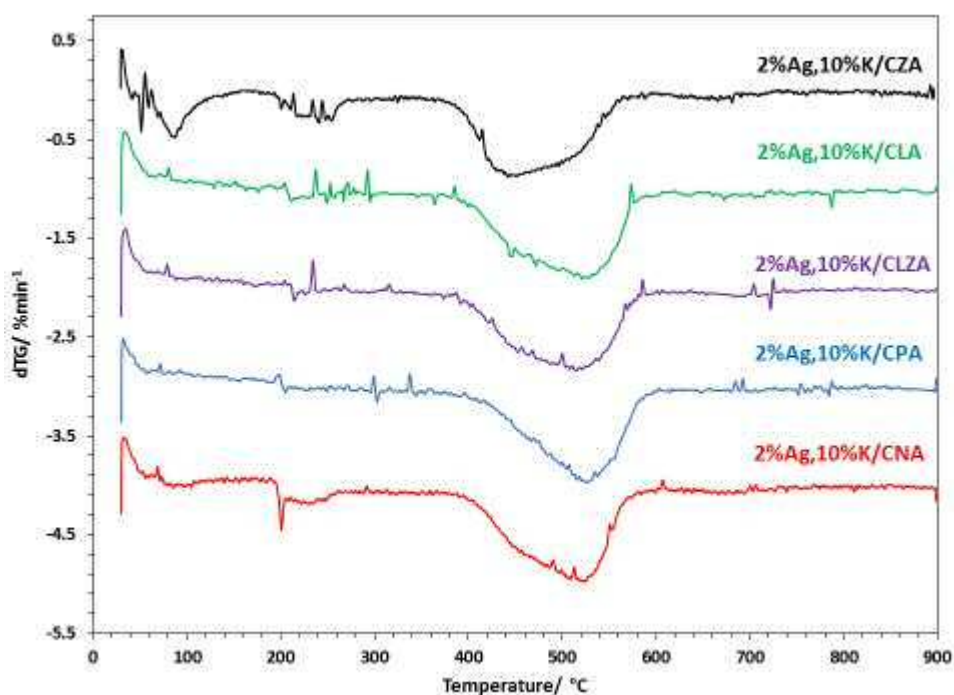


**Figure 5.14** dTG plots of catalyst/soot mixtures containing: 2%Ag,10%K on CZA (black), CLA (green), CLZA (purple), CPA (blue) and CNA (red)

The testing showed that the presence of the supported metals enhanced the catalytic activity compared to the bare CMA supports. The dTG plots of 2%Ag,10%K with CLA, CLZA and CNA all clearly showed a shoulder to the main soot oxidation curve, indicating the distinctive two-

process soot oxidation previously observed and described in the case of 2%Ag,10%K/CZA in section 5.1.2 attributed to the combustion of hydrocarbons. However in these cases the lower-temperature curve was not the dominant process, which meant the peak soot oxidation temperature occurred during the higher temperature process, hence the considerable difference seen in table 5.4 in this regard between 2%Ag,10%K/CZA and the other catalysts. The shoulder peak was also observed in the case of 2%Ag,10%K/CPA however it was much less prominent even than the aforementioned CLA/CLZA/CNA catalysts. This was demonstrated in the onset and extrapolated onset temperatures presented in table 5.4 which were lowest in the case of 2%Ag,10%K/CZA and highest with 2%Ag,10%K/CPA, while the other three catalysts all displayed comparable temperatures in between.

**Table 5.4** Soot oxidation temperatures of samples mixed with 2%Ag,10%K/CMA on their 1<sup>st</sup> and 2<sup>nd</sup> use

Catalyst	T <sub>o</sub> (°C)		T <sub>eo</sub> (°C)		T <sub>p</sub> (°C)		T <sub>f</sub> (°C)	
	1 <sup>st</sup> run	2 <sup>nd</sup> run	1 <sup>st</sup> run	2 <sup>nd</sup> run	1 <sup>st</sup> run	2 <sup>nd</sup> run	1 <sup>st</sup> run	2 <sup>nd</sup> run
<b>Soot (no catalyst)</b>	465		535		<b>622</b>		651	
<b>2%Ag,10%K/CZA</b>	363	376	388	442	<b>450</b>	<b>535</b>	564	589
<b>2%Ag,10%K/CLA</b>	387	357	395	408	<b>522</b>	<b>521</b>	574	576
<b>2%Ag,10%K/CLZA</b>	388	370	396	409	<b>514</b>	<b>508</b>	586	575
<b>2%Ag,10%K/CPA</b>	396	402	410	435	<b>527</b>	<b>522</b>	603	579
<b>2%Ag,10%K/CNA</b>	387	386	397	428	<b>523</b>	<b>503</b>	602	572

Repeat testing of the samples was conducted as with previous catalysts. The dTG plots of these tests are provided in figure 5.15 and are offset by 1 %min<sup>-1</sup> in order to compare with their initial run. The data extracted from these plots is presented in table 5.4.

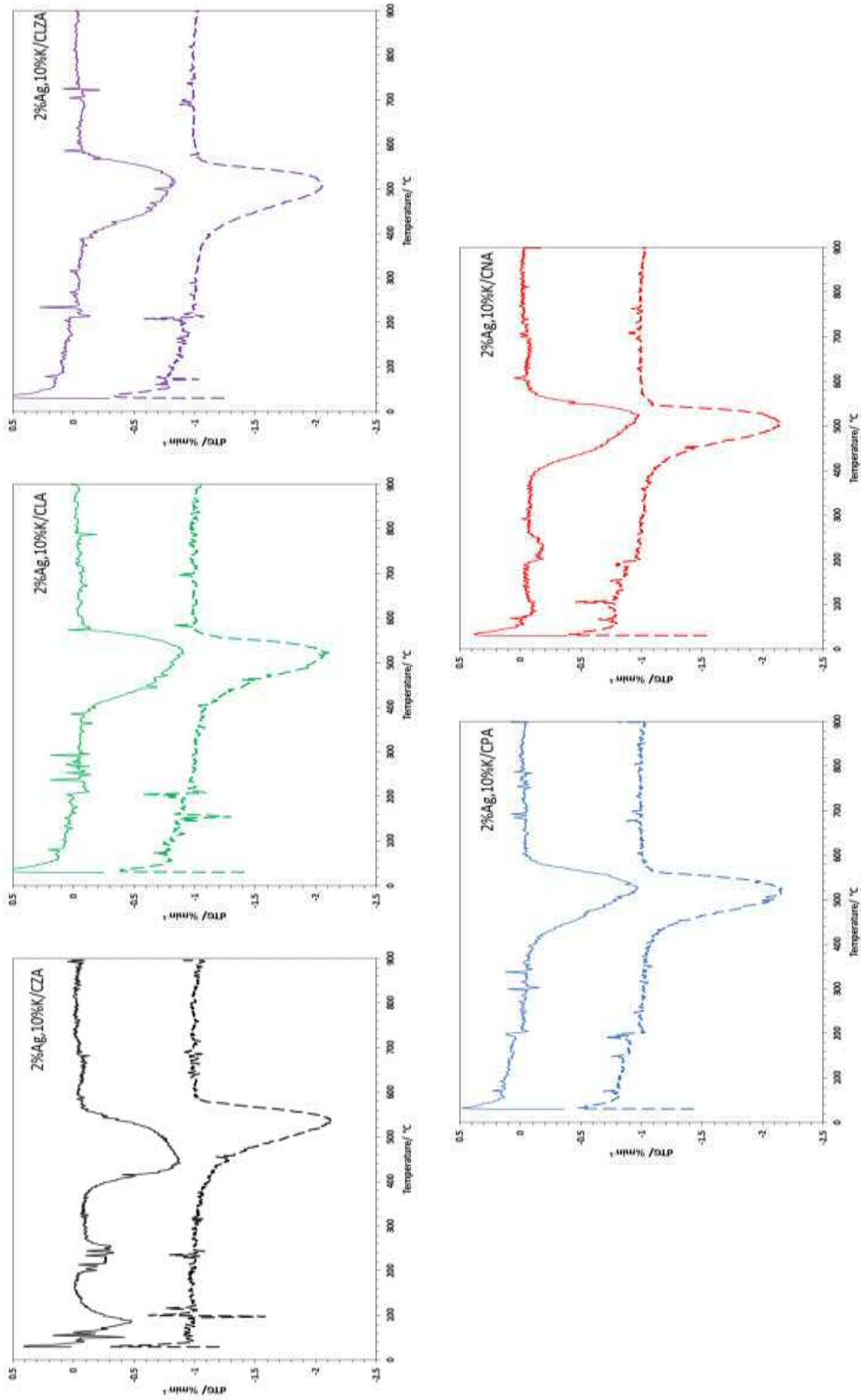


**Figure 5.15** dTG plots of catalyst/soot mixtures containing: 2%Ag,10%K on CZA (black), CLA (green), CLZA (purple), CPA (blue) and CNA (red) on the first run (solid line) and second run (dashed line)

From these plots it was observed that, as with the repeat testing of 2%Ag,10%K/CZA described in 5.1.2, the shoulder to the soot oxidation curve observed during the first run did not appear during the second run of any of the catalysts. This suggested the combustion of hydrocarbons at the lower-temperature did not occur on repeated use of the catalysts, and resulted in an increase in the extrapolated onset temperature in each case. However unlike in the case of 2%Ag,10%K/CZA, significant increases in the onset, peak and final temperatures of soot oxidation with the remaining catalysts were not observed during the repeat testing, suggesting the impregnated metals retained their activity on these supports after subjection to high temperatures. In the case of 2%Ag,10%K/CNA a significant improvement was observed in the peak and final soot oxidation temperatures on the second run compared to the first. This was attributed to the improvement to the catalytic activity of the support as described in Chapter 4. However it is important to note that the activity of the used impregnated catalyst was greater than the activity of the used bare support, which suggested the impregnated metals contributed to a further increase in activity after exposure to high temperatures. These tests suggested that despite the loss of the low-temperature shoulder, the activity of the reused impregnated catalysts remained higher than their respective bare supports. This demonstrated that it was possible to maintain the improved catalytic activity provided by the impregnated metals after initial use.

### **5.3 Screening of alternative transition metals for impregnation on CZA**

The previous sections as well as numerous reports in literature have shown the high activity provided by silver for the catalysis of soot oxidation. However it has also been observed that silver is often not capable of maintaining this high activity when exposed to higher temperatures. This is a significant obstacle for the real-world application of soot combustion catalysts due to the temperatures that can often be reached in the exhausts of passenger vehicles<sup>4,17</sup>. For this reason there is a reluctance in industry for the use of silver-containing catalysts, and while their use is relevant in a scientific context, the ultimate goal of this project is to produce viable soot oxidation catalysts for real-world applications. In this section, the use of alternative transition metals (Fe, Co, Ni, Cu) as substitutes for silver were investigated in an attempt to provide a more stable active soot oxidation catalyst. As described in

Chapter 1, several of these transition metals have shown activity for soot oxidation due to their redox abilities, allowing for the release of oxygen at the catalyst/soot interface<sup>18</sup>.

In this investigation, these were not combined with potassium as the focus was solely on the role of the transition metal. Each of the transition metals (TM) were impregnated on the same batch of CZA support for initial screening, with the aim of applying the most promising candidate to the other CMA supports, as already done with the 2%Ag,10%K catalysts. A loading of 5 wt% was chosen so as to obtain clear signals by XPS. Therefore a 5 wt% Ag on CZA catalyst was also prepared in order to make a fair comparison.

The catalysts in this section are referred to collectively as 5%TM/CZA.

### 5.3.1 Characterisation

The X-ray diffractograms of the 5%TM/CZA catalysts are shown in figure 5.16. Each of the catalysts showed the typical reflections associated with ceria widely reported in this work.

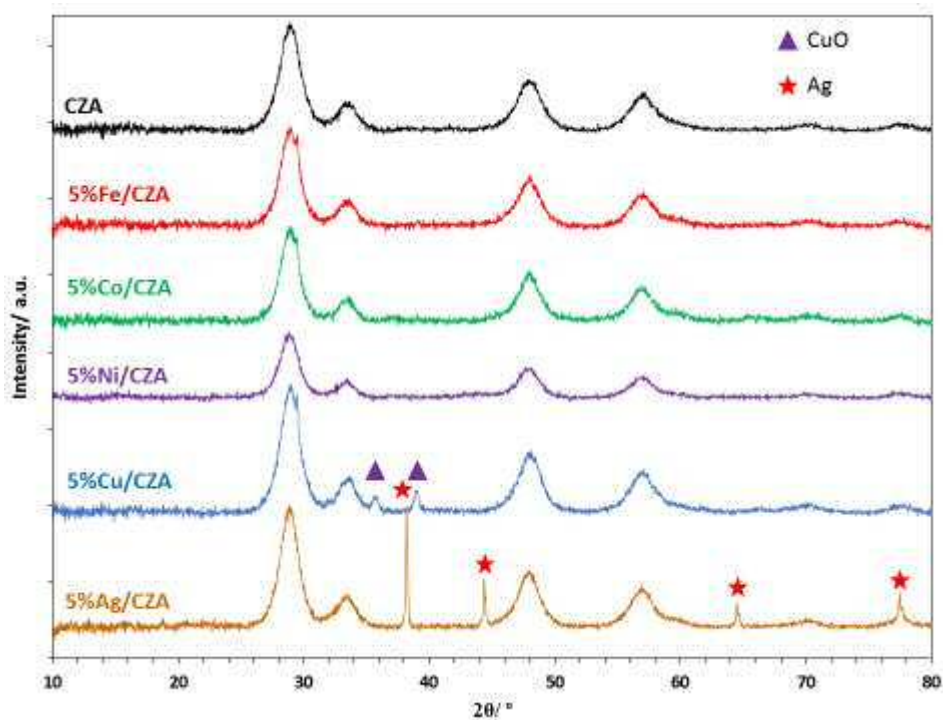


**Figure 5.16** X-ray diffractograms of CZA (black), 5%Fe/CZA (red), 5%Co/CZA (green), 5%Ni/CZA (purple), 5%Cu/CZA (blue) and 5%Ag/CZA (brown)

The positions of these reflections were unaltered from the bare CZA support at 28.9°, 33.5°, 48.0°, 57.0° suggesting no significant change to the bulk structure of the support occurred upon the impregnation of the transition metals. No additional phases were observed in the Fe, Co, Ni/CZA catalysts, however there were reflections observed in the Cu and Ag/CZA catalysts denoting additional crystalline phases associated with these metals. In the case of 5%Cu/CZA, reflections at 35.7° and 39.0° indicated the presence of monoclinic CuO (JCPDS 65-2309<sup>19</sup>) representing the (002) and (111) planes, respectively.

X-ray photoelectron spectroscopy and BET surface area analysis were performed on the catalysts in order to determine their surface properties.

Figure 5.17 shows the regions of the XPS spectra relevant to the respective impregnated metal for each of catalysts. A signal was detected in each of these regions, confirming the presence of the impregnated metal on the surfaces of all the catalysts. Quantification of the surface elements was calculated for each of the catalysts, and is shown in table 5.5 along with the BET surface areas. The equivalent data for the bare CZA support is also presented for comparison.

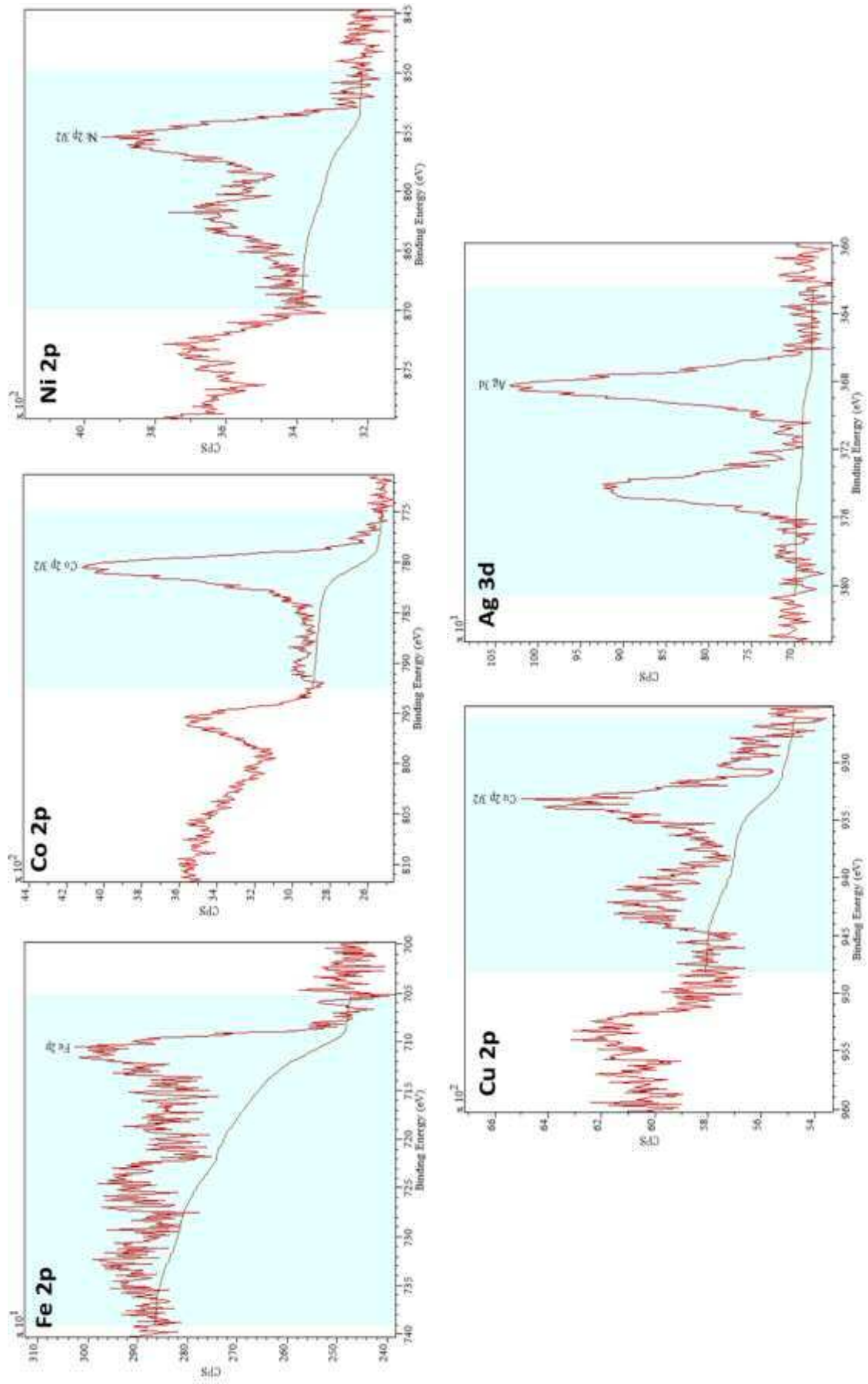


Figure 5.17 XPS spectra of respective TM regions of 5%TM/CZA

**Table 5.5** Surface properties of 5%TM/CZA catalysts provided by XPS and BET analyses

Catalyst	Atomic conc. (%)								Surface area (m <sup>2</sup> g <sup>-1</sup> )
	TM*	Ce 3d	Zr 3d	Al 2p	O 1s	C 1s	Na 1s	N 1s	
<b>CZA</b>	-	6.22	1.27	17.03	51.51	7.25	16.73	-	36 (±1)
<b>5%Fe/CZA</b>	<b>1.97</b>	2.71	0.53	12.41	54.86	10.91	14.35	<b>2.26</b>	28 (±0)
<b>5%Co/CZA</b>	<b>2.28</b>	3.38	0.77	12.15	51.61	12.28	15.86	<b>1.67</b>	28 (±2)
<b>5%Ni/CZA</b>	<b>2.01</b>	1.63	0.32	10.60	52.91	17.57	13.25	<b>1.71</b>	34 (±1)
<b>5%Cu/CZA</b>	<b>1.77</b>	3.35	0.68	14.02	52.99	10.19	15.44	<b>1.56</b>	21 (±1)
<b>5%Ag/CZA</b>	<b>0.35</b>	3.10	0.34	11.59	56.07	13.41	14.77	<b>0.37</b>	20 (±0)

\* TM = Fe 2p/Co 2p/Ni 2p/Cu 2p/Ag 3d

The table shows that the impregnated metals accounted for around 2% of the atomic concentration on the surfaces of the catalysts. The exception to this was silver, which only accounted for 0.35% of the surface. This was explained by the relative atomic mass of silver being much higher than the other metals, therefore resulting in a much lower number of moles. Also highlighted in table 5.5 is the appearance of an N 1s signal in each of the impregnated catalysts which was not observed in the bare CZA support. This suggested that the nitrate precursors did not fully decompose during calcination. Table 5.6 compares the TM/nitrogen ratio in each of the precursor nitrates and the same ratio calculated from the XPS quantification. The final column shows the surface TM/nitrogen ratio normalised to take into account the precursor ratio. This showed that a similar degree of nitrate decomposition had taken place in Fe, Co, Ni and Cu/CZA, with around 40% remaining relative to the impregnated metal. In the case of Ag/CZA there was an almost equimolar ratio of silver to nitrogen.

**Table 5.6** Ratio of transition metal to nitrogen in precursors and catalyst surfaces

Catalyst	Precursor	Precursor TM : N	Surface TM : N	Normalised TM : N
<b>5%Fe</b>	Fe(NO <sub>3</sub> ) <sub>3</sub>	1 : 3	1 : 1.14	1 : 0.38
<b>5%Co</b>	Co(NO <sub>3</sub> ) <sub>2</sub>	1 : 2	1 : 0.73	1 : 0.37
<b>5%Ni</b>	Ni(NO <sub>3</sub> ) <sub>2</sub>	1 : 2	1 : 0.85	1 : 0.42
<b>5%Cu</b>	Cu(NO <sub>3</sub> ) <sub>2</sub>	1 : 2	1 : 0.88	1 : 0.44
<b>5%Ag</b>	AgNO <sub>3</sub>	1 : 1	1 : 1.06	1 : 1.06



The TM and N 1s peak positions were taken for each of the catalysts and are presented in table 5.7.

**Table 5.7** Comparison of TM & N 1s peak positions with reference values for their respective oxides and nitrates

Catalyst	Binding energy (eV)				
	Impregnated TM 2p/3d			N 1s	
	Catalyst	TM-oxide (OS) [Ref]	TM-nitrate [Ref]	Catalyst	TM-nitrate [Ref]
5%Fe/CZA	710.6	710.9 (+3) [25]	710.1 [25]	406.7	406.7 [25]
5%Co/CZA	780.3	779.9 (+3/+2) [26]	780.9 [27]	407.2	399.2 [27]
5%Ni/CZA	855.4	854.0 (+2) [26]	856.9 [28]	407.2	407.6 [28]
5%Cu/CZA	933.2	933.6 (+2) [24]	935.5 [28]	407.2	406.2 [29]
5%Ag/CZA	368.2	368.2 (0) [23] 368.1 (+1) [30]	368.2 [22]	407.2	406.6 [22]

The N 1s peak in the 5%Fe/CZA spectrum matched the reference value for the  $\text{Fe}(\text{NO}_3)_3$  precursor, while the Fe 2p peak was found to be between reference values for both  $\text{Fe}_2\text{O}_3$  and  $\text{Fe}(\text{NO}_3)_3$ . This suggested that the iron nitrate precursor was intact on the surface of the catalyst before partially decomposing to the oxide upon calcination. In both cases Fe remained in the +3 oxidation state. Similarly, the positions of the Co 2p and Ni 2p peaks were also observed between the reference values for their respective nitrates and oxides. In the case of Co, the lack of a shoulder to the main peak at around 786 eV indicated that it was predominantly  $\text{Co}_3\text{O}_4$  (and therefore containing  $\text{Co}^{2+}$  and  $\text{Co}^{3+}$ ) rather than  $\text{CoO}$ <sup>20</sup>. Ni exists in the +2 oxidation state in both nitrate and oxide form. However the position of the N 1s peak in these spectra did not match the reference values of their respective metal nitrates, instead matching that of sodium nitrate,  $\text{NaNO}_3$ <sup>21</sup>. This may have suggested that the nitrate ions bonded with sodium on the surface of the support during the preparation method. Peaks at the same binding energy were observed in the N 1s region of both 5%Cu and 5%Ag/CZA, suggesting the same process occurred in the preparation of these catalysts also. The binding energy of the Ag 3d peak did match that of a reference value for  $\text{AgNO}_3$ , however as shown in the table this also has the same binding energy as metallic Ag<sup>22,23</sup>. The presence of a strong satellite peak between 940 eV and 945 eV in Cu 2p region of the 5%Cu/CZA spectrum indicated that CuO was present. As shown in table 5.7, the position of the main peak had a

slightly lower binding energy than the reference value for CuO, this suggested that some of the surface copper had been reduced, possibly by interactions with the cerium on the surface of the support<sup>24</sup>.

The TPR profiles shown in figure 5.18 show that the reduction behaviour of the catalysts was altered significantly by the impregnation of the various transition metals on the CZA support. In the case of 5%Ag/CZA, the peak at 259 °C is similar in position to the peak observed in figure 5.4 belonging to the 2%Ag/CZA catalyst presented in section 5.1.1. This can therefore be attributed to the same Ag-Ce interactions described in that section.

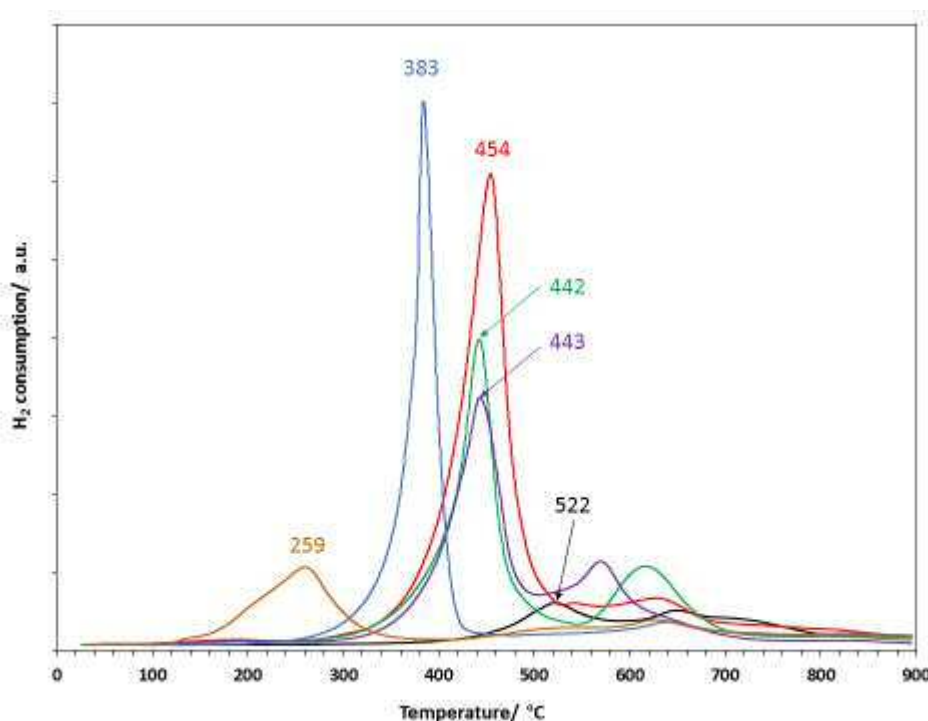


**Figure 5.18** TPR profiles of CZA (black), 5%Fe/CZA (red), 5%Co/CZA (green), 5%Ni/CZA (purple), 5%Cu/CZA (blue) and 5%Ag/CZA (brown)

The reduction profiles of catalysts containing Fe, Co and Ni all showed an intense peak at around 450 °C, while the catalyst containing copper also showed an intense peak at a lower temperature of 383 °C. These peaks were attributed to the reduction of the relevant transition metal in each case. Although appearing to represent a single reduction, the asymmetrical shape of the peaks indicated multiple overlapping reductions taking place in each case i.e. CuO to Cu<sub>2</sub>O to Cu<sup>31</sup>.

The same reduction profiles can be seen in figure 5.19, in this case each is shown alongside the reduction profile of the original bare CZA support for comparison. The surface  $\text{Ce}^{4+}$  reduction peak observed in the profile of the bare support was not present in the same intensity in the profiles of the 5%Co, Cu and Ag/CZA catalysts, suggesting a change had taken place. As explained in the previous section, interactions between  $\text{Ag}^0$  and ceria resulted in a decrease in the  $\text{Ce}^{4+} \rightarrow \text{Ce}^{3+}$  reduction temperature and hence the formation of a reduction peak at 259 °C and a decrease in the intensity of the peak at 522 °C. It is also possible that interactions between cobalt/copper and cerium could have resulted in a decrease in the reduction temperature of surface cerium<sup>32,33</sup>, as the intensity of the peak at 522 °C is significantly decreased in the TPR profiles of these catalyst also. However since cobalt and copper species are much more reducible than  $\text{Ce}^{4+}$  a lower temperature ceria reduction peak would be dwarfed and indistinguishable from the cobalt and copper reduction peaks<sup>31,32,34,35</sup>. From the TPR profiles of both 5%Fe and Ni/CZA the reduction of the respective impregnated TMs are again the dominant feature, however the shape of these curves suggested that the reduction of surface  $\text{Ce}^{4+}$  was still taking place at a similar temperature as on the bare CZA support. This indicated that the impregnated metals on these two catalysts did not interact with the support and the reduction of cerium was unaffected.

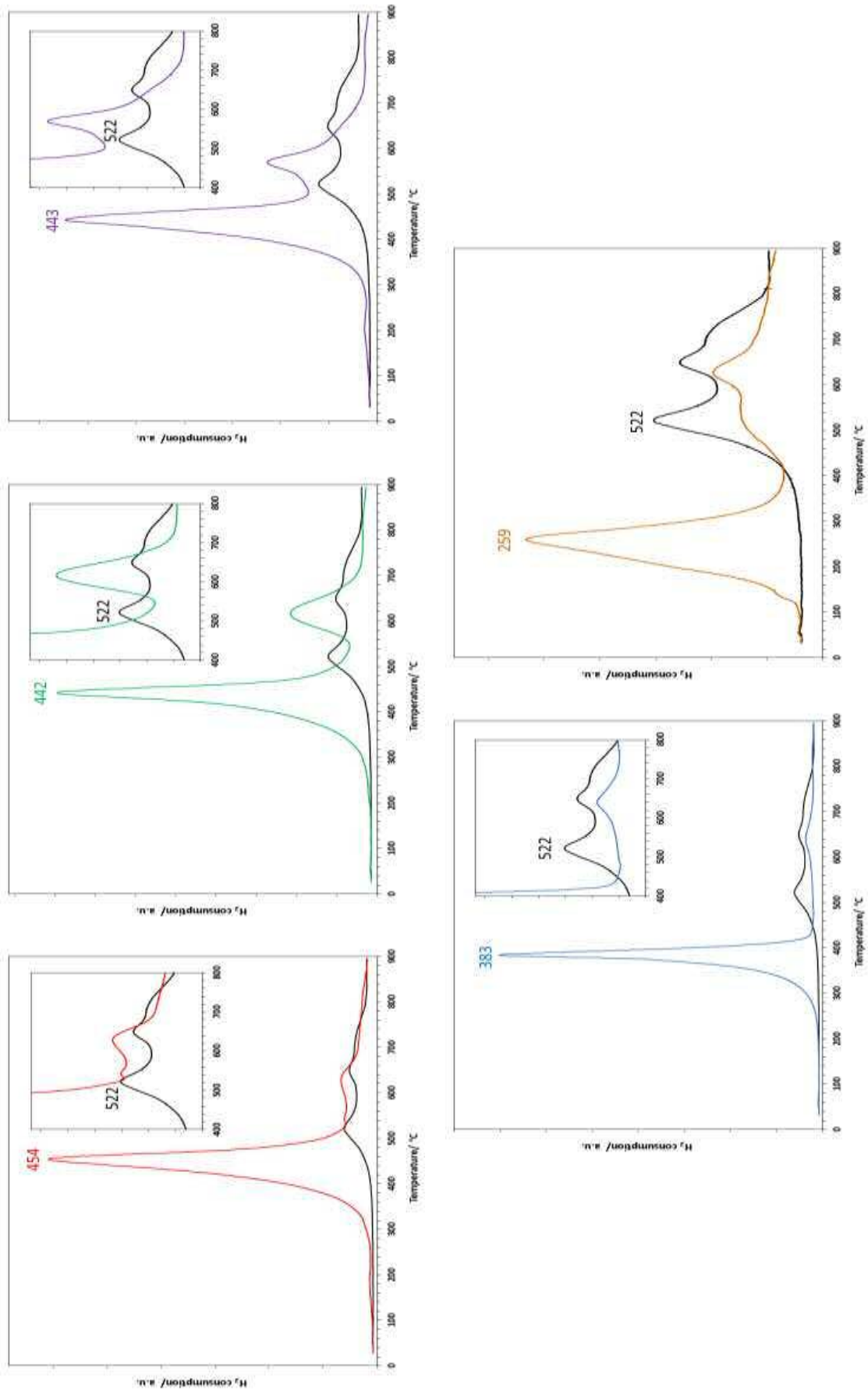


**Figure 5.19** TPR profiles of 5%Fe/CZA (red), 5%Co/CZA (green), 5%Ni/CZA (purple), 5%Cu/CZA (blue) and 5%Ag/CZA (brown) each compared with bare CZA support (black)

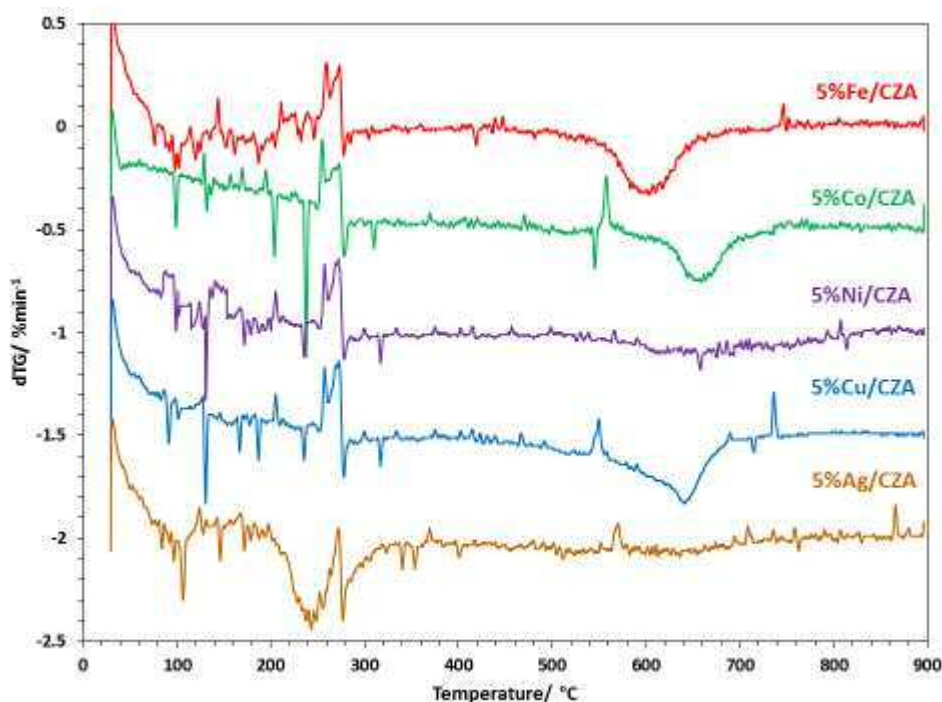


**Figure 5.20** dTG plots of 5%Fe/CZA (red), 5%Co/CZA (green), 5%Ni/CZA (purple), 5%Cu/CZA (blue) and 5%Ag/CZA (brown)

The presence of reduction peaks above 600 °C were attributed to the decomposition of nitrates as identified by XPS. Thermogravimetric analysis was undertaken on the catalysts and the derivative plots are presented in figure 5.20. The plots indicated mass losses at similar temperatures to these TPR peaks in the cases of 5%Fe, Co and Cu/CZA. Slight losses of mass were also observed for 5%Ni and Ag/CZA in this region.

### 5.3.2 Soot oxidation testing

The 5%TM/CZA catalysts were each tested for soot oxidation by thermogravimetric analysis in the usual manner. The derivative plots are presented in figure 5.21, with each of the samples offset by 1 %min<sup>-1</sup> for ease of comparison.

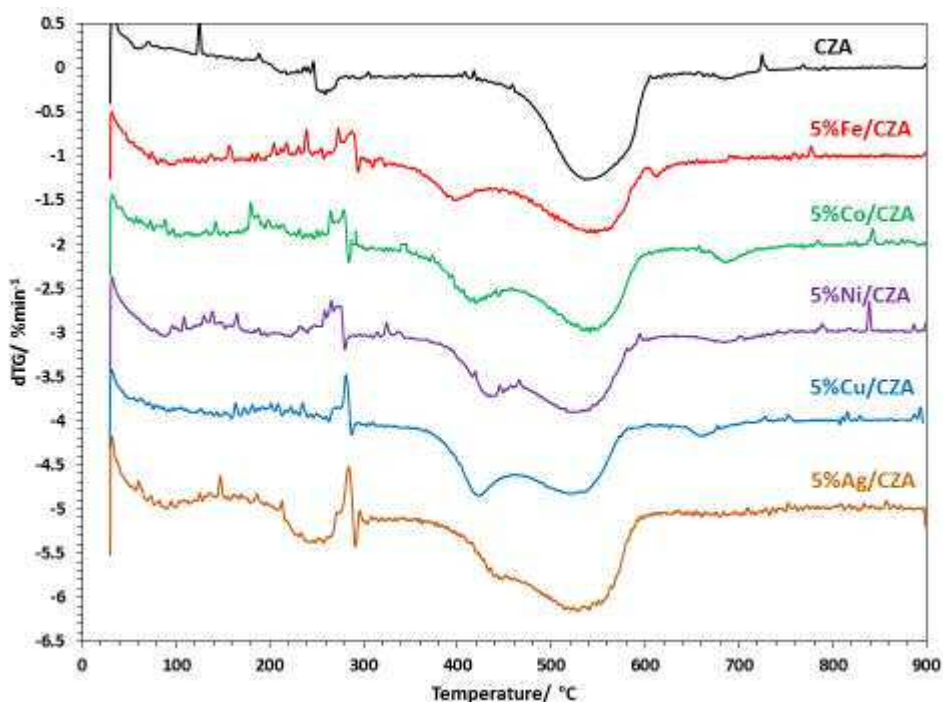


**Figure 5.21** dTG plots of catalyst/soot mixtures containing: CZA (black), 5%Fe/CZA (red), 5%Co/CZA (green), 5%Ni/CZA (purple), 5%Cu/CZA (blue) and 5%Ag/CZA (brown)

As with the previous silver-containing catalysts presented in this chapter, a significant shoulder peak appeared beside the major soot oxidation curve with 5%Ag/CZA. This shoulder was also observed with the other 5%TM catalysts. With these catalysts it was even more distinct from the main curve, almost forming a completely separate peak in the case of 5%Fe/CZA. The peak temperatures of these shoulders are provided in table 5.8. With the exception of 5%Ag/CZA, these peaks were at similar temperatures to the sharp reduction peaks observed in the TPR profiles of the catalysts. This suggested that the release of oxygen as the TM-oxides were reduced was able to be utilised in the oxidation of soot (possibly the hydrocarbon fraction) at this lower temperature. This also served to lower the  $T_o$  considerably in each case compared to the bare CZA support. Interestingly, of these catalysts only 5%Ni and Cu/CZA were able to lower the  $T_p$  and  $T_f$  of soot oxidation compared to the CZA support. This provided further evidence that the two soot oxidation processes acted independently of each other, and suggested that once the oxygen provided by the TM-oxide was depleted, the continuation of soot oxidation was reliant on the activity of the CZA support.

**Table 5.8** Soot oxidation temperatures of samples mixed with 5%TM/CZA on their 1<sup>st</sup> and 2<sup>nd</sup> use

Catalyst	T <sub>o</sub> (°C)		Minor T <sub>p</sub> (°C)		Major T <sub>p</sub> (°C)		T <sub>f</sub> (°C)	
	1 <sup>st</sup> run	2 <sup>nd</sup> run	1 <sup>st</sup> run	2 <sup>nd</sup> run	1 <sup>st</sup> run	2 <sup>nd</sup> run	1 <sup>st</sup> run	2 <sup>nd</sup> run
<b>Soot (no catalyst)</b>	465		535		622		651	
<b>CZA</b>	410	389	-		<b>542</b>	<b>538</b>	605	597
<b>5%Fe/CZA</b>	320	437	396	-	<b>546</b>	<b>554</b>	602	625
<b>5%Co/CZA</b>	356	413	420	-	<b>542</b>	<b>557</b>	616	615
<b>5%Ni/CZA</b>	342	424	436	-	<b>525</b>	<b>561</b>	594	615
<b>5%Cu/CZA</b>	359	372	422	409	<b>521</b>	<b>538</b>	583	591
<b>5%Ag/CZA</b>	365	424	447	-	<b>527</b>	<b>549</b>	601	610

This was further demonstrated by the dTG plots of soot oxidation on the catalysts' second use, which are shown in figure 5.22, overleaf (offset by 1 %min<sup>-1</sup> for comparison with their respective first use plots). With the exception of 5%Cu/CZA, the minor soot oxidation peak observed during the first use of the catalysts was not present during the second use. This suggested that the impregnated TM in these cases was reduced during the initial test and was not re-oxidised sufficiently to repeat the process during the second tests. This resulted in these catalysts regressing to the activity of the bare CZA support and in some cases even worse. For 5%Cu/CZA the shoulder peak observed during the first test was retained on second use. However there was a regression in terms of the major soot oxidation process, which can be seen in the increases to the T<sub>p</sub> and T<sub>f</sub> in table 5.8. This suggested that, as with the other 5%TM/CZA catalysts on their first use, the copper acted independently of the CZA support.

In conclusion it was found that none of the 5%TM/CZA catalysts were able to provide thermal stability after exposure to temperatures up to 900 °C. However, 5%Cu/CZA was the most promising as it was the only catalyst able to retain the low temperature oxidation process provided by the reduction of the TM-oxide. It was therefore decided to proceed with the impregnation of copper onto the other CMA 7:3:10 supports from Chapter 4 in order to investigate whether this activity could be further improved on other ceria-based supports.

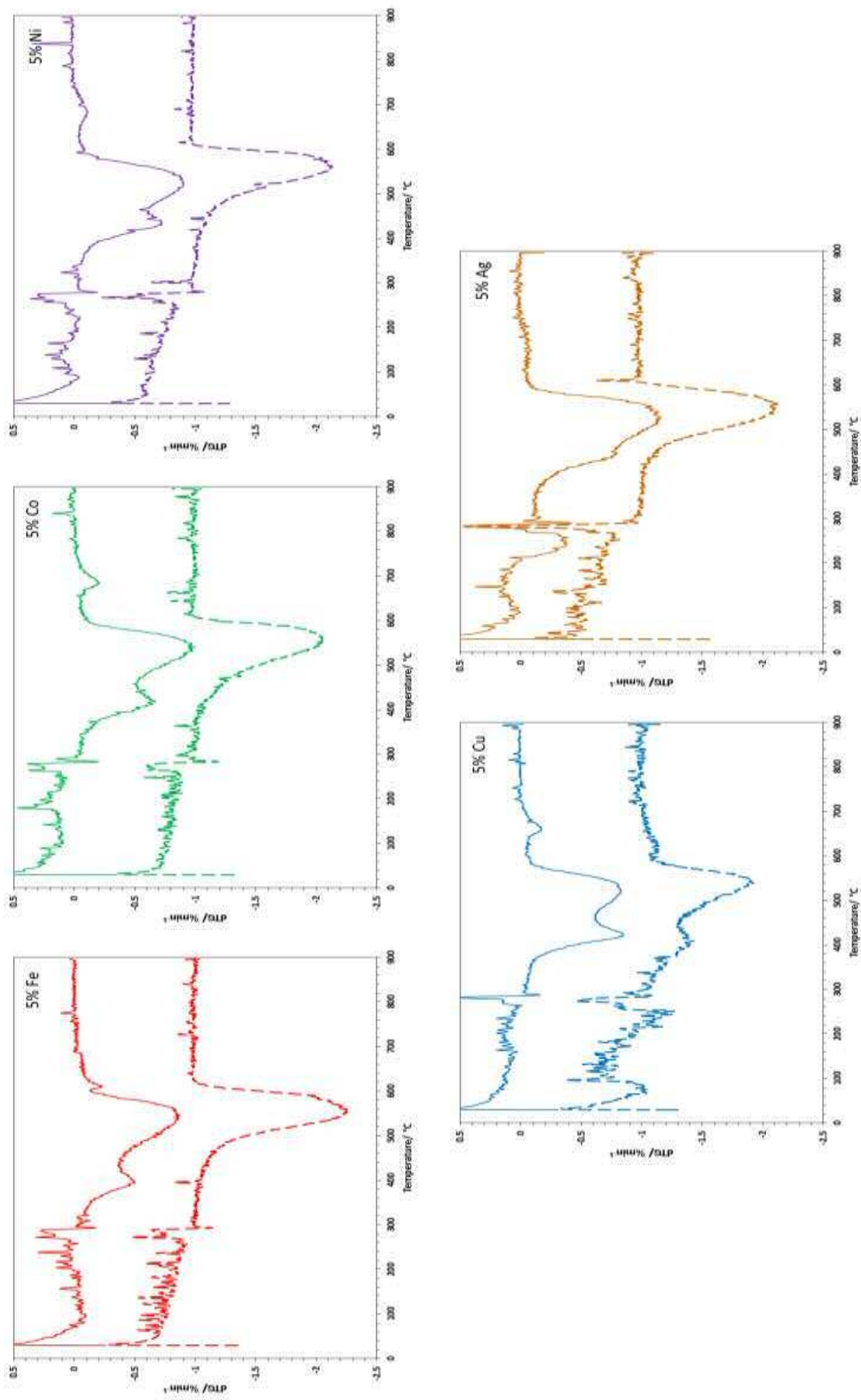


**Figure 5.22** dTG plots of catalyst/soot mixtures containing: 5%Fe/CZA (red), 5%Co/CZA (green), 5%Ni/CZA (purple), 5%Cu/CZA (blue) and 5%Ag/CZA (brown) on the first run (solid line) and second run (dashed line)



## 5.4 Impregnating copper on catalyst supports

The 5%TM/CZA catalysts did not provide the improved thermal durability that was desired compared to the silver catalyst. However as noted, 5%Cu/CZA provided evidence that it was able to partially oxidise soot particulates at a low temperature on repeated use and after exposure to high temperatures. Despite the remaining soot oxidation taking place at the same temperature as with the bare support, this still represented an improvement to the overall catalyst. This justified investigating copper further by applying the same method and loading to the other CMA supports from Chapter 4. These catalysts are referred to collectively as 5%Cu/CMA.

### 5.4.1 Characterisation

Each of the catalysts were characterised using the usual techniques.

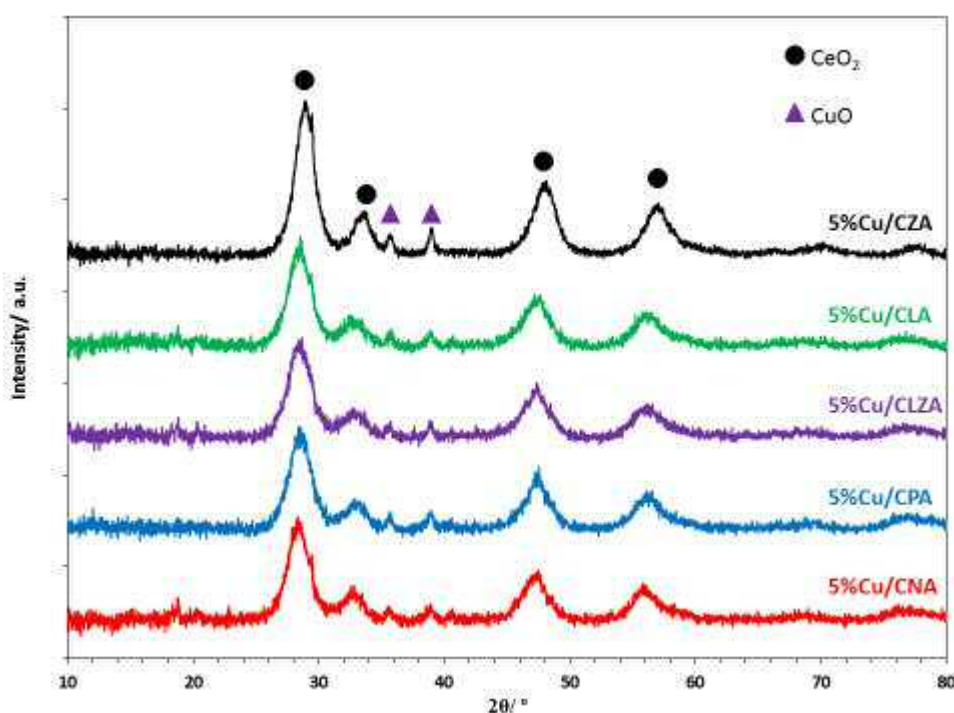


**Figure 5.23** X-ray diffractograms of 5%Cu on CZA (black), CLA (green), CLZA (purple), CPA (blue) and CNA (red)

As in the case of the 2%Ag,10%K catalysts, the X-ray diffractograms of the 5%Cu catalysts – shown in figure 5.23 – showed no change in the positions of the ceria reflections compared to those of their respective bare CMA supports. Each of the catalysts' diffractograms contained reflections at 35.7° and 39.0° which, as stated in section 5.3.1., indicated the presence of a CuO phase.

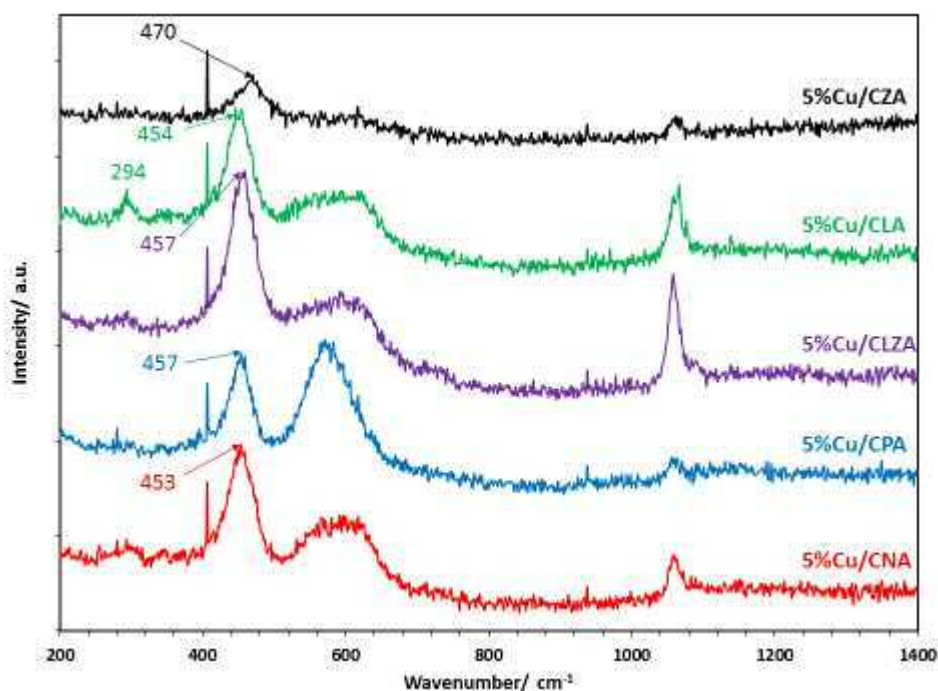


**Figure 5.24** Raman spectra of 5%Cu on CZA (black), CLA (green), CLZA (purple), CPA (blue) and CNA (red)

The Raman spectra of the catalysts are presented in figure 5.24. The peak position of the  $F_{2g}$  signal between  $450\text{ cm}^{-1}$  and  $470\text{ cm}^{-1}$  attributed to the Ce-O stretching mode was the same as that of the respective bare CMA support in each case, indicating the impregnation of Cu had no influence on the lattice parameters of ceria within the structure of the support. The prominence of the broad signal at  $500\text{--}650\text{ cm}^{-1}$  compared to the  $F_{2g}$  signal indicated high levels of oxygen vacancies within the ceria structure of the RE-metal-containing catalysts, most notably in the cases of 5%Cu/CPA and CNA, however this was already the case prior to the impregnation and so it was unclear to what extent – if any – this was influenced by the presence of Cu. The presence of a broad signal in the  $1040\text{--}1080\text{ cm}^{-1}$  region indicated the presence of nitrates, which was later confirmed by XPS described below. A weak signal at around  $495\text{ cm}^{-1}$  (observed most prominently on the spectrum of 5%Cu/CLA) was attributed to the  $A_g$  mode of  $\text{CuO}$ <sup>36</sup>, which complemented the findings of XRD and also the observations made by XPS, again provided in further detail below.

XPS used to quantify the surface elements of the catalysts, and these are presented in table 5.9. The concentration of copper on the surface of the catalysts was fairly consistent in each case with the exception of 5%Cu/CLA, which contained a much higher quantity. As in the previous section, peaks were detected for each of the catalysts in the N 1s region of the spectra. These were detected between 407 eV and 408 eV indicating the presence of nitrates, however the concentration was lower in these catalysts than the 5%TM/CZA catalysts presented in the previous section (including 5%Cu/CZA). As observed with all the impregnated catalysts in this chapter, the surface areas of the catalysts were significantly lower than their bare supports, as shown in table 5.9.

**Table 5.9** Surface properties of 5%Cu/CMA catalysts provided by XPS and BET analyses

Catalyst	Atomic conc. (%)								Surface area (m <sup>2</sup> g <sup>-1</sup> ) (bare support)
	Cu 2p	Ce 3d	M*	Al 2p	O 1s	C 1s	Na 1s	N 1s	
<b>5%Cu/CZA</b>	1.77	3.35	0.68	14.02	52.99	10.19	15.44	<b>1.56</b>	21 ±1 (36)
<b>5%Cu/CLA</b>	3.16	2.98	3.91	12.26	55.10	7.22	14.67	<b>0.70</b>	9 ±0 (21)
<b>5%Cu/CLZA</b>	1.69	2.73	1.03	14.82	56.89	6.55	15.61	<b>0.68</b>	8 ±0 (40)
<b>5%Cu/CPA</b>	1.82	1.43	0.82	15.72	55.94	6.16	17.20	<b>0.91</b>	3 ±0 (30)
<b>5%Cu/CNA</b>	1.84	2.23	2.86	13.85	56.14	6.51	15.97	<b>0.60</b>	6 ±0 (30)

\*M = Zr 3d/La 3d/La 3d+Zr 3d/Pr 3d/Nd 3d

In agreement with the previous characterisations, the XPS spectra of the catalysts identified the presence of copper as CuO. This can be seen from the Cu 2p regions shown in figure 5.25, overleaf which all showed peaks at similar binding energies to the reference value for CuO of 933.6eV. The strong satellite peak at 940-945eV confirmed this. The Cu 2p peak of 5%Cu/CPA also overlapped with the two Pr 3d peaks (observed in the region between 927 eV and 933 eV) from the surface of the support. The Cu 2p peak has therefore been highlighted red in this spectrum for clarity.

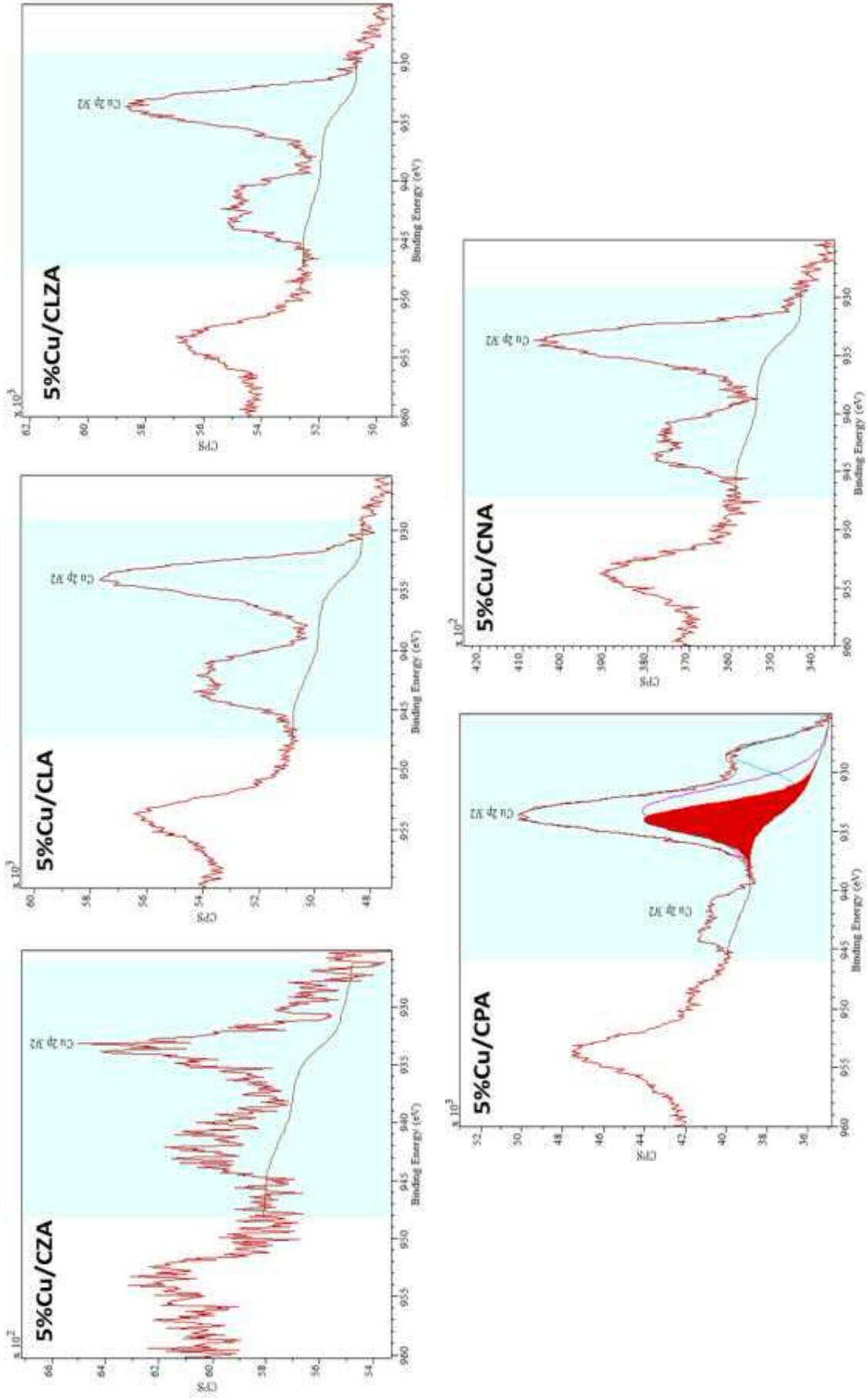
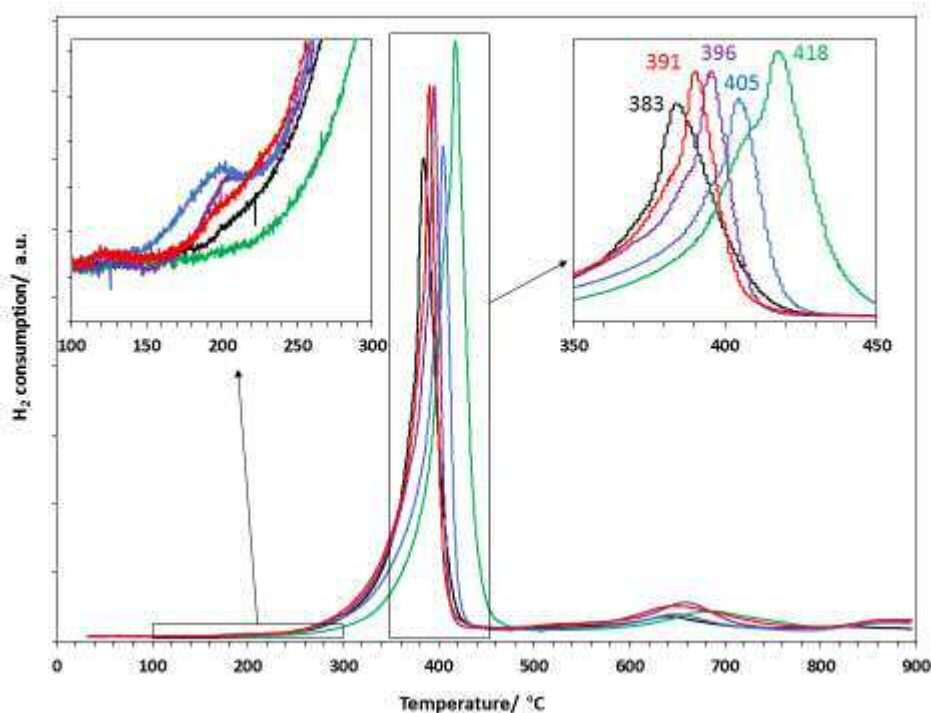


Figure 5.25 XPS spectra of Cu 2p regions of 5%Cu/CMA



**Figure 5.26** TPR profiles of 5%Cu on CZA (black), CLA (green), CLZA (purple), CPA (blue) and CNA (red)

The TPR profiles of the 5%Cu/CMA catalysts are shown in figure 5.26. Each showed a sharp reduction curve which peaked between 383 °C for 5%Cu/CZA and 418 °C for 5%Cu/CNA. This curve was attributed to the reduction of CuO as identified by the characterisation above. The enlarged section of the profile on the right hand side of the figure shows the region containing these curves. From this image it was possible to observe the asymmetrical shape of the curves, in some cases this appeared as a distinct shoulder to the main peak. This was attributed to the two-step reduction of  $\text{Cu}^{2+}$  to Cu via  $\text{Cu}_2\text{O}$ <sup>31</sup>. However, literature values for the reduction of CuO are much lower than observed in these profiles at around 200 °C<sup>31,34,35</sup>. The enlarged section on the left hand side of the figure shows a much smaller shoulder peak on several of the catalysts which could be attributed to any CuO that was not stabilised by the support and therefore underwent reduction at the typical temperature.

Figure 5.27 shows the same TPR profiles along with the respective bare CMA supports for comparison. As in section 5.3.1 these profiles showed that the presence of the sharp CuO reduction peak coincided with a decrease in intensity of the surface  $\text{Ce}^{4+}$  reduction peak observed during the reduction of the bare supports. This again suggested that the reduction of cerium was influenced by the presence of copper on the surface of the support.

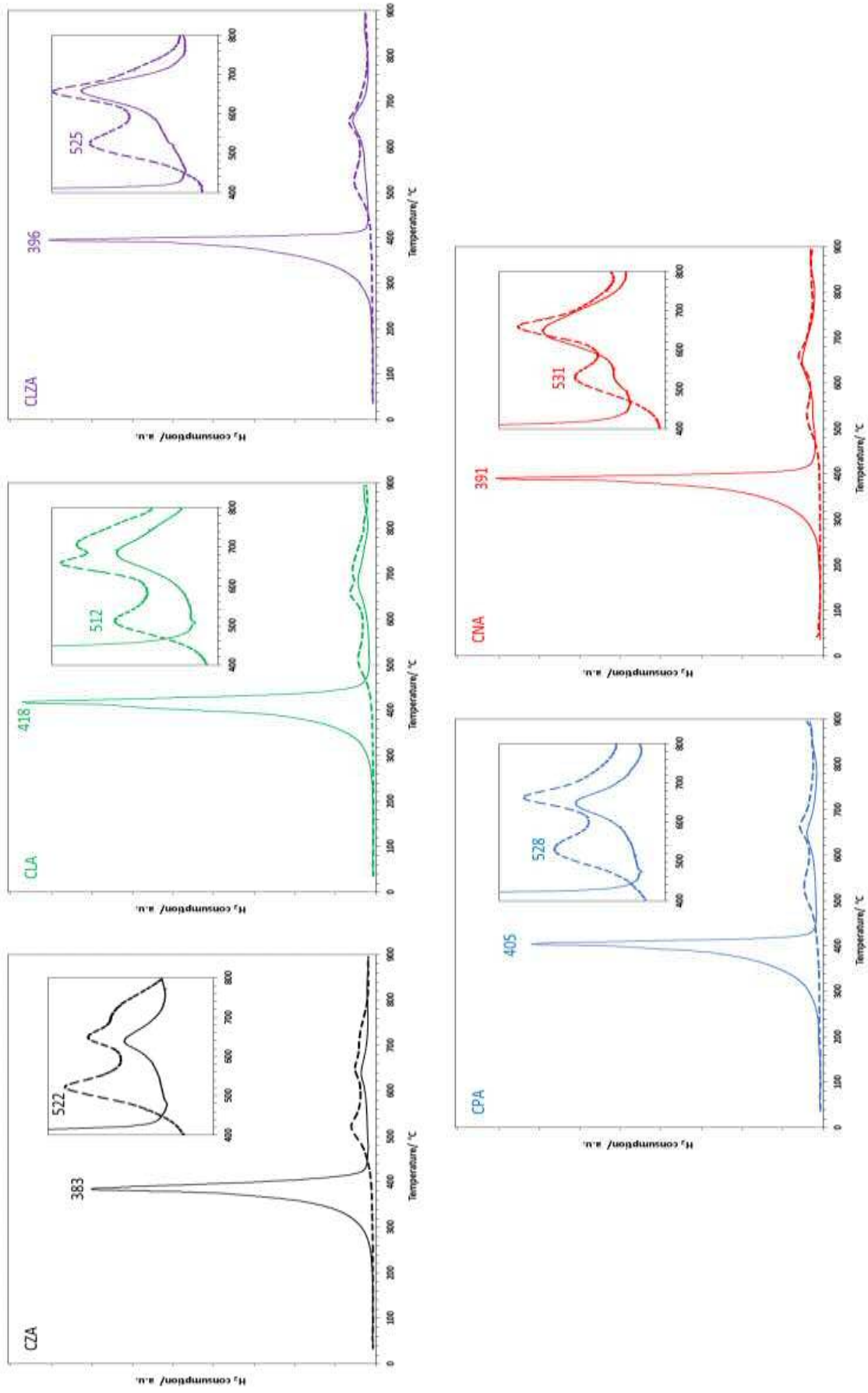


**Figure 5.27** TPR profiles of 5%Cu on CZA (black), CLA (green), CPA (blue) and CNA (red), (all solid lines) compared with their respective bare supports (dashed lines)

### 5.4.2 Soot oxidation testing

The 5%Cu/CMA catalysts were each tested for soot oxidation by thermogravimetric analysis in the usual manner. The derivative plots are presented in figure 5.28, with each of the samples offset by 1 %min<sup>-1</sup> for ease of comparison.

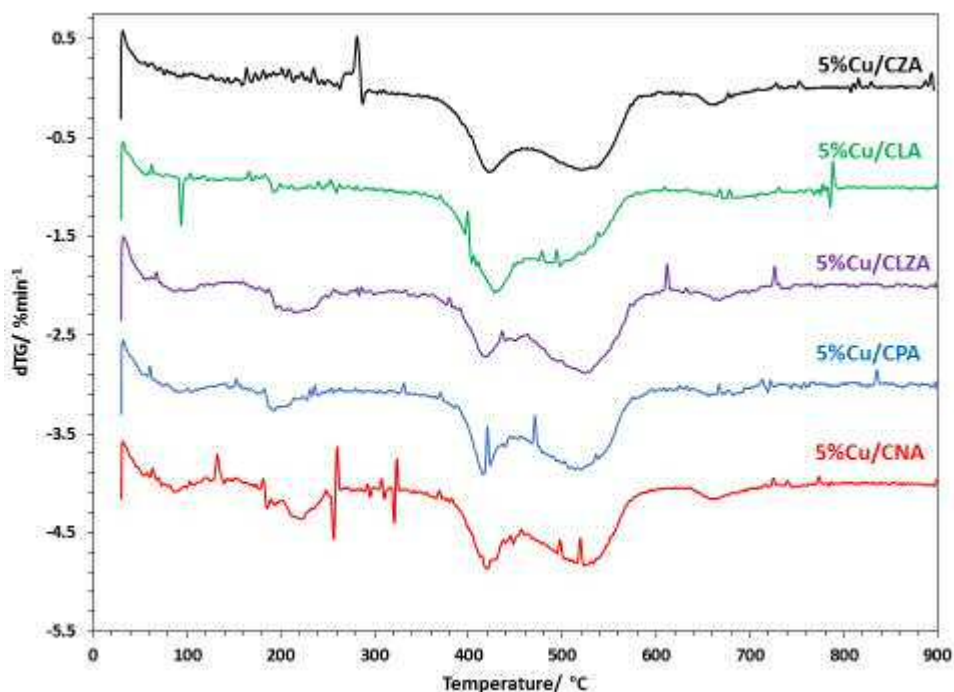


**Figure 5.28** dTG plots of catalyst/soot mixtures containing: 5%Cu on CZA (black), CLA (green), CLZA (purple), CPA (blue) and CNA (red)

The soot oxidation tests resulted in similar dTG patterns now familiar for TM-impregnated catalysts in this chapter – namely, the appearance of a lower temperature oxidation between 400 °C and 450 °C prior to the main oxidation curve. As explained in the previous section, this was attributed to the reduction of CuO as determined by TPR, which provided oxygen able to be utilised for the oxidation of the hydrocarbons present on the soot particles. Once this oxygen supply was depleted, the remaining soot was oxidised by the support. The peak temperatures for the lower-temperature minor oxidation curve are shown in table 5.10, and which appear at a similar temperature to the reduction of CuO, reaffirming this hypothesis. This also greatly decreased the onset temperature of soot oxidation compared to the bare supports in each case. The peak temperature of the main soot oxidation curve was also

lowered compared to the supports. As with the Ag-containing catalysts, this was attributed to the exotherm caused by the initial soot oxidation.

**Table 5.10** Soot oxidation temperatures of samples mixed with 5%Cu/CMA on their 1<sup>st</sup> and 2<sup>nd</sup> use

Catalyst	T <sub>o</sub> (°C)		Minor T <sub>p</sub> (°C)		Major T <sub>p</sub> (°C)		T <sub>f</sub> (°C)	
	1 <sup>st</sup> run	2 <sup>nd</sup> run	1 <sup>st</sup> run	2 <sup>nd</sup> run	1 <sup>st</sup> run	2 <sup>nd</sup> run	1 <sup>st</sup> run	2 <sup>nd</sup> run
<b>Soot (no catalyst)</b>	465		-		<b>622</b>		651	
<b>5%Cu/CZA</b>	359	372	422	409	<b>521</b>	<b>538</b>	583	591
<b>5%Cu/CLA</b>	353	413	428	-	<b>498</b>	<b>533</b>	592	579
<b>5%Cu/CLZA</b>	364	411	419	-	<b>525</b>	<b>535</b>	614	597
<b>5%Cu/CPA</b>	332	423	417	-	<b>520</b>	<b>548</b>	595	596
<b>5%Cu/CNA</b>	341	409	420	-	<b>523</b>	<b>513</b>	615	568

However unlike 5%Cu/CZA described in the previous section, the remaining 5%Cu/CMA catalysts were unable to produce the lower temperature oxidation on repeated use, as seen in the dTG plots of these tests in figure 5.29. With the exception of 5%Cu/CNA, this resulted in a regression in overall catalytic activity, with the peak soot oxidation temperature returning to a similar temperature as observed with the bare support. It was not possible to determine to what extent, if any, the presence of copper was a factor in maintaining a low soot oxidation temperature with 5%Cu/CNA. However given the overwhelming evidence of the deactivation of copper on the remaining supports it was deemed more likely that this was due to the improvement to the catalytic activity of the CNA support as described in Chapter 4.



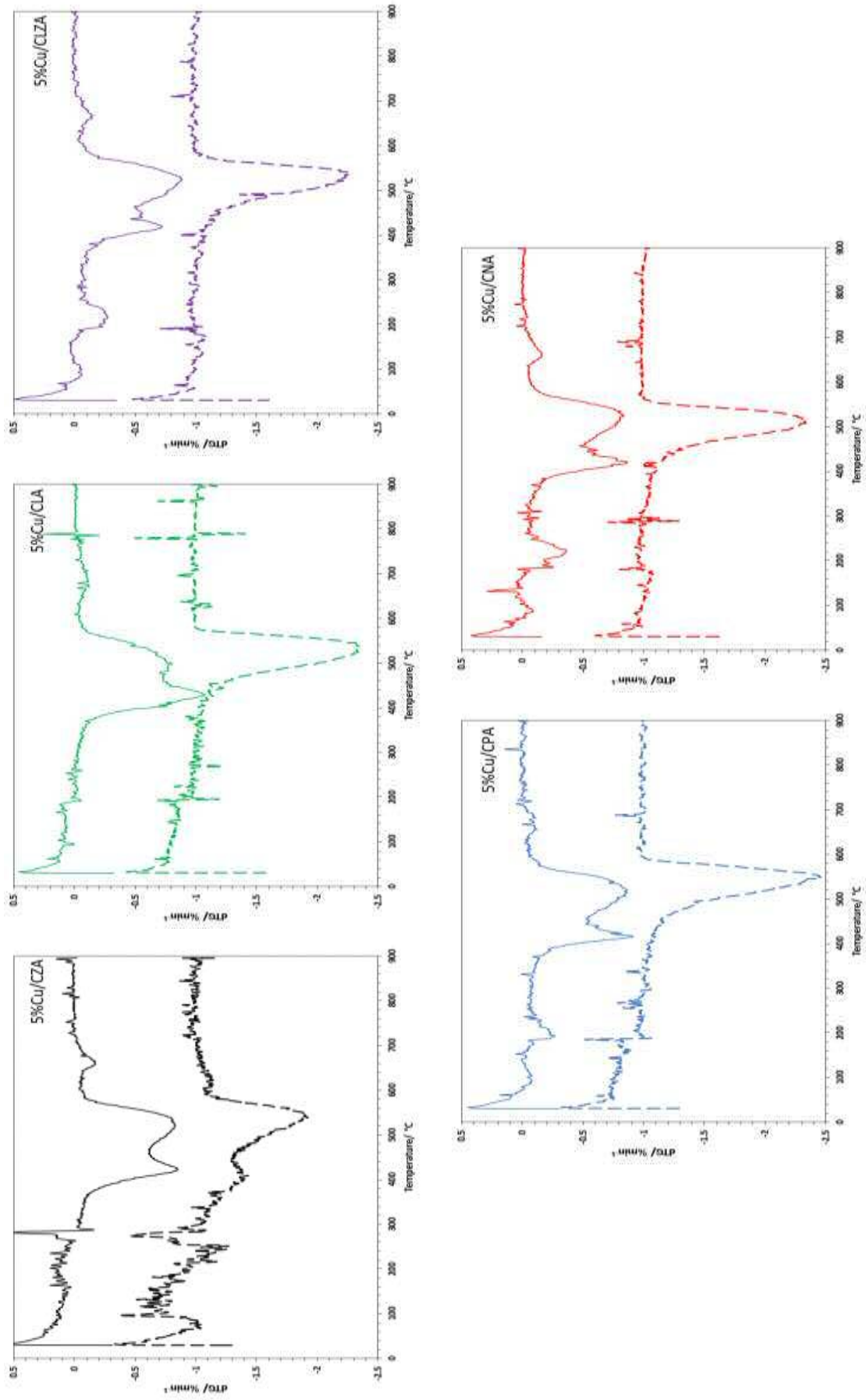


**Figure 5.29** DTG plots of catalyst/soot mixtures containing: 5%Cu on CZA (black), CLA (green), CLZA (purple), CPA (blue) and CNA (red) on the first run (solid line) and second run (dashed line)

## 5.5 Conclusions

In this chapter the viability of supporting active species for soot oxidation onto the ceria materials prepared in the previous chapter was investigated. Each of the catalysts displayed an ability to decrease the temperature of soot oxidation further than that of their respective bare supports.

The dTG plots of the soot oxidation tests with the 2%Ag,10%K catalysts showed a significant shoulder to the main soot oxidation curve, suggesting a two-step process which was attributed to the lower temperature oxidation of the hydrocarbons present in the soot. The presence of Ag was thought to be responsible for this, since it was not observed in the case of the 10%K/CZA catalyst. The plots also resembled the dTG curve observed during tight contact soot oxidation, which implied that the silver-containing catalysts were able to achieve a better contact with the soot. The oxidation of the remainder of the soot was also able to proceed at a lower temperature due to the exotherm produced by the combustion of the hydrocarbon fraction of the soot. The presence of the lower temperature step was also attributed to the findings of TPR, which showed a significant decrease in  $Ce^{4+}$  reduction temperature due to Ag-Ce interactions weakening the Ce-O bonds on the surface of the support. This allowed the release of active oxygen species at a much lower temperature than observed with the bare support, which were able to rapidly oxidise soot particulates with which it had close contact.

Despite not exhibiting this low-temperature step, the 10%K/CZA catalyst was able to decrease the temperature of the entire soot oxidation process more successfully than 2%Ag/CZA. This was thought to be due to the mobility of potassium on the surface of the catalyst improving contact with the soot. As reported in previous work, a synergistic effect was observed when both Ag and K were used together, lowering the soot oxidation temperature considerably compared to their individual examples. This combination improved the activity of all the CMA supports.

The 5%TM/CZA catalysts also exhibited two-step soot oxidation dTG plots. In this case the low-temperature step was observed as an almost completely distinct curve, and appeared at a similar temperature to the reduction of their respective TM-oxides, provided by TPR. This

suggested that unlike Ag, the other TMs acted independently of the support, resulting in two distinct oxidation processes.

The major issue identified by this study was the thermal stability of the catalysts. In particular, the two-step process described above did not occur during the second run subsequent to exposure to 900 °C, and this often resulted in the performance of the catalyst regressing to that of the bare support. Further analysis of the post-test samples would be required in order to understand the reasons for this deactivation. In the case of the 5%TM/CZA catalysts, this was likely due to the failure of the reduced metals to re-oxidise, which could be investigated by repeated TPR-TPO experiments. Sintering of the metals at higher temperatures could also be an explanation, as has been reported for Ag, which could lead to catalyst deactivation<sup>3,37</sup>. One other possibility which would be worth investigating is whether the lower-temperature hydrocarbon oxidation was caused by decomposition of nitrates on the surface of the catalysts (of which XPS suggested had increased compared to the bare supports) to NO<sub>2</sub>, which is known as being much more reactive for soot oxidation than O<sub>2</sub><sup>17</sup>. This would explain why this step was not observed on repeated use, as the nitrates were no longer present. However, no evidence that this occurred was observed from either TPR or TGA analysis, and this could easily be ruled out by substituting the nitrate precursors in each case for an alternative.

**Table 5.11** Peak soot oxidation temperatures of 2%Ag,10%K and 5%Cu catalysts compared to their respective bare supports

Catalyst	Bare Support		2%Ag,10%K		5%Cu	
	1 <sup>st</sup> use	2 <sup>nd</sup> use	1 <sup>st</sup> use	2 <sup>nd</sup> use	1 <sup>st</sup> use	2 <sup>nd</sup> use
<b>CZA</b>	542	538	450	535	521	538
<b>CLA</b>	541	539	522	521	498	533
<b>CLZA</b>	531	534	514	508	525	535
<b>CPA</b>	544	549	527	522	520	548
<b>CNA</b>	547	525	523	503	523	513

As shown in table 5.11, in contrast to their 5%Cu equivalents, the disappearance of the low temperature shoulder in their dTG plots did not prevent the 2%Ag,10%K/CMA catalysts displaying improved peak soot oxidation temperature on their 2<sup>nd</sup> use compared to their respective bare supports. This indicated that the impregnated species were still beneficial to

the soot oxidation process. Continued repeated testing of these catalysts is required in order to better establish their viability for real-world applications.

The catalyst containing 10%K on CZA support also showed evidence of deactivation on repeated use, this is despite a similar catalyst in Chapter 3 (K-CZA 0.5L) maintaining its activity. This may have resulted from the differences in preparation method, with the former using wet impregnation of  $K_2CO_3$  and the latter co-precipitation during the formation of the support. Another interesting investigation would be to see whether thermal stability could be improved for all the active species presented in this chapter if they were similarly added during the co-precipitation of the supports.

## 5.6 References

1. S. Liu, X. Wu, D. Weng and R. Ran, *J. Rare Earths*, 2015, **33**, 567–590.
2. R. Ramdas, Thesis, Cardiff University, 2014.
3. D. Kong, G. Wang, Y. Pan, S. Hu, J. Hou, H. Pan, C. T. Campbell and J. Zhu, *J. Phys. Chem. C*, 2011, **115**, 6715–6725.
4. E. Aneggi, J. Llorca, C. de Leitenburg, G. Dolcetti and A. Trovarelli, *Appl. Catal. B Environ.*, 2009, **91**, 489–498.
5. H. Liang, S. Wu, Y. Hong, S. Li, Y. Chen, X. Yu and D. Ye, *Catal. Lett.*, 2014, **144**, 685–690.
6. K. Shimizu, H. Kawachi and A. Satsuma, *Appl. Catal. B Environ.*, 2010, **96**, 169–175.
7. R. Kimura, S. P. Elangovan, M. Ogura, H. Ushiyama and T. Okubo, *J. Phys. Chem. C*, 2011, **115**, 14892–14898.
8. E. Aneggi, C. de Leitenburg, G. Dolcetti and A. Trovarelli, *Catal. Today*, 2008, **136**, 3–10.
9. J. P. A. Neeft, M. Makkee and J. A. Moulijn, *Fuel*, 1998, **77**, 111–119.
10. V. Shapovalov and H. Metiu, *J. Catal.*, 2007, **245**, 205–214.
11. S. Liu, X. Wu, W. Liu, W. Chen, R. Ran, M. Li and D. Weng, *J. Catal.*, 2016, **337**, 188–198.
12. P. Hu, Z. Amghouz, Z. Huang, F. Xu, Y. Chen and X. Tang, *Environ. Sci. Technol.*, 2015, **49**, 2384–2390.
13. Y. Gao, A. Duan, S. Liu, X. Wu, W. Liu, M. Li, S. Chen, X. Wang and D. Weng, *Appl. Catal. B Environ.*, 2017, **203**, 116–126.
14. G. Neri, L. Bonaccorsi, A. Donato, C. Milone, M. G. Musolino and A. M. Visco, *Appl. Catal. B Environ.*, 1997, **11**, 217–231.
15. Y. Kobayashi and R. Hikosaka, *Bull. Chem. React. Eng. Catal.*, 2017, **12**, 14–23.
16. H. Shimokawa, Y. Kurihara, H. Kusaba, H. Einaga and Y. Teraoka, *Catal. Today*, 2012, **185**, 99–103.
17. A. Bueno-López, *Appl. Catal. B Environ.*, 2014, **146**, 1–11.

18. J. P. A. Neeft, M. Makkee and J. A. Moulijn, *Appl. Catal. B Environ.*, 1996, **8**, 57–78.
19. X. Wang, J. Yang, L. Shi and M. Gao, *Nanoscale Res. Lett.*, 2016, **11**, 125.
20. XPS Interpretation of Cobalt, <http://xpssimplified.com/elements/cobalt.php>.
21. K. Burger, F. Tschisnarov and H. Ebel, *J. Electron Spectrosc. Relat. Phenom.*, 1977, **10**, 461–465.
22. V. K. Kaushik, *J. Electron Spectrosc. Relat. Phenom.*, 1991, **56**, 273–277.
23. XPS Interpretation of Silver, <http://xpssimplified.com/elements/silver.php>.
24. G. Avgouropoulos and T. Ioannides, *Appl. Catal. Gen.*, 2003, **244**, 155–167.
25. Y. Lin, J. Li, L. Lin, X. Liu, L. Chen and D. Li, *Adv. Nanoparticles*, 2013, **02**, 294.
26. N. S. McIntyre and M. G. Cook, *Anal. Chem.*, 1975, **47**, 2208–2213.
27. C. A. Strydom and H. J. Strydom, *Inorganica Chim. Acta*, 1989, **159**, 191–195.
28. V. I. Nefedov, E. K. Zhumadilov and L. Baer, *Zhurnal Neorganicheskoi Khimii*, 1978, **23**, 2113.
29. P. C. Mondal, J. Yekkonni Lakshmanan, H. Hamoudi, M. Zharnikov and T. Gupta, *J. Phys. Chem. C*, 2011, **115**, 16398–16404.
30. L. J. Gerenser, *J. Vac. Sci. Technol. Vac. Surf. Films*, 1990, **8**, 3682–3691.
31. A. Aranda, S. Agouram, J. M. López, A. M. Mastral, D. R. Sellick, B. Solsona, S. H. Taylor and T. García, *Appl. Catal. B Environ.*, 2012, **127**, 77–88.
32. J. Xu, G. Lu, Y. Guo, Y. Guo and X.-Q. Gong, *Appl. Catal. Gen.*, 2017, **535**, 1–8.
33. Y. Cao, L. Liu, F. Gao, L. Dong and Y. Chen, *Appl. Surf. Sci.*, 2017, **403**, 347–355.
34. G. Fierro, M. Lo Jacono, M. Inversi, P. Porta, F. Cioci and R. Lavecchia, *Appl. Catal. Gen.*, 1996, **137**, 327–348.
35. L. Kundakovic and M. Flytzani-Stephanopoulos, *J. Catal.*, 1998, **179**, 203–221.
36. J. F. Xu, W. Ji, Z. X. Shen, W. S. Li, S. H. Tang, X. R. Ye, D. Z. Jia and X. Q. Xin, *J. Raman Spectrosc.*, 1999, **30**, 413–415.
37. E. Aneggi, C. de Leitenburg, G. Dolcetti and A. Trovarelli, *Catal. Today*, 2006, **114**, 40–47.

## 6. Conclusions

### 6.1 Final conclusions

The aim of this study was to identify materials capable of catalysing the complete combustion of soot particulates. Previous studies had identified ceria as a promising material for this purpose due to its outstanding oxygen storage properties and formation of active oxygen species. Therefore this work focused on the use of ceria-based catalysts for soot oxidation. Ceria was doped with various metals in order to enhance both its catalytic and thermal durability properties, so as to provide a suitable catalyst for use in exhaust aftertreatment technologies. Other dopants, reported as having their own catalytic properties for soot oxidation were also investigated in order to determine whether synergistic effects could take place with ceria.

In Chapter 3 the co-precipitation method of preparing a mixed-metal oxide ceria-zirconia-alumina material in a 7:3:10 molar ratio was investigated, based on the findings of a previous Cardiff University study which showed this to be both an active and stable soot oxidation catalyst<sup>1</sup>. The purpose of the investigation was to determine whether the method was successful at producing active ceria-based catalysts, and its reproducibility for future studies. The three batches prepared by this method each displayed soot oxidation activity, lowering the onset and peak soot oxidation temperatures. However, their performances were not consistent, as well as discrepancies appearing between the materials in several characterisations – most notably TPR. Persisting with this method of preparation would therefore have undermined any conclusions drawn from comparisons between catalysts of different compositions. The availability of autotitrator equipment provided a mechanically standardised co-precipitation method, as well as allowing the process to be scaled-up to produce larger batches of catalyst.

The CZA catalyst prepared by the autotitrator was significantly more active than those prepared by the previous manual co-precipitation method. The surface area and reduction profile of this catalyst compared to its manually prepared counterparts indicated a significant change in the physical structure and chemical properties of the material produced by this method. These were attributed to the increased level of sodium species present on the catalyst – evidenced by both Raman and XPS characterisation. As mentioned in Chapter 1,

alkali metals are well-known for their catalytic activity, improving catalyst/soot contact and providing an intermediate pathway to soot oxidation<sup>2</sup>. The presence of sodium species on the catalyst was concluded to be a consequence of scaling-up the process and the deficiency of post-filtration washing in removing the sodium carbonate precipitating agent. The subsequent investigation into removing sodium by increasing washing proved to be unsuccessful, with XPS indicating that sodium on the surface of the catalyst had actually increased. However, increasing the washing above 1.0 L of warm deionised water resulted in improved consistency between batches of CZA materials, evidenced from the composition of the catalyst surfaces provided by XPS, and supported by their reduction profiles and soot oxidation testing.

The influence of the precipitating agent on the soot oxidation activity of the CZA materials was observed when  $\text{Na}_2\text{CO}_3$  was replaced with  $\text{K}_2\text{CO}_3$  and  $\text{Cs}_2\text{CO}_3$ . These catalysts lowered the peak soot oxidation temperature by at least a further 20 °C. However, it was also observed that increasing washing was effective at removing potassium from the CZA catalyst. The significantly higher soot oxidation temperatures achieved with this catalyst compared to those with a high alkali metal content confirmed they were responsible for improving the activity of CZA.

The work conducted in this chapter served to establish a reproducible method of preparing ceria-based mixed metal oxide catalysts, and was utilised again for the catalysts prepared in Chapter 4. It was decided to continue to use sodium carbonate as the precipitating agent as it had improved the activity of the catalyst on first and repeated use, as well as proving resistant to removal by washing, ensuring the material retained a relatively consistent composition.

In Chapter 4, the use of alternative ceria-dopants to zirconium was investigated. This focused on the rare-Earth metals; lanthanum, praseodymium and neodymium. Initially, the 7:3:10 molar ratio used for CZA in the previous chapter was applied. Characterisation showed that the bulkier cations of these elements compared to  $\text{Ce}^{4+}$  resulted in an expansion of the ceria lattice compared to CZA. This did not result in an increase in surface  $\text{Ce}^{4+}$  reduction however, with each of the RE-containing catalysts showing a peak reduction temperature comparable

with CZA, and a lower intensity reduction curve. It was also observed that soot oxidation activity was not improved when Zr was completely replaced by one of the RE-metals – each showing a peak soot oxidation temperature between 540 °C and 550 °C. However, a 1:1 mix of Zr and La did show an improvement compared to CZA, with a  $T_p$  of around 530 °C.

When the study was expanded to investigate different Ce/dopant ratios, it was observed that the rare-Earth metals did not form solid solutions with ceria. XRD showed that at higher ratios, each of the rare-Earth metals formed separate crystalline phases. In the cases of La and Nd these were oxycarbonate phases which suggested the calcination conditions were not sufficient to decompose their respective carbonates formed during co-precipitation. With the exception of the CPA catalysts, in which  $\text{Pr}^{4+}$  ions were able to reduce, increasing the ratio of rare-Earth metal generally decreased the reducibility of the materials due to the decrease in cerium content. The activities of the catalysts containing Pr and Nd were seen to deteriorate as their ratios increased, while those containing La improved. An overall trend between the reducibility of the surfaces of the catalysts and their soot oxidation activity could not be established, which suggested the volume of lattice oxygen released from the catalyst was not the determining factor. It was tentatively proposed that the proportion of  $\text{Ce}^{3+}$  ions (detected on the surface of the catalysts by XPS), and hence the number of oxygen vacancies, was a major contributing factor to the soot oxidation activity. While there was no universal trend, in general the better performing catalysts contained a higher proportion of  $\text{Ce}^{3+}$  on their surface than those which performed relatively poorly.

This hypothesis was further strengthened by the investigation into the calcination conditions of the neodymium-containing catalysts, which was pursued due to the significant improvement in activity of the original CNA catalysts observed during their second test run. All CNA catalysts calcined under static air were found to be able to decrease the  $T_p$  of soot oxidation by at least 20 °C on their second test run compared to their first, with CNA 5:5:10 decreasing it by over 30 °C. Calcining the CNA catalyst at 750 °C under a flowing atmosphere resulted in a significant increase in catalyst activity; the  $T_p$  of soot oxidation was lowered to 512 °C in the case of the catalyst calcined under flowing air, significantly lower than other catalysts presented in Chapter 4. This was despite their TPR profiles showing a low intensity reduction of surface cerium ions, which again suggested this was not a determining factor for soot oxidation activity. However, the proportion of  $\text{Ce}^{3+}$  on the surfaces of these catalysts was



exceptionally high compared to their low-activity counterparts. As mentioned in the introduction, there is evidence to suggest that increasing oxygen vacancies in the ceria lattice can promote the formation of highly reactive oxygen species, such as  $O_2^-$  superoxide, which could explain the improvement in activity.

The work conducted in Chapter 5 aimed to improve on the activity of the CMA 7:3:10 catalysts prepared in Chapter 4 by utilising these as supports for various other active soot oxidation materials. A previous study at Cardiff University had established an optimum loading of 2% Ag and 10% K on a CZA support as an active soot oxidation catalyst, and was therefore applied to the aforementioned ceria-based materials from Chapter 4. It was observed that both silver and potassium were individually able to enhance the catalytic activity of the CZA support, however the dTG plots of these tests concluded that they achieved this in different ways. The silver-promoted catalyst showed evidence of two distinct soot oxidation processes, both of which took place at a lower temperature than achieved by the bare CZA support. This was attributed to the ability of metallic silver (evidence of which was provided by XRD and XPS) to lower the ceria reduction temperature (which had been observed from TPR) and form highly reactive oxygen species. It was concluded that the lower temperature process was the oxidation of soot particles in close contact to the catalyst, and possibly the more reactive hydrocarbon fraction, as had been observed in previous studies<sup>3,4</sup>. The remaining soot oxidation was likely catalysed by the CZA support, and took place at a lower temperature due to the exotherm produced by the lower-temperature reaction, as well as increasing the concentration of reactive sites on the surface of the soot. The dTG plot of soot oxidation with the K/CZA catalyst produced only a single curve, indicating that potassium had decreased the temperature at which all soot had reacted. The contrasting effects of the two promoters was attributed to the ability of potassium to achieve contact with a greater amount of soot. A synergistic effect was observed when the two promoters were combined on CZA. The two-process soot oxidation was again observed, however the lower-temperature process was much more intense, leading to a lower overall soot oxidation temperature. This combination of active promoters was used on the other CMA supports and also proved to be successful in improving activity. On repeat use it was observed that the lower-temperature process was lost from the silver-containing catalysts, which resulted in an increase to the onset

temperatures achieved by these catalysts. In the case of the CZA catalysts this also resulted in significant increases to the peak and final soot oxidation temperatures. However, those with the rare-Earth containing supports showed comparable peak and final temperatures on repeated use.

Similar to the silver containing catalysts, the dTG plots of soot oxidation with the various other transition metals on the CZA support also showed two distinct processes taking place. The minor lower-temperature process in these cases coincided with the temperature at which the metals had been observed to reduce by TPR. This indicated that the release of oxygen from the impregnated metal oxides was able to oxidise soot at a lower temperature and independently of the CZA support, which oxidised the remaining majority of soot. Of these catalysts, only 5%Cu/CZA was able to maintain the lower-temperature soot oxidation process on repeated use, although the temperature of the major soot oxidation process was seen to increase, indicating an overall loss of activity. The remainder of the catalysts reverted to the activity of the CZA support. These observations indicated that the transition metals were not durable at high temperatures. Similar observations were made when copper was impregnated on the other CMA materials from Chapter 4. In each case it was observed from XRD that the catalyst contained a CuO crystalline phase. The TPR profiles and soot oxidation tests of these catalysts again suggested that the reduction of this phase and the subsequent release of oxygen was responsible for the oxidation of a fraction of soot at a lower temperature than achieved by the ceria-based supports. Repeat testing again showed that the impregnated species did not function after exposure to high temperatures, with the catalyst again reverting to a similar activity to the bare support.

To summarise; it has been observed that the activity of ceria-based catalysts for soot oxidation prepared in this study benefited from the use of an alkali metal carbonate precipitating agent during preparation. The presence of residual sodium from the preparation of the material resulted in a decrease in peak soot oxidation temperature by a further 40 °C than achieved by an equivalent catalyst without sodium. It was demonstrated that further improvements to the activity of these catalysts could be achieved by altering the structure of ceria by varying the dopant metal and increasing the proportion of oxygen vacancies. The addition of other active soot oxidation species onto these ceria-based materials by

impregnation was able to increase activity even further. In the case of the transition metals this was achieved by drastically decreasing the temperature at which soot particles in close contact with the catalyst (possibly the hydrocarbon fraction, more susceptible to oxidation) were oxidised, and with potassium by improving overall soot oxidation by increasing catalyst/soot contact and providing an alternative reaction pathway via carbonate intermediates. With very few exceptions, the ceria-based materials presented in Chapters 3 and 4 exhibited good thermal stability by retaining their soot oxidation activity on repeated use. Many of the impregnated catalysts in Chapter 5 suffered activity loss on repeated use, however they were rarely observed to deteriorate beyond the activity of the bare support, which indicated that the ceria support remained stable. This demonstrated the success of the alumina “diffusion barrier” as described in Chapter 1 in preventing the deactivation of the ceria-based catalysts by sintering. In particular, the high activity of the CNA catalysts despite enduring high temperature calcinations and/or repeated soot oxidation tests was a promising development.

## 6.2 Future work

The work conducted in this project has opened up numerous avenues of investigation which could be pursued further.

While it was conclusively demonstrated that the alkali metals involved in the co-precipitation of the ceria-based catalysts were responsible for improving their activities, it would be interesting to prepare these catalysts with a non-alkali metal carbonate as the precipitating agent. This would allow a fairer comparison of the activities of the various catalysts prepared by this method, and the effects of the various dopant metals would be more apparent. Careful consideration would need to be given to the choice of precipitating agent, as differences in solubility and the pH of the resulting solution would affect the volume and rate of addition into the mixture required to maintain the desired conditions of the reaction. Ammonium carbonate,  $(\text{NH}_3)_2\text{CO}_3$  would be an obvious alkali metal-free candidate. Conversely, it would be interesting to determine the activity of the alkali metals on similarly-prepared materials that were not themselves active soot oxidation catalysts, i.e. by removing the cerium precursor from the preparation method.

Further work could also be conducted on the rare-Earth metal dopants in Chapter 4. The combination of both zirconium and lanthanum as dopants for ceria showed good soot oxidation activity. Without time constraints, a similar study could be conducted on combinations of other dopants. It would also be beneficial to widen the calcination study of the CNA catalysts to include those containing the 5:5:10 and 3:7:10 ratios. Catalysts with higher a neodymium content would provide a better indication of whether decomposition of  $\text{Nd}_2\text{O}_2\text{CO}_3$  to  $\text{Nd}_2\text{O}_3$  took place at the higher calcination temperature. Further calcination studies could also be conducted with the various other catalyst compositions presented in this work in order to determine the optimum conditions for each.

Many of the impregnated catalysts in Chapter 5 suffered from poor thermal durability during testing, possibly due to sintering/loss of the metal promoters. It was observed in Chapter 3 that a CZA catalyst containing potassium through co-precipitation was able to maintain its activity on repeated use, while the impregnated 10%K/CZA catalyst presented in Chapter 5 was less durable. It would be interesting to see whether introducing the metal promoters during the co-precipitation of the ceria-based support would provide greater stability, and prevent sintering and thus deactivation. As described in Chapter 1, a previous study of the co-precipitation of silver with ceria was seen to form a rice-ball morphology where ceria particles prevented the sintering of silver. This was also deemed to increase the interaction of silver and ceria, which was favourable for soot oxidation<sup>5</sup>. It has also been shown in the case of cobalt and iron that co-precipitation favoured greater dispersion on the ceria support than impregnation, which resulted in better catalytic activity<sup>6,7</sup>.

The soot oxidation tests conducted in this work were carried out under a narrow set of reaction conditions using thermogravimetric analysis. While the purpose of using the loose contact method of mixing catalyst and soot was to mimic conditions on a particulate filter, in reality the conditions in a vehicle exhaust would alter significantly from those used in the TGA tests. A fixed-bed reactor placed within a temperature-controlled furnace and connected to a gas chromatograph (GC), and a gas flow regulated by mass flow controllers could provide a more comprehensive analysis of soot oxidation under various conditions. This would allow for the testing of the catalysts under various atmospheres, including exhaust gas compositions and varying levels of  $\text{O}_2/\text{NO}_x$ . This could also allow for greater analysis of the products formed during soot oxidation, and the selectivity of the catalysts towards the

formation of CO<sub>2</sub>. Further soot oxidation tests could also be carried out using a TAP reactor with labelled oxygen, as investigated by Bueno-Lopez *et al.*, in order to better study the role of lattice and gas-phase oxygen on the reaction<sup>8</sup>.

As mentioned, the ceria-based supports generally showed good thermal durability, maintaining their soot oxidation activity after exposure to high temperatures. However, these tests were short-term and under an atmosphere of synthetic air. In order to determine whether these catalysts would be suitable for use in exhaust conditions the scope of the durability testing would need to be expanded. A wide range of conditions, including varying the temperatures and the periods of time that the catalysts are exposed to them, as well as varying the composition of the atmosphere, could be investigated using the apparatus described above. It was observed in this study that sodium was difficult to remove from the catalysts by washing with water, but this could also be investigated further by conducting harsher hydrothermal aging studies, as described in previous work on alkali metal catalysts<sup>2</sup>.

### 6.3 References

1. R. Ramdas, Thesis, Cardiff University, 2014.
2. E. Aneghi, C. de Leitenburg, G. Dolcetti and A. Trovarelli, *Catal. Today*, 2008, **136**, 3–10.
3. Y. Kobayashi and R. Hikosaka, *Bull. Chem. React. Eng. Catal.*, 2017, **12**, 14–23.
4. G. Neri, L. Bonaccorsi, A. Donato, C. Milone, M. G. Musolino and A. M. Visco, *Appl. Catal. B Environ.*, 1997, **11**, 217–231.
5. K. Yamazaki, T. Kayama, F. Dong and H. Shinjoh, *J. Catal.*, 2011, **282**, 289–298.
6. E. Aneghi, C. de Leitenburg, G. Dolcetti and A. Trovarelli, *Catal. Today*, 2006, **114**, 40–47.
7. P. G. Harrison, I. K. Ball, W. Daniell, P. Lukinskas, M. Céspedes, E. E. Miró and M. A. Ulla, *Chem. Eng. J.*, 2003, **95**, 47–55.
8. A. Bueno-López, K. Krishna, M. Makkee and J. A. Moulijn, *J. Catal.*, 2005, **230**, 237–248.

## 7. Appendix

### 7.1 Characterisation

#### 7.1.1 Raman

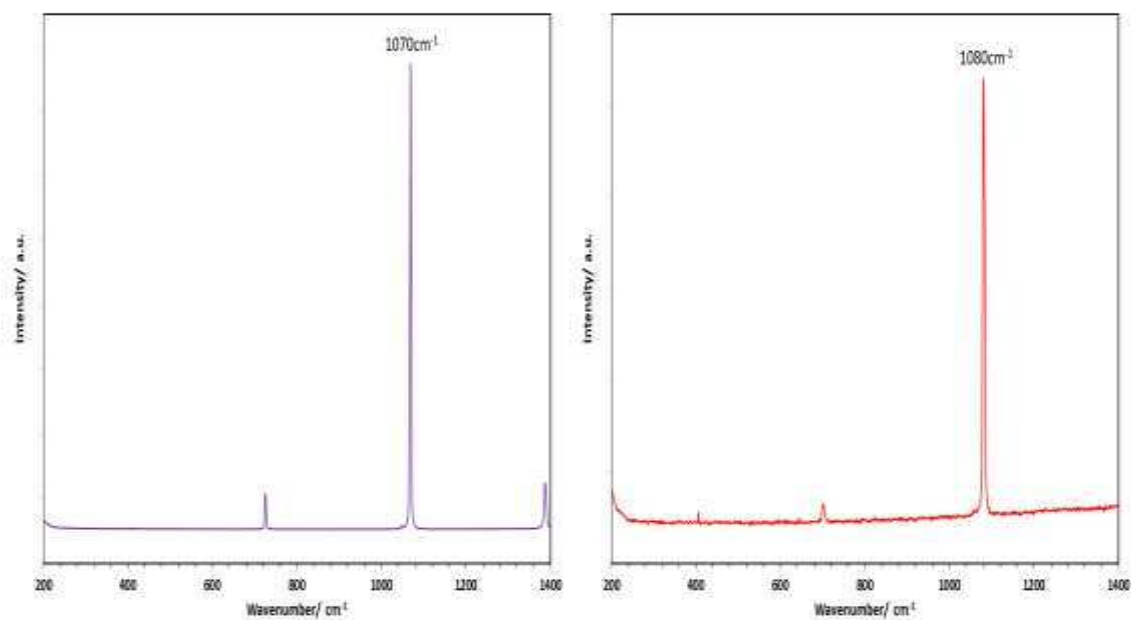


Figure 7.1 Raman spectra of (left)  $\text{NaNO}_3$ , and (right)  $\text{Na}_2\text{CO}_3$

#### 7.1.2 XPS

##### 7.1.2.1 Chapter 3

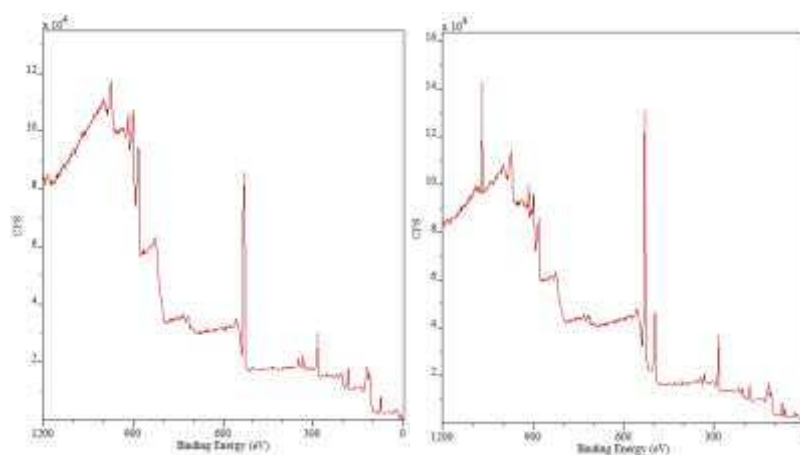


Figure 7.2 XPS wide scan spectra of (left) manual-CZA, and (right) auto-CZA

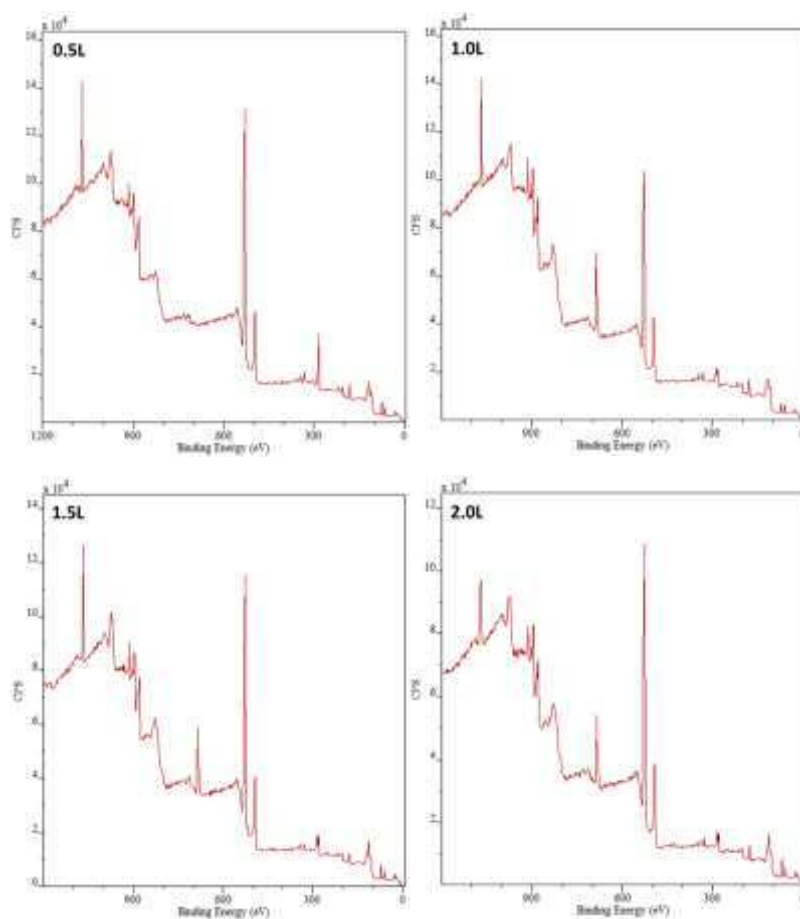


Figure 7.3 XPS wide scan spectra of Na-CZA catalysts

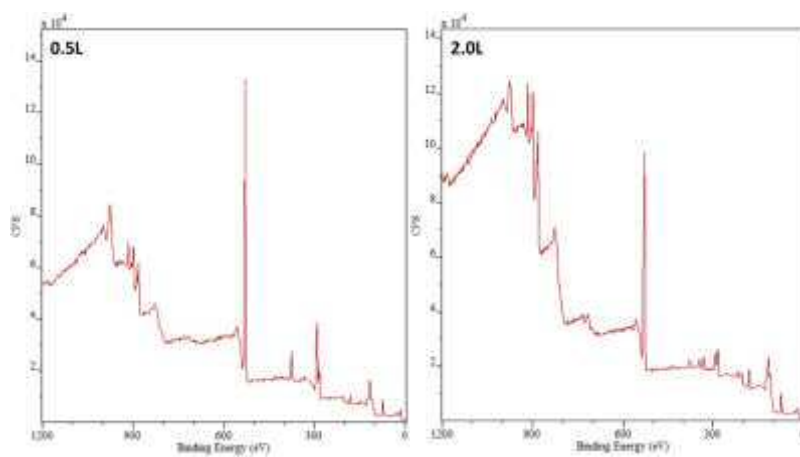


Figure 7.4 XPS wide scan spectra of K-CZA catalysts

## 7.1.2.2 Chapter 4

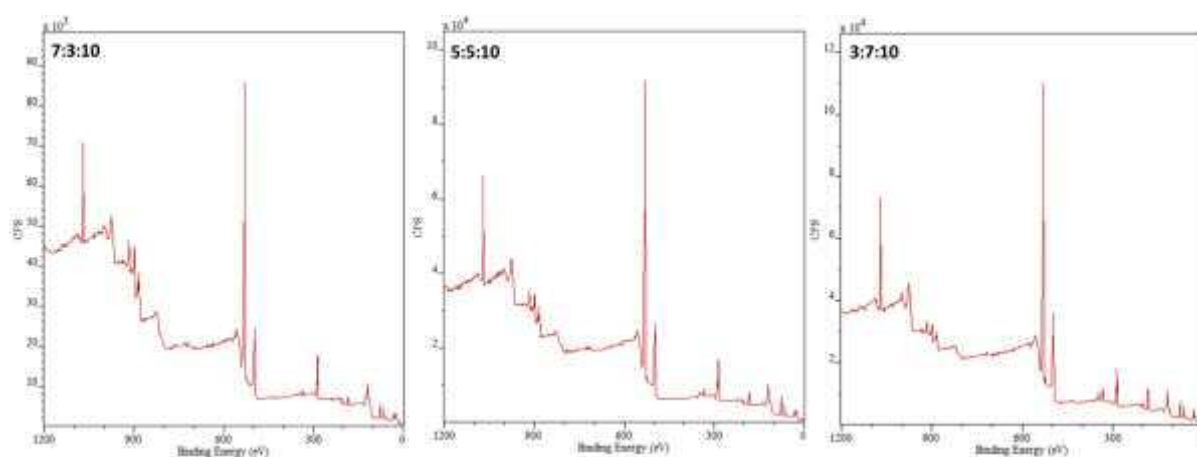


Figure 7.5 XPS wide scan spectra of CZA catalysts

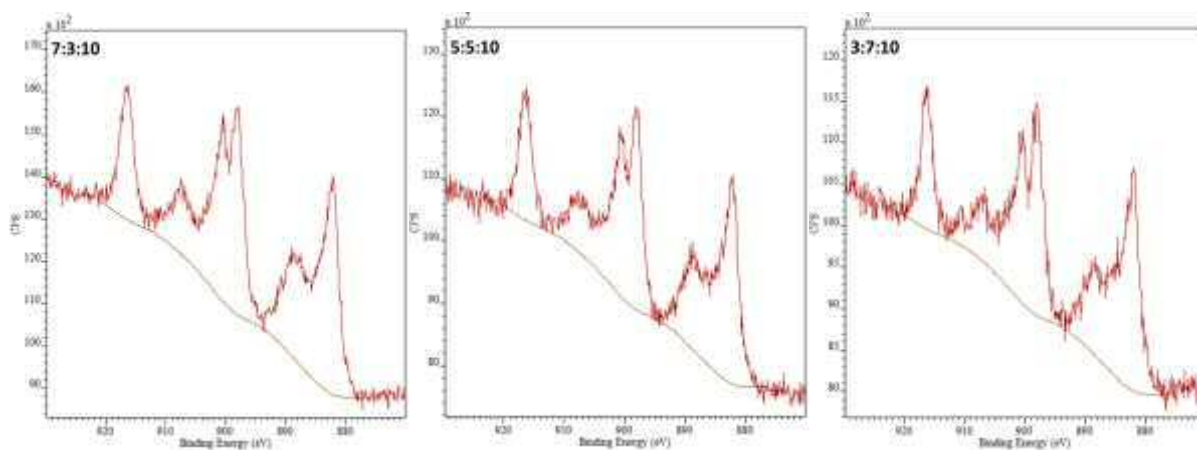


Figure 7.6 Ce 3d regions of CZA catalysts

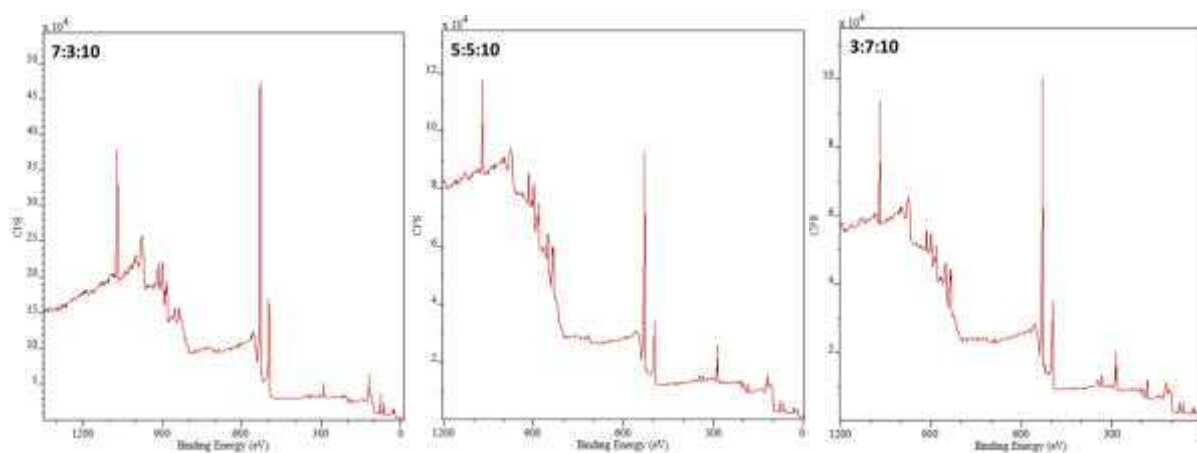


Figure 7.7 XPS wide scan spectra of CLZA catalysts



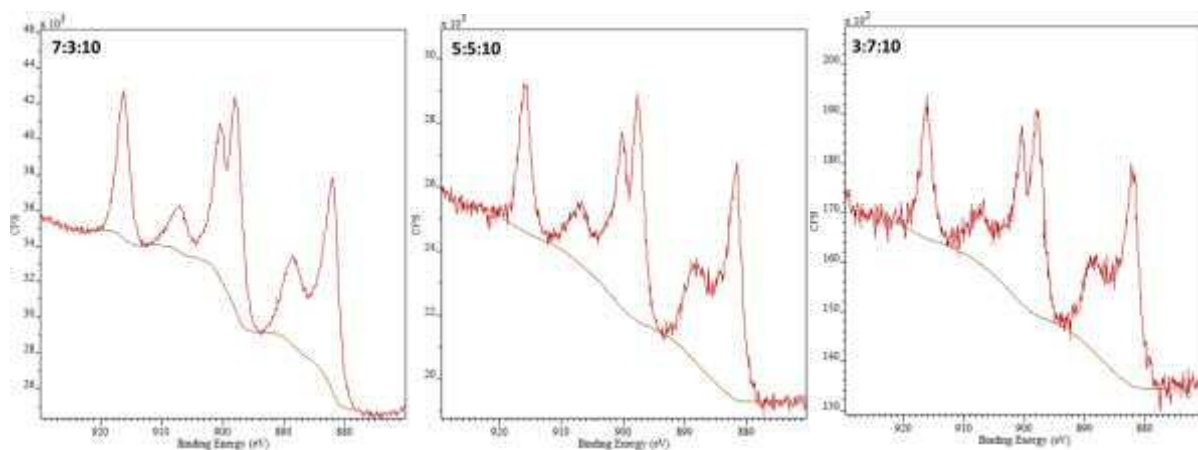


Figure 7.8 Ce 3d regions of CLZA catalysts

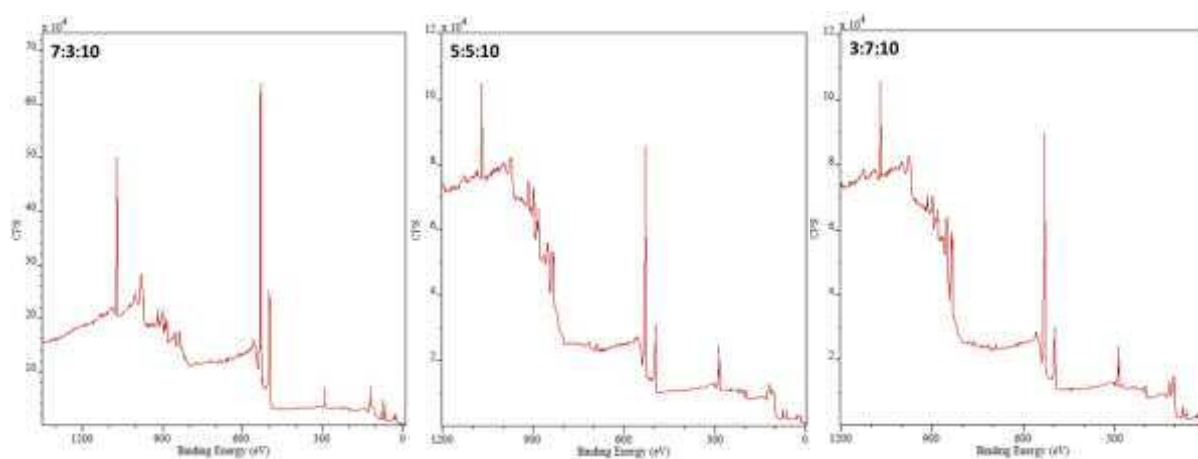


Figure 7.9 XPS wide scan spectra of CLA catalysts

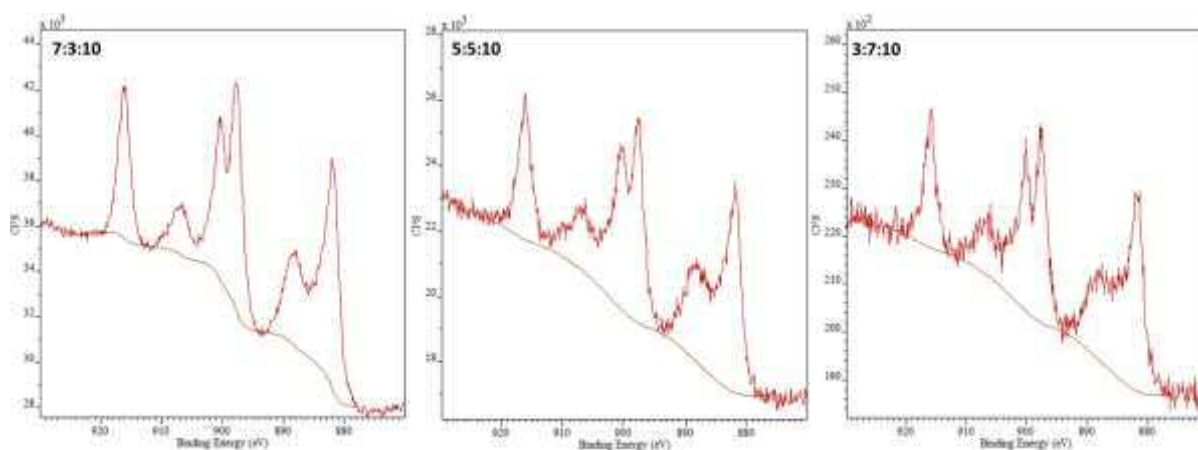


Figure 7.10 Ce 3d regions of CLA catalysts

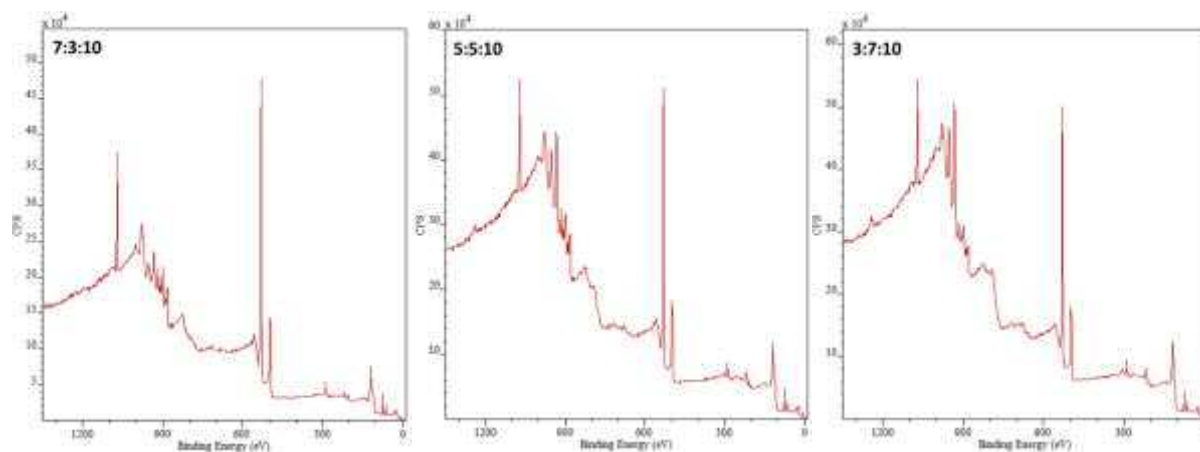


Figure 7.11 XPS wide scan spectra of CPA catalysts

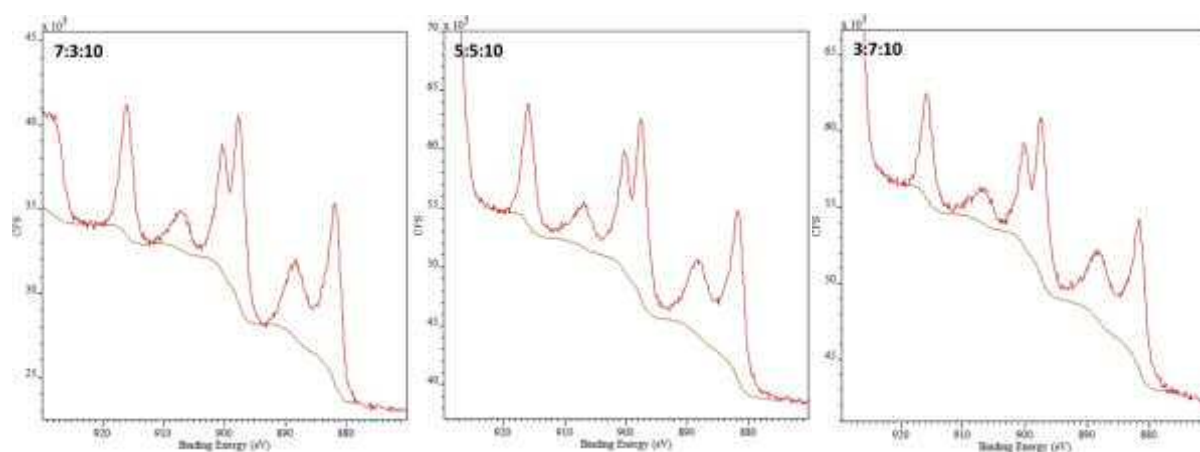


Figure 7.12 Ce 3d regions of CPA catalysts

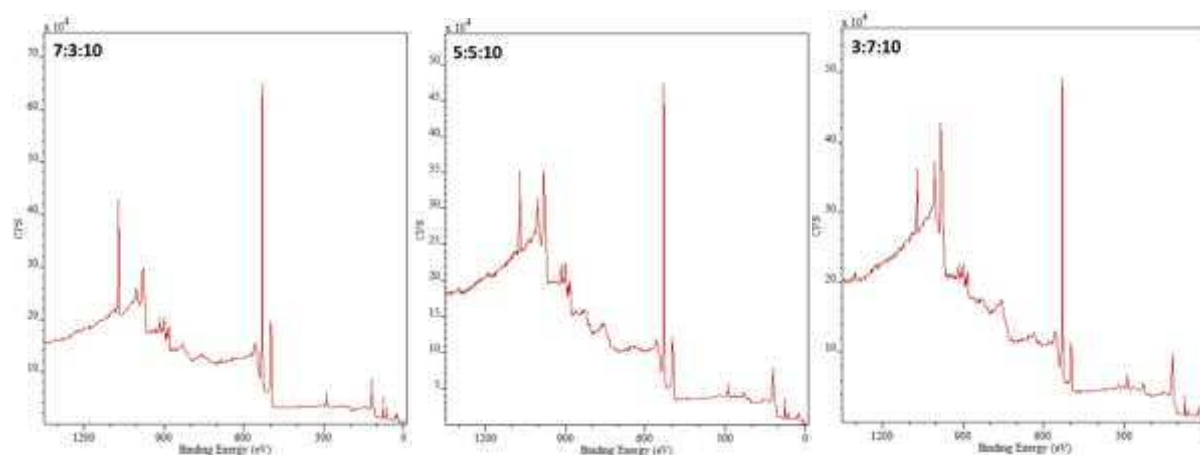


Figure 7.13 XPS wide scan spectra of CNA catalysts

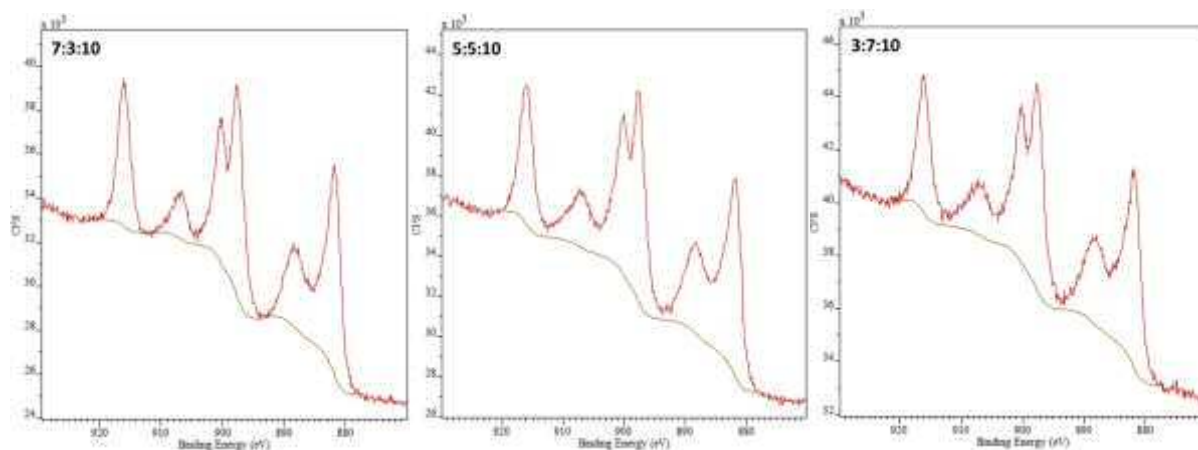


Figure 7.14 Ce 3d regions of CNA catalysts

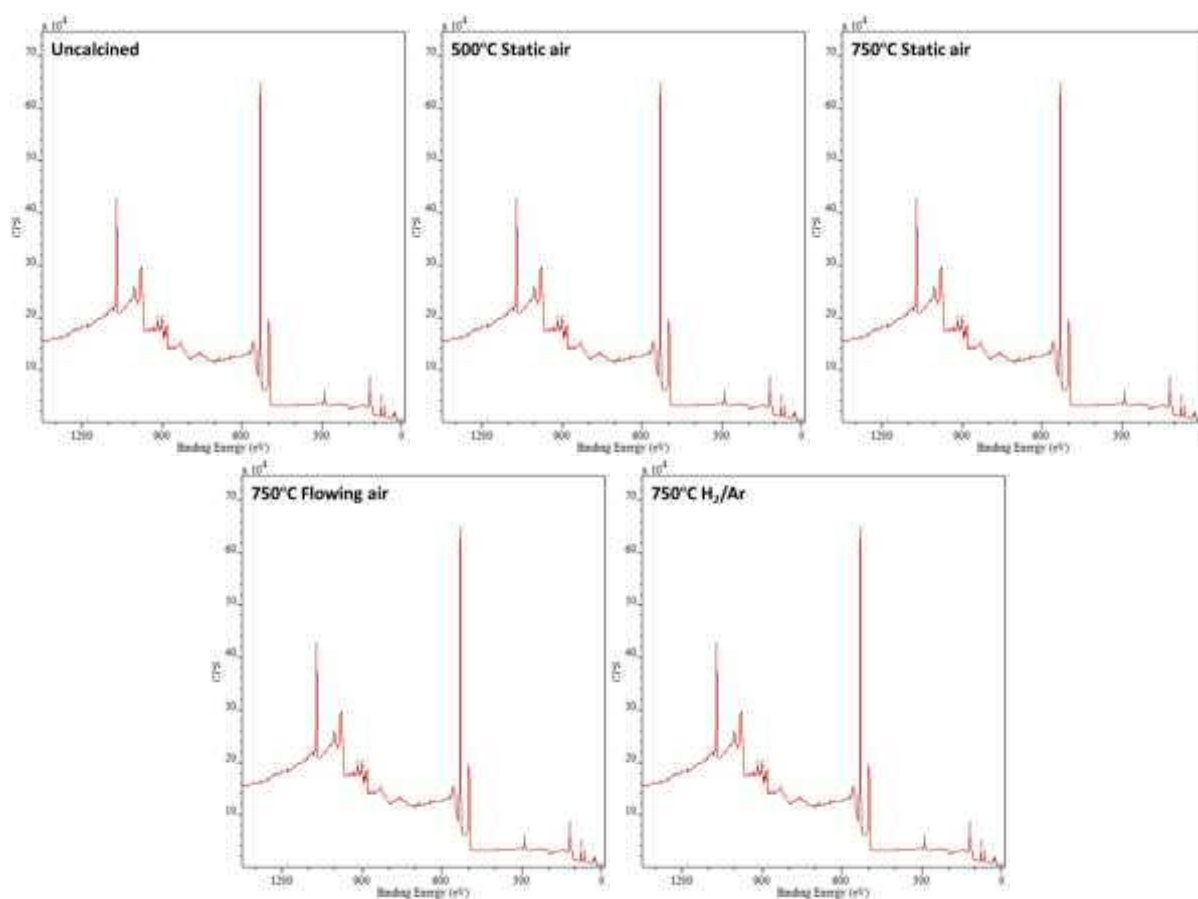


Figure 7.15 XPS wide scan spectra of CNA 7:3:10 catalysts prepared under various calcination conditions

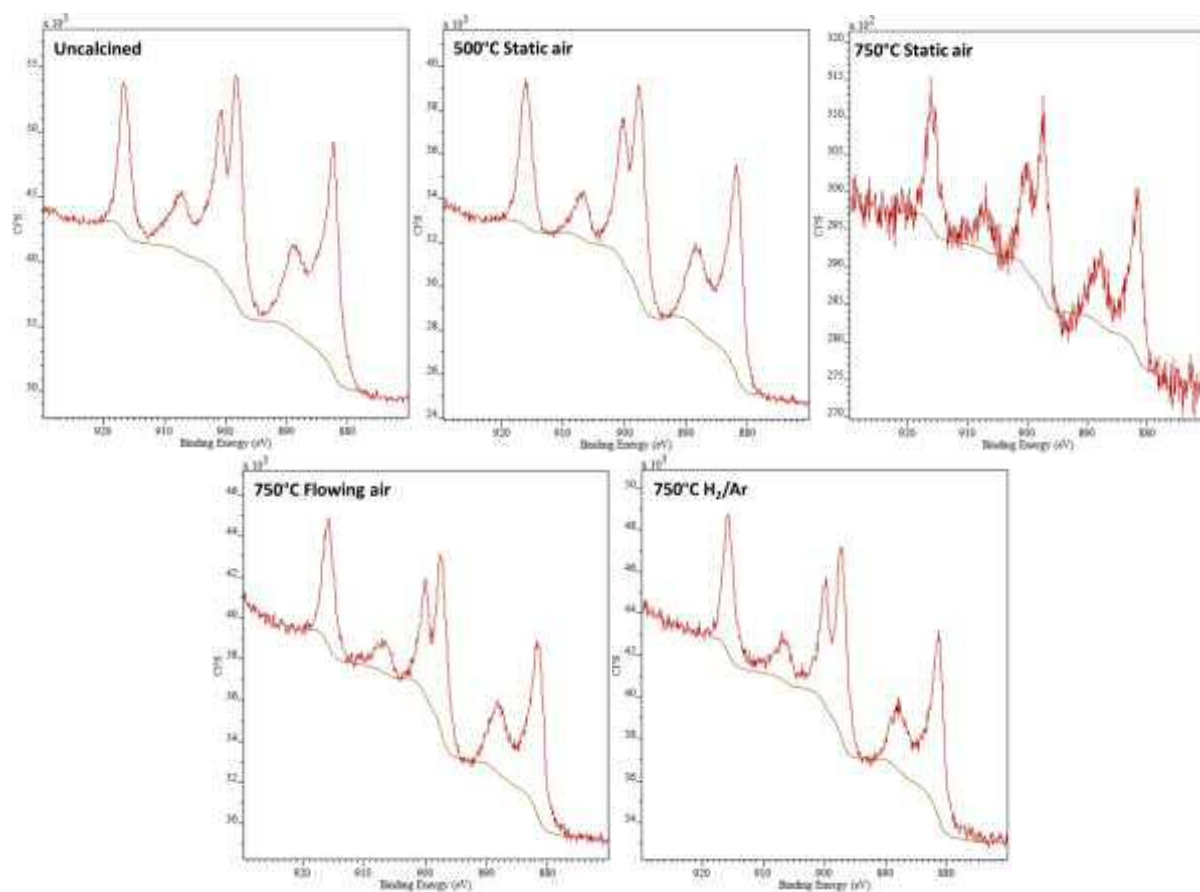


Figure 7.16 Ce 3d regions of CNA 7:3:10 catalysts prepared under various calcination conditions

### 7.1.2.3 Chapter 5

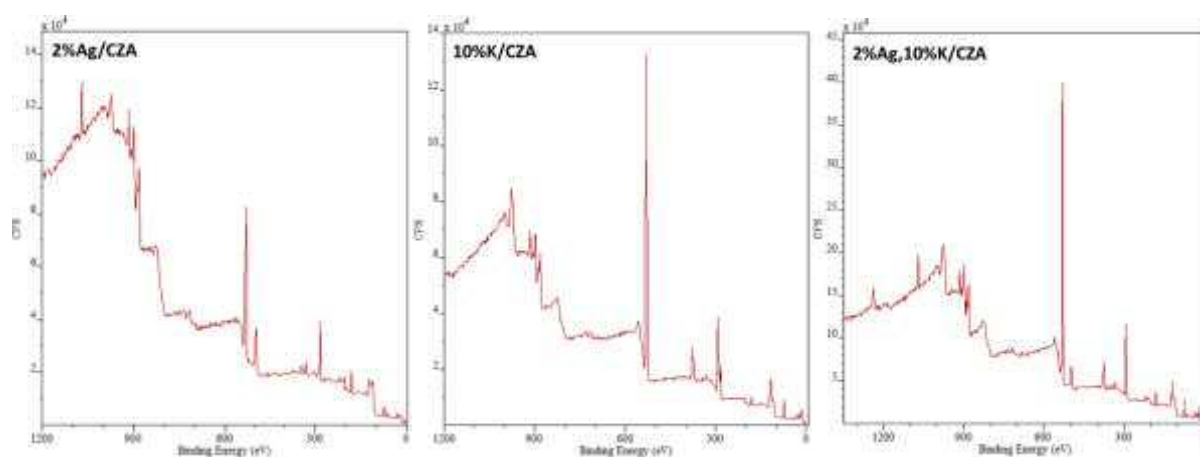


Figure 7.17 XPS wide scan spectra of 2%Ag, 10%K and 2%Ag/CZA, 10%K/CZA and 2%Ag, 10%K/CZA

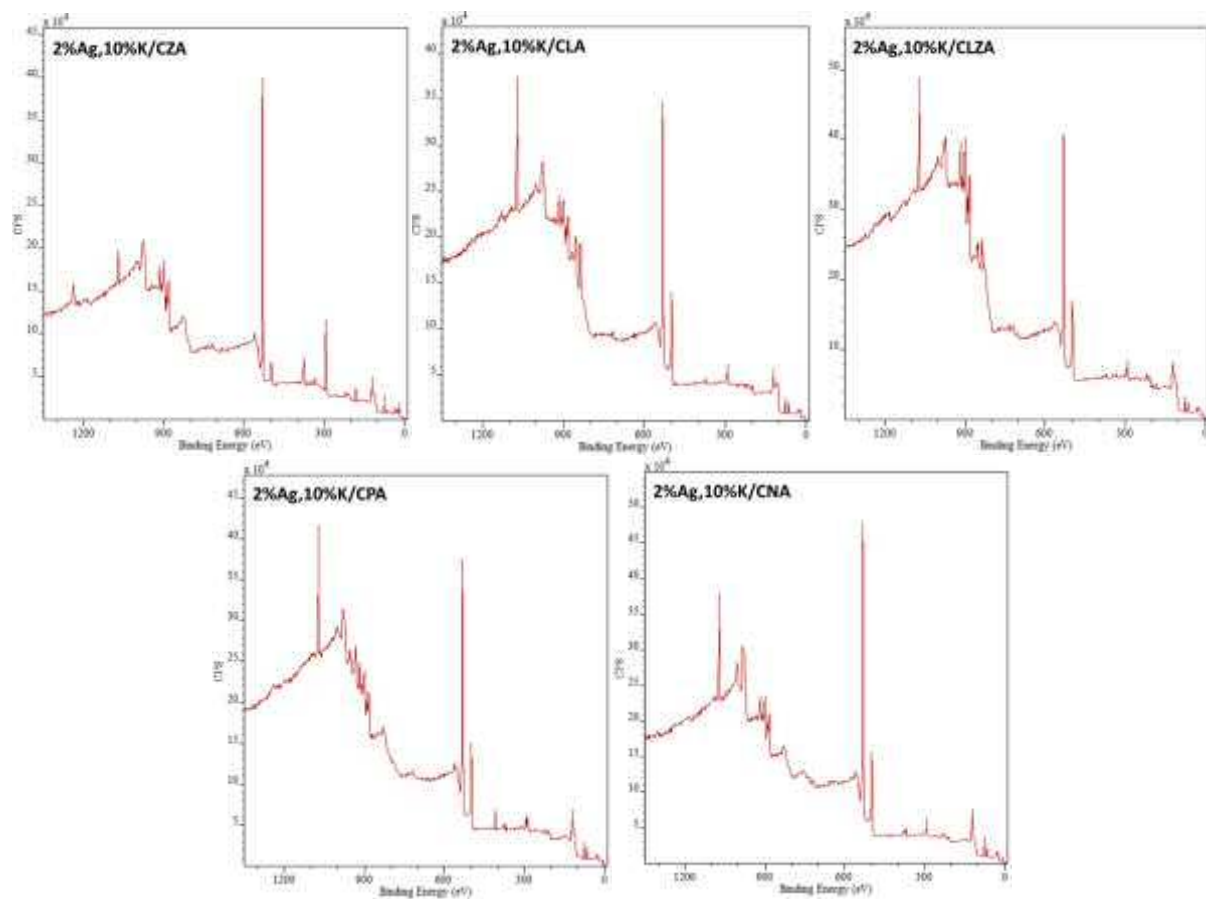


Figure 7.18 XPS wide scan spectra of 2%Ag,10%K on CZA, CLA, CLZA, CPA and CNA

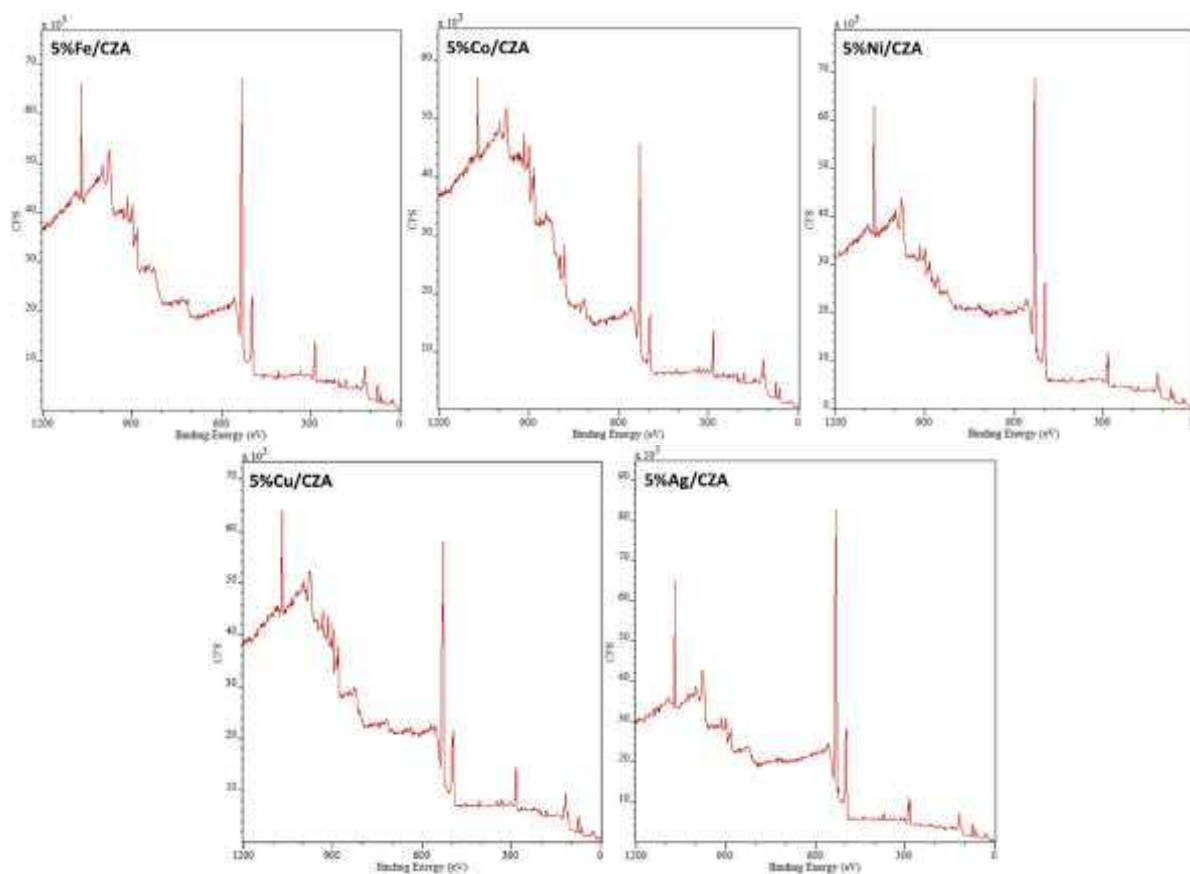


Figure 7.19 XPS wide scan spectra of 5%Fe, 5%Co, 5%Ni, 5%Cu and 5%Ag on CZA

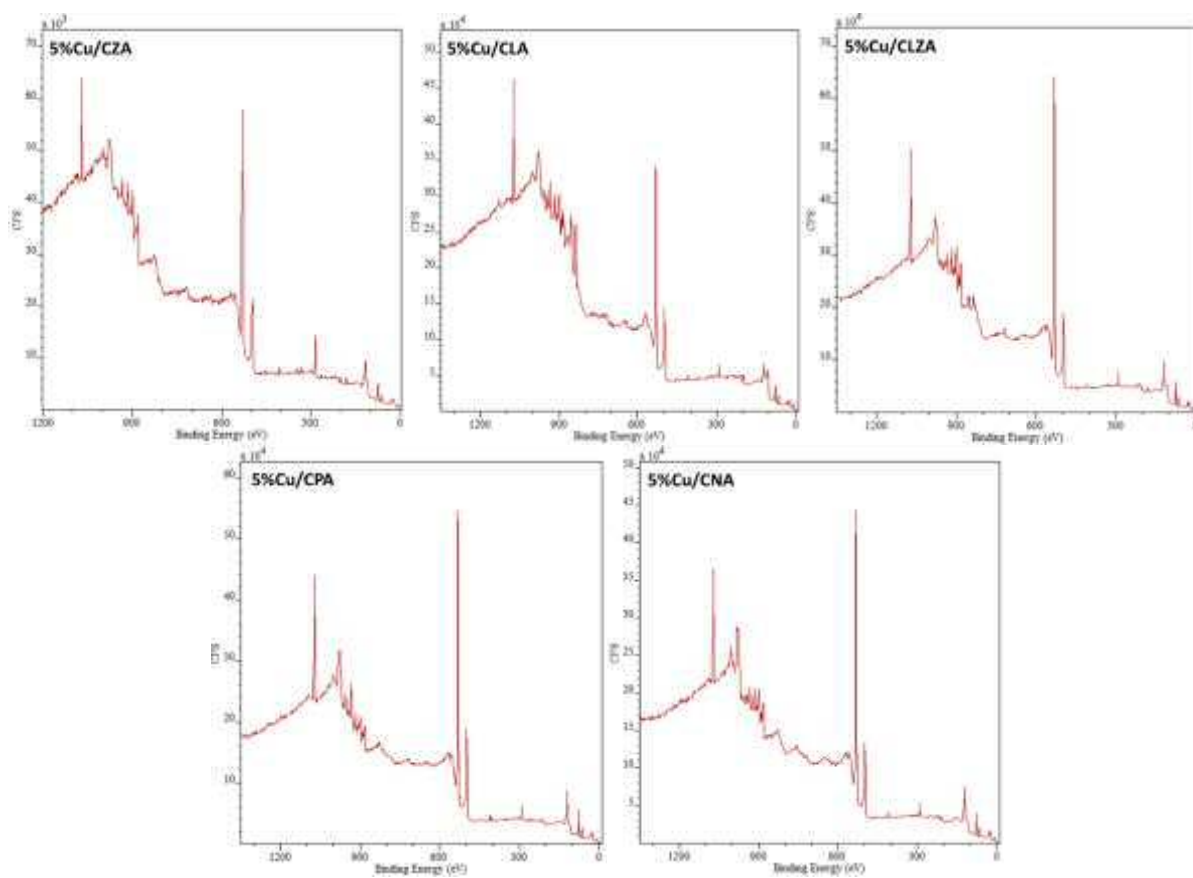


Figure 7.20 XPS wide scan spectra of 5%Cu on CZA, CLA, CLZA, CPA and CNA

### 7.1.3 Thermogravimetric analysis

#### 7.1.3.1 Chapter 4

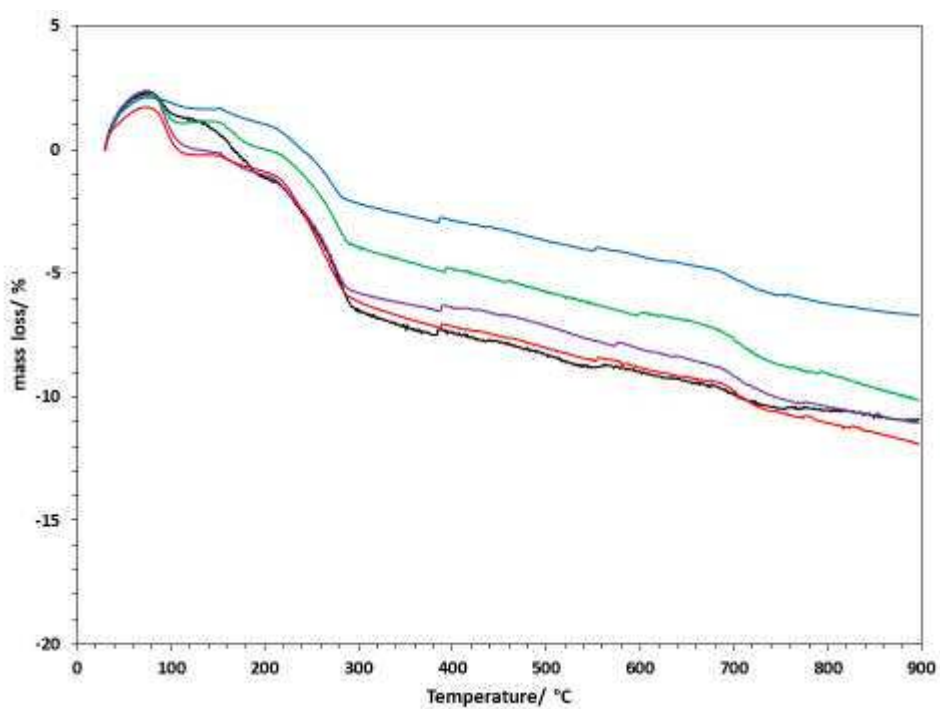


Figure 7.21 TGA plots of CZA 7:3:10 (black), CLZA 7:3:10 (purple), CLA 7:3:10 (green), CPA 7:3:10 (blue) and CNA7:3:10 (red)

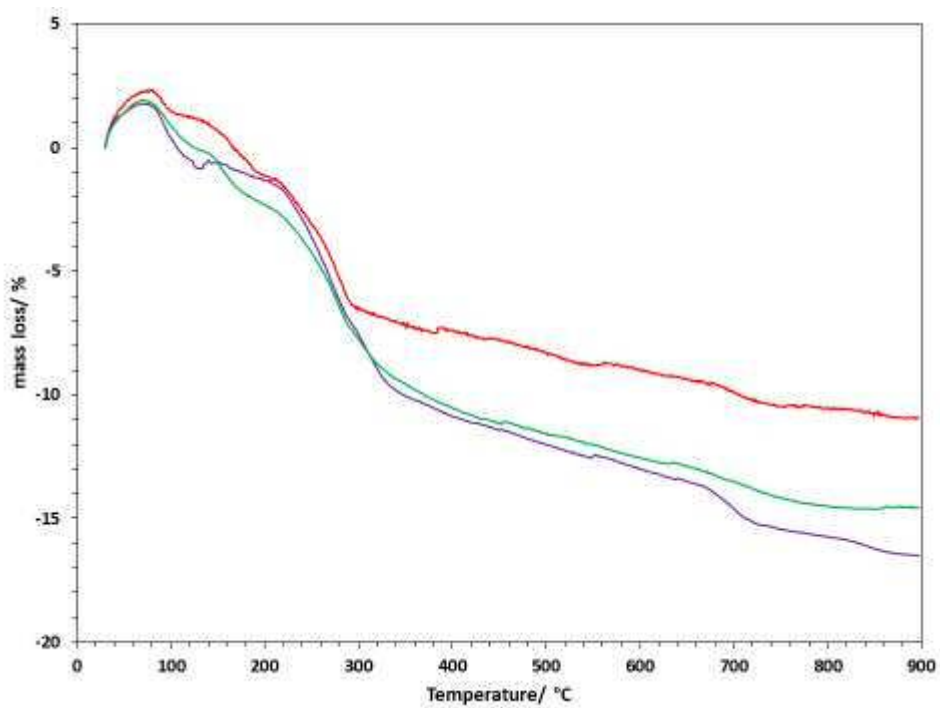


Figure 7.22 TGA plots of CZA catalysts; 7:3:10 (red) 5:5:10 (purple) and 3:7:10 (green)

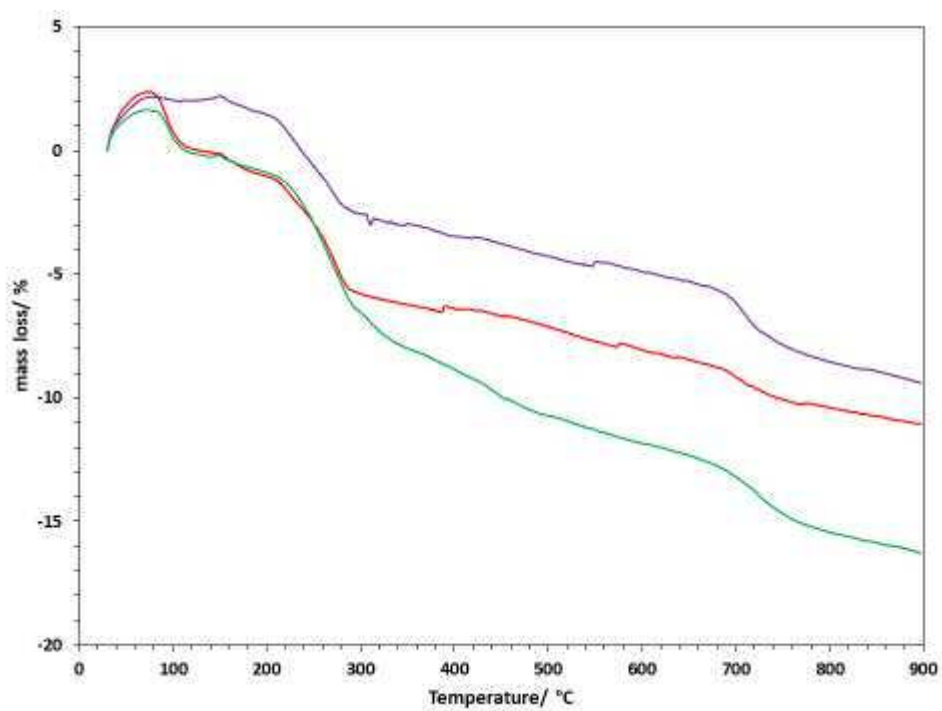


Figure 7.23 TGA plots of CLZA catalysts; 7:3:10 (red) 5:5:10 (purple) and 3:7:10 (green)

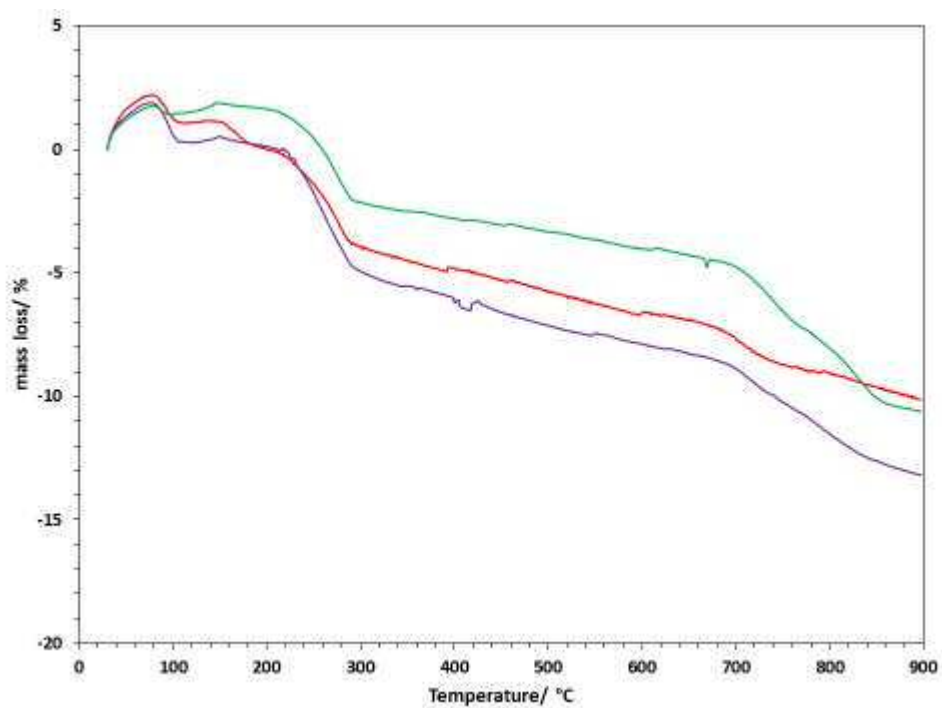


Figure 7.24 TGA plots of CLA catalysts; 7:3:10 (red) 5:5:10 (purple) and 3:7:10 (green)



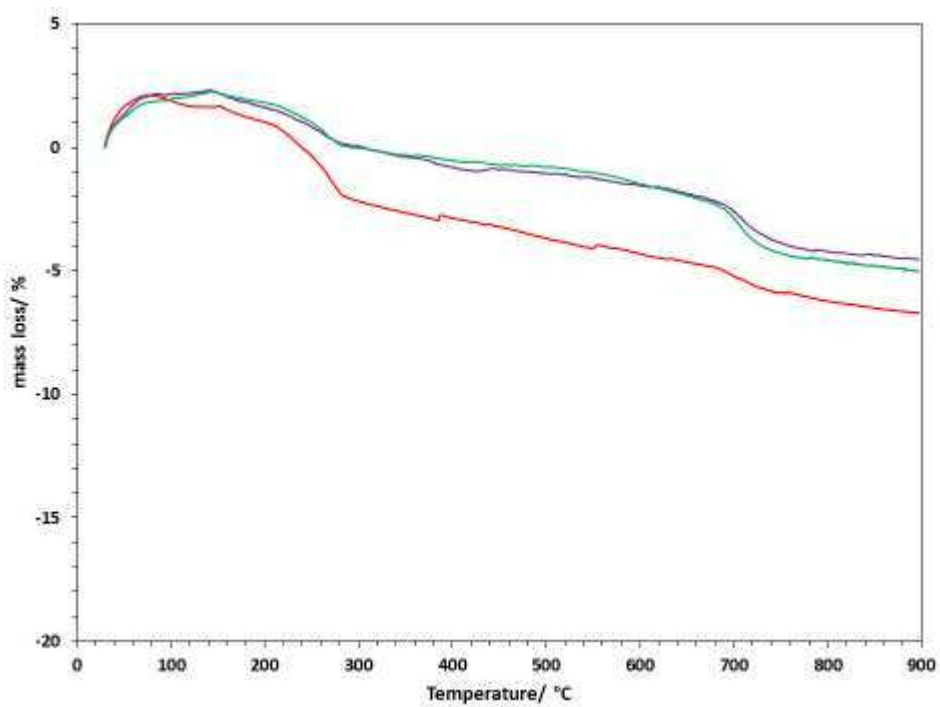


Figure 7.25 TGA plots of CPA catalysts; 7:3:10 (red) 5:5:10 (purple) and 3:7:10 (green)

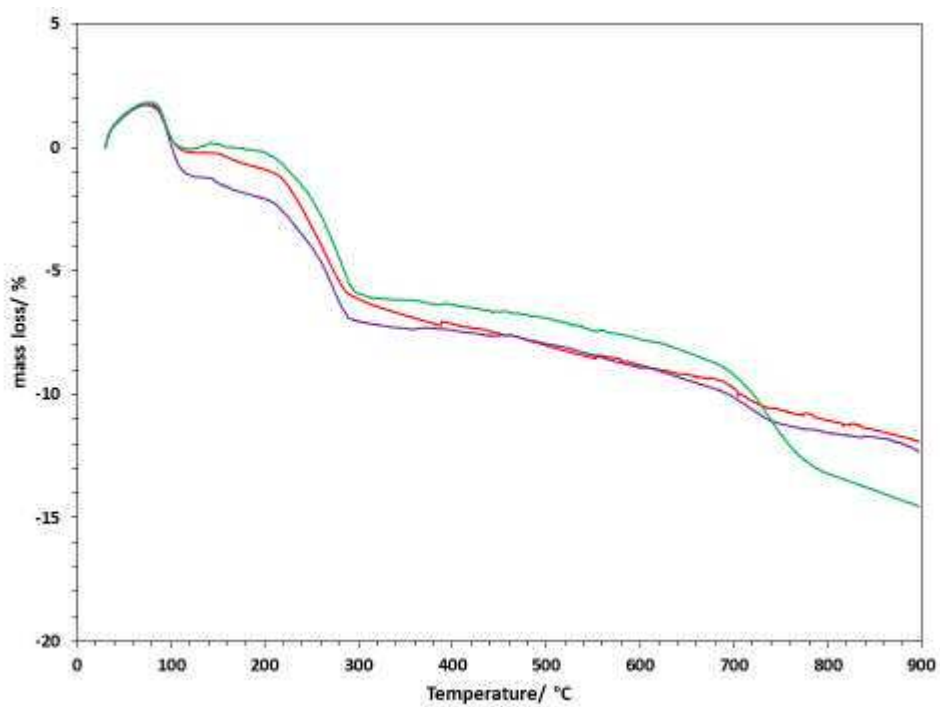


Figure 7.26 TGA plots of CNA catalysts; 7:3:10 (red) 5:5:10 (purple) and 3:7:10 (green)

## 7.1.3.2 Chapter 5

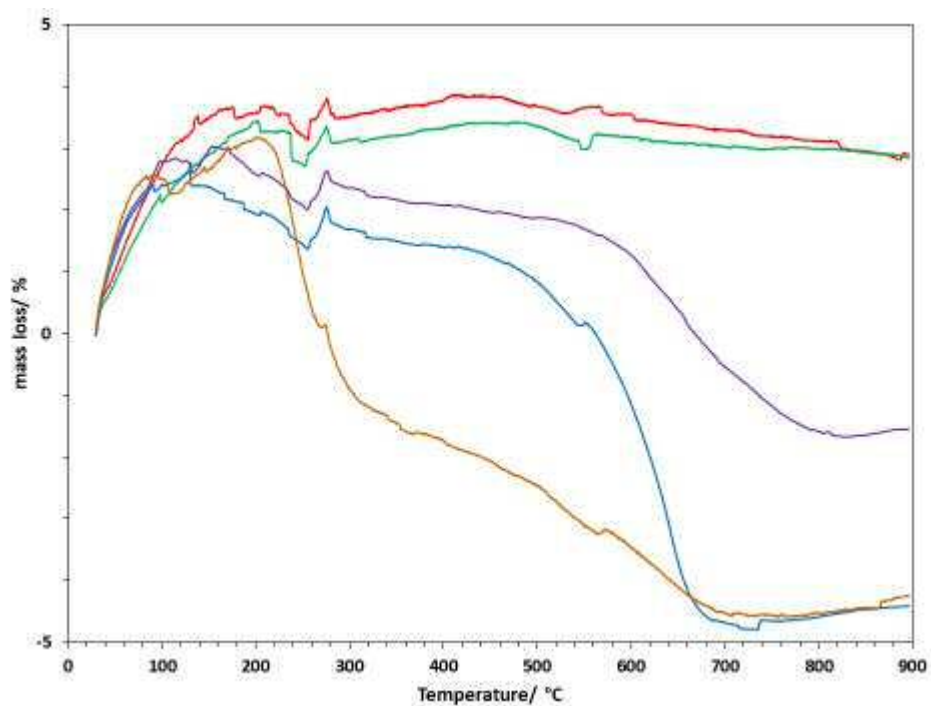


Figure 7.27 TGA plots of 5%Fe/CZA (red), 5%Co/CZA (green), 5%Ni/CZA (purple), 5%Cu/CZA (blue) and 5%Ag/CZA (brown)

## 7.2 Soot oxidation testing – TGA

## 7.2.1 Chapter 3

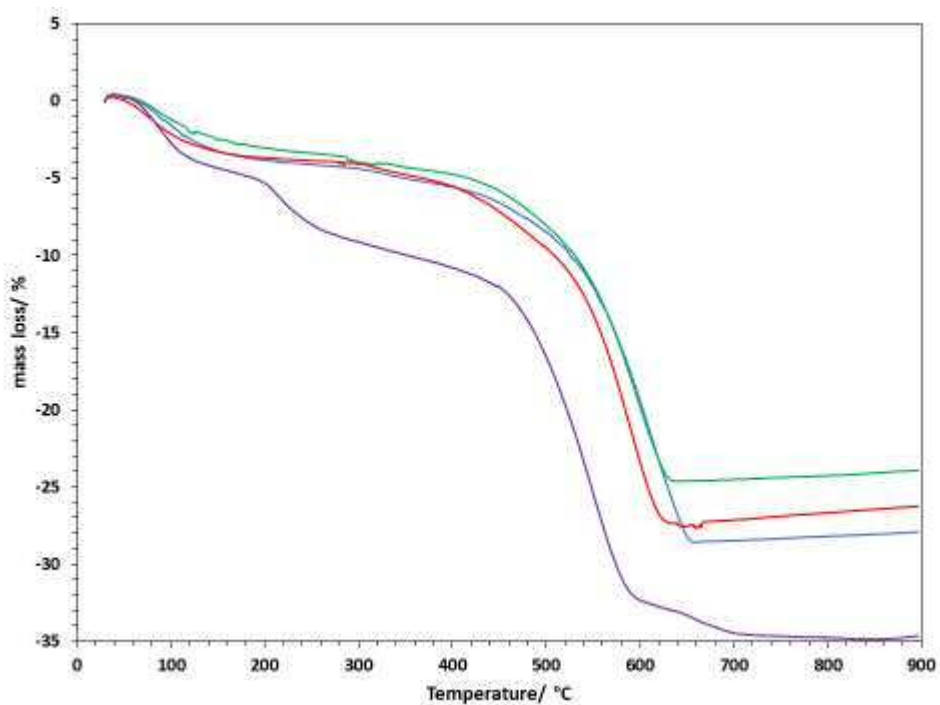
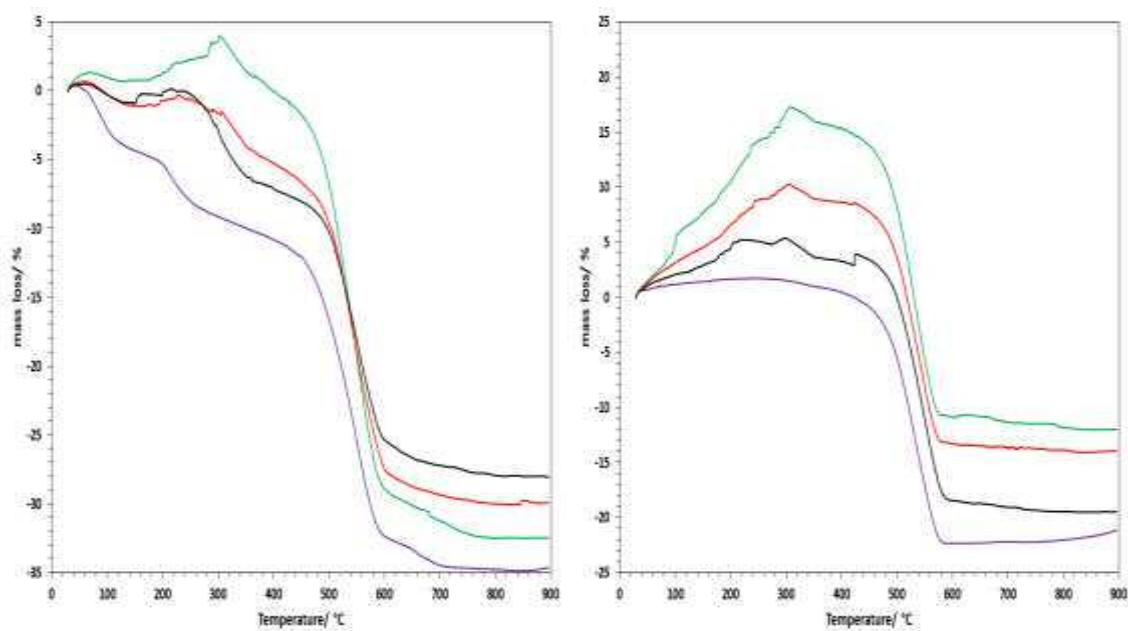
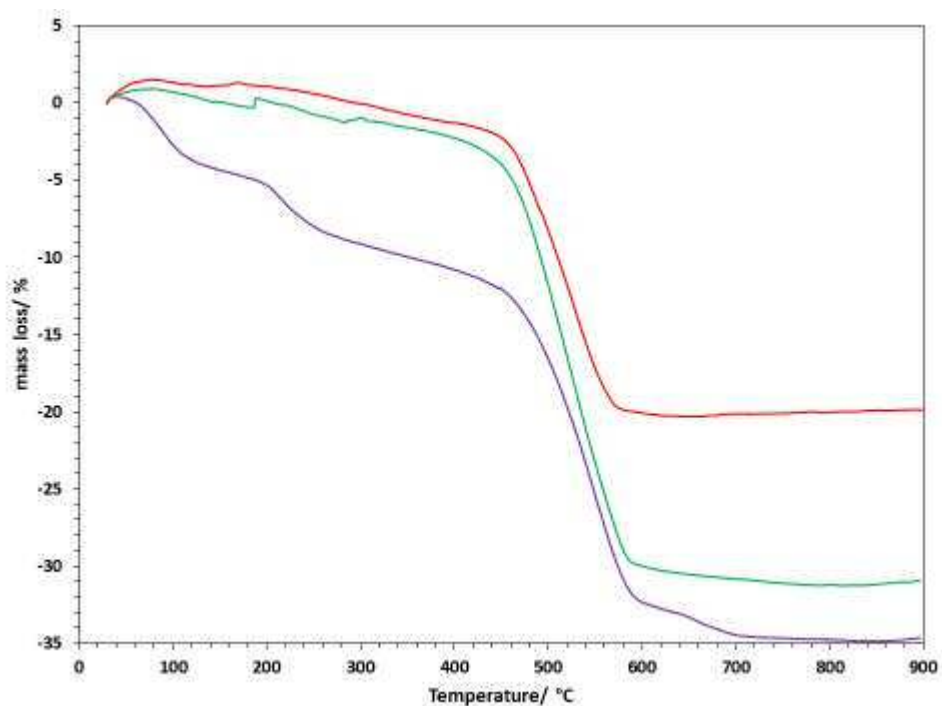


Figure 7.28 TGA plots of catalyst/soot mixtures containing: manual CZA supports (blue, green, red) and automated CZA (purple)



**Figure 7.29** TGA plots of catalyst/soot mixtures containing: Na-CZA0.5L (purple), Na-CZA1.0L (green), Na-CZA1.5L (red) and Na-CZA2.0L (black) on their first run (left) and second run (right)



**Figure 7.30** TGA plots of catalyst/soot mixtures containing: Na-CZA0.5L (purple), K-CZA0.5L (green), Cs-CZA0.5L (red)

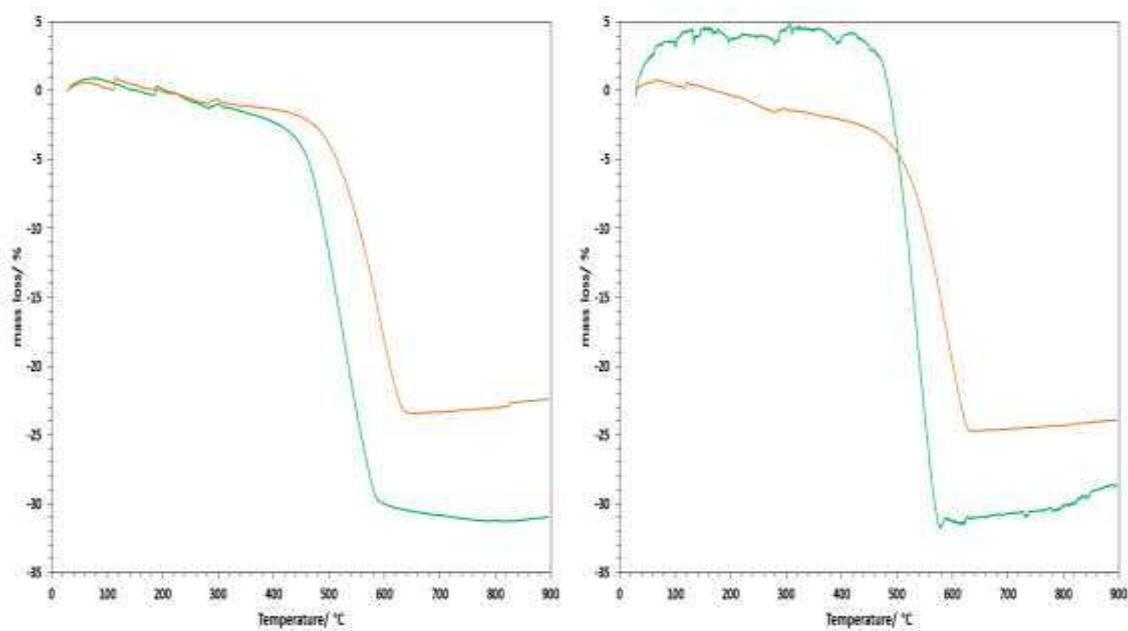


Figure 7.31 TGA plots of catalyst/soot mixtures containing: K-CZA0.5L (green) and K-CZA2.0L (orange) on their first run (left) and second run (right)

## 7.2.2 Chapter 4

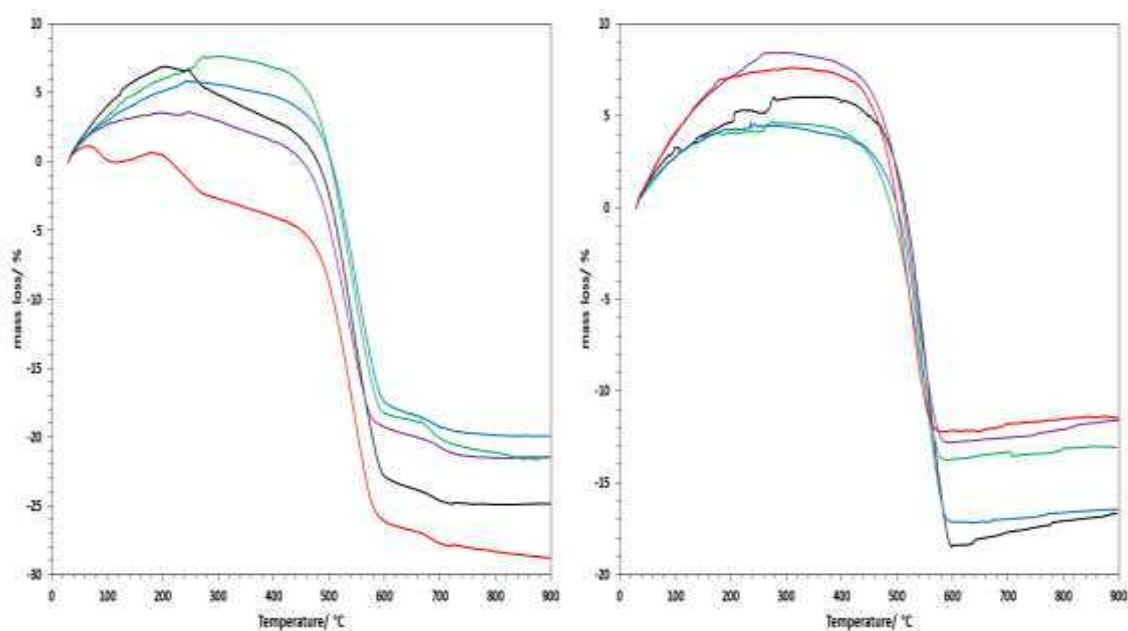
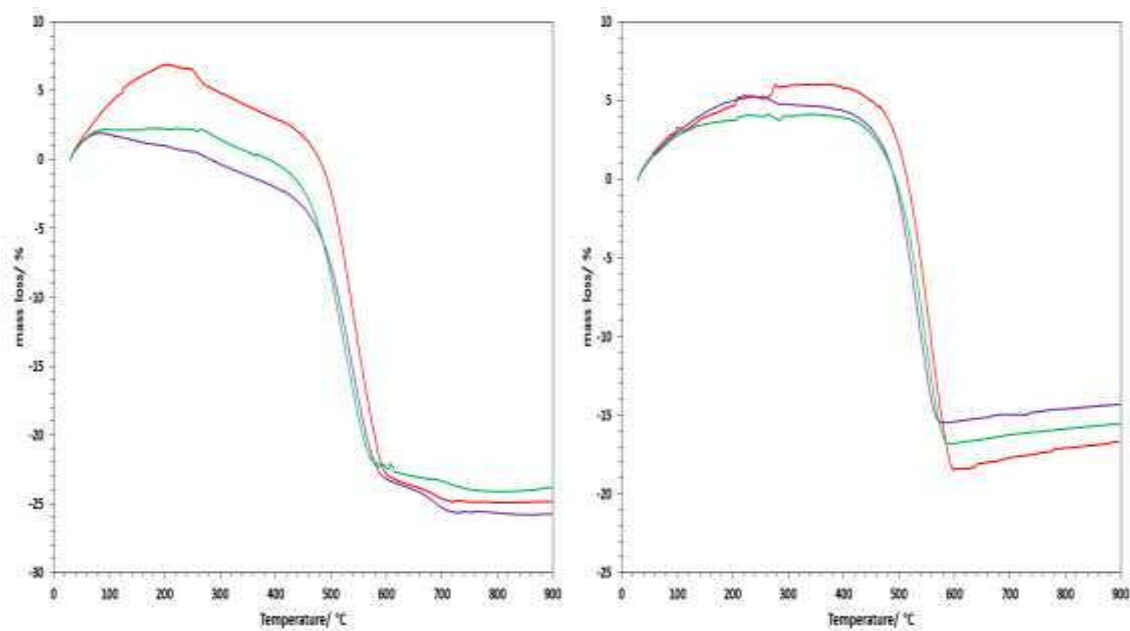
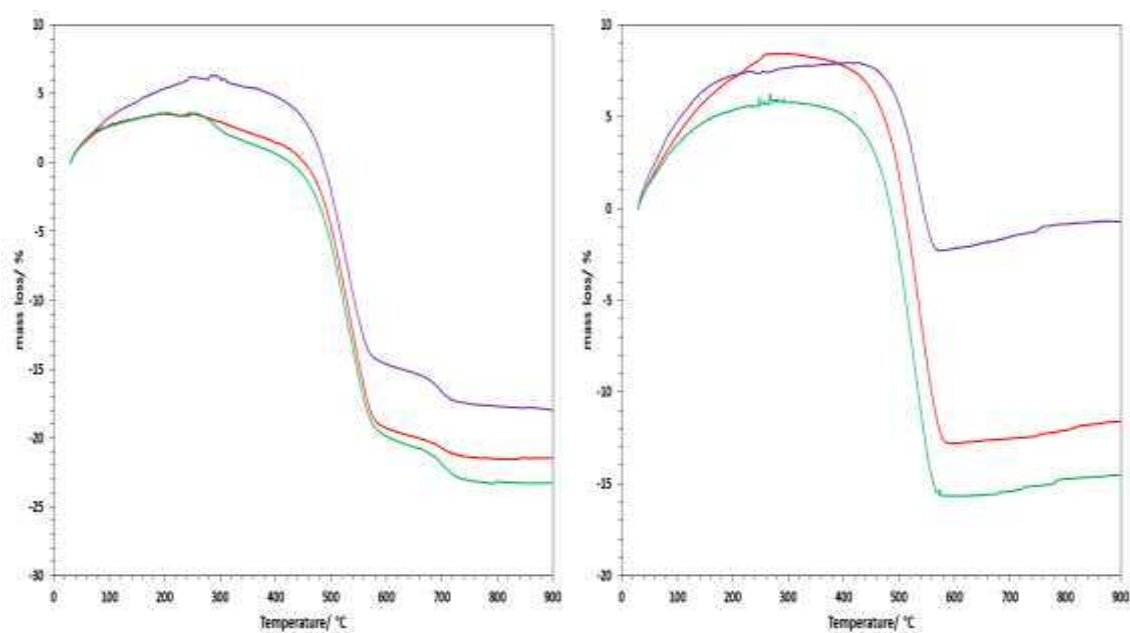


Figure 7.32 TGA plots of CMA 7:3:10 catalyst/soot mixtures containing: CZA (black), CLZA (purple), CLA (green), CPA (blue) and CNA (red) on their first run (left) and second run (right)



**Figure 7.33** TGA plots of catalyst/soot mixtures containing CZA: 7:3:10 (red), 5:5:10 (purple) and 3:7:10 (green) on their first run (left) and second run (right)



**Figure 7.34** TGA plots of catalyst/soot mixtures containing CLZA: 7:3:10 (red), 5:5:10 (purple) and 3:7:10 (green) on their first run (left) and second run (right)

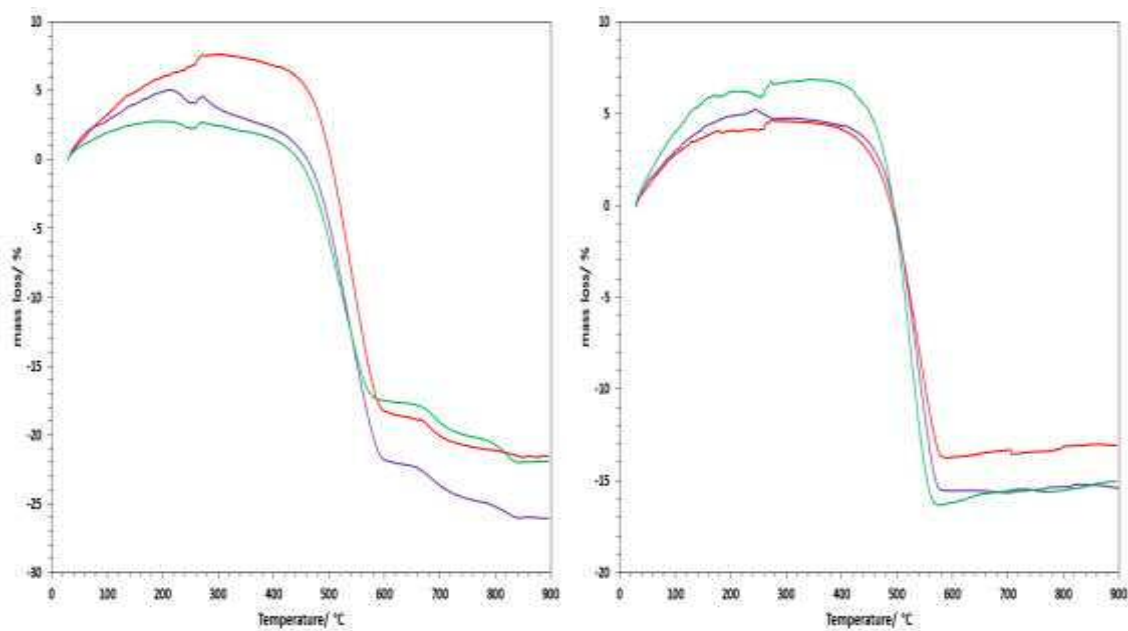


Figure 7.35 TGA plots of catalyst/soot mixtures containing CLA: 7:3:10 (red), 5:5:10 (purple) and 3:7:10 (green) on their first run (left) and second run (right)

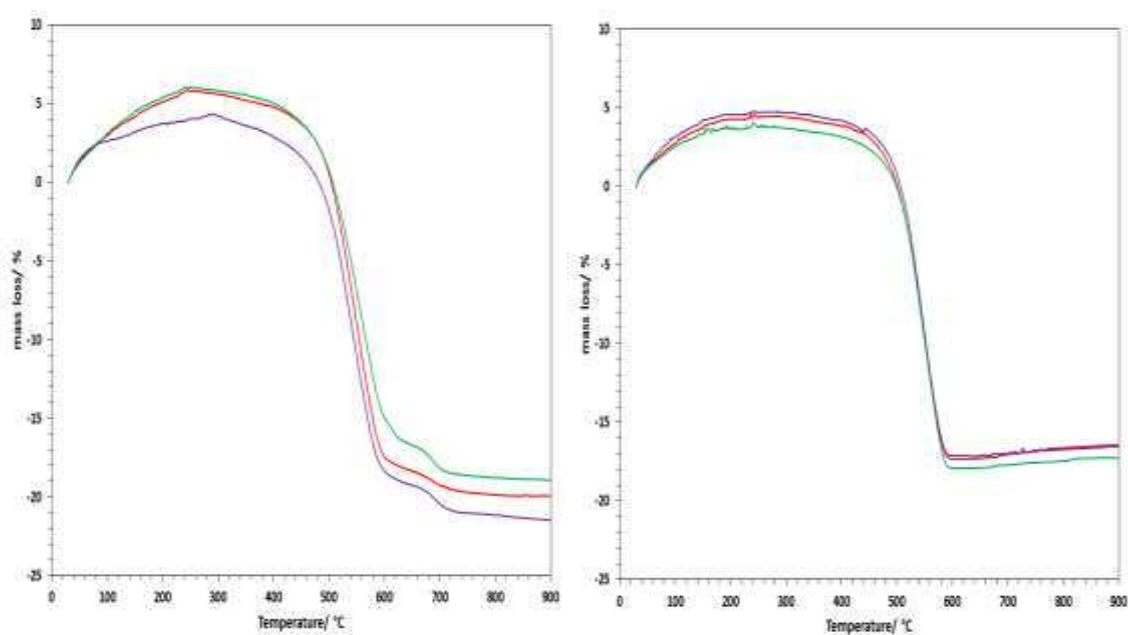
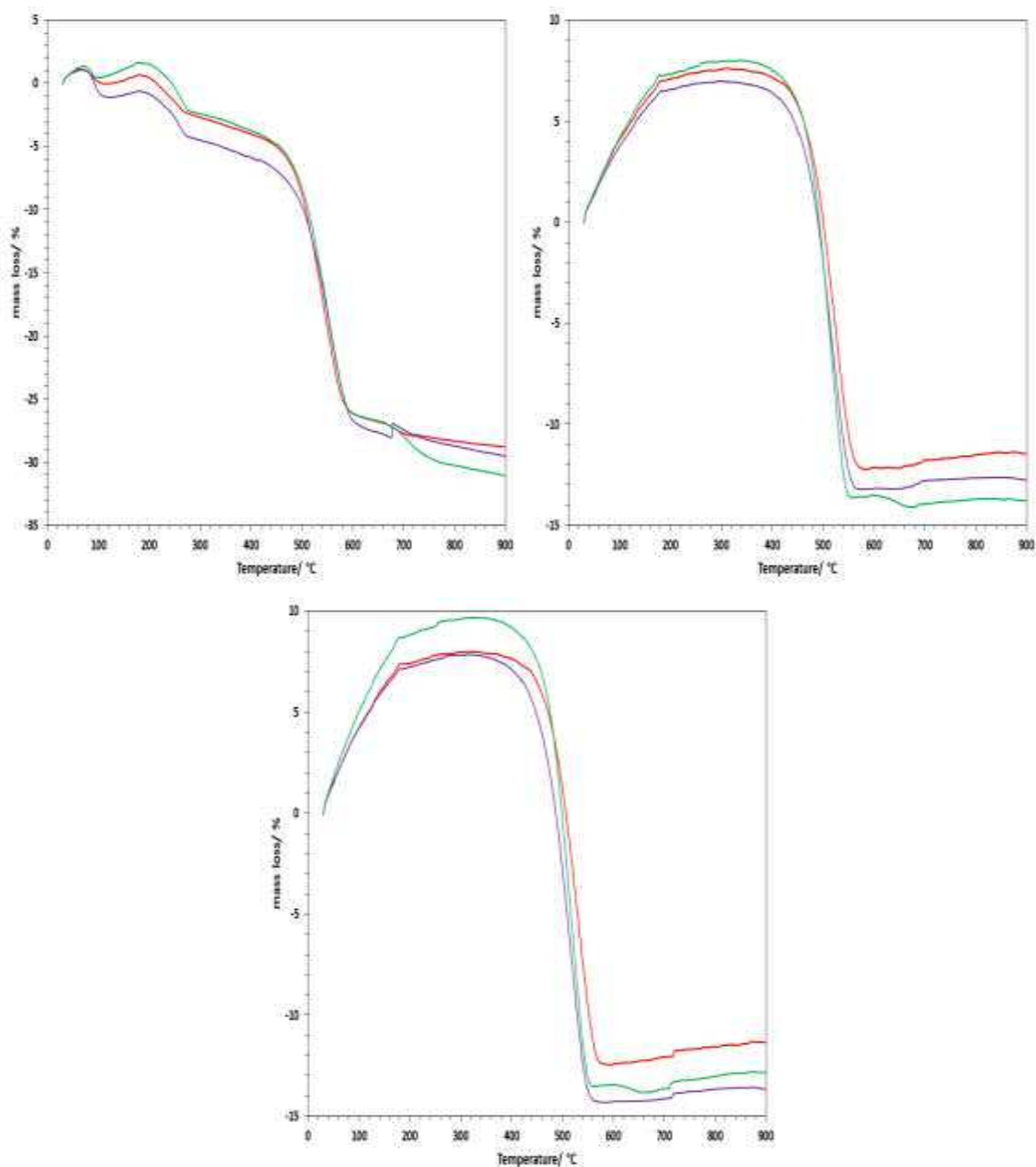
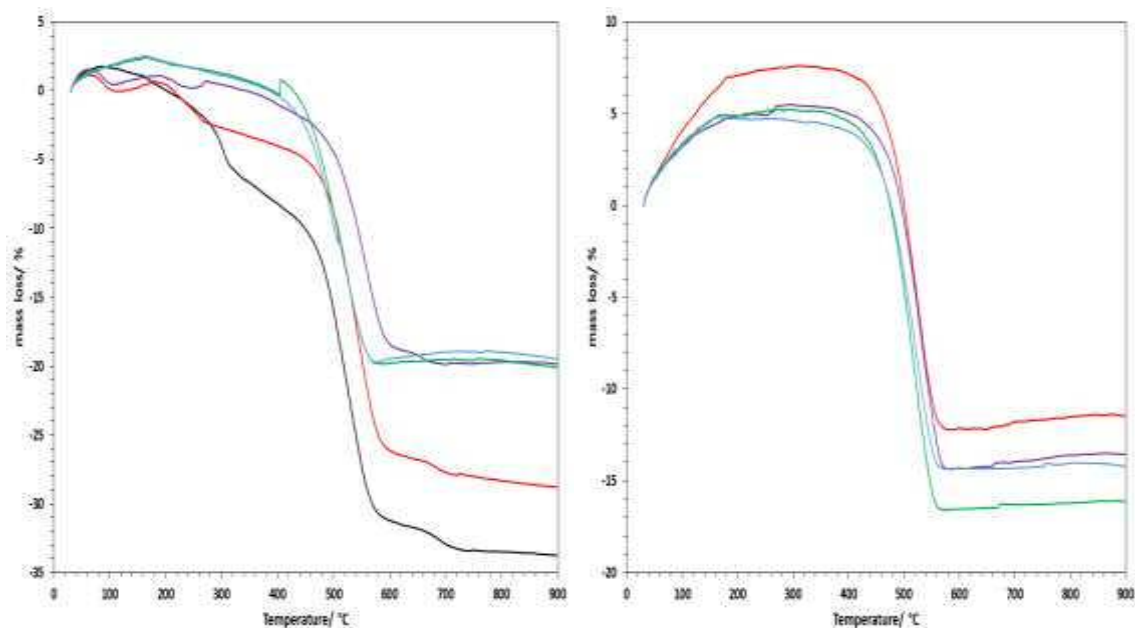


Figure 7.36 TGA plots of catalyst/soot mixtures containing CPA: 7:3:10 (red), 5:5:10 (purple) and 3:7:10 (green) on their first run (left) and second run (right)



**Figure 7.37** TGA plots of catalyst/soot mixtures containing CNA: 7:3:10 (red), 5:5:10 (purple) and 3:7:10 (green) on their first run (top left), second run (top right) and third run (bottom)



**Figure 7.38** TGA plots of catalyst/soot mixtures containing CNA: Uncalcined (black), 500°C static air (red), 750°C static air (purple), 750°C flowing air (green), 750°C 10% $H_2$ /Ar (blue) on their first run (left) and second run (right)

### 7.2.3 Chapter 5

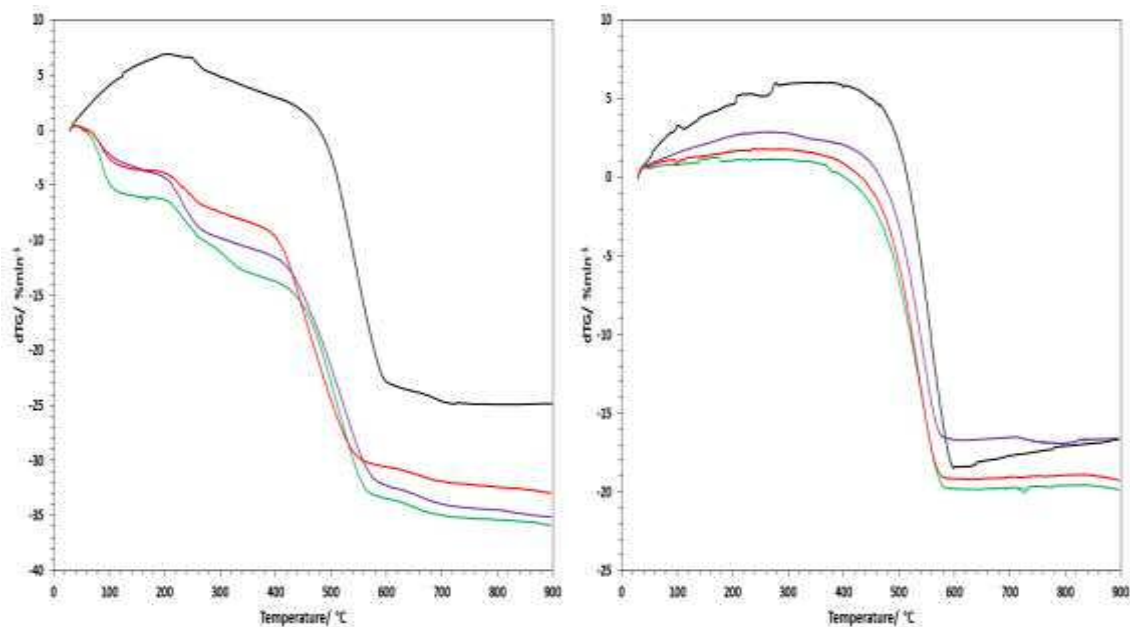


**Figure 7.39** TGA plots of catalyst/soot mixtures containing: CZA (black), 2%Ag/CZA (purple), 10%K/CZA (green) and 2%Ag,10%K/CZA (red) on their first run (left) and second run (right)



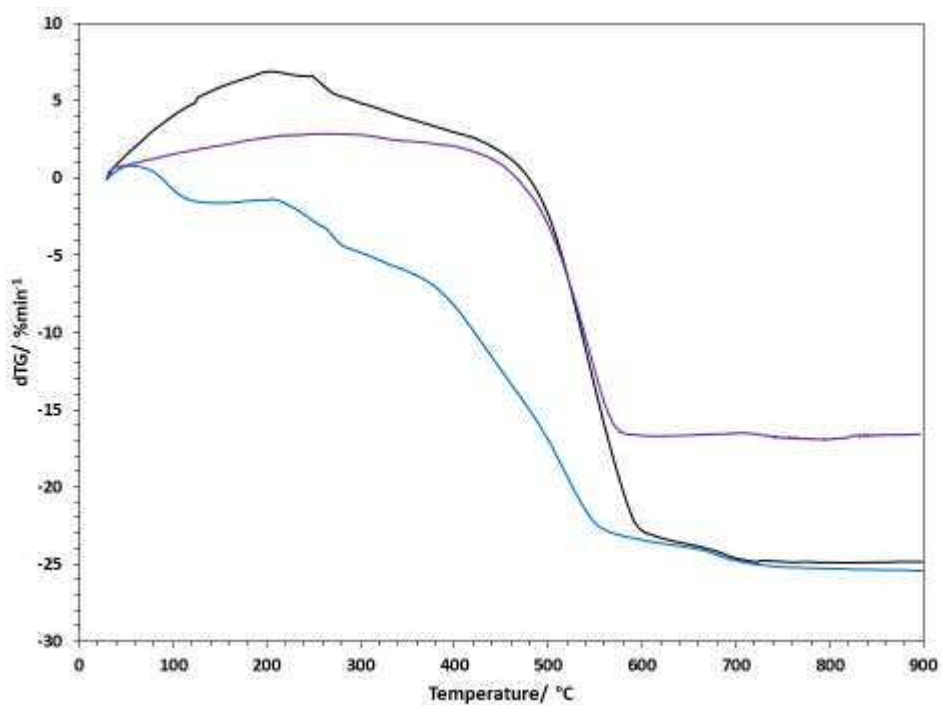


**Figure 7.40** TGA plots of catalyst/soot mixtures containing: CZA (black), 2%Ag/CZA (purple) in loose contact, and CZA in tight contact (blue)

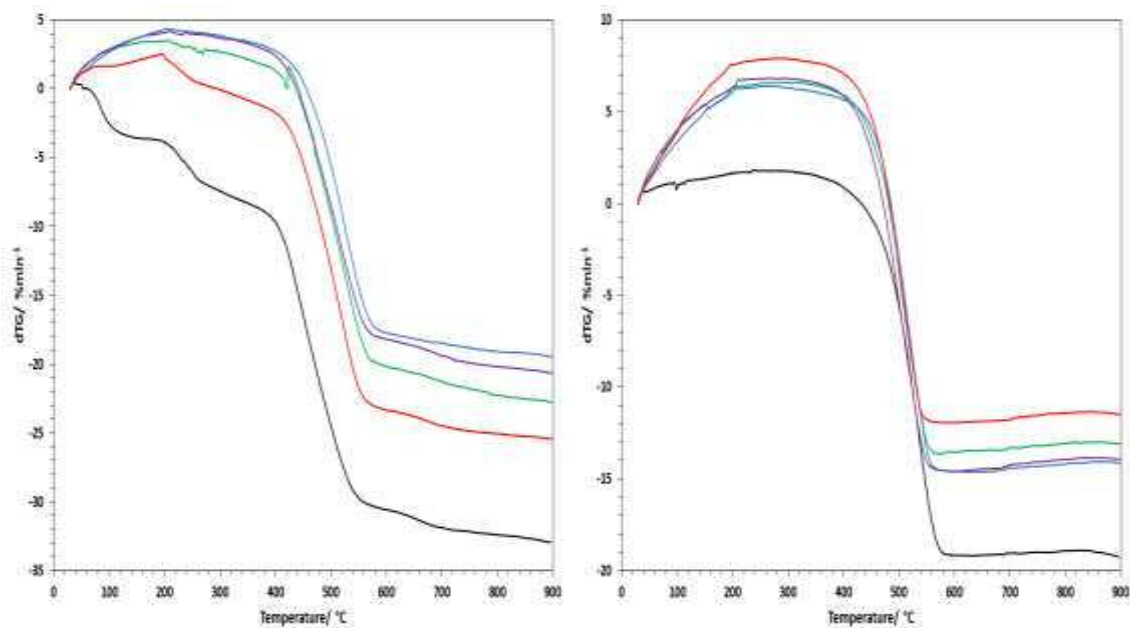


**Figure 7.41** TGA plots of catalyst/soot mixtures containing: 2%Ag,10%K on CZA (black), CLA (green), CLZA (purple), CPA (blue) and CNA (red) on their first run (left) and second run (right)

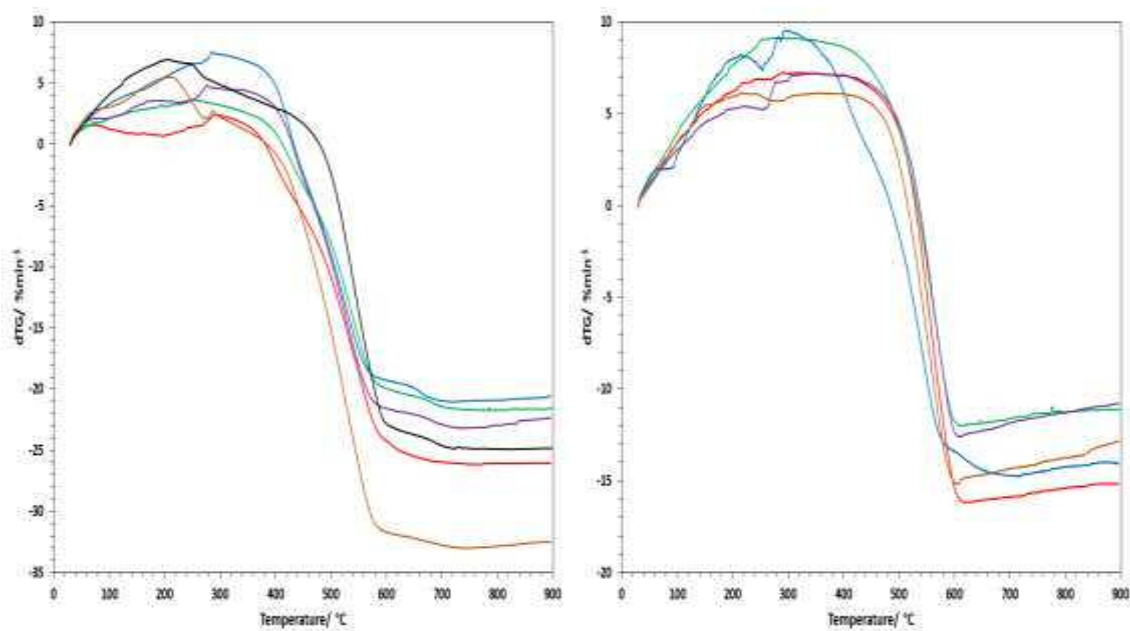


**Figure 7.42** TGA plots of catalyst/soot mixtures containing: CZA (black), 5%Fe/CZA (red), 5%Co/CZA (green), 5%Ni/CZA (purple), 5%Cu/CZA (blue) and 5%Ag/CZA (brown) on their first run (left) and second run (right)

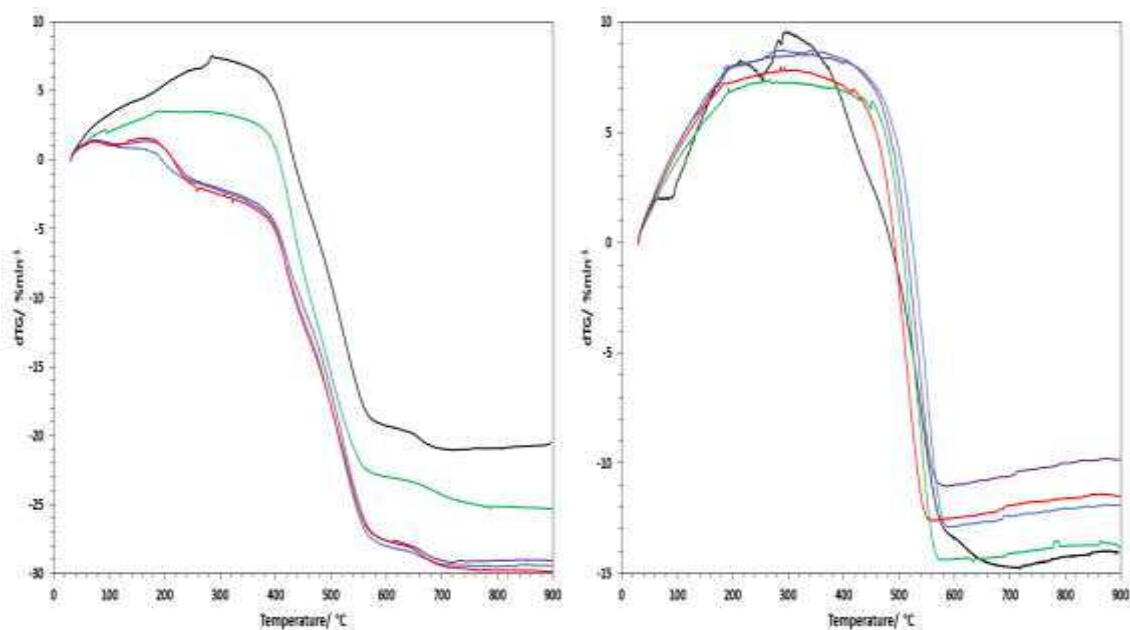


**Figure 7.43** TGA plots of catalyst/soot mixtures containing: 5%Cu on CZA (black), CLA (green), CLZA (purple), CPA (blue) and CNA (red)